THE UNIVERSITY OF CHICAGO

NANOSCALE ENGINEERING OF ADVANCED NANOMATERIALS FOR ENVIRONMENTAL SUSTAINABILITY

A DISSERTATION SUBMITTED TO

THE FACULTY OF THE PRITZKER SCHOOL OF MOLECULAR ENGINEERING

IN CANDIDACY FOR THE DEGREE OF

DOCTOR OF PHILOSOPHY

BY

XIAOYU SUI

CHICAGO, ILLINOIS

MARCH 2022

To my mother and father, and Wen

TABLE OF CONTENTS

LIST OF FIGURES

LIST OF TABLES

ACKNOWLEDGEMENTS

First, I would like to acknowledge my advisor, Prof. Junhong Chen, for all the support and guidance he gave me, during my Ph.D. study. His careful thinking and serious effort always encourage me to have a deeper understanding on scientific phenomena. This benefits me a lot.

I hope to give specific acknowledgements to my colleague Dr. Arnab Maity for his major contribution in developing the new signal transduction mechanism, physical model explanation, and portable meter development, displayed in the water sensor research work. Thanks to Dr. Haihui Pu for his efforts on percolation theory analysis. I would like to acknowledge my colleague Dr. Xingkang Huang for helping me assemble the coin cells for electrochemical measurements, and relevant helpful discussions on the research work about batteries. I acknowledge the wonderful collaboration from the entire NSF Scalable Nanomanufacturing project team consisting of Drs. Mark Hersam, Shiyu Zhou, Nathan Salowitz, Deyang Qu, and Junhong Chen groups. In particular, many thanks go to Dr. Mark Hersam's group from Northwestern University, for all their efforts on the collaborative investigation of sensor nanomanufacturing by inkjet printing.

Finally, I acknowledge the financial support from National Science Foundation (NSF) No. CMMI-1727846, CMMI-2039268, and IIP-1516207.

ABSTRACT

Exploring novel functional materials is pivotal in the advancement of science, technology, and society. Nanomaterials often exhibit distinctive and fascinating physicochemical properties, providing scientific solutions to various challenges that human beings are facing. Rational design and integration of different materials at the nanoscale is an effective way to maximize the advantages of nanomaterials and to realize real device applications. The main objectives of this dissertation research are to synthesize novel composite nanomaterials, design and fabricate nanostructures through nanoscale engineering for environmental sustainability including water sensors for advanced environmental monitoring and lithium/potassium-ion batteries for energy storage.

First, an improved method is developed for the deposition of graphene oxide (GO) onto electrodes, which enables a reliable and high-quality fabrication of reduce graphene oxide (rGO)-based field-effect transistor (FET) devices. Through the combination of probe modified 0D Au nanoparticles, 2D rGO, and Al_2O_3 thin film, an effective FET sensing platform for water contaminant monitoring is demonstrated. Assisted by a novel pulse-driven capacitive signal transduction mechanism, this sensing platform can achieve selective and highly sensitive detection of lead ions in water, with a limit of detection (LOD) < 1 ppb and a sensitivity ~350% at 2.5 ppb. When employed for the Ebola-glycoprotein (GP) detection, among those different electronic parameters driven by an AC voltage input, the maximum sensitivity was calculated from the inflection-resonance frequency on the phase spectrum: a sensitivity of ∼36−160% corresponding to 0.001−3.401 mg/L of Ebola-GP can be achieved from high inflection-resonance frequency. More importantly, the sensing platform design and high-efficient signal transduction mechanism can be applied in other FET based sensing

devices with enhanced performance. In order to reduce the fabrication cost of the 2D material-based FET sensors, scalable micromolding-in-capillary method and inkjet printing technique were explored for rGO and MoS_2-based sensor fabrication, following the theoretical percolation analysis using a 2D continuum model. The percolation theory analysis indicates that the 2D flake shape dominates in forming the electrical connection, and the required mass concentration of 2D materials for percolation can be estimated in spite of their arbitrary shapes. Using the inkjet printing technique, robust MoS_2 semiconducting channels exhibiting current on/off ratio up to the order of 10^3 (V_g from -38 V to 38 V) have been prepared. The semiconducting channel can be hundreds of micrometers long, which is compatible with the inkjet printing resolution to facilitate a fully printed FET water sensor device.

Lithium-ion batteries (LIBs) dominate in the field of portable energy storage devices. High-capacity LIBs are highly demanded for electric vehicles. Combining the high capacity of 0D SnO_2 nanoparticles with excellent mechanical and electrical properties of rGO, a SnO_2/Sn-rGO sandwiched nanocomposite has been prepared through a facile metal-organic precursor coating on GO and in-situ transformation strategy, and applied as an anode for LIBs. Its structural robustness and electrochemical reversibility are validated by the superior Li storage capability: a reversible capacity of 1,307 mAh g^{-1} at a current density of 80 mA g^{-1} and a stable capacity of 767 mAh g^{-1} after 200 cycles when cycling at 400 mA g^{-1}. Moreover, the SnO_2/Sn-rGO composite delivers a highly stable capacity of 449 mA g^{-1} without obvious decay after 400 cycles at the higher current density of 1,600 mA g^{-1}. Because of the abundance of potassium reserves, potassium-ion batteries (PIBs) have the potential to realize large-scale applications at a low cost. In order to harness the high-capacity of red P as anodes for PIBs, Zn-MOF-74 derived nanoporous carbon nanorods as an

impregnation matrix have been demonstrated through facile morphology adjustment on Zn-MOF-74 using a mixed-solvent strategy. The obtained porous carbon nanorods enable a high loading capacity and perfect encapsulation of P while reserving free spaces to accommodate the volume change of P in the composite anode, resulting in outstanding potassium storage performance in terms of initial Coulombic efficiency (78.5%), reversible capacity (up to 595.8 mAh g^{-1}), rate capability (187.5 mAh g^{-1} at 5 A g^{-1}), and long-term cycling stability (retaining 150.7 mAh g^{-1} at 2.5 A g^{-1} after 400 cycles). This morphology modulation of Zn-MOF-74 promotes advanced applications of Zn-MOF-74 as well as its derived carbon materials, which potentially opens a general pathway for the directed evolution of various carboxylate-based MOFs.

Through nanoscale engineering of advanced nanomaterials, this dissertation study demonstrates a high-performance rGO and MoS_2-based FET sensor platform and novel energy storage devices. Highly sensitive and selective real-time water sensors are achieved through sensor structure optimization and novel signal transduction mechanism, and can potentially enable intelligent water systems. The rational sensor design and novel transduction mechanism are applicable to other FET-based sensing devices for enhanced performance. Furthermore, scalable nanomanufacturing of these sensor devices, e.g., through micromolding-in-capillary and inkjet printing, can potentially enable low-cost, large-scale sensor deployment. LIBs and PIBs based on novel nanocomposites with carefully tailored carbon matrix are useful for a wide range of energy storage applications.

CHAPTER 1 INTRODUCTION AND LITERATURE REVIEW

1.1 Introduction

Environmental degradation is a prominent challenge for the sustainable development of human society in the 21st century. The growing global population and society development inevitably load much higher pressure on environment and energy consumption. Environmental pollution in air, water, and soil has become a serious threat to human health. In 2015, diseases caused by environmental pollution gave rise to an estimated 9 million premature deaths --- 16% of total deaths worldwide.[1] Real-time and onsite environmental pollution monitoring is in great demand to ensure health and environmental safety. Our energy systems also have significant environmental impacts. Conventional and current fossil fuels (coal, oil and gas) dominating energy supplies produce greenhouse gases like carbon dioxide (CO_2), which causes global climate change, and various environmental pollutants (e.g., NO_x from automobile exhaust). Developing clean, renewable energy techniques and transforming energy structure are necessary to overcome the limited sources of fossil fuels and maintain a sustainable development.

Nanomaterials, exhibiting fascinating physicochemical properties distinct from bulk materials, continue to show great potential to meet the challenges that human beings are facing in environment and energy fields. In the past few decades, nanomaterials have been explored explosively and contributed significantly to these areas, such as secondary batteries, solar cells, fuel cells, supercapacitors, CO_2 conversion, sensors, air and water purification.[2-7] Nanomaterials

and nanotechnology promise the scientific solutions to environmental safety and clean energy challenges.

Water, serving as the pivotal link between the human society and the natural world, is at the core of sustainable development. Water safety, especially drinking water safety, is directly related to human health, so it is very important to monitor the water containments in real time. Although conventional standard detection methods, such as inductively coupled plasma mass spectrometry (ICP-MS), atomic emission spectrometry (AES), and atomic absorption spectroscopy (AAS), are capable of accurate and specific chemical determination, it is almost impossible to use these methods for a point-of-care, real-time and popularized detection, due to the specialized instruments, professional operations, tedious sample pretreatments, and relative high cost.[8] Nanomaterials-enabled sensors are promising to provide potentially low-cost and widespread drinking water monitoring, and thus have attracted increasing levels of attention from the worldwide scientific community.[9] Nanosensors based on field-effect transistors (FETs) are especially compelling because of their low-cost, high sensitivity, rapid, real-time and in situ detection.[7]

Global energy consumption has increased at an exponential rate in the past decades, and this increasing tendency is still ongoing. Specifically, the world consumed 153,595 terawatt-hours (TWh) of primary energy in 2017.[10] At present, more than 85% of the consumed energy is still derived from fossil fuels, resulting in a potential severe energy crisis and relevant environmental issues. Research efforts are demanded to reduce our dependence on fossil fuels by exploiting environment-friendly, alternative energy sources, including fuel cell, solar, wind, hydro, and

geothermal energy.[2, 11] To make full use of the renewable energy sources that are intermittent (e.g., solar and wind energy), efficient energy storage systems are indispensable to balance the fluctuations in power production, and accommodate intermittent spikes or instant availability in their output. Battery, as an electrochemical energy storage system, exhibits high energy density and becomes a favorite choice. Despite the great success of lithium (Li)-ion battery (LIB) in portable electronics (e.g., cell phones and laptops) for the past decades, it is still a great challenge to develop a cheap and high-performance (e.g., high energy density, good rate capability) battery system to further meet the requirements from large-scale applications, like electrical vehicles and electrical grids.[12] Nanomaterials engineering has emerged as a very efficient approach to solve the fundamental problems in traditional battery materials and boost battery performance.[13]

In this dissertation, various nanomaterials and their composite structures are designed and explored for environmental sustainability including water sensor and battery applications.

1.2 Literature review

1.2.1 0D nanoparticles: Au and SnO_2

Nanomaterials are defined as low dimensional materials with building blocks of nanoscale, usually ranging from 1 nm to 100 nm, at least in one dimension, and have size effects.[14] Based on their nanoscale dimensions, nanomaterials can be classified into zero-dimensional (0D) nanoparticles and clusters; one-dimensional (1D) nanotubes, fibers and rods; two-dimensional (2D) films; and three-dimensional (3D) polycrystals and nanomaterial composites, as illustrated by Fig. 1.1.[15] Generally, the specific surface area or surface-to-volume ratio increases remarkably when the size

of materials decreases to nanometer scale, which means a much higher percentage of surface atoms in nanomaterials.[16] Nanomaterials may exhibit new physical and chemical properties distinct from those of bulks, such as tunable electronic structures, different magnetism, free energy, thermal stability, electronic absorption, and catalytic activity, mainly due to the lower coordination number of surface atoms and quantum size effects on the interior of nanocrystals.[16, 17]

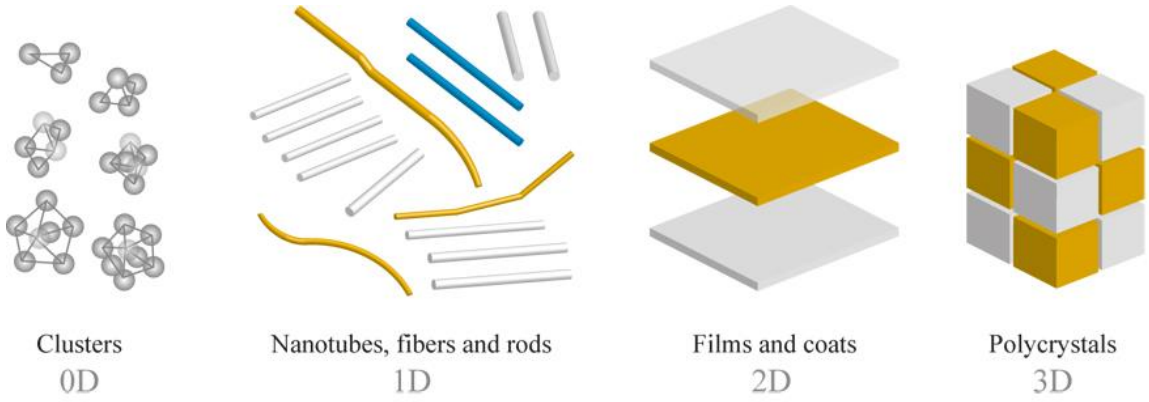

Fig. 1.1 Nanomaterial classification by size of structural elements.[15]

0D nanomaterials have been extensively used in industry and our daily life for decades (e.g., traditional printing industry), owing to their new exhibiting properties and cost-efficiency. Fig. 1.2 shows some representative examples of inorganic solid properties and their applications. Size diminution of materials affords large specific surface area, which allows sustainable large-area application of solids, such as car painting and solar cells, in which the surface functionalization requires only a nanometer-thick active materials coating.[18] Moreover, the reduced size, boosted surface area, and unique properties of nanoparticles may significantly enhance the catalytic[19-22] and electrochemical activities[23-26]. These features make nanoparticles, especially precious metal

nanoparticles (e.g., Pt, Au and Pd), extremely attractive for catalysis, energy conversion, and storage applications.

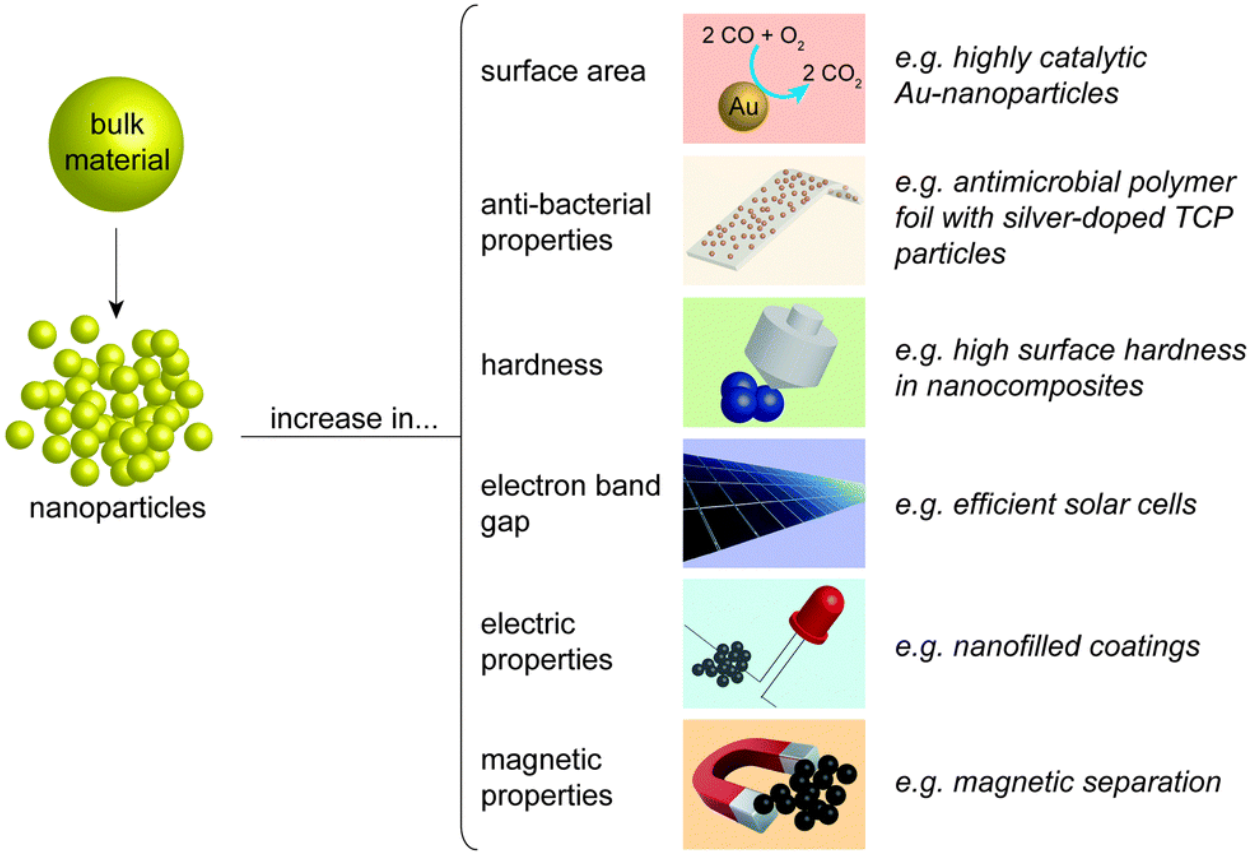

Fig. 1.2 Typical properties of inorganic nanoparticles and their applications.[18]

Au nanoparticles can be the most outstanding and prominent example of the "size-effect" on materials. Generally, Au is highly chemical stable, and it does not react with oxygen. This property is very favorable for coinage, jewelry and arts. But, when the size diminishes to nanoscale (< 5 nm), Au shows very effective catalytic properties when the size diminishes to nanoscale (< 5 nm), mainly due to the high activity of low-coordinated Au atoms on the surface (specially at the corners).[19, 22] Since Michael Faraday reported the formation of "fine particles" through reduction

of gold chloride by phosphorus in solution and stabilized by carbon disulfide,[27] the colloidal synthesis methods are still the major approach to obtaining Au nanoparticles, in which solvated gold salt is reduced in the presence of capping agents to prevent aggregation of the particles.[28] Abundant functional molecules can be used in the conjugation of Au nanoparticles with anchoring groups such as thiolate,[29, 30] dithiolate,[31, 32] selenide,[33, 34] amine,[35-37] carboxylate,[38] and phosphine[39, 40] moieties. Generally, the bonding strength follows Pearson's hard-soft acid-base (HSAB) theory with a soft Au surface. Thiol-based anchoring groups are usually employed for non-labile applications because of the strong bonding, while carboxylate or amine anchors for labile/reversible applications.[28] The facile surface functionalization enables versatile properties and applications of Au nanoparticles in biomedicine,[28, 31] bioimaging,[41] catalyst,[18, 23, 42] and sensing[43, 44].

Several physical properties of Au nanoparticles have been explored and utilized for chemical and biological sensing platforms, as shown in Fig. 1.3.[43] For example, glutathione functionalized Au nanoparticles have been used by Chai et al. to detect lead ions via the colorimetric response of aggregated Au nanoparticles in the presence of Pb^{2+}, and a detection limit of 100 nM was achieved. Control samples suggested much higher affinity of GSH to Pb^{2+} compared with other heavy metal ions.[45] Thakur et al. employed antibody modified Au nanoparticles as probes in graphene-based FET sensors to realize a rapid single *E. coli* bacteria detection, exhibiting great potential for practical application.[46]

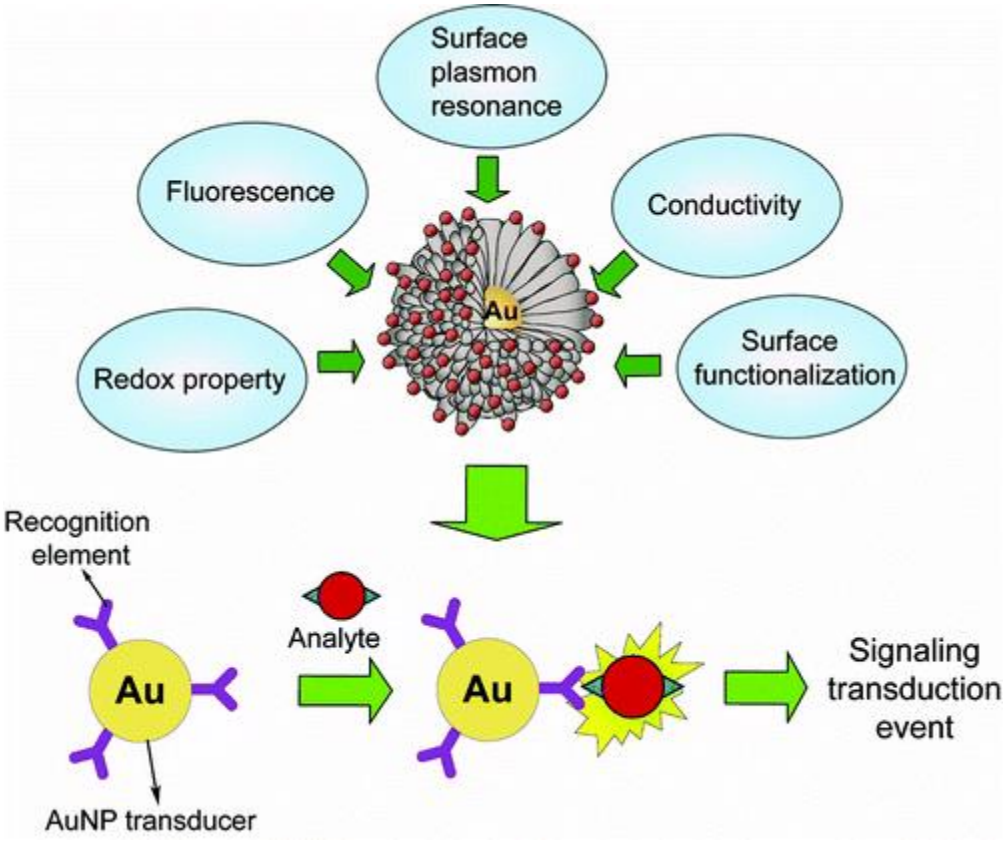

Fig. 1.3 Physical properties of Au nanoparticles as signal transduction for sensors.[43]

Tin oxide (SnO_2) as a typical metal oxide is a n-type, wide band gap (3.6 eV) semiconductor. Owing to the good optical, electrical, and electrochemical properties, SnO_2 nanoparticles are exploited for photovoltaic devices, catalytic support matrixes, chemical sensors, high-capacity lithium storage, and so on.[47] In particular, the excellent receptivity to various gaseous environments, high sensitivity, and outstanding chemical stability make SnO_2 one of the most effective gas-sensing materials.[48] SnO_2 demonstrates adequate sensitivities to detect NO_x, CO, CO_2, H_2, ethanol, and water vapor.[47] The oxidation-reduction reaction of adsorbed targeting gases with surface-chemisorbed ionized oxygen species (e.g., O^-, O_2^- and O^{2-}), which changes the conductance of the sensor, is well accepted as the sensing mechanism.[47-49] SnO_2 has also been

extensively explored as a high-performance anode material for its high theoretical capacity, low cost, and environmental benignity.[50] SnO_2 nanoparticles show great advantages compared with the bulk SnO_2 in alleviating volume change (> 200%) during lithiating/delithiating processes for better cycling performance due to their relatively small volume. It is also reported that the electrochemical reversibility of SnO_2 nanoparticles upon Li^+ gets considerable improvements compared with bulk counterpart, having the potential to reach the maximum theoretical capacity of 1,494 mAh g^{-1}, which is much higher than that of commercialized graphite (372 mAh g^{-1}).[51-53]

Accurate size control[54-56] and rational component design to create heteroatom-doped,[53, 57] or multicomponent complex nanostructures,[58-60] can be an effective approach to further enhancing the performance of nanoparticles.

1.2.2 2D nanomaterials: graphene, graphene oxide, MoS_2 and Al_2O_3 thin film by ALD

2D nanomaterials are atomically thin sheets and have attracted tremendous attention in the past two decades or so due to their supreme physical and chemical properties. The constituent elements of a 2D nanomaterial exhibit strong covalent in-plane bonding while weak interlayer interaction (often through van der Waals forces). As a representative 2D material, graphene was first successfully isolated from the layered bulk form graphite by Geim's group in 2004.[61] It exhibits a series of fascinating properties, such as superlative mobility of 15,000 cm^2 V^{-1} s^{-1} even under ambient conditions[62] and record high mechanical strength with breaking strength of 42 N m^{-1}. The discovery of graphene and its amazing properties have stimulated extensive research interest in other 2D materials. Transition metal dichalcogenides (TMDCs) refer to a series of more than 40

layered compounds, in which a layer of transition metal atoms (e.g., Mo and W) is sandwiched between two atomic planes of a chalcogenide (such as S, Se, or Te).[63] The renewed interest in TMDCs was sparked by the demonstration of monolayer MoS_2-based transistors with an I_{ON}/I_{OFF} ratio exceeding 1×10^8 in 2001, [64] although the first production of ultrathin MoS_2 flakes was reported as early as in 1963,[65] and monolayer MoS_2 was achieved in 1986.[66] Recently, layered black phosphorus (or phosphorene, in monolayer) has joined in the family of 2D materials and has attracted great attention because of its excellent transistor performances. The mobility can reach 1000 $cm^2\ V^{-1}\ s^{-1}$ and drain current can be modulated on the order of 10^5 at room temperature for FETs made of ~10 nm thick phosphorene.[67]

2D materials are ideal channel materials in FET devices because of their superior electronic properties, such as high carrier mobility and versatile band structures. The unique atomically-thin structures endow 2D materials with adequate flexibility and maximum surface-to-volume ratio. The fully exposed surface atoms can directly interact with analytes, making 2D materials extremely sensitive to local perturbations. Therefore, 2D materials-based FET sensors may promise ultimate sensitivity. Compared with 1D nanomaterials (e.g., carbon nanotubes and Si nanowires), the relatively large lateral size and flexibility of 2D materials facilitate control over the channel structure and form conformal and intimate contact with metal electrodes during FET fabrication.[68] Their 2D nature also facilitates the surface functionalization for a hybrid 2D material/sensing probe sensor structure. Moreover, because the shape and thickness of 2D materials could be precisely controlled via either varying synthesis conditions or post-synthesis nanolithography, both the morphology and electrical properties of 2D materials can be tuned effectively to fit various needs. The outstanding sensing abilities of 2D materials-based FET

sensors are being demonstrated by the continuous progress on water contaminants (e.g., heavy metal ions and bacteria) detection, in addition to commonly detecting gas and biomolecules, with high sensitivity, excellent low limit of detection (LOD) and rapid response.[68]

Benefiting from the enlarged specific surface area, exposed active surface, and excellent electrical properties, 2D materials also have been applied to energy storage systems including batteries and supercapacitors.[69, 70] In addition, the flexible and robust thin film structures and admirable electrical conductivity of 2D materials make them the ideal building blocks for nanocomposites to buffer the volume change during cycling and maintain the structural integrity of electrode materials in batteries.[71]

Graphene, the first available 2D atomic crystal, has brought us many breakthroughs in science since its discovery in 2004. As the fundamental element of all graphitic forms (Fig. 1.4), graphene is a flat monolayer of carbon atoms packed into a perfect honeycomb lattice through sp^2 hybridization. The resulting electronic band structure is a gapless, linear dispersion, making the charge carriers to be massless Dirac fermions.[62] The strong C-C bonds in graphene give rise to a high mechanical strength, and the absence of dangling bonds results in chemical inetness.[72] The pristine graphene is a semi-metal with a zero bandgap and has a super high carrier mobility at room temperature. It has attracted considerable interest as the channel materials in FET sensors owing to its superior electronic properties, large specific surface area (~2,600 m^2 g^{-1}) [73] and extreme sensitivity to environmental perturbations. The high sensitivity can be mainly attributed to the superior carrier mobility of graphene and its 2D atomic thin structure, which means all the carbon

atoms are surface atoms that can interact with analytes directly. In spite of the lack of dangling bonds in the basal plane, graphene can be functionalized through the van der Waals interactions between its hydrophobic surface and long alkyl chains,[74, 75] widely used π-π stacking with aromatic molecules,[76, 77] or arbitrarily introducing anchors (e.g., Au nanoparticles) for chemical linkage.[78] The functionalization of graphene enables the selectivity to specific analytes of graphene-based FET sensors.

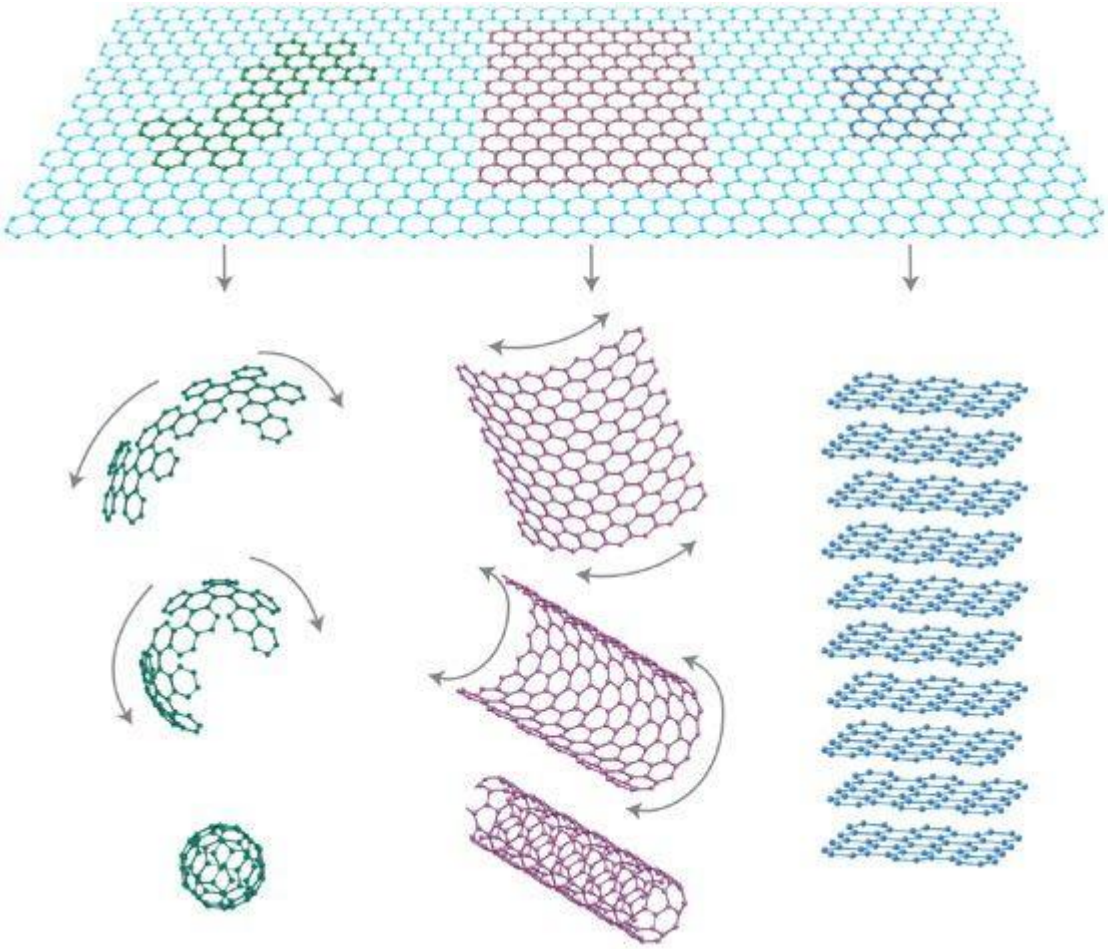

Fig. 1.4 Graphene: the mother of all graphitic forms.[62]

Different from the semi-metallic property of graphene, TMDCs are a large family of 2D semiconductor materials. Among them, MoS_2 is the most extensively studied material due to its robustness and excellent electronic properties. As shown in Fig. 1.5, bulk MoS_2 consists of vertically stacked layers with a monolayer thickness of 6.5 Å that are held together by a weak van der Waals force.[64] Depending on the coordination configurations of the transition metal atoms, MoS_2 can form two common structural phases, octahedral (1T) and trigonal prismatic (2H), which have different properties. Bulk MoS_2 is semiconducting with an indirect band gap of 1.29 eV, while monolayer MoS_2 has a direct band gap of ~1.9 eV, showing layer-dependent transition (Fig. 1.5c).[79] Monolayer MoS_2 has successfully displayed excellent electrical characteristics when used as the conductive channel of FET, including a room-temperature mobility of 200 $cm^2\ V^{-1}\ s^{-1}$ and a current on/off ratio exceeding 1×10^8 (Fig. 1.5b).

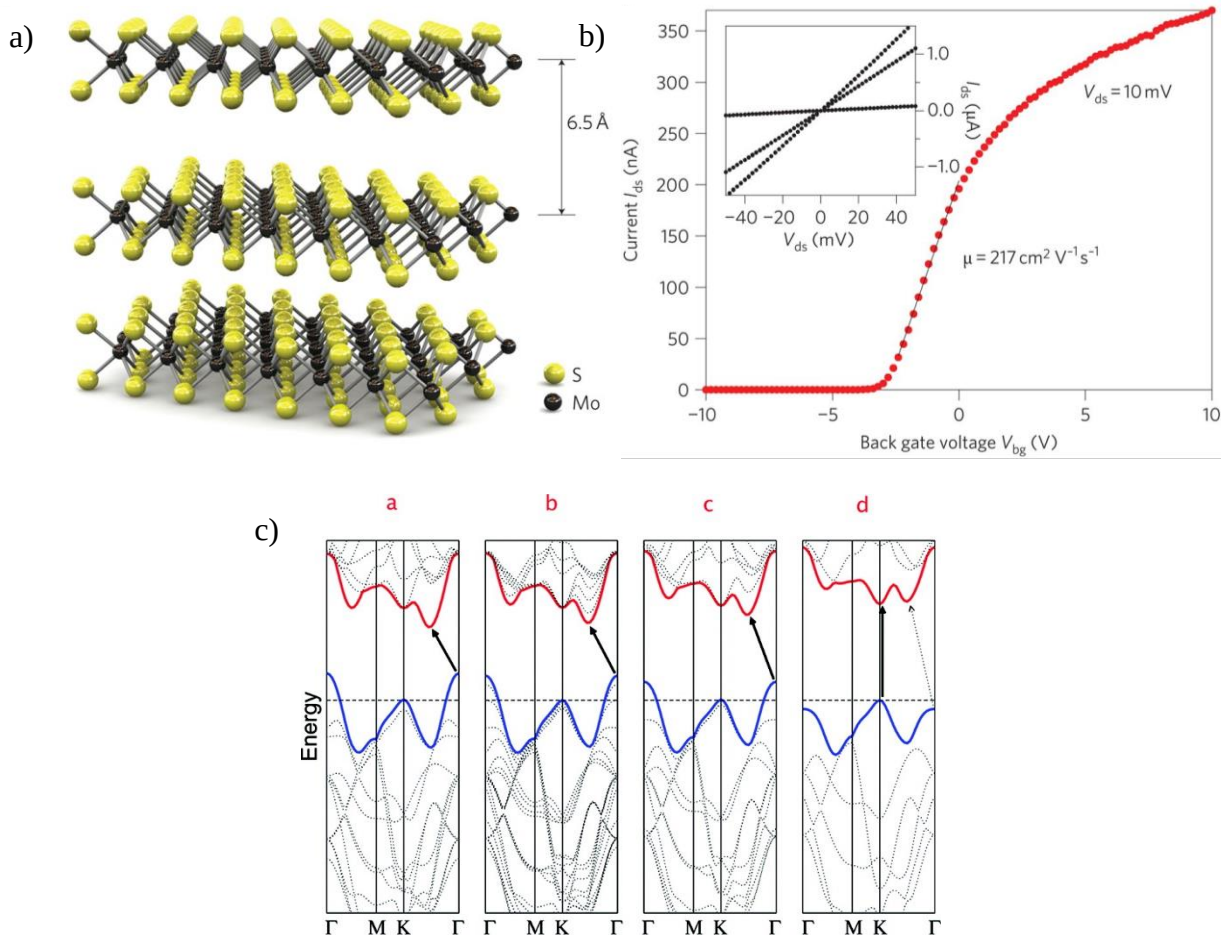

Fig. 1.5 a) Schematic structure of MoS_2. b) Room-temperature transfer characteristics from the FET with a bias voltage V_{ds} of 10 mV. Back-gate voltage V_{bg} is applied to the substrate. Inset: I_{ds}–V_{ds} curves acquired for the V_{bg} values of 0, 1, and 5V.[64] c) Calculated band structures of bulk, quadrilayer, bilayer, and monolayer MoS_2 (a)-(d).[79]

2D materials are typically produced by three different methods: mechanical exfoliation, physical vapor deposition (PVD), and chemical vapor deposition (CVD) as shown in Fig. 1.6. These methods can usually produce high quality 2D crystals with less defects. For the case of graphene, in addition to the above methods, a widely exploited approach is to reduce graphene oxide (GO).[80] Though reduced graphene oxide (rGO) contains much more defects compared with pristine

graphene, its much lower cost and massive scalability promise cost-effective sensor fabrication and other massive applications. Unlike the semi-metallic graphene, rGO is typically a p-type semiconductor under ambient environment, and its FET properties (e.g., band gap and source-drain I_{ON}/I_{OFF} ratio) can be tuned by regulating reduction conductions.[81] Its band gap is expected to decrease with less oxygen-containing groups in rGO. Recently, electrochemical exfoliation of MoS_2 through quaternary ammonium molecules intercalation has also been demonstrated to produce uniform, phase-pure, semiconducting 2H-MoS_2 at a high production, promoting the low-cost device fabrication.

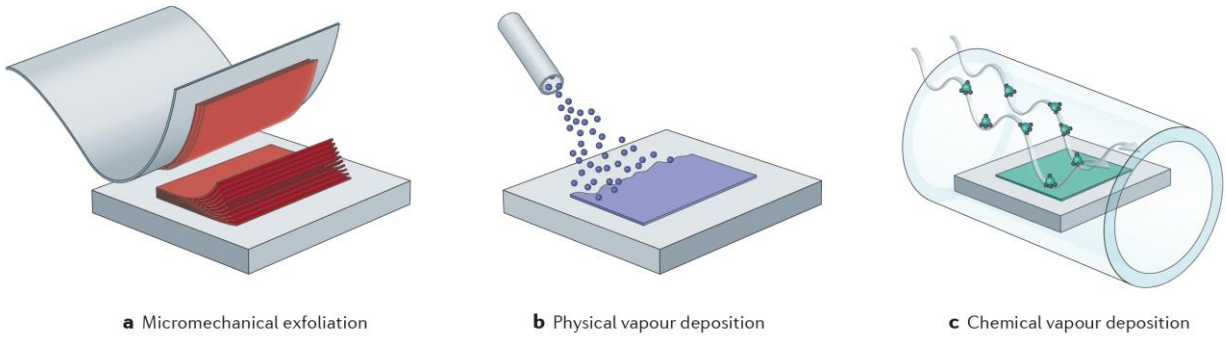

Fig. 1.6 Typical synthesis methods of 2D materials.[72]

Instead of graphene, reduced graphene oxide (rGO) are generally employed in batteries, because of not only its low-cost and easy synthesis, but also its large amount of surface chemical active sites, which provide the possibilities for chemical modifications (e.g., heteroatom-doping) and anchoring sites for nanocomposites construction. As an example, nitrogen doping on rGO is a common approach to improve the electrical conductivity of rGO and provide more active sites for the lithium, sodium, and potassium storage.[82-84]

Atomic layer deposition (ALD) is an arbitrary deposition method of synthesis and coating materials in the form of 2D thin film. The layered molecular structure of material is not the precondition for ALD. Various materials with distinctive properties like metals,[85] oxides,[86-88] sulfides,[89, 90] nitrides,[91] and so on have been deposited as 2D thin films (Table 1.1). The name of atomic layer deposition points out the kernel of this process, and the representative deposition of Al_2O_3 using trimethylaluminum (TMA) and water is illustrated in Fig. 1.7. In each cycle, the substrate is exposed to typical two sequential gaseous chemical reactants. The individual gas-surface reaction is one "half-reaction", that is, enough precursor molecules are introduced to fully react with the active sites on the substrate surface, leaving no more than a monolayer product on the surface as a self-limiting surface chemistry. This is then followed by another "half-reaction" from the counter-reactant to create one layer of the targeting material. The film thickness can be adjusted accurately through varying the number of reaction cycles. ALD has emerged as a powerful tool in semiconductor,[91, 92] energy systems,[93] and many other technologies.[94]

Table 1.1 Materials grown by ALD.[92]

Elemental	**Oxides**	**Nitrides**	**Sulfides**	**Other compounds**
C, Al, Si, Ti, Fe, Co, Ni, Cu, Zn, Ga, Ge, Mo, Ru, Rh, Pd, Ag, Ta, W, Os, Ir, Pt	Li, Be, B, Mg, Al, Si, P, Ca, Sc, Ti, V, Cr, Mn, Fe, Co, Ni, Cu, Zn, Ga, Ge, Sr, Y, Zr, Nb, Ru, Rh, Pd, In, Sn, Sb, Ba, La, Ce, Pr, Nd, Sm, Eu, Gd, Tb, Dy, Ho, Er, Tm, Yb, Lu, Hf, W, Ir, Pt, Pb, Bi	B, Al, Si, Ti, Cu, Ga, Zr, Nb, Mo, In, Hf, Ta, W	Ca, Ti, Mn, Cu, Zn, Sr, Y, Cd, In, Sn, Sb, Ba, La, W	Li, B, Mg, Al, Si, P, Ca, Ti, Cr, Mn, Co, Cu, Zn, Ga, Ge, As, Sr, Y, Cd, In, Sb, Te, Ba, La, Pr, Nd, Lu, Hf, Ta, W, Bi

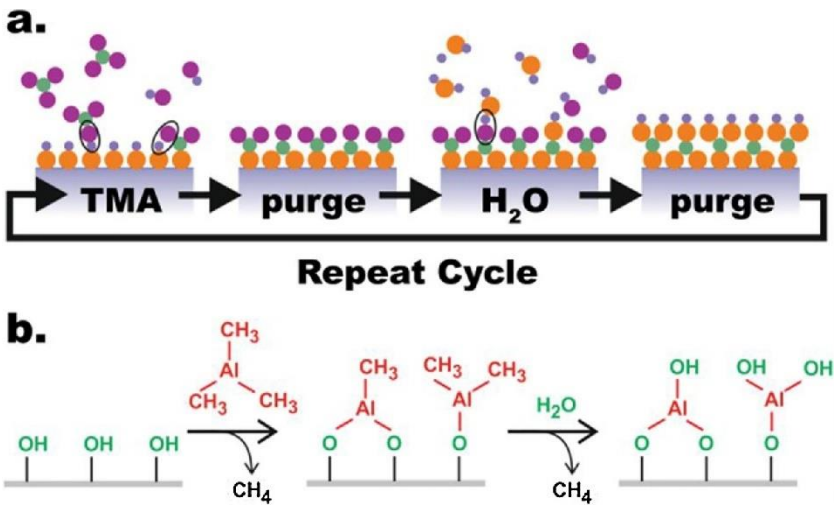

Fig. 1.7 Schematic of representative ALD of Al_2O_3 via trimethylaluminum (TMA) and water. (a) Scheme of ALD cycles; (b) idealized stoichiometry of the surface reactions.[95]

1.2.3 3D nanomaterial composites: MOF and MOF-derivatives

In order to maximize or further improve the capabilities of nanomaterials through synergistic effects, nanomaterials are often composited with each other to construct more complex 3D architectures for device applications. For example, many metal oxide (i.e., SnO_2, Fe_3O_4, and Co_3O_4) nanoparticles exhibit high initial electrochemical capacities in LIBs; however their cycling performance is normally unfavorable, due to their large volume expansions, particle coarsening, and electrode pulverization during lithiation/delithiation processes.[25, 96] Forming oxide/C composites by uniformly distributing oxide particles onto/into carbonaceous materials (such as graphene, carbon nanotube, and amorphous carbon) has been proved an efficient way to relieve these severe problems and enhance the performance significantly. It has been concluded that the

introduced carbonaceous scaffolds not only provide a conductive network, but also as a cushion, effectively alleviate the volume change and particle aggregation during cycling.[50, 96]

Metal-organic frameworks (MOFs), organized by the regular coordination between varied metal ions/clusters and organic ligands, have become one of the research hotspots in chemistry and material communities.[2] The prominent features such as ultrahigh porosity, crystalline nature, highly tailorable chemical components and structures enable the successful applications of MOFs in gas capture, separation, and storage, chemical sensing, catalysis, and energy applications.[97-100] Moreover, the permanent porosity, crystalline structures, and tailorable components of MOFs make them distinctive templates and precursors to create diverse nanomaterials and nanostructures from carbon-based materials to metal-based materials (e.g., oxides, carbides, chalcogenides, and phosphides), which normally inherit the high porosity and high surface area from MOFs.[5] Through a rational combination of pristine MOFs or MOF-derivatives with other suitable materials (e.g., graphene and enzyme), advanced composite materials can be achieved, which could exhibit better performances as a whole.[101-103] The MOF-derivatives and MOF based composites dramatically widen the applications of pristine MOF and highlight the extreme versatility of MOF-based materials (Fig. 1.8). As an example, MOF derived porous carbon materials with an ultrahigh specific surface area, controllable porosity, and diverse morphologies (including 0D polyhedral, core-shell and hollow structures; 1D nanorods and tubes; 2D nanosheets; and 3D arrays and frameworks) have become the excellent composite matrices for electrochemical active materials functionalization. As a result, composite nanomaterials have broad applications in catalysis, energy storage and coversion.[5, 104-106]

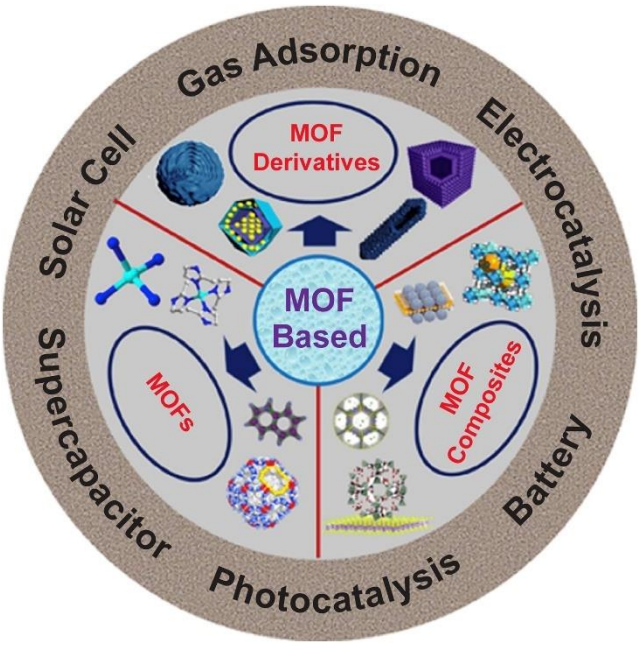

Fig. 1.8 Schematic organization of MOF-based materials and some major applications.[2]

1.2.4 FET water sensors

Water is essential for human beings, because it affects almost all aspects of our life: water for drinking and hygiene is vital for everyone; water plays a key role for maintaining a healthy ecosystem; water is necessary for agricultural and food production; and many more. However, based on the report from the World Health Organization (WTO), 844 million people were still lack of even a basic drinking service and at least two billion people used drinking water without safety management in 2015.[107]

A variety of harmful contaminants including pathogenic microorganisms (e.g., bacteria and viruses) and heavy metal ions (e.g., lead, arsenic, and mercury) are widely present in water systems. For instance, heavy metal ions are highly toxic and cause serious damages to brain, lunges, liver,

kidney, and other important organs, resulting in muscular dystrophy, Parkinson's disease, Alzheimer's disease, and many other degenerative diseases. Children are especially susceptible to heavy metal toxicity, which may damage the development of the nervous system.[108] These contaminants are severe threats to human health, and effective monitoring is absolutely necessary, especially in the drinking water system. Even though the conventional sensing technologies such as inductively coupled plasma mass spectrometry (ICP-MS) can be used for heavy metal ions detection and electron microscopy can be used for the observation of viruses to realize accurate and specific contaminant detection, the complex sample pretreatments, advanced instruments, professional operation are still the barriers for low-cost, point-of-care, and widespread detections.[8, 109, 110] Many new sensing technologies, such as surface-enhanced Raman spectroscopy (SERS), electrochemical approach, and magneto-fluorescence method, have been developed in past decades, trying to solve these challenges.[9] Among these new technologies, FET-based nanosensor platforms are very promising, owing to their extremely high sensitivity, in-situ and rapid detection, simple device structure, and easy operation.

An FET sensor typically consists of source, drain and gate --- three metal electrodes, and a conductive sensing channel bridging the source and drain electrodes. The change in conductance of the sensing channel induced by the interaction from analyte is monitored as the sensing signal. Charge transfer and gating effects are two common working principles for the sensing response of FET sensors, which were discussed in detail in these reports.[7, 111]

The sensing channel material plays a pivotal role in an FET senor, which almost determines the sensitivity, response speed, and even the selectivity specially for gas sensor to some extent. With the explosive research efforts on 2D nanomaterials in the past decade, the superior electrical properties (e.g., high carrier mobility and remarkable I_{ON}/I_{OFF} ratio), large surface area, and extreme sensitivities to environmental perturbations, make 2D nanomaterials ideal sensing channel materials for FET sensors.[7] For example, a fully integrated FET sensor was fabricated with a monolayer CVD graphene sheet for the label-free Pb^{2+} detection in aqueous solution.[77] The chemical linkers were first immobilized on graphene surface via the π-π stacking, then G-rich DNA strands as the probe to Pb^{2+} were captured by the DNA capture strands linked to the immobilized chemical linkers to complete the surface functionalization of graphene. This graphene-based FET sensor is able to realize a specific quantification of Pb^{2+} with LOD down to 164 ng/L. The sensing mechanism can be attributed to the G-quadruplex structure-switching of negatively charged DNA strands induced by Pb^{2+} ions, which significantly alters the charge distribution in the vicinity of graphene surface, and thus the carrier concentration of graphene. This event can be monitored through the Dirac point shift and the conductivity variation of the graphene channel as the sensing signal (Fig. 1.9).

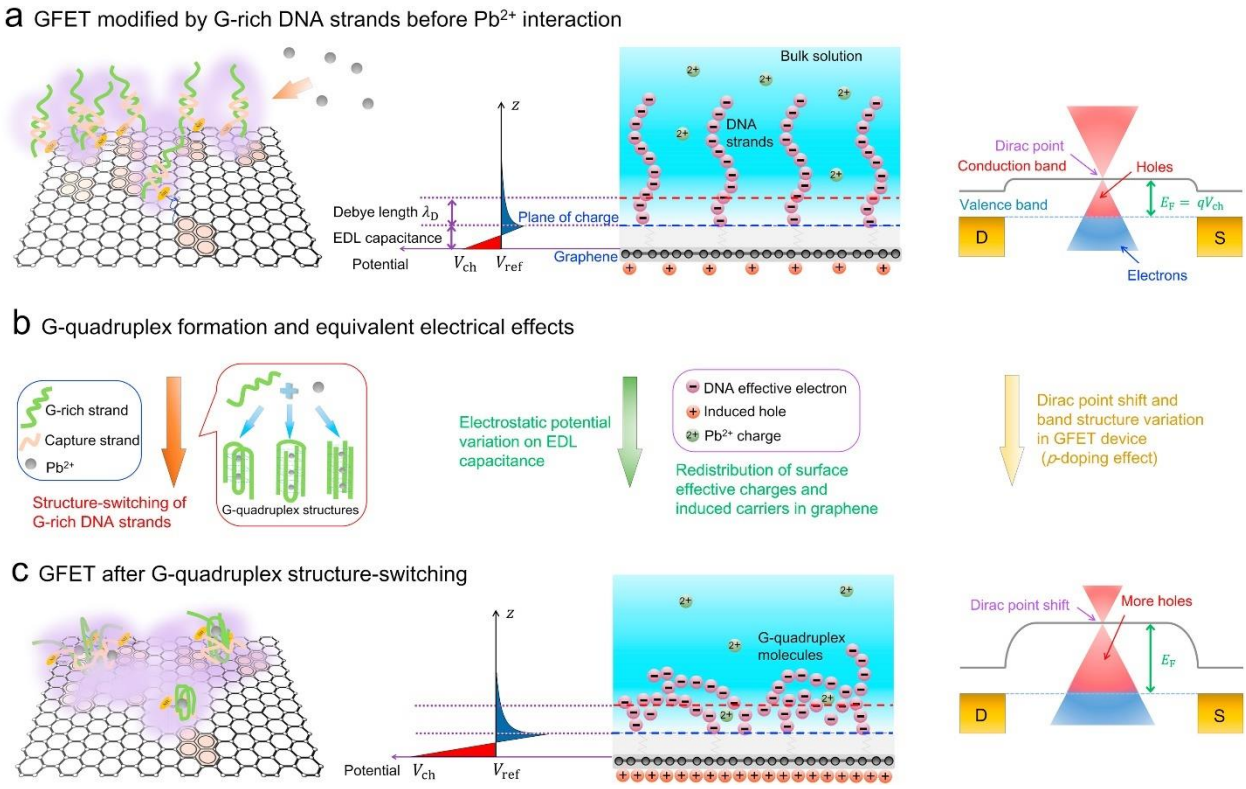

Fig. 1.9 Schematic illustrations of G-quadruplex structure-switching principle and electrical response mechanism in the graphene-based FET sensor.[77]

Compared with pristine graphene, rGO offers much cheaper FET sensor applications. Using the rGO coated with thioglycolic acid (TGA) functionalized Au NPs as the sensing channel, Chen et al. prepared FET sensors for detecting mercury ions (Hg^{2+}) in water (Fig. 1.10a).[112] The sensor response can be characterized in terms of the conductance variation of the rGO channel. It is believed that the possible charge transfer from rGO, caused by the TGA coupled Hg^{2+}, increases the hole concentration of the rGO channel, thereby increasing the drain current. The sensor showed a rapid (a few seconds), specific sensing performance to Hg^{2+} with a detection limit of 25 nM. As mentioned above, for FET sensors, there are two possible sensing mechanisms between analytes and sensing channels: 1) charge transfer, in which target analyte has a direct interaction with

channel material, inducing the charge transfer from channel; and 2) gating effect due to the charged nature of attracted targets, in which direct interaction does not happen in the presence of chemical probes and/or a protection layer.[7, 111] Both of the mechanisms can modulate the carrier concentration and thus the conductance of the sensing channel. But the general opposite sensing response trends complicate the sensing signal output. For example, in the case of Hg^{2+} detection with p-type rGO-based FET sensor, the charge transfer would increase the conductivity of the rGO channel, while its conductance would decrease due to the positive gating effect of accumulated Hg^{2+} on the surface. The competition between these two sensing mechanisms undermines the sensitivity of the FET sensors. To accommodate this issue, a thin layer of gate oxide like Al_2O_3 can be deposited on the channel surface as a top gate to isolate 2D material channel from analytes, resulting in a dominant gating effect on the channel to improve the device sensitivity. A typical thin Al_2O_3 layer passivated rGO FET sensor structure is demonstrated in Fig. 1.10b. Under this circumstance, the sensor works as a top-gated FET, and better semiconductor properties such as higher I_{ON}/I_{OFF} ratio and adequate threshold voltage would lead to a better sensitivity. With the rGO-based FET sensor platform and judiciously selected specific probes, better sensing performance can be expected.

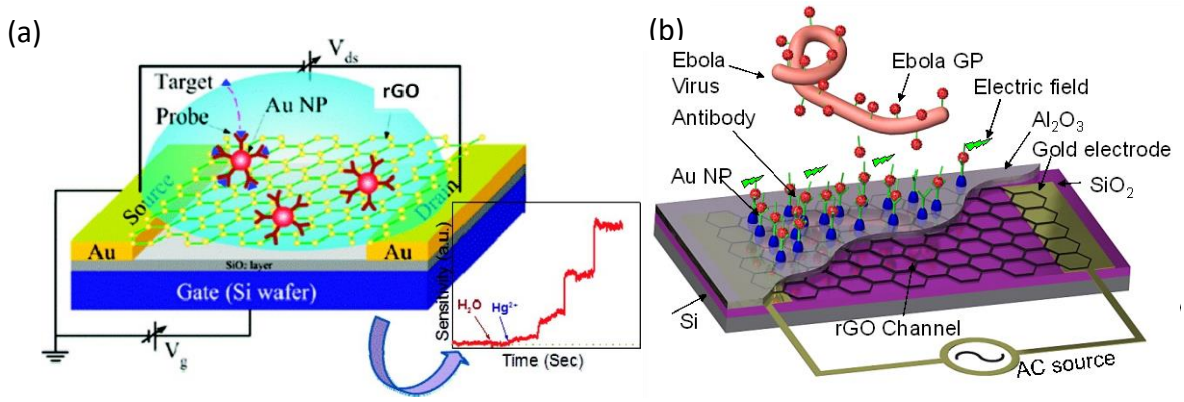

Fig. 1.10 a) rGO FET sensor structure and real-time sensing response for Hg^{2+} detection.[112] b) rGO FET sensor with a thin Al_2O_3 passivation layer for Ebola-glycoprotein diagnosis.

Because semiconducting MoS_2 flakes have much higher I_{ON}/I_{OFF} ratio compared with rGO, a better sensing performance could be expected from MoS_2-based FET sensor devices. As a representative study, FET sensors with specific DNA functionalized MoS_2 nanosheet as the sensing channel were prepared and applied for Hg^{2+} detection in water.[113] The dynamic response demonstrated that the sensor is quite sensitive to Hg^{2+} with a response time of a few seconds and a LOD of 0.1 nM, which is much lower than the LOD (25 nM) of the reported rGO-based sensor device.[112] Because of the specific binding between Hg^{2+} and the DNA molecules, the sensor also exhibited good selectivity.

Although these sensing performances enabled by 2D nanosheets are encouraging, the device fabrication cost is relatively high and a lithographic process is required to accommodate the small size of flakes. Material printing technologies are a subset of additive manufacturing that offer a solution for large area, low-cost, high-throughput, and reproducible production of nanoelectronics and sensors on various substrates.[114, 115] In the past decade, significant progress has been achieved

for printing fabrication of nanomaterials in different types of sensors (e.g., force, temperature, light, chemical, and pH sensors).[116] Therefore, the printing technique is promising in promoting commercial applications of nanomaterial-based sensing platforms at the industrial scale.

1.2.5 Lithium/potassium-ion batteries

The past two decades have witnessed the unprecedented development of potable electronics, ranging from smart bands, smartphones to laptops. These cannot happen without high-performance rechargeable LIBs. LIBs have prominent advantages of high energy density and good cycle life, compared with other rechargeable battery systems such as lead-acid batteries and nickel-metal hydride batteries.[117] The LIB cell works through the reversible Li-ion intercalation/deintercalation cycles between typically layered anode and cathode compounds, which are separated by a membrane, as shown in Fig. 1.11. Transition metal oxides or phosphates materials (e.g., $LiCoO_2$, $LiMn_2O_4$, and $LiFePO_4$) are usually applied as a cathode compound, providing lithium source, while graphite is the most commonly used anode active material.

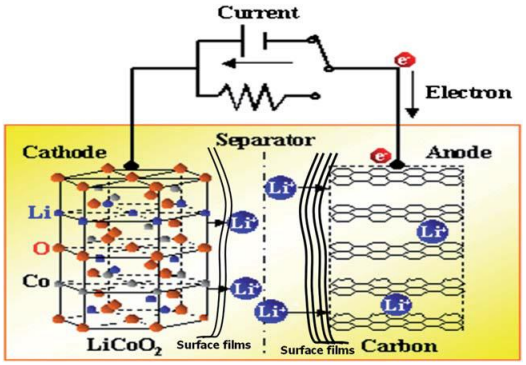

Fig. 1.11 Schematic of the representative LIB based on $LiCoO_2$ cathode and graphite anode.[118]

For many years, the commercialized LIBs support portable consumer electronics relatively well, while two aspects emphasized recently drive the developing better battery systems strongly: 1) The transformation from gasoline cars to electric vehicles (EVs), in order to deal with "oil crisis" and fossil fuels consumption induced emission of pollutants and greenhouse gases; and 2) stationary grid storage to accommodate the electrical energy fluctuation supplied by renewable energy sources such as wind and solar power on a large scale at a low cost.[117] For these applications, higher energy density and low-cost batteries are urgently needed. For common LIBs, graphite anode allows only one Li^+ intercalation with six carbon atoms to form LiC_6 as the final product with a maximum reversible capacity of 372 mAh g^{-1}. Moreover, the mediocre Li-ion diffusivity rate of ~10^{-11}-10^{-6} cm^2 s^{-1} in graphite limits the rate capacity. Graphite anode also suffers from serious transport-induced surface structure destruction (especially at high rates), which undermines the cycle performance.[119, 120] So, lots of efforts have been devoted to exploring advanced anode materials with a higher capacity, a better rate, and better cycle performance. Si, P, Sn, and SnO_2-based nanocomposites have attracted considerable research interest for their much higher lithium storage capacity.[13, 121, 122]

Due to the limited lithium reserves (0.0017 weight %), its uneven distribution in the Earth's crust, relative high cost, and potential price increase, LIBs may not meet the requirements of very-large-scale applications at a low cost.[123] Researchers try to find suitable substitutes for lithium in rechargeable battery systems. Much more abundant and low-cost sodium and potassium become the good candidates. Compared with sodium [-2.71 V versus standard electrode (E^0)], potassium has a lower redox potential of K/K^+ (-2.93 V versus E^0), which is close to that of lithium (-3.04 V

versus E^0).[124] This low redox potential endows potassium-ion batteries the potential for a high energy density. Even though potassium has the largest atomic radius (1.38 Å) compared with sodium (0.74 Å) and lithium (0.68 Å), the Stokes' radius of K^+ (3.6 Å) is smallest compared to that of Na^+ (4.6 Å) and Li^+ (4.8 Å) in propylene carbonate (PC) solvents,[125] indicating the highest ion conductivity and mobility of K^+. Nevertheless, K with the largest atomic size will induce a greater volume change of electrode materials during the K-ion insertion/extraction, resulting in materials pulverization and thus fast capacity decay. Rationally designed anode materials are needed to address this problem as one of the major challenges in potassium-ion battery.[126]

The studies on potassium-ion batteries are still in their early stage, but nanocomposites synthesized by the cooperation of high-capacity active materials, including P,[12, 127, 128] Sn_4P_3,[129] Bi, and Sb,[130] with various conductive carbonaceous supports (e.g., rGO,[131] carbon nanotube[127] and amorphous carbon[12, 129, 130]), have been successfully demonstrated as anodes in potassium-ion batteries, demonstrating greatly improved performance. For instance, Liu et al.[128] synthesized carbon nanotube-backboned mesoporous carbon via a sol-gel method, then red P was loaded into the porous carbon through a vaporization-condensation-conversion approach. With a P content of ~40 wt.%, the obtained P/C nanocomposite delivered an impressive reversible capacity of ~500 mA g^{-1} at a small current, and a stable capacity of 244 mAh g^{-1} at 500 mA g^{-1} for 200 cycles. It is believed that designed porous carbon with carbon nanotube as the backbone, not only provides the electronic channel to improve the electrochemical activity of P, but also leaves enough free space to accommodate the huge volume expansion of P during potassiation.

1.3 Summary

In summary, nanomaterials and nanostructures have exhibited great potential to deal with the environment and energy challenges we are facing, because of their new discovered unexpected physicochemical properties and high efficiency. In particular, 2D materials represented by graphene become great sensing channel materials in FET-based sensors, owing to their excellent, tunable electrical properties, high sensing area, and extremely high sensitivity to environmental perturbation. Low-cost solution processable 2D materials offer the opportunity for cheap sensor fabrication. However, accurate morphology control on 2D materials, rational sensor structure design, and reliable device fabrication technology are still urgently demanded to manifest the superior properties of 2D materials for better sensing performance. Benefiting from the excellent electronic conductivity, flexible and robust 2D structure, rGO also has wide applications in energy storage systems. Nanocomposites via the combination of rGO with high-capacity active materials, including SnO_2 and P, exhibit impressive performance as anodes in lithium-ion or potassium-ion batteries. Besides graphene-based carbon, MOFs-derived nanoporous carbonaceous materials have also been proved as excellent carbon matrixes for electrochemical active materials (i.e., P and S) loading, resulting in advanced nanocomposite anode materials.

1.4 Objectives and outline of the dissertation research

The main objectives of this dissertation are to: (1) synthesis novel composite nanomaterials; (2) design and fabricate novel devices based on nanostructures via nanoscale engineering of different dimensional nanomaterials; and (3) apply composite nanomaterials and nanodevices to advanced environmental monitoring and energy storage applications, including water sensors and

lithium/potassium-ion batteries. In particular, through device structure optimization and novel signal transduction mechanism, rGO-based FET water sensors were prepared for lead ion and Ebola-glycoprotein detection. Scalable micromolding-in-capillary method and inkjet printing technique were also investigated in the sensor fabrication to lower the sensor cost. SnO_2 and P with high electrochemical activity were composited with 2D rGO or MOF-derived nanoporous carbon for advanced lithium/potassium ion batteries. To this end, the dissertation is organized as following tasks.

Chapter 1 presents the background and literature review on different dimensional nanomaterials and nanocomposites for environmental monitoring in FET water sensors and energy storage systems such as LIBs and PIBs.

Chapter 2 describes the application of a structure-optimized rGO based FET water senor assisted by a novel pulse-driven capacitive signal transduction mechanism for lead ion detection, in order to achieve better sensing sensitivity and selectivity.

Chapter 3 presents a resonance-frequency modulation enabled high-performance rGO-based FET sensor for highly selective and sensitive detection of Ebola-glycoprotein.

Chapter 4 focuses on the rGO percolation network construction based on 2D continuum model threshold analysis. The obtained continuous rGO network was employed as sensing channel in FET sensors to realize real-time lead ion detection in water.

In chapter 5, the tailored and scalable inkjet printing technology was investigated for FET sensing system fabrication with 2D MoS_2 and graphene-based nanomaterials.

Chapter 6 describes the synthesis of a metal-organic precursor-derived SnO_2/Sn-rGO sandwiched nanocomposite and its superior lithium storage performance.

Chapter 7 presents the morphology adjustment on Zn-MOF-74 by a mixed-solvent strategy. The optimized MOF derived nanoporous carbon rods were applied as a carbon matrix for high loading of red P, resulting in high-performance anode materials for potassium-ion batteries.

In the end, a summary of the dissertation study is presented, and further research directions are proposed in Chapter 8. This study contributes to nanomaterials synthesis and integration for real device applications, such as FET water sensors and rechargeable Li/K-ion batteries, in addressing challenges around environmental sustainability.

CHAPTER 2 PULSE-DRIVEN CAPACITIVE LEAD ION DETECTION WITH REDUCED GRAPHENE OXIDE FIELD-EFFECT TRANSISTOR

2.1 Introduction

Recently, lead contamination and related health hazards raised a serious global concern. Direct intake of lead through drinking water on a daily basis can affect the central nervous system, hematopoietic, hepatic and renal system.[132] An alarming level of increase of lead was found in the blood of people living in the city of Flint, Michigan, USA due to the poor condition of water supply system (lead leaching from the pipeline during the water conveyance).[133-136] The conventional inductively coupled plasma mass spectrometry (ICP-MS), atomic absorption spectroscopy (AAS), and atomic emission spectrometry (AES) tests are costly due to their long procedure, bulky setup and need of a professional operator.[77] Electrochemical stripping analysis using voltammetry has also been successfully used for measuring various metal ions in trace level selectively with high reproducibility.[137-139] However, it is limited by working electrode maintenance with proper cleaning, reduction/oxidation potential peak position drifting due to the aging of reference electrode, background current instability. Also, the presence of high concentration common metal ions in real water can significantly affect the results. Therefore, a rapid, portable, low-cost automated detection of lead ions in water is in great demand.

Graphene as a representative 2D material is found promising for FET-based sensor applications due to its unique one atomic layer structure, high specific surface area, great signal/noise ratio, excellent mechanical strength, and small size.[140-142] Chemical exfoliation in liquid phase can

produce one atomic layer thickness of ultrafine nano-sheets in large scale from bulk graphite. The high surface area of graphene can be functionalized with various ligands to attract metal ions,[112, 143] bio-molecules,[144-149] and gas species[141, 150] for sensing applications. Sudibya et al. used micro-patterned, protein-functionalized rGO film as sensing semiconductor channel to realize Pb^{2+} real-time detection.[151] Our group also reported a self-assembly method constructed rGO sensing platform for Pb^{2+} monitoring.[143] In general, the signal from such FET-based sensor device is transduced through resistance/current measurements considering the channel as a chemiresistor. One potential problem is the continuous voltage across ultrathin 2D nanomaterials can generate heat and modify the intrinsic conductivity that leads to a long stabilization time and signal drift. This unsaturated baseline with continuous drift is incompatible with rapid evaluation and interferes the response in the presence of analytes, thereby increasing the measurement error. In addition, the resistance/current response% (change percentage in resistance or current due to sensing event) to analytes is always relatively low (Table 2.1), which may also lead to notable errors in practice.

Table 2.1 Comparison of capacitance-based sensing performance with other techniques reported in the literature.

Sensing materials and test method	Concentration detected (nM) and chemical target	Response (%)	Selectivity ($k_{target—other}$)*	Ref.
rGO/GSH-Au NPs (DC)	10 nM Pb^{2+}	1.7%	$k_{Pb^{2+}—Hg^{2+}}(10\mu M) = 3.3$ $k_{Pb^{2+}—Zn^{2+}}(10\mu M) = 30$	143
Ti_3C_2–MXene (DC)	100 nM dopamine	<0.01%	--	152

Table 2.1 Comparison of capacitance-based sensing performance with other techniques reported in the literature (continued).

Graphene/ olfactory receptors (DC)	0.04 * 10^{-6} nM odorant (amyl butyrate)	<2%	--	153
PII2T-Si polymer/33-base thiolated DNA probe-Au NPs (DC)	10000 nM Hg^{2+}	10%	$k_{Hg^{2+}—Pb^{2+}(1mM)} = 3.2$ $k_{Hg^{2+}—Zn^{2+}(1mM)} = 2.7$	154
Polypyrrole/ rGO (DC)	0.1 nM H_2O_2	1.4%	$k_{H2O2(0.05mM)—Uric\ acid(1mM)} = 3.3$ $k_{H2O2(0.05mM)—Ascorbic\ acid(1mM)} = 5.7$ $k_{H2O2(0.05mM)—Ascorbic\ acid(1mM)} = 22.8$	155
Pt NPs/rGO (DC)	2.4 nM SsDNA	<0.01%	--	149
Bismuth-Coated Carbon Electrodes (Stripping voltammetric)	1-150 ppb Pb^{2+}	--	--	137
rGO/GSH-Au NPs (Pulse)	12 nM Pb^{2+}	347%	$K_{Pb^{2+}—Hg^{2+}, Fe^{3+}, Mg^{2+}, Zn^{2+}, Na^{+}(48nM)} \sim (10\text{-}30)$	This work

* $k_{target—other}$ is the ratio of signal response to target and other chemicals

Therefore, an alternative strategy is needed to address these issues. First, we greatly improved previously reported cysteamine (AET)-assisting GO deposition method[143] to realize a uniform GO flakes deposition onto the interdigitated electrodes, resulting in uniform sensor devices. Then, we

replaced the continuous voltage across the sensor with a periodic square pulse wave (using a function generator) and did the conventional sensing study. It was found that in the presence of analytes, the sensing signal across sensor quickly changed to stable slanting charge/discharge transients that represent a high capacitive influence. Upon drying the solution, the signal again regains its pure square wave instantly. We then hypothesized that a pulse signal in combination of capacitance measurement might be beneficial to get the rapid change in signal in the presence of analytes to replace the conventional constant voltage mode resistance measurement for this GFET sensor. To validate this, we have developed a pulsed capacitance measuring system with a programmed microcontroller to evaluate the sensing performance. The proposed capacitance based portable device with simple droplet-based measurement system shows rapid stabilization in background deionized water (DI water), negligible drift, high sensitivity, and selectivity towards lead ion detection in real-time measurements.

2.2 Experimental methods

2.2.1 Chemicals and equipment

Single layer graphene oxide (GO) water dispersion (10 mg/ml) with the size of 0.5–2.0 μm is purchased from ACS Material. Cysteamine (AET), L-Glutathione reduced (GSH) and metal chloride or nitrate salts used to prepare Pb^{2+}, Hg^{2+}, Cd^{2+}, Ag^{+}, Fe^{3+}, Na^{+}, Mg^{2+} and Zn^{2+} solutions were all purchased from Sigma-Aldrich. Since the main forms of arsenic within a 2–11 pH range can be H_2AsO^{4-}, $HAsO_4^{2-}$ in natural water, disodium hydrogen arsenate [Na_2HAsO_4] from Sigma-Aldrich was used to prepare the test solution. Inductively-Coupled Plasma Mass Spectrometer (ICPMS) method was used to quantify the prepared metal ion solutions with an error less than 5%.

Real water samples were filtered with Millipore filters to remove larger particles, algae, and other biological contaminates before sensing tests, and the actual concentrations of various metal ions were analysed by ICPMS. Savannah S 100 atomic layer deposition (ALD) was used to deposit Al_2O_3 layer with a precise thickness control. Au nanoparticles (Au NPs) were sputtered with an Au target by an RF (60 Hz) Emitech K575x sputter coater machine.

2.2.2 Sensor chip fabrication and electrical characterization

Au interdigitated electrodes with finger-width and interfinger spacing of 1.5 μm and a thickness of 50 nm were fabricated on a 100 nm SiO_2 layer coated silicon wafer by a lithographic method. An electrostatic self-assembly method has been used to deposit GO sheets on electrodes. First, the Au electrodes were incubated in AET solution and then rinsed with DI water to attach a mono-layer of AET on the Au electrodes. Second, the modified Au electrodes were immersed in DI water diluted GO solution to obtain single layer GO attachment through the electrostatic interaction between the positively charged amino groups of AET and the negatively charged GO sheets in solution. Unanchored GO sheets were removed through rinsing with DI water. A quick annealing process for 10 mins at 400 °C in a tube furnace with Argon gas was used to both reduce the GO and improve the contact between the GO and the electrodes, after which the samples were cooled to room temperature spontaneously. Next, a thin Al_2O_3 passivation layer was deposited on the sensor surface by atomic layer deposition (ALD) with trimethyl-aluminum (TMA) and water precursors at 100 °C. Uniformly distributed and high density of Au NPs were sputtered on the Al_2O_3 as the anchors for chemical GSH probes.[143] A GSH water solution was dropped on the top of the sensing area, and the devices were incubated at room temperature for 1 h, then rinsed with DI water to remove extra GSH and dried with compressed air before heavy metal ion detection.

The electrical properties are characterized by a Keithley 4200 semiconductor characterization system.

2.2.3 Pulsed capacitance measurements

For pulse measurement and visualization of morphed signal, a standard function generator (3390, Keithley, USA) and digital oscilloscope (DSO 1052B, Agilent, USA) were used. The Arduino Uno microcontroller (Atmega 328P, ATMEL, USA) development board was used for automated pulse based capacitance measurement in real time. Arduino is an open-source electronics platform based on user friendly hardware and software. The microcontroller is programmed in such a way that it continuously gives the square voltage pulse to sensor, measures the RC time constant (τ_{RC}) and then calculates the capacitance with internal resistance as a reference. For real-time monitoring, a capacitance meter is fabricated using this Arduino Uno board which can take capacitance measurements down to the pF range. The Arduino has several analog input pins which are used to take the measurements. For this meter, two i/o pins are used (A0 and A1). The voltage is applied at zero to start, and then voltage pulse is applied to the A1 pin. This voltage is then converted into a quantized value by the 10-bit ADC on the microcontroller of the Arduino. From the capacitor charging equation we get $V_c(t)=V_{in}(1-\exp(-\tau/RC))$ where, $V_c(t)$ is the voltage across a capacitor at time t, V_{in} is the input voltage, R is the reference internal resistance of the controller, C is the capacitance of the sensor and τ is the time constant when V_c reaches 63.2% of the input voltage. Then the capacitance can be evaluated from the relation

$$C = -\frac{\tau}{R\ln(1-\frac{V_c}{V_{in}})} \tag{2.1}$$

The calculated capacitance values are displayed and sent via HyperTerminal of the computer for data storage. The program for signal generation, mathematical calculation of capacitance and data transmission is written in C language in Arduino platform. HyperTerminal software (Hilgraeve, Monroe, Michigan, USA) has been used for data acquisition with a laptop. The software code is written in C program. Therefore, a continuous capacitive measurement with the meter is feasible with this miniaturized micro-controller-based system.

2.3 Results and discussion

Fig. 2.1a shows the SEM image of overall reduced graphene oxide (rGO) distribution in low magnification. As identified, lots of GO flakes are deposited on the interdigitated electrodes quite uniformly without accumulation. The deposited GO shows a well transparent (single layer like impression) and connects as a channel between source-drain gold interdigitated electrodes. Because of the strong attraction between the positively charged AET on the gold fingers and the negatively charged GO sheets, the GO sheets prefer to deposit on the fingers and can be maintained during the following rinse process, while those GO sheets sit on the gap (SiO_2 substrate) were removed completely during rinsing. Fig.2.1b shows that most of the small GO fakes attach on the gold fingers, and only those flakes that are large enough can act as the single layer channels finally. This feature helps to get rid of the influence of small GO flakes accumulation which increases the contact resistance in the electronic device, decreasing signal-to-noise ratio. The AFM image of the as-deposited GO nanosheet with line scan of calculated height are shown in Fig. 2.1c. The typical thickness of the nanosheet bridging the electrode gap is found ~1 nm, which confirms the single atomic layer thickness of the deposited GO sheet. In the Raman spectrum (Fig. 2.1d), two typical peaks at 1,344 cm^{-1} and 1,603 cm^{-1} are assigned to D-band and G-band of deposited GO nanosheets,

respectively. The D-band in the spectrum indicates the presence of disorder in GO because of oxygen-containing groups and defects on the carbon basal plane.[156] Also, 2D-band and S3 peaks can be observed at 2,670 cm^{-1} and 2,923 cm^{-1}, respectively.[45] A quick annealing process was applied to reduce GO and improve the contact between GO flakes and Au electrodes. A statistical analysis on resistances of a batch of devices (AET modified electrodes were incubated in 12.5 µg/mL GO suspension for 3 h) is provided in Fig. 2.2. The narrow resistance distribution of so many devices (with an average value of 13.4 kΩ and a population standard deviation of 71.8) indicates the uniform GO deposition and resulting device properties. Moreover, the device resistance can be adjusted by simply varying the concentration of GO suspension and incubation time. Thus, the applied AET modification of the electrodes and GO solution immersion method is an easy, self-limiting and tunable method to construct single layer rGO channel on interdigitated electrodes directly, resulting in attractive semiconductor properties of the device.

After GO deposition and thermal annealing treatment, a thin layer of Al_2O_3 is used to separate analytes from rGO channels to protect the device electrical stability and exclude the charge transfer between the ions and the semiconductor channels. The Al_2O_3 can also passivate the gold finger electrodes from interaction with further modified GSH probes (the probes can be anchored only on the Au NPs sputtered next) resulting in more effective probes on the top of rGO channels to improve the sensor performance. After the Al_2O_3 deposition, due to the electron accumulation of the insulating Al_2O_3 at a high voltage, it is hard to see the GO sheets on the electrodes. Fig. 2.1e shows the uniform isolated Au NPs distribution after Au sputtering. The size of the Au NPs is about 3-5 nm, and the density is high, which facilitates more probe modification to enhance the sensor sensitivity in the sensing test.

To characterize the FET property of the sensor, the drain current (I_{ds}) was measured as a function of sweeping back gate voltage from -40 to 40 V. A smooth p-type FET curve with an on-off ratio ~1.6 is achieved from the single layer rGO channel (Fig. 2.1f). A linear I_{ds}– V_{ds} relationship of the sensor for the drain voltage (V_{ds}) ranging from -2 to +2 V indicates the good ohmic contact between the rGO channel and the gold electrodes (shown in the inset of Fig. 2.1f). The measurement circuit diagram is shown in Fig. 2.3a.

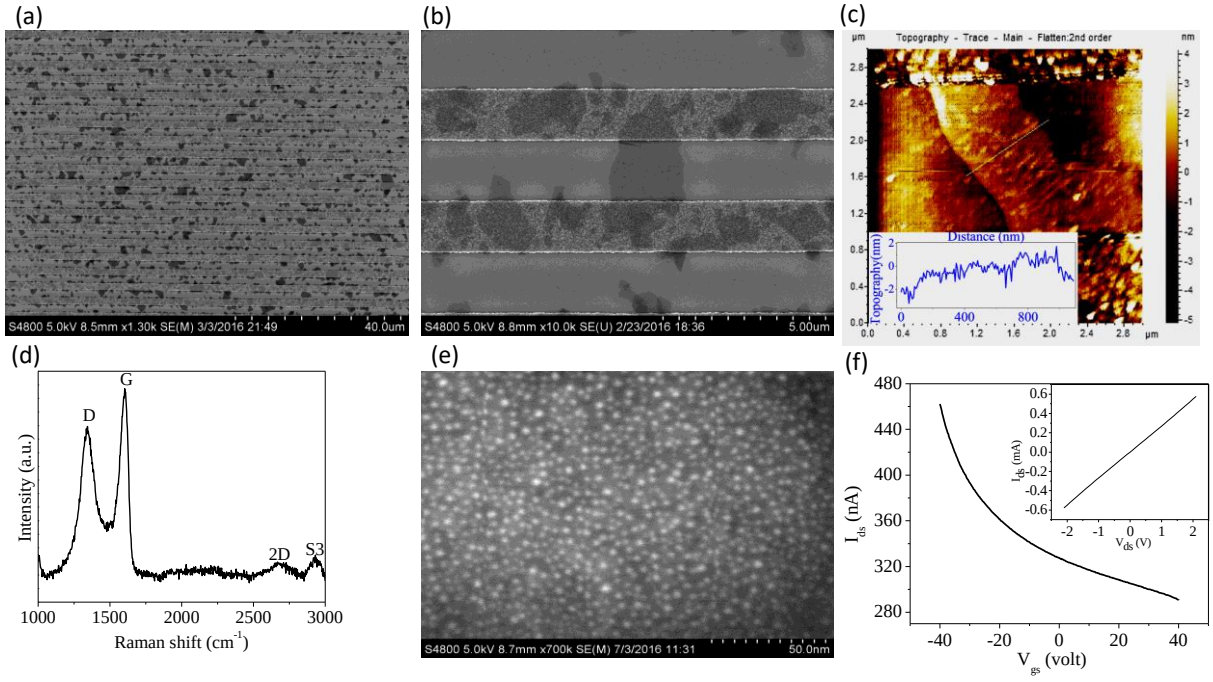

Fig. 2.1 SEM images of rGO sheets bridging the interdigitated electrodes at (a) low and (b) high magnifications. (c) AFM image of a single layer GO channel on the electrode (the line scan thickness profile is in the inset), (d) Raman spectrum of as-deposited GO nanosheets. (e) SEM image of sputtered Au NPs on the surface of Al_2O_3. (f) I_{ds}– V_{gs} characteristics of the sensor for V_{ds}= 0.1 V, V_{gs} = -40 to 40 V, step = 0.2 V (I_{ds}– V_{ds} characteristics of the sensor is in the inset).

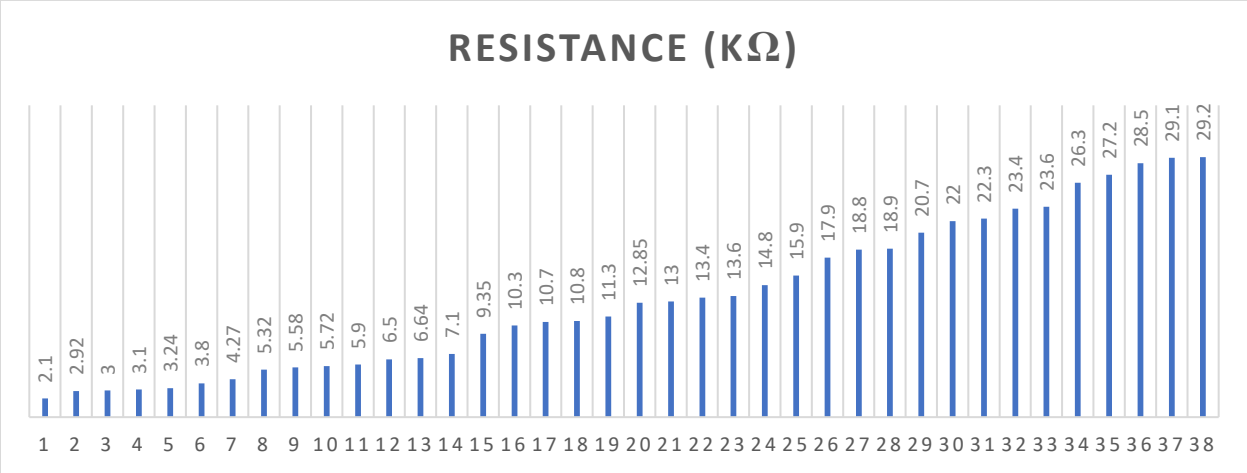

Fig. 2.2 Resistance distribution for a batch of rGO FET devices (38 devices).

The capacitance measurement is performed with a square pulse wave based technique that calculates the time constant of the morphed signal across the drain-source interface of the sensor which is connected in series with a reference resistor (R_{ref}) (Fig. 2.3b). With the known value of resistance (R_{ref}), the capacitance value can be obtained through time constant (τ) measurement. We first used a standard function generator (3390, Keithley, USA) to generate the short duration square pulse and a digital oscilloscope (DSO 1052B, Agilent, USA) to visualize how the signal is changed across drain source interface in the presence of water and metal ion sample (Fig. 2.3c). As shown in Fig. 2.3d, when the FET sensor is in air the output signal resembles a perfect square wave. However, when a drop of DI water is exposed on the surface of the sensor, the signal is quickly changed and looks like a slow slanted transient.[157] The time constant (τ) is estimated by calculating the time to reach 63.2% value of the maximum change in the charging/discharging voltage (Details are shown in above 2.2.3 Pulsed capacitance measurements). Upon injection of

the Pb^{2+} ion solution, the transient becomes more slanted due to the adsorption of lead ions by the chemical GSH probes on the sensor surface which change the capacitance and the corresponding time constant. Fig. 2.3e shows the normalized plot of the signal in the presence of air, water and Pb^{2+} solution. The time constant of the sensor in water (τ_1) and lead solution (τ_2) increased systematically with respect to the blank sensor. The responses in DI water and Pb^{2+} sample from blank sensor state (air) are also very fast. Interestingly, when the water was removed, the signal again regained its original square waveform (Fig. 2.3f). Therefore, the change in signal is influenced by the change in larger dielectric constant of water (~80) compared with air (~1) that affects the gate capacitance of the sensor under test.[158] In view of this, it is understood that this transient information through relative change in capacitance can be utilized for an FET type of water sensor to quantify the Pb^{2+} concentration.

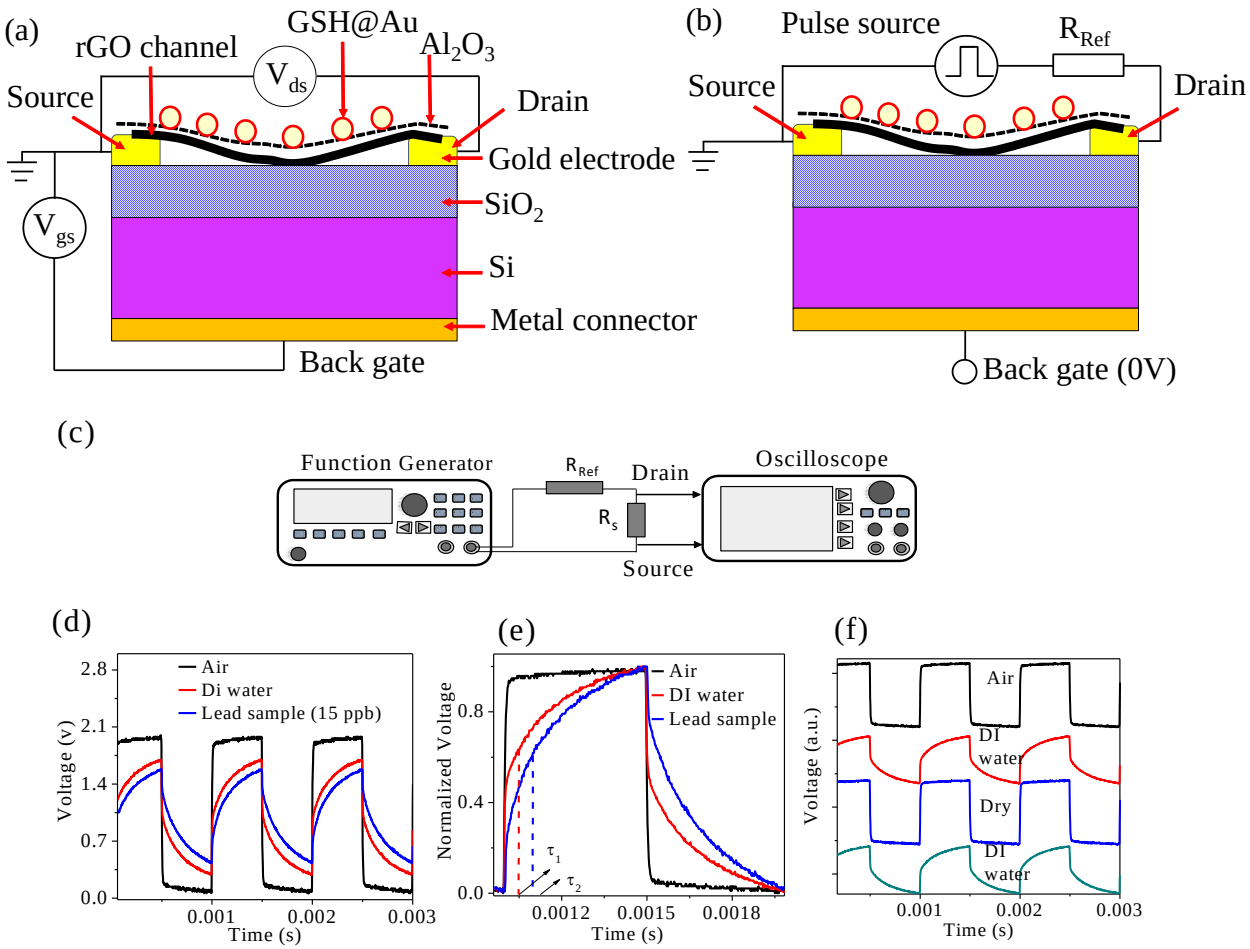

Fig. 2.3 Circuit schematic of (a) FET measurement with back-gate potential and (b) pulse measurement with zero back-gate potential. (c) Pulse generation and measurement circuit with standard instruments with reference resistance (R_1) and sensor (R_s). (d) Square pulse and its transient waveform in the presence of DI water and Pb^{2+} solution and (e) normalized pulse wave visualized plots. (f) The waveform reproducibility in the presence of water and under drying condition.

For real time application, a miniaturized Arduino-based micro-controller has been used and programmed for pulse generation, capacitance signal measurement, and continuous data recording

from this FET type rGO sensor. A portable device with a droplet-based measurement system has also been developed. Fig. 2.4a shows the schematic of the measurement platform. The capacitance value is displayed in the LCD. The stray capacitance is approximately 24 pF, determined through calibrations of measuring other capacitance values and compared with multi-meter readings. This hand-held prototype consisting of LCD, LEDs, and in house cavity for sensor connecting is integrated and schematically shown in Fig. 2.4b. The response% of this chemo-capacitance based FET is defined as,

$$R(\%) = \frac{(C - C_0)}{C_0} \cdot 100\% \qquad (2.2)$$

where, C_0 is the capacitance in DI water as background and C is the charged capacitance in the presence of various metal ion solution.

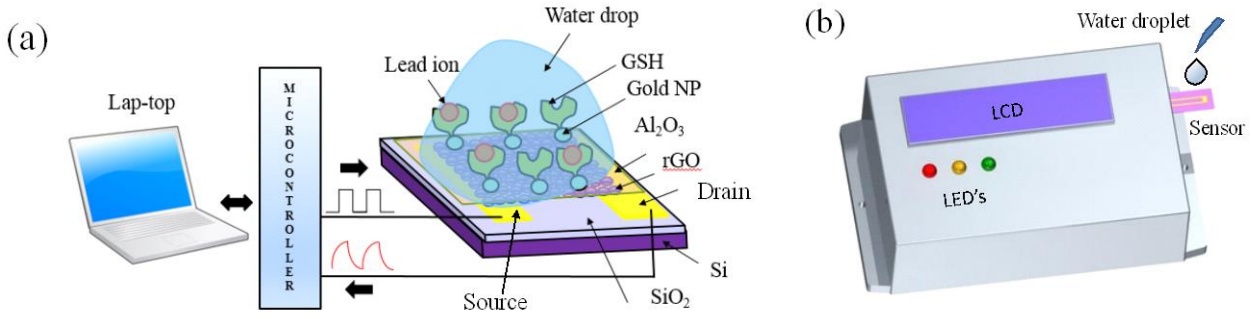

Fig. 2.4 (a) Microcontroller-based pulse-controlled portable capacitance measurement system. (b) Schematic of a packaged portable meter prototype with the integrated micro-sensor chip via a USB connector.

Fig. 2.5a displays the measured capacitance by the meter with multiple cycles of dropping and drying of DI water on the sensor surface. When the DI water (2 µl) is dropped on the sensor surface,

an instant and large change (~5 times of the dry sensor) in capacitance is found. It quickly goes to saturation within 1-2 s. When DI water is taken out, the capacitance quickly reverts to its original value under dry condition. Several cycles of dropping and drying are performed to demonstrate the highly repeatability of the change, which can be attributed to the instant variation of dielectric environment as mentioned above. Interestingly, a quick stabilization with negligible drift in capacitance in the presence of DI water over time (10 min) is found for this arrangement (Fig. 2.5b), compared with much longer stabilization time caused by signal drifting in a common resistance measurement may due to the continuous voltage across the ultra-thin graphene sensor surface and generated heat which changes the intrinsic property of the sensor channel. Once a stable baseline in DI water is obtained, Pb^{2+} solution is injected on the sensor surface (Fig. 2.5c). Again, the change in capacitance in the presence of Pb^{2+} is instantaneous (response time ~1 s) and a very high response% (R~347%) was found even for a low concentration of 2.5 ppb. These advantages make our sensing platform exceed common resistance measurement of the FET sensors where significantly longer stabilization time is always needed and signal continuously drifts in the presence of analytes (Fig. 2.6a). Which causes unfavourable lower response%, bi-directional response, slower detection and larger error (Fig. 2.6b,c). When the Pb^{2+} solution is injected sequentially, a step like, fast increase in capacitance corresponding to the increases of Pb^{2+} concentrations. As the maximum contaminant limit (MCL) by US Environmental Protection Agency (EPA) for lead in drinking water is 15 ppb,[159] our sensor can easily detect lead concentrations lower than this limit and works well around this critical value for real application. The relationship between concentration and response% fits well with an exponential function (Fig. 2.5d), which was loaded into the controller. Then, the concentration prediction can be shown in

the LCD of our meter (Fig. 2.4b), accompanied by LED indicators, Safe (Green (0-5 ppb)), Moderate (Yellow (5-15 ppb)) and Danger (Red (>15 ppb)).

The sensor exhibits a much higher response to Pb^{2+} compared with other common cations and heavy metal contaminants (Zn^{2+}, Mg^{2+}, Fe^{3+}, Na^{+}, Hg^{2+}, Cd^{2+}, $HAsO_4^{2-}$, Ag^{+} etc.) in water. The representative real time capacitance transient for Hg^{2+} (5-100 ppb) with Pb^{2+} (2.5 ppb) is selected to demonstrate the selectivity (Fig. 2.5e). As shown in the plot, relative change in capacitance in Hg^{2+} ion solution is quite insignificant compared with that of Pb^{2+}. Even to the mixed metal ion solution (with all the other metal ions except Pb^{2+}), the response from our sensing platform is still very weak (inset of Fig. 2.5e). It is favourable that the response to lead ions is much higher than other metal ions (Fig. 2.7), which confirms the good selectivity of the sensor due to the special GSH binding with Pb^{2+}.[45] Fig. 2.5f shows a response% comparison of Pb^{2+} (2.5 ppb) with other metal ions (10 ppb). The calculated response from these individual interfering ions and mixed ions did not show any significant sensitivity. The present chemo-capacitance based FET sensor platform shows potential advantages as compared with our previous work and other literature reports using this FET system in terms of a higher response, selectivity, and a shorter evaluation time (Table 1).[143, 149, 152-155, 160]

To verify the practical performance of these sensors, various real water samples from natural and domestic sources have been tested with our platform, including the recent tap water from city of Flint, fresh tap water from Milwaukee and other natural water samples from Lake Michigan and Milwaukee River. The real-time response% calculated from real-time capacitance transients (Fig.

2.8) for these water samples are displayed in Fig. 2.5g. As found from ICP measurements (Table 2.2), the lead ion concentration in Flint tap water is higher (2.38 ppb) than other samples (<0.8 ppb); therefore, it shows higher response than the other water samples; the Milwaukee tap water did not show detectable lead from ICP measurement and the response% is very feeble (R~30%), which may be due to the other interferential ions. Subsequently, the response% become higher for Flint water (R~180%) and other water samples (river and lake water, R~100-130%) owing to the presence of relatively higher amount of lead ions (0.4-2.38 ppb). Fig. 2.5h shows the comparison of the results tested by our sensor with that from ICP measurements. The predicted data points with error bar (measured with 10 devices), locate closely to the ideal prediction line, which suggests our sensor can be used for evaluating lead ions in real water samples.

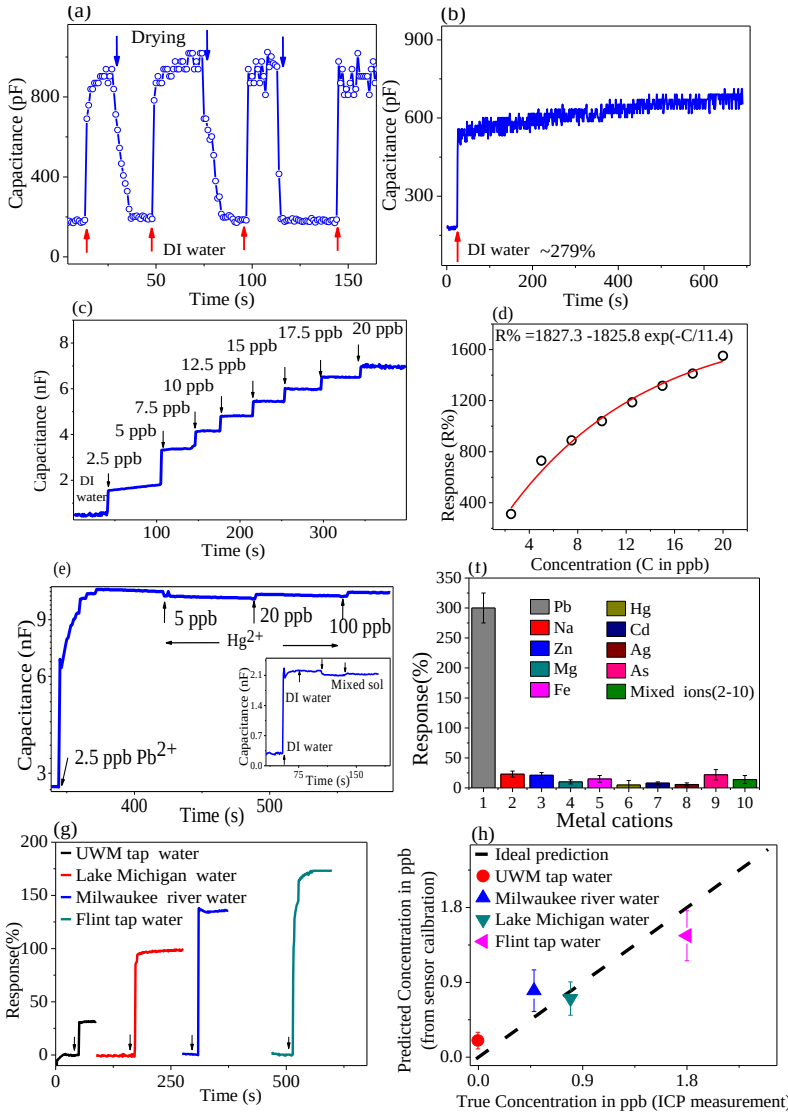

Fig. 2.5 (a) Reversibility test in DI water and under drying condition. (b) Stabilization test of the sensor in DI water. (c) Real time Pb^{2+} testing results with micro-controller-based measurement system and (d) response% vs. concentration graph for the calibration. (e) Typical real time transient data for selectivity test for Hg^{2+} and mixed ions measurement (shown in the inset, the second drop of DI water was used to exclude the volume influence). (f) Comparison of the response% of Pb^{2+} (2.5 ppb) with other individual and mixed metal cations (10 ppb). (g) Testing results of real water samples (the arrow stands for the injection of water sample). (h) Comparison of the predicted lead ion concentration from sensors with the standard values from ICP measurements.

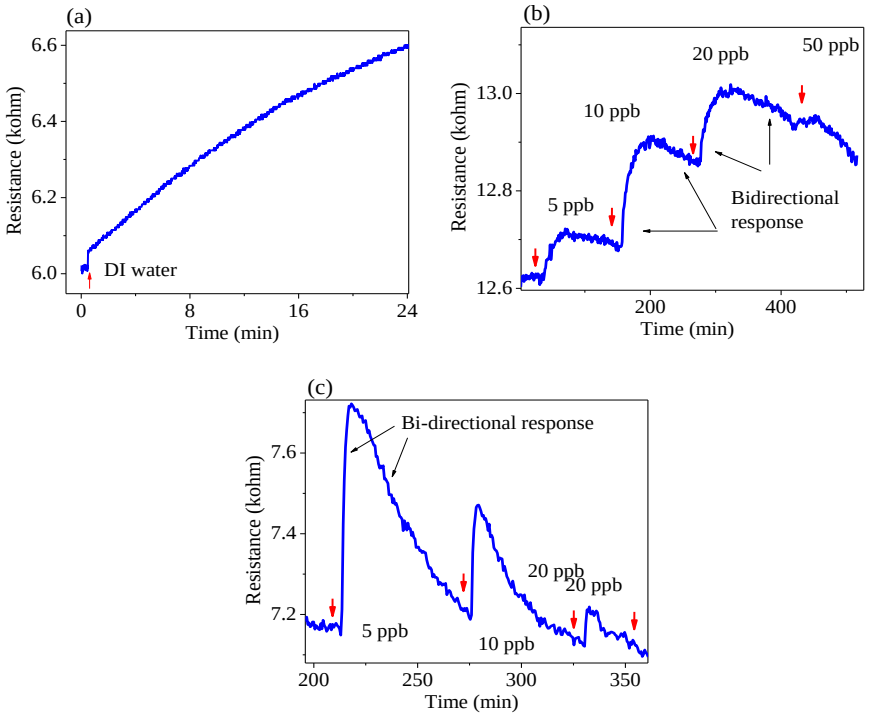

Fig. 2.6 (a) Real-time resistance measurement data of the rGO FET sensor in DI water for background and stabilization test. (b) and (c) Typical resistance transients with bi-directional response for lead ion.

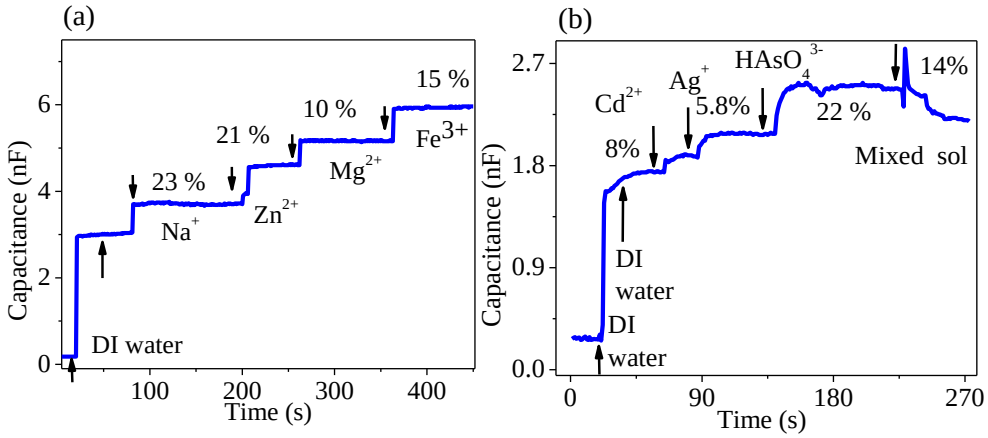

Fig. 2.7 Real-time measured capacitance transients of (a) common metal ions and (b) other heavy metal ions with mixed ions.

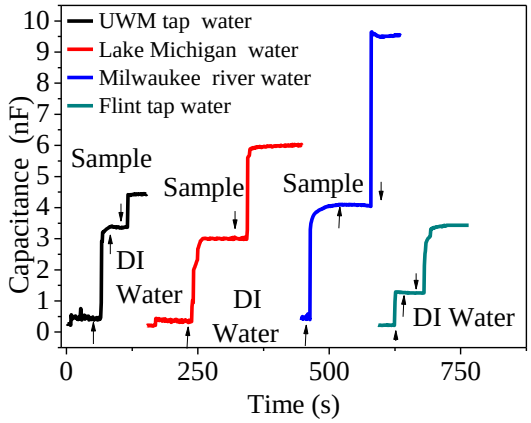

Fig. 2.8 Real-time capacitance transients of real water sample from UWM tap water, Lake Michigan, Milwaukee river and Flint tap water. Up and down arrows signify the time instant of injection of DI water and sample water respectively.

Table 2.2 Measured concentrations of various metal ions from real water samples by ICP measurements.

Metal Ions	**Flint tap water**	**Milwaukee tap water**	**Milwaukee river water**	**Lake Michigan water**
Pb	**2.38 ppb**	**- -**	**0.48 ppb**	**0.79 ppb**
Ag	0.61 ppb	0.16 ppb	0.14 ppb	0.48 ppb
Cd	0.20 ppb	0.12 ppb	0.053 ppb	0.07 ppb
As	0.30 ppb	0.32 ppb	0.21 ppb	0.87 ppb
Zn	62.61 ppb	78.83 ppb	- -	12.19 ppb
Fe	27.36 ppb	89.74 ppb	- -	66.80 ppb
Cr	0.33 ppb	0.30 ppb	0.155 ppb	1.77 ppb
Na	4.08 ppm	4.75 ppm	10.06 ppm	28.34 ppm
K	1.23 ppm	0.65 ppm	1.21 ppm	5.12 ppm
Mg	0.71 ppm	0.68 ppm	1.03 ppm	2.54 ppm
Ca	14.76 ppm	16.93ppm	37.37 ppm	81.71 ppm

To benchmark the present study with conventional FET structure with dc resistance measurements and our earlier work as stated in Table 2.1, the present capacitive measurement with improved single layer GO deposition strategy shows one order magnitude higher response with step like transient, excellent selectivity, and much shorter evaluation time. Such a sharp change in capacitance due to gate voltage is also observed by another study using organic semiconductor with an insulator gate.[161] This study shows that due to very small change in gate voltage, capacitance can be changed instantly, whereas, mobility of the device shows slow change. The minimization of Joule heat by using pulse as compared to common continuous voltage (dc measurement) can also be another reason for the quick and sustaining response in signal stabilization. Additionally, from microcontroller based device perspective, the system is small, programmable, portable and able to recognize the Pb^{2+} in real time. We have made efforts from direct use and end users perspective, which is hardly found in most literature. When compared to other methods (non-FET), such as, voltametry, the system is maintenance free and not affected by drifting and background current instability. We also demonstrate the capability of real water analysis with the developed meter. Therefore, for rapid heavy metal testing of onsite water quality, portable digital recording and operational ease, the present system shows greater advantages.

To interpret the sensing result, we adopted the equivalent circuit model of this FET system and top gate potential influence on the sensing performance (Fig. 2.9a). There is apparently no influence of the back-gate terminal (Si/SiO_2) on sensing measurements as it is not exposed to the sensing environment, and is kept at 0 Volt. The current in channel is changed by the top-gate (ultrathin Al_2O_3 oxide layer) capacitive coupling with rGO channel. There might be some other aspects, for example, influence from the rGO/Au electrode contact. So, the system is electrically equivalent to

a resistance-capacitance pair (RC) from channel/oxide interface (R_{Ch} and C_1) and channel-contact interface (R_C and C_C). Here, R_{Ch} and R_C are the channel and contact resistance, respectively. C_1 is an electric double layer (EDL) capacitance formed at the rGO/Al_2O_3 interface. The EDL capacitor consists of stern layer (C_I, formed due to charge transfer near the p-type rGO and n-type Al_2O_3 interface) and diffuse layer (C_D, formed away from the channel towards Al_2O_3 matrix where holes are diffused in a cloud of opposite charges).[162] Diffuse layer capacitor forms far from the channel and are primarily affected by the environmental factors. Both capacitors are connected in series but parallel to the rGO channel resistance. Therefore, the capacitance at the rGO/Al_2O_3 interface (C_1) can be expressed as $C_I \cdot C_D/(C_I+C_D)$. Fig. 2.9b shows the equivalent circuit model which consists two RC parallel network connected in series and finally the entire system can be expressed as single equivalent RC pair (R_{eq} and C_{eq}). The incoming periodic pulse will face the resultant or equivalent RC time constant from superposition of these contributions. In the presence of a higher dielectric medium like water the capacitance of the top gate becomes higher and the interface capacitance is significantly influenced by periodic signal. When the Pb^{2+} are further attracted by GSH probes, the amount of negative charges at the channel increases due to ion-induced top gate positive potential and the total capacitance further increases owing to the increase of C_D. The diffusion capacitance (C_D) and positive ion induced gate voltage (ψ_a) can be expressed from the Gouy-Chapman model,[162]

$$C_D = \left(\frac{\varepsilon\varepsilon_0}{\lambda_D}\right) \coth\left(\frac{l}{\lambda_D}\right) \cosh\left(\frac{e\psi_a}{2k_bT}\right) \quad (2.3)$$

Where, ε and ε_0 are the relative dielectric constant of the material and vacuum permittivity, respectively, λ_D is the Debye length, l is thickness of the capacitor region, e is electronic charge, k_b is Boltzmann constant, and T is the absolute temperature. Therefore, it is presumed that medium (DI water) induced larger dielectric constant and electrostatic top gate field (ψ_a, due to

electrostatically positively charged Pb^{2+}) increases the magnitude of EDL capacitances (C_1). This change in capacitance eventually affects the equivalent capacitance (C_{eq}) and the overall time constant of the system becomes larger. Thus, the incoming periodic pulse signal faces a greater time constant and further delayed charging and discharging. Microcontroller calculates this change in capacitance (C_{eq}) with calculated time constant (τ_{eq}). Further study is still needed to get detailed electronic information about the structure and this could be an interesting research direction for various 2D layered materials based FET sensor.

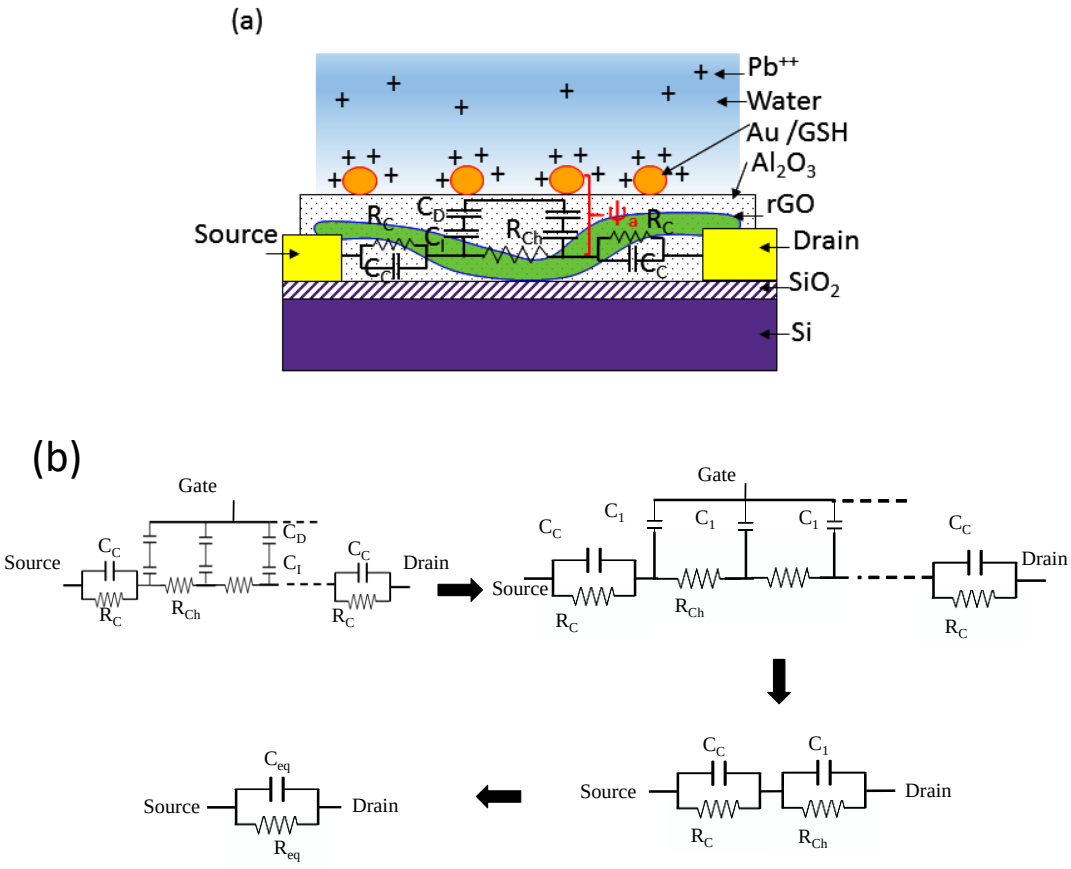

Fig. 2.9 (a) Simplified model of insulated GFET structure with attached probes (Au/GSH) in Pb^{2+} solution and (b) equivalent circuit model of the FET structure.

2.4 Summary and conclusions

In summary, with an improved self-assembly single layer GO deposition method, a new pulse driven chemo-capacitance based lead ion detection using droplet-based measurement has been demonstrated. As a proof of concept, it was shown that how the square pulse signal and related time constant become modified in the presence of a blank sensor (in air), DI water, and lead ion sample. This transient feature reveals a great potential as a new transducing method. Practical change in environment (water and Pb^{2+} solution) can significantly tune the dielectric constant of the system, charge the channel by electrostatic gating, and modulate the interface capacitance extensively. Finally, a microcontroller based pulsed mode capacitive measurement device has been developed to measure capacitance across the drain-source interface. Benefiting from the optimized sensor structure: reliable single layer rGO channel, effective Al_2O_3 passivation layer, and novel pulse measurements, the micro-system with a GFET sensor chip shows rapid response and stabilization (1-2 s) in DI water and lead ion solution, negligible drift, a LOD < 1 ppb, extra higher response (e.g. R~347% for 2.5 ppb) and excellent selectivity (one order of magnitude higher than other ions) towards lead ion. The step-like behaviour in various concentrations ensures an exponential calibration line for the prediction of lead ion concentration and has been used for analysis of various real water samples successfully. The overall assay time for this simple “drop and measure” technique is ~10 s, which is much faster than most conventional techniques. The relevant mechanism is explained by the gate induced change in the double layer capacitance and equivalent RC circuit time constant. The experimental findings might open a new dimension in 2D materials-based FET sensor applications, high speed chemical computation, environmental monitoring and chemical cybernetics.

CHAPTER 3 RESONANCE-FREQUENCY MODULATION FOR RAPID EBOLA-GLYCOPROTEIN DIAGNOSIS WITH REDUCED GRAPHENE OXIDE FIELD-EFFECT TRANSISTOR

3.1 Introduction

The Ebola epidemic commenced in west Africa (Guinea, Liberia, Nigeria, Senegal, and Sierra Leone) in December 2013, and the World Health Organization (WHO) declared it to be a "public health emergency of international concern".[163] The number of confirmed and possible cases of Ebola-virus disease is at 28 603, with 11 301 resulting in death. As per the recent outbreak in Congo, the WHO reported 39 suspected, probable, and confirmed cases of Ebola between April 4 and May 13, 2018, including 19 deaths. The Ebola virus is commonly spread through contact with bodily fluids. The outbreak can only be stopped by a combination of early diagnosis, patient segregation with effective care, and safe burial.[164] Ebola-virus infection and confirmation are generally made using the following investigations: antibody-capture enzyme-linked immunosorbent assay (ELISA), antigen-capture detection tests, serum-neutralization tests, reverse-transcription− polymerase-chain-reaction (RT-PCR) assay, electron microscopy, and virus isolation by cell culture.[163] Although widely used for clinical diagnosis, these methods do not allow for quick, easy, or effective onsite, point-of-care (POC) detection; for example, ELISA is limited by its low sensitivity, whereas RT-PCR results can vary with external environment, temperature, and sample preparation.[165-167] Several bioassays regarding Ebola detection can be found in the current literature, and most of the reported works are based on the antigen−antibody reaction through photo- or electroluminescence, nanoparticle-plasmonics-based technology, interferometry imaging, and fluorescence-resonance-energy transfer.[168-171] However, most of these methods are

inadequate for low-cost and miniaturized POC detection because they require expensive equipment, considerable amounts of time, and trained professionals. To stop the spread of the deadly Ebola virus before an epidemic occurs, an effective, rapid, reliable, and user-friendly sensing platform for onsite detection of the Ebola virus is greatly needed.

In recent years, the use of label-free biosensors has emerged as a technique for detecting various infectious diseases and pathogens.[169, 172-184] Such biosensors require suitable biomarkers or probes to attract targeted species, as well as a variety of resonance-based transduction mechanisms such as surface-plasmon resonance (SPR),[177] mechanical resonance,[178] optical resonance,[169] and acoustic resonance.[179, 180] There are several advantages and disadvantages to these approaches. For example, optical sensors can be operated without any physical interaction of the detected species with the light source or the detection sensor. In addition, they are independent of the solution's pH, ionic strength, and other properties.[181] In the presence of test species, the optical signal can be transformed into the electrical analogue, from which the sensitivity can be correlated with changes in resonance-frequency shifting or intensity quenching. Yanik et al. demonstrated successful pseudotyped-Ebola detection using the optical-resonance method.[169] Optical sensors can also be unfavorable, as they require high-precision light alignment to capture the successful pairing of probes and target species and expensive hardware for measurements and calculations and have other drawbacks (such as uncertainty in measurements, conformational changes, and scattering) that could make them unsuitable for point-of-care diagnosis.[185, 186] Mechanical and acoustic sensors are largely based on quartz-crystal-microbalance (QCM), cantilever, and surface-acoustic-wave (SAW) sensors.[179, 180] The fundamental mechanism for these types of sensors is based upon monitoring the mechanical-resonance-frequency shift as the probe-modified cantilevers or quartz

crystals interact with biological species. This interaction occurs through a specific binding event, which bends the cantilever or changes the mass of the system; however, mass resolution of this type of sensor is insufficient when operated in solution.[187] These sensors are also sensitive to external noise and thermal drift, which is another significant problem for practical implementation in POC diagnosis.

Field-effect transistors (FET) are an excellent choice, as they can be operated by simple resistance measurements. Many interesting reports can be found for graphene-based FET sensors (GFET) for biomolecule and heavy-metal detection because of the monatomic 2D-layer structure, high specific surface area, and low electronic noise.[112, 144, 145, 152, 188, 189] The sensing mechanism is based on the change in the resistance or current of the probe-modified transistor channel. This is accomplished by inducing short-range electrostatic fields when interaction with specifically targeted species occurs through a known biorecognition procedure. When the transistor channel is passivated with a dielectric oxide top gate, possible influences from medium and other conducting species can be segregated from the measurement electrodes.[190] This important feature gives insulated, gated FET-based sensors a significant advantage over the noninsulated FET structure; however, there are several technical challenges (e.g., lower sensitivity and moderate selectivity due to very weak, short-range electrostatic forces) that still need to be resolved for this type of sensing platform to be used reliably as a POC diagnostic tool.[149, 154, 155] For these reasons, dielectric-gated FET structures need to be investigated for proper understanding of the device, its circuit components that are directly measured, and its impact on Ebola sensing.

In this report, we have discovered that the device's electronic-resonance frequency can be exploited as a promising transduction mechanism for enhancing the sensitivity and selectivity for Ebola glycoprotein (GP). Unlike optical-spectral resonance-based techniques, it does not need highly sophisticated instruments to capture the successful pairing of antigen-antibody that causes a resonance shift.[169, 186] This is a potential problem for optical resonance to obtain a reasonable resonance-wavelength shift from a very low Ebola-GP concentration.[169] Our electronic-resonance-based system can realize faster (~1−2 min)[191] and stable detection, avoiding external noise or disturbance, which is a significant challenge for other resonance-based techniques, as previously discussed. We conducted impedance measurements over a wide frequency range to evaluate the various circuit components, such as contact and channel impedance in terms of the pair of *RC* components, and electronic-resonance frequencies to investigate their influence on sensing performance. For an *RC* circuit, resonance mainly comes from the characteristic frequency (f_c, where the imaginary part of impedance is maximum and related to the *RC* time constant) and the inflection frequency [f_i, where the phase angle reaches a maximum (θ_{max}); i.e., $d\theta/d\omega = 0$, where θ and ω are the phase angle and angular frequency, respectively]. For an insulated, gated FET structure, the frequency-dependent channel impedance is governed by charge-carrier trapping−release at interface states between the channel−gate oxide and channel−source or drain contacts.[192, 193] Each of these influences are designated by a certain relaxation process with specific time constant and can be represented by an *RC* pair as an electronic equivalent. Through a variable frequency input (impedance spectroscopy), these relaxation processes can be identified by monitoring the local maxima (resonance peaks) of the respective spectrum. The effect of trapped-charge carriers on MOSFET electronics is important, as they control the transport properties of the device by creating an internal field.[194] The trap-charge internal field further controls the charge-

injection properties from the source−drain and can show hysteresis because of the faster rate of bias-voltage sweeping.[195-197] The sweep rate of bias voltage is important as it controls the charging−discharging time scale. For a conventional dc measurement ($\omega \sim 0$), this trapping-release time is faster ($\tau_{trap} \sim 1\ \mu s$ to $\tau_{detrap} \sim 250\ \mu s$);[197] however, it is slower than the high-frequency impedance measurement. Therefore, it is expected that the channel could show frequency-dependent behavior as the trapped charges may not release during this high-frequency ac measurement. In other words, the relaxation of trapped charge should show some frequency-dependent behavior that directly affects the device conductance, which can be identified by the measured phase shift. Practically, a phase shift of ∼0° signifies an ideal resistive system, whereas it transits to capacitive behavior when the phase angle starts to increase (∼90° for a perfect capacitive or insulating system). When charges are trapped with a significant delay in emission as compared with the measurement frequency, the channel shows an insulating (capacitive) effect as the phase shift increases. Therefore, it is interesting to explore how these trapped-charge-relaxation dynamics, identified through resonance phase shift, are affected by a top-gate-induced field through the Ebola antigen−antibody interaction and how it impacts various electronic parameters that are used for measuring the sensitivity of the GFET device.

3.2 Experimental methods

3.2.1 Chemicals

Single layer graphene oxide (GO) water dispersion was ordered from ACS Materials. Cysteamine (AET), glutaraldehyde, PBS buffer, ferritin, and human Ig G protein were all purchased from

Sigma-Aldrich. SuperBlock Tween 20 was ordered from Thermo Scientific. Ebola-glycoprotein, and human antibody KZ 52 were obtained from IBT Bioservices.

3.2.2 Sensor fabrication

Using a standard lithographic method, interdigitated gold electrodes with both a finger-width and an interfinger space of 1.5 μm and a thickness of 50 nm were fabricated on a 100 nm SiO_2-layer-coated silicon wafer. A self-assembly electrostatic method was used to deposit single-layer commercial graphene oxide (GO) sheets on the electrodes.[198] First, the Au electrodes were incubated in AET solution and then rinsed with ultrapure water to attach a monolayer of AET onto them. Second, the modified Au electrodes were immersed in ultrapure-water-diluted GO solution to obtain single-layer GO attachment through the electrostatic interaction between the positively charged amino groups of AET and the negatively charged GO sheets in water. The negative charge on the GO sheets can prevent multilayer stacking during the deposition process. Finally, unanchored GO sheets were removed by rinsing with ultrapure water. A quick annealing process for 10 min at 400 °C in a tube furnace with Ar gas was used to both reduce the GO and improve the contact between the GO and the electrodes. The samples were then cooled to room temperature spontaneously. Next, an ultrathin 3 nm Al_2O_3-passivation dielectric oxide layer was deposited onto the sensor surface by atomic-layer deposition (ALD) with trimethylaluminum (TMA) and water precursors at 100 °C. Uniformly distributed and high-density Au NPs were sputtered on the Al_2O_3 as the anchoring site for further modifications. After Au NP deposition, 1 μg/mL AET solution was dropped on the sensor surface and incubated for 30 min. The AET reacted with the Au NPs through the well-known thiol−Au interaction. Next, the sensor was immersed and washed with ultrapure water to remove extra AET molecules; this was followed by drying with nitrogen gas.

Then, glutaraldehyde solution (5%, diluted with ultrapure water) was drop-casted onto the sensor surface to make a linkage with AET via NH_2 groups, which had already been anchored on the Au NPs in the last step. After 30 min of incubation, the sensor was again washed with ultrapure water and dried with nitrogen. In the next step, antibody solution (200 μg/mL diluted initial antibody solution, KZ 52) with 0.01 M PBS buffer (1 M, pH ~7.4) was immobilized on the sensor surface to functionalize the Au NPs with glutaraldehyde. This was incubated for 30 min and then washed with ultrapure water and dried gently with nitrogen. Glutaraldehyde can react with several functional groups of proteins, such as amines, phenols, and imidazoles, because the most reactive amino acid side chains are nucleophiles. Therefore, glutaraldehyde serves as a linker between the amine groups of AET and the amino acid groups of KZ 52 antibody protein. After that, Tween 20 solution (0.1% Super Block Tween 20 in PBS) was drop-casted on the sensor and incubated for 30 min to prevent the nonspecific binding of analytes. Finally, the sensor was washed with ultrapure water and dried with nitrogen. Although the actual Ebola virus could not be used for sensing because of biosafety issues, the glycoprotein was used because it has an equivalent chemical and biological signature on the external surface of Ebola's viral membrane; AC impedance was measured at the source and drain interfaces with an electrochemical analyzer (PARSTAT 4000A, Ametek Scientific Instruments) in the 1 Hz to 5 MHz frequency range.[199]

3.3 Results and discussion

3.3.1 Ebola-recognition scheme

Using crosslinking chemistry, the antibody probes were functionalized with gold nanoparticles with cysteamine (AET) and glutaraldehyde as linkers. The thiol groups of AET made chemical

linkages with the gold nanoparticles sputtered onto the Al_2O_3 passivation layer, which was predeposited on the reduced graphene oxide (rGO) surface. In between, glutaraldehyde acts as a bridge between the amine groups of both the antibody probe (KZ 52) and AET through its −CHO-group interaction. The antibody probe (KZ 52) was purchased from a commercial source, which provided KZ 52 human antibody derived from a human convalescent patient who survived an Ebola-virus (EBOV) infection during the 1995 outbreak in Kikwit, Democratic Republic of the Congo.[200] The antibody detects recombinant EBOV GP without the transmembrane region (EBOV rGPΔTM) expressed in both mammalian and insect cells. The details of the interaction between KZ 52 antibody and Ebola glycoprotein (GP) can be found elsewhere.[200] Briefly, the EBOV GP has two subunits, termed GP1 (responsible for cell-surface attachment) and GP2 (responsible for fusion of viral and host-cell membranes). KZ 52 acts as a bridge for both the attachment (GP1) and fusion (GP2) subunits of the Ebola GP. With this interaction mechanism, in our FET structure, the functionalized KZ 52 antibody probes on the sensor's surface serve as active sites to recognize Ebola GP.

3.3.2 Device configuration and sensing mechanism

Fig. 3.1a shows the device configuration and circuit diagram of the FET sensor. Ebola-glycoprotein detection was accomplished using standard antigen−antibody-conjugation principles.[200] Fig. 3.1b shows a schematic configuration of the GFET device realizing charge transport using ac signal inside the rGO channel that involves injection, trapping, and release at the channel−oxide and channel−electrode interfaces. Because of the variation of the position of the charge trap inside the oxide from the channel, the trapping−release-time constants can vary. For this reason, each trap corresponds to a different relaxation frequency in the presence of a wide

frequency-measurement range of the ac signal. Practically, the phase angle is near zero at low frequencies; however, it systematically increases when the measurement frequency is swept from low to high, until the resonance occurs. The phase shift increases as the trapping-release time of the charge carrier seems slower in comparison with the high-frequency ac measurements through an interface-capacitance effect. Because of the distribution of relaxation time, the measured phase angle versus the frequency spectrum, which is a superposition of these possible relaxation processes, becomes broad with a specific local maximum that represents the resonance center (Fig. 3.1c). Because of the generation of top-gate electric field by the specific interaction of Ebola-antigen−antibody, the charge-carrier concentration inside the channel is modulated, and the associated relaxation processes influence the electronic parameters (channel and contact impedance) by shifting the resonance-frequency position. Using equivalent-circuit modeling, the resonance-frequency shift has been correlated with channel-contact-impedance change, resulting in generalized analytical equations, discussed in detail later. It is to be noted that interface trap can also form at the bottom-gate dielectric (SiO_2); however, the sensing event mainly occurs on the top-gate oxide (Al_2O_3). Therefore, influence from the back-gate is not considered and is assumed to be background.

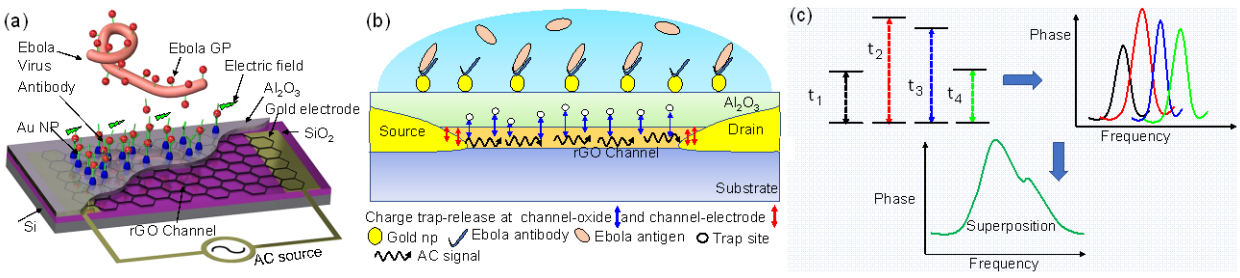

Fig. 3.1 (a,b) Schematic diagrams of (a) insulator-gated FET-based Ebola-sensor device and (b) charge-injection-trapping-release-transfer mechanism at the channel-oxide and channel-electrode interfaces. (c) Trapping- and release-time constants (or relaxation frequency) corresponding to different activation energies, which can vary because of the varying position of the charge trap inside the oxide from the channel. In ac measurement, the phase angle vs frequency spectrum is a superposition of possible relaxation processes with a specific resonance center (frequency at which the phase angle becomes maximum). Resonance-frequency shift occurs when the top-gate field is generated by antigen-antibody interactions.

3.3.3 Microstructure and electrical characterization of the sensor device

Fig. 3.2 shows a field-emission-scanning-electron-microscopy (FESEM) image of the single-layer rGO with low and high magnifications (Fig. 3.2a,b, respectively). It is clearly seen that single-layer rGO channels are formed between gold electrodes without further flocculation. This suggests the high quality of the device, which resembles a perfect 2D-nanomaterial-based measurement platform. Fig. 3.2c shows the atomic-force-microscopy (AFM) image of a single-layer rGO nanosheet bridging the two electrodes. The thickness profile is shown in the inset of Fig. 3.2c, which suggests a single layer of rGO nanosheet (~1 nm). To study the FET property, the drain current (I_{ds}) was measured as a function of varying gate voltage (V_{gs}) on the backside of the silicon

wafer (Fig. 3.2d). The measurement was made from −40 to 40 V (scanning step of 0.2 V), which resulted in a *p*-type, smooth FET curve with an on-off current ratio of ~1.29. A linear $I_{ds} - V_{ds}$ measurement curve for drain-source voltage (V_{ds}) ranging from −1 to 1 V suggests ohmic contact between the rGO nanosheet and the gold electrodes (shown in the inset of Fig. 3.2d).

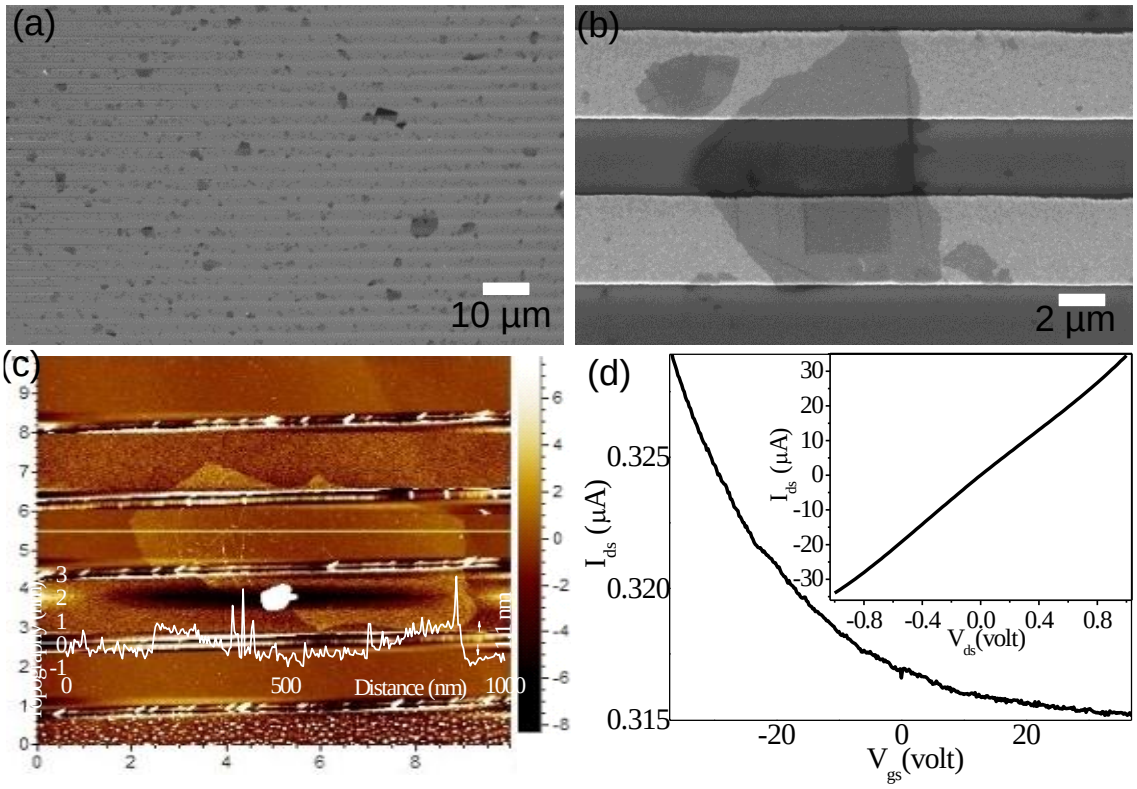

Fig. 3.2 (a,b) FESEM image of rGO nanosheets distributed on the electrode in (a) low and (b) high magnifications. (c) AFM image of a single-layer rGO nanosheet with the thickness profile shown in the image. The distance scale (nm) is the same for both images. (d) $I_{ds} - V_{gs}$ curve for V_{gs} = −40 to 40 V with a scanning step of 0.2 V for the rGO-based sensor. $I_{ds} - V_{ds}$ characteristics for V_{ds} = −1 to 1 V are shown in the inset.

3.3.4 Ebola-glycoprotein-sensing measurement for electronic-parameter evaluation

After the sensor device is fabricated, a sensor-chip cell is connected to the impedance-measurement system with its drain−source interface. Although live Ebola virus could not be used because of biosafety issues, the glycoprotein, which has a chemical and biological signature equivalent to that of the external surface of the Ebola-virus membrane, was procured (see Fig. 3.1a). A small-amplitude sinusoidal voltage (0.01 V) was applied at the drain−source interface, and the impedance spectra were recorded in air.

Sequentially, the buffer (∼2.5 μL) was injected inside the cell to produce a baseline, and the impedance spectra were recorded again. Different concentrations of Ebola-glycoprotein solutions (0.001−3.401 mg/L, ∼2.5 μL) were then injected, and similar impedance measurements were consecutively performed for each concentration. Fig. 3.3a shows the Nyquist plot for the sensor in air, buffer, and Ebola-glycoprotein test solutions with various concentrations. From the plot, it is apparent that only one semicircle is found in air; however, in the presence of buffer and test solution, a new semicircle at a high frequency arises (shown in the inset). Fig. 3.3b shows the equivalent circuit, which is a series combination of two parallel *RC* networks (R_1C_1 and R_2C_2), with a series combination of external resistance (R_3, from external measurement wires and cables). All the data were fitted to calculate the resistance and capacitance changes in buffer and various Ebola-glycoprotein solutions using the Levenberg−Marquardt algorithm. Here R_1C_1 and R_2C_2 represent contact and channel resistance−capacitance, respectively. From the Nyquist plot, it appears that low-frequency semicircles in buffer and protein solutions are suppressed. The suppressed semicircle signifies the presence of an imperfect capacitive element in the system and is generally replaced by the constant-phase element (CPE), which arises as a result of the presence

of the double-layer capacitor.[192, 201] Therefore, the capacitance (C_2) is replaced with CPE during the fitting. The details of double-layer-capacitance formation and its influence on the sensing mechanism are discussed later. The experimental (dotted) and fitted (line) curves in buffer and in 0.001 and 3.401 mg/L protein solutions, are shown in Fig. 3.4a−c, respectively. The extracted parameters for all cases are shown in Table 3.1. It was found that measured channel resistances (R_2) are higher than contact resistances (R_1) and change linearly with increasing protein concentrations (Fig. 3.3c). The value of external resistance, R_3 (from external wires or cables), remains constant and is not affected by the sensing performance. The calculated values of C_1 and C_2 in buffer and various protein concentrations are also shown in Fig. 3.3d. C_2 was derived from CPE parameters, such as the pre-exponential factor, Q, and exponent, n (see Table 3.1). The unit of Q is nanoSiemens (nS). A systematic linear increase in C_2 was found for different protein concentrations, whereas the change in the C_1 value was not so significant. The value of n, as obtained from fitting for all cases, is close to 1, and thus, CPE behaves as a capacitor. Here, the value of C_2 is calculated from two different models (Table 3.1). The calculated capacitances (C_2) from both models are shown in Fig. 3.5, which shows that both calculated values exhibit almost equal orders of magnitude, suggesting the validity of the calculation. It should be noted that because of the one semicircle in air, it is impossible to separate the relative contribution from the channel and the contact resistance in air. When the sensor is exposed to an aqueous environment (e.g., buffer), the sensing environment is switched from a lower-dielectric-constant medium (∼1) to a higher-dielectric medium (∼80). This influences the second capacitance (C_2), and eventually the channel resistance (R_2) is separately coupled with C_2. This produces a time constant ($\tau_2 = R_2C_2$) different from the contact resistance−capacitance time constant ($\tau_1 = R_1C_1$). Consequently, two semicircles are found in the aqueous environment.

Fig. 3.6a shows the phase-angle change versus the frequency plot for all cases discussed above. The maximum peak of the phase angle (θ_{max}) in the presence of the aqueous environment and protein solutions shows two distinct peaks in the low frequency (3.2−5.5 kHz) and the high-frequency (>100 kHz) ranges. This signifies the presence of two different time constants, as previously discussed, because of the channel and the contact *RC* pair, respectively. At a lower frequency range, the shifting θ_{max} values can also be related to different concentrations. It should also be noted that the resonance frequency for θ_{max} (inflection frequency, f_i^l) is also systematically shifted to a higher frequency when the concentration of the Ebola-glycoprotein test solution increases sequentially (indicated by a upward-slanted solid arrow). Therefore, the resonance-frequency shift (Δf_i^l) at θ_{max} could be used for calibrating the different concentrations. It is also noted that a satellite resonance peak (f_i^h) at a high frequency due to contact influence can also be found (indicated by a downward-slanted dotted arrow in Fig. 3.6a). It also shifts to a higher frequency when glycoprotein is added and seems much more sensitive than the low-frequency one, but this peak position is not strong enough because of the large influence from the low-frequency-resonance tail edge and is not considered for calculating sensitivity. Details of this relation of individual resonance-peak positions from various circuit components and simulations are discussed later.

To calculate the characteristic frequency (f_c), the imaginary part of the impedance (Z'') is plotted against frequency, as shown in Fig. 3.6b. A decrease in f_c is observed upon injection of the Ebola-glycoprotein solution and is also used for relating to the change in concentrations. Additionally, the channel-resistance change (ΔR) and channel-capacitance change (ΔC) are considered for

correlating different concentrations from Fig. 3.6a,b, which is generally followed for various FET biosensors.[112, 144, 145, 152, 188, 189] Therefore, the sensitivity values based on these five different parameters (ΔR, ΔC, $\Delta\theta$, Δf_i^l, and Δf_c) are compared with various Ebola-glycoprotein concentrations. Fig. 3.6c,d shows plots of θ_{max}, f_i^l, and f_c versus the concentration. The sensitivity for each case is evaluated by the following relations. Here, R_0, C_0, θ_0, $f_0^{i\_l}$, and f_0^c are the initial values of the channel resistance and capacitance, maximum phase angle (θ_{max}), inflection-resonance frequency in the low-frequency region, and characteristic frequency in the buffer solution, respectively. R_p, C_p, θ_p, $f_p^{i\_l}$, and f_p^c are the corresponding values in the presence of the injected Ebola-glycoprotein solution. Calculated sensitivity values from the changes of all these parameters are compared in Fig. 3.6e. As found from the plot, the sensitivity related to resonance shifting is higher than the sensitivity based on other calculated parameters. Moreover, the change in f_i^l for various Ebola-glycoprotein concentrations provides the highest sensitivity among all of them. Therefore, changes in f_i^l are used as an optimized parameter for comparing the selectivity of the sensors.

Fig. 3.6f,g show the phase angle versus the frequency plot of human IgG and ferritin protein, respectively. It was found that there was no significant shift of the inflection-resonance frequency (indicated by a vertical arrow). Fig. 3.6h shows a comparison of the sensitivity shift of f_i^l for Ebola glycoprotein, human IgG, and ferritin. This suggests our sensor has also excellent selectivity because of the very specific interaction between Ebola-glycoprotein and the antibody probe. Overall, this could be an interesting finding for rGO-based, impedimetric dielectric-gated FET biosensors, as they are generally limited by lower sensitivity.[149, 154, 155, 202-204]

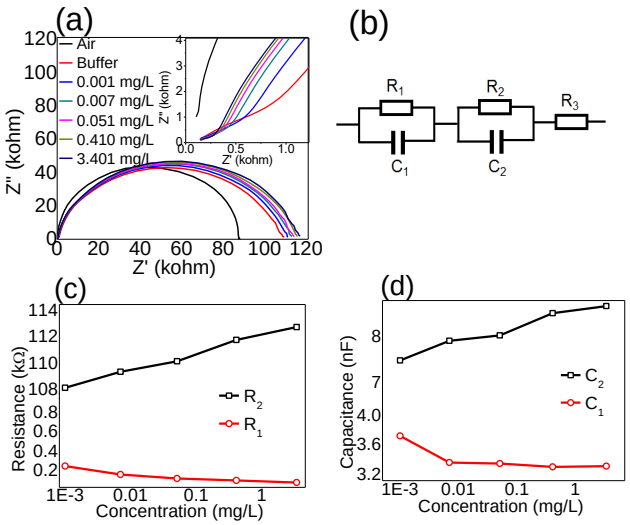

Fig. 3.3 (a) Nyquist plot for the sensors measured in air and buffer and with various Ebola-protein concentrations. (b) Equivalent circuit for the evaluation of circuit parameters. (c,d) Plots of calculated (c) resistances and (d) capacitances from the *RC*-circuit fittings for buffer and various Ebola-glycoprotein concentrations.

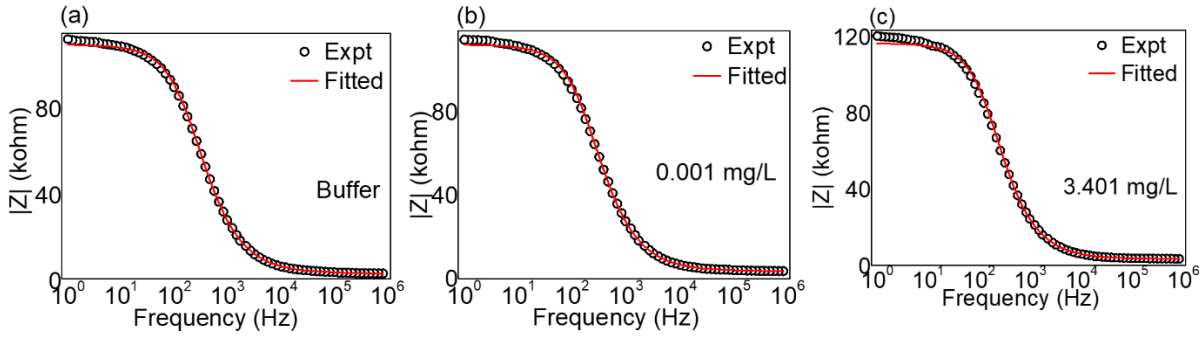

Fig. 3.4 The experimental (dotted) and fitted (line) impedance spectrum for (a) Buffer, (b) 0.001 mg/L and (c) 3.401 mg/L.

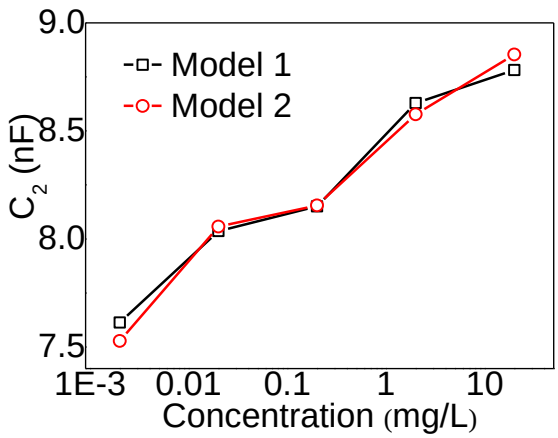

Fig. 3.5 Comparison of calculated C_2 from *CPE* parameters for model 1 and 2. Model 1: $C_2 = (Q * R_2)^{(1/n)} / R_2$ from parallel resistance R_2, and model 2: $C_2 = Q * (\omega_{max})^{(n-1)}$ from ω_{max}, the angular frequency at which the imaginary part impedance is maximum.

Table 3.1 Calculated parameters from equivalent *RC* circuit fitting from impedance measurement data.

Condition (mg/L)	R_1 (Ohm)	R_2 (Ohm)	C_1 (nF)	*CPE*		C_2(nF)from model 1	C_2(nF) from model 2
				Q(nS)	N		
0	455.08	106400	3.934	16.821	0.884	7.359	7.309
0.001	295.28	108500	3.805	15.943	0.895	7.613	7.527
0.007	208.71	109710	3.445	15.842	0.903	8.036	8.057
0.051	167.70	110510	3.431	15.832	0.905	8.150	8.155
0.410	147.07	112130	3.386	16.253	0.908	8.628	8.576
3.401	126.13	113100	3.39	16.389	0.909	8.781	8.853

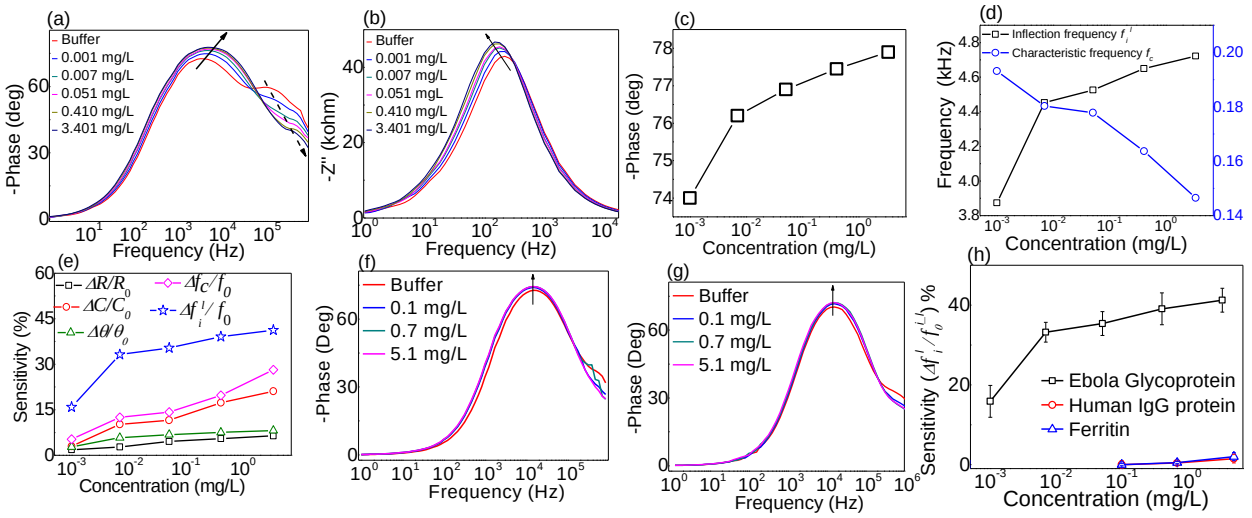

Fig. 3.6 (a) Phase angle vs frequency and (b) Z'' vs frequency plot for buffer and various Ebola-glycoprotein concentrations for evaluating inflection (f_i^l) and characteristic (f_c) frequencies, respectively. (c,d) Plots of changes in (c) maximum phase angle (θ_{max}) and (d) inflection frequency (f_i^l) and characteristic frequency (f_c) vs various Ebola-GP concentrations. (e) Comparison of sensitivity for all parameters. (f,g) Phase angle vs frequency plot for (f) human IgG and (g) ferritin. (h) Sensitivity vs concentration plot for the selectivity study for the Ebola-GP sensor.

3.3.5 Sensing mechanism and modeling of the resonance-based-sensing performance

It is known that for dielectric-oxide-gated FET-based sensors, the capacitance of the oxide layer is influenced by the external gate voltage and modifies the channel conductivity by creating an opposite charge in the channel through relation Equation 3.1.[161]

$$I_{ds}=\mu C_{ox}\frac{W}{L}\left[\left(V_{gs}-V_{th}\right)V_{ds}-\frac{V_{ds}^2}{2}\right] \quad (3.1)$$

Where, I_{ds} is the drain−source current, and V_{gs}, V_{ds}, and V_{th} are the gate voltage, drain-source voltage, and threshold voltage, respectively. μ, C_{ox}, W and L are the linear mobility, gate oxide

capacitance, and the width and the length of the transistor channel, respectively. Thus, the dielectric constant of the oxide layer and its thickness control the effective capacitance of the passivation layer and influence the current in the channel. It was reported in literature that electric double-layer capacitance (EDL) can be formed in deposited aluminium oxide and in the graphene channel.[162, 205] The charge transfer across the rGO−Al_2O_3 interface creates the interface layer (C_S) which is associated with trap, and diffused positive charges from the channel are further diffused through the gate oxide layer form diffusion capacitance (C_D). Here, C_S and C_D capacitors are connected in series, and the gate capacitance ($C_{OX} \sim C_2$) can be expressed as,

$$C_2 = C_S.C_D/(C_S+C_D). \quad (3.2)$$

Fig. 3.7a shows the schematic of the equivalent circuit of the proposed model. Because the signal is applied at a coplanar configuration with source−drain, the capacitive effect mainly comes from charge-trapping phenomena at the rGO−Al_2O_3 interface, as discussed before. When the sensor is exposed to the buffer, the sensing environment is switched to an aqueous environment with a dielectric constant (~80) much larger than that of air (~1). This influences the gate capacitance of the sensor under testing and might be the reason for the increased capacitance.[206] This modified capacitance (C_2) is then coupled with gate-voltage-induced modified channel transresistance (R_2) by forming a different time constant (τ_2). The contact resistance−capacitance forms a separate time constant (τ_1). Because of the presence of two time constants, two separate semicircles in the Nyquist plot and two separate peaks in the phase angle versus frequency plots are observed for the buffer solutions. When various Ebola-glycoprotein solutions (diluted in buffer) of different concentrations are injected systematically, the specific binding of the immobilized antibody probe and the Ebola antigen creates a localized electrostatic field from the top-gate oxide layer. As found

from the literature, KZ52 human antibody can interact with Ebola GP through its two subunits (GP1 and GP2).[200] Using the protein sequence, the calculated isoelectric points of these subunits from the literature were found to be 6.26 and 5.25, respectively.[207] However, during the GP−antibody interaction, it is reported that most of the GP surface, buried by KZ52, belongs to GP2;[200] therefore, it is presumed that the charge states of other subunits can be an important factor for creating the field. The estimated isoelectric points of other subunits of Ebola GP can vary from 5 to 12. When compared with the pH of the buffer (~7) it is hard to estimate the overall charge distribution of the protein; however, because of the presence of many amino acid groups in the protein structure, a net-positive electric field can appear across the sensor surface as a gating effect and increases the channel resistance (R_2) by inducing the electronic charge in the *p*-type rGO channel. Thus, the increased top-gate potential due to this specific antigen−antibody binding modifies the time constant ($\tau_2 = R_2C_2$) which is faced by the incoming periodic signal when measured for a higher Ebola-GP concentration, resulting in a relative change in the characteristic frequency ($f_c = 1/2\pi\tau_2$). The systematic decrease in contact resistance at metal−rGO is related to the gated Schottky behavior that is caused by transition from thermionic to field emission (tunneling) because of the increase in the top-gate field.[161] As the antibody in the probe is not specific to mismatching proteins (e.g., IgG and ferritin), no specific-binding phenomena occurred. Because of absence of field, the negligible change for θ_{max} and f_i^l confirms that the sensors do not experience interference.

In the phase spectrum, the observed resonance peaks at low- and high-frequency regions signify characteristic emission frequencies of the surface trap level from channel−oxide- and channel−source- and drain-access regions. As mentioned before, when the carriers are injected

through the source−drain, the carriers are trapped across the multiple defect (trap) sites at the channel−oxide interface and again emitted back to the channel. This trapping and release have some distribution of time constants that depends on the distance from the channel. Because of ac voltage perturbation, the mentioned trapping−release time of the carrier is slower as compared with that of the high-frequency impedance measurement, resulting in a capacitive effect. This may eventually create the observed phase lag between voltage and current through the interface capacitive influence. Fig. 3.7b demonstrates typical cases for a channel−oxide trapping mechanism at different ac frequencies and their effect on modulating the phase shift. Thus, the measured phase angle is close to zero at a low frequency and systematically increases when the frequency increases until resonance occurs. At higher frequencies (beyond resonance), it is probably so fast that the device does not feel any capacitance by minimizing the trapping, and the phase angle starts to reduce again. For the same reason, the second resonance peak appears because of different relaxation processes or time constants with the source−drain-contact influence that arises from trapped charge at the channel−source- or drain-access region.[161] This relationship between resonance frequencies and resistance parameters has been investigated to make a generalized equation for a resonance-shift mechanism. Fig. 3.8 shows the schematic of the equivalent circuit model used for the calculation of the inflection-resonance-frequency position for (i) higher and (ii) lower frequencies, respectively. For the first case, the total impedance and phase angle can be estimated as

$$Z = \frac{R_3\left(1+\omega^2 C_1^2 R_1^2\right)+R_1-j\omega C_1 R_1^2}{1+\omega^2 C_1^2 R_1^2} \tag{3.3}$$

$$\theta = tan^{-1}\left[\frac{\omega C_1 R_1^2}{R_3\left(1+\omega^2 C_1^2 R_1^2\right)+R_1}\right] \tag{3.4}$$

The maximum phase angle (or resonance) occurs when $\frac{d\theta}{d\omega} = 0$. Then the inflection-resonance frequency ($\omega_{\mathrm{i}}^{h} = 2\pi f_{\mathrm{i}}^{h}$) at θ_{max} for the high-frequency region can be estimated as

$$\omega_i^h = \frac{1}{R_1 C_1} \sqrt{1 + \frac{R_1}{R_3}} \tag{3.5}$$

Similarly, by adopting the second circuit schematic of Fig. 3.8 (ii), the resonance frequency ($\omega_{\mathrm{i}}^{l} = 2\pi f_{\mathrm{i}}^{l}$) at θ_{max} for the low-frequency region can be estimated as,

$$\omega_i^l = \frac{1}{R_2 C_2} \sqrt{1 + \frac{R_2}{R_1 + R_3}} \tag{3.6}$$

Here, R_1, R_2, and R_3 are the contact resistance, channel resistance, and external resistance (which comes from external measurement wires and cables), respectively. To verify the relevance of the low- and high-frequency-resonance positions with measured circuit parameters, a plot of the phase angles versus the frequency for inflection-frequency-resonance positions was simulated using the estimated circuit parameters and equivalent circuit model (Fig. 3.8i,ii). Typical simulated profiles for inflection-resonance frequencies at low and high frequencies for buffer (0 mg/L) and 0.001 mg/L Ebola GP are shown in Fig. 3.9. The superposition of these two resonance contributions with the respective peak positions at low and high frequencies follows the same trend as the experimental resonance-peak position. From the fitting, it is evident that the high-frequency-resonance position is more sensitive (~36−160%, Fig. 3.10) than the low-frequency-resonance position (~17−40%). When compared in terms of resistance, both resonance mechanisms showed much higher sensitivity values than a conventional resistance-based measurement. In Fig. 3.11, a comparison is shown for a typical 0.001 mg/L Ebola-GP concentration. It is evident that the response directions for R_1 and R_2 are opposite to each other. Hence, the total resistance change is affected by a compensative effect. Whereas for resonance, the contributing circuit elements with

both high frequency and low frequency are not related by a simple addition but rather in a much more complex way. The resonance shift equations can be simplified as,

$$\omega_i^h = \sqrt{\frac{1}{C_1^2 \quad R_1^2} + \frac{1}{C_1^2 R_1 R_3}} \tag{3.7}$$

$$\omega_i^l = \sqrt{\frac{1}{C_2^2 \quad R_2^2} + \frac{1}{C_2^2 R_2 (R_1 + R_3)}} \tag{3.8}$$

From Equation 3.7 for high frequency, both two terms of $1/C_1^2 \quad R_1^2$ and $1/C_1^2 R_1 R_3$ increase as R_1 decreases due to GP addition (Fig. 3.12a,b). This results in a very large shift in frequency indicated in Fig. 3.10. The Equation 3.8 for low frequency part contains competitive circuit elements (R_1 decreases and R_2 increases). The first term ($1/ C_1^2 \quad R_2^2$) decreases and second term $[1/(C_2^2 R_2 (R_1 + R_3))]$ increases (Fig. 3.12c,d). The second term in Equation 3.8 is two orders of magnitude higher than the first term (Fig. 3.12c,d) and dominantly controls the positive frequency shift. Due to these reasons, the high frequency shift is more sensitive than low frequency one. So, it is likely that the high-frequency position is more sensitive than the low-frequency one because of the absence of the competitive circuit term. However, the low-frequency-resonance-peak position is so prominent and the high-frequency peak is suppressed in the superimposed spectrum. Therefore, the low-frequency-resonance peak is easier to be used to estimate the resonance shift.

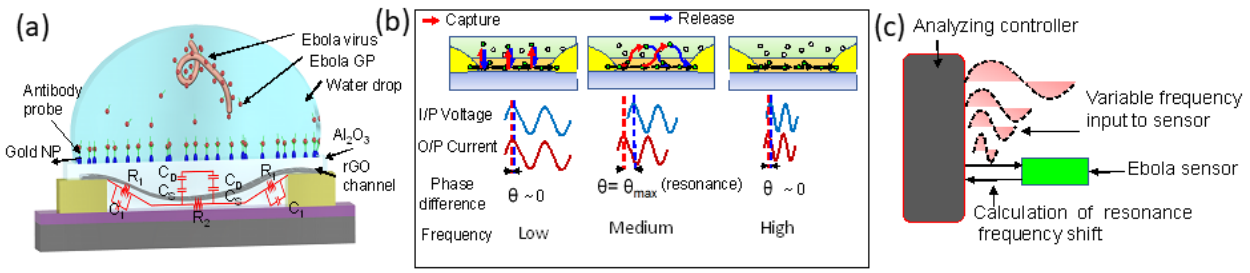

Fig. 3.7 (a) Equivalent circuit of the sensing platform. (b) Schematic model for phase-shift relation with charge capture−release at dielectric−channel interfaces for low, high, and very high frequencies. (c) Electronic-circuit model of resonance-frequency-based Ebola-GP detection.

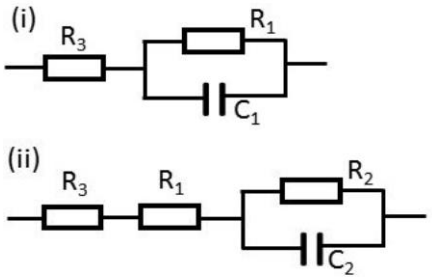

Fig. 3.8 The circuits used for calculating phase angle as a function of frequency to evaluate (i) high and (ii) low frequency inflection resonance.

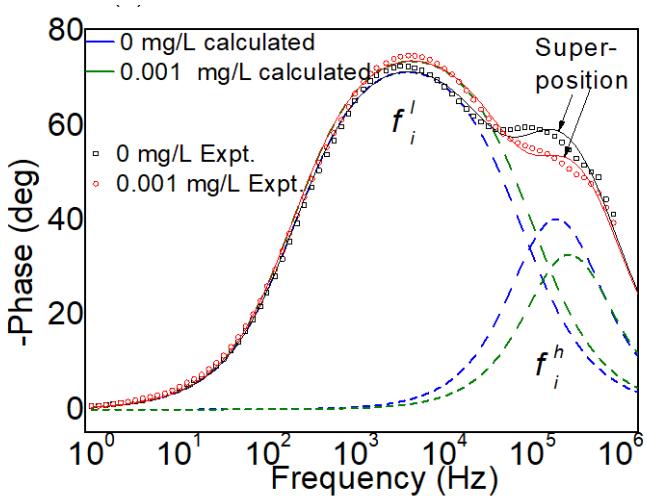

Fig. 3.9 Plot of calculated phase angle at low (f_i^l)- and high (f_i^h)-frequency-resonance (dotted line) estimated from *RC* circuit modelling to compare with experimental data (point) for buffer (0 mg/L) and Ebola-GP (0.001 mg/L). The superposition of these two components are also shown (solid line).

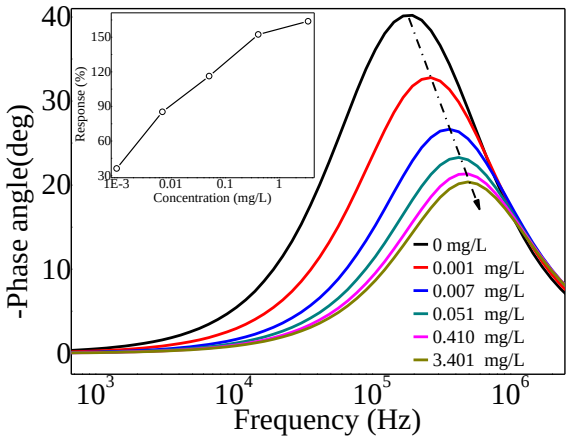

Fig. 3.10 The extracted high-frequency-resonance position (f_i^h) from calculated circuit elements. The dashed line shows the shift in resonance-frequency position during the Ebola-GP addition. The calculated sensitivity is shown in the inset.

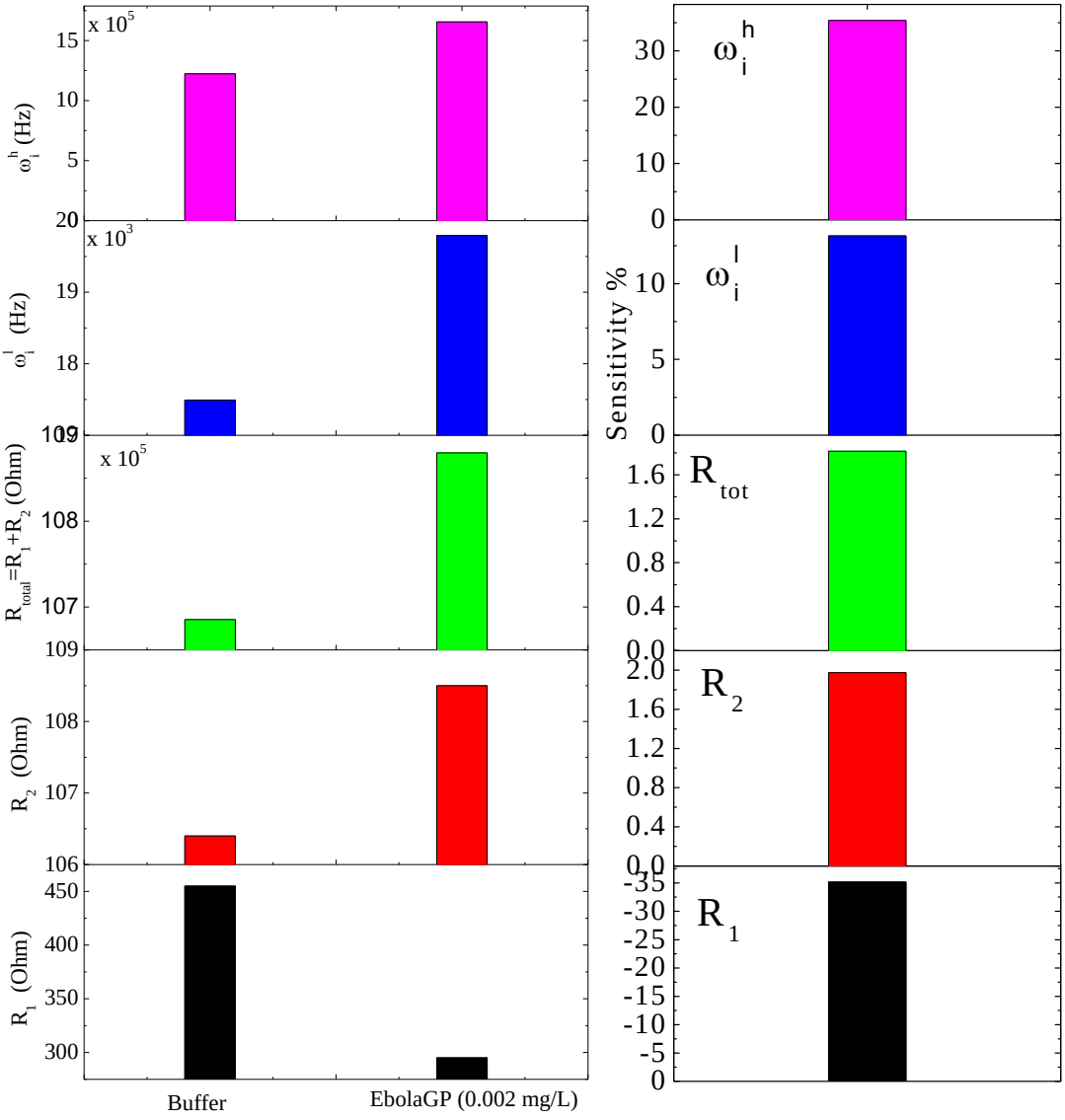

Fig. 3.11 The comparison of calculated sensitivity from contact resistance (R_1), channel resistance (R_2), total resistance change (R_{tot}) with low and high inflection-resonance-frequency (ω_i^l and ω_i^h) shifting for 0.001 mg/L Ebola-GP sensing. The resistance changes of channel and contact are opposite to each other. This creates a subtractive effect, and thus, decreases the sensitivity from total resistance. However, for the resonance, the frequency shifts are complex due to the influence of a variety of circuit elements as found in Equation 3.5 and 3.6.

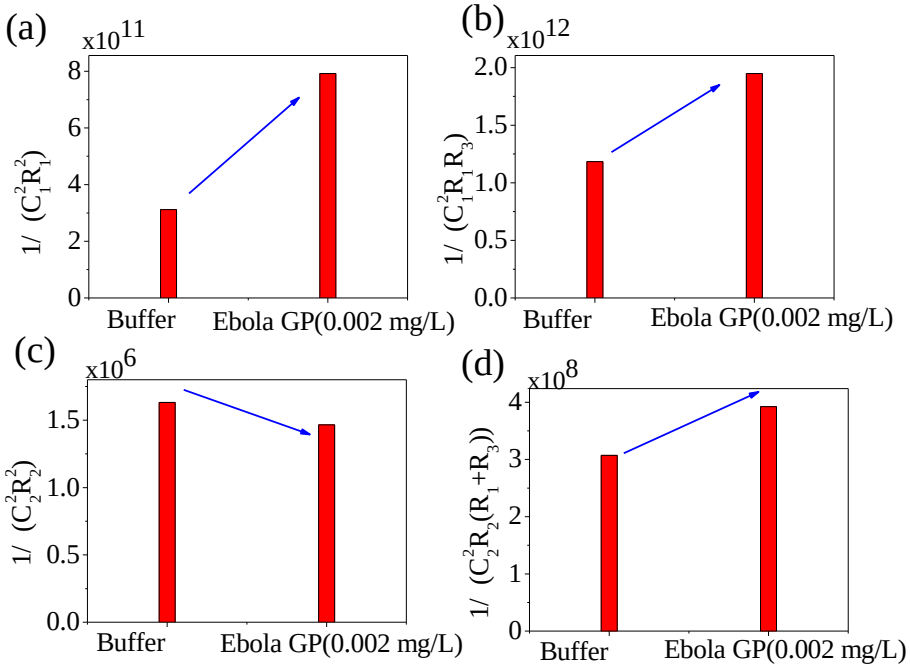

Fig. 3.12 The individual contributing terms from resonance-frequency equations (Equation 3.7 and 3.8) are plotted for high frequency (a-b) and low frequency (c-d).

In Table 3.2, comparison of Ebola-sensing performance has been made between the current resonance technique and various literature reports and commercial products. Considering these results, a micro-ac-measurement-system could be developed for point-of-care detection using advanced microcontrollers and high-speed ADCs (Fig. 3.7c). Using a closely spaced frequency interval, these mechanisms calculate the change in resonance frequency in a confined frequency range of interest, one that excludes the complex fitting of the entire frequency-measurement spectra as required for evaluating contact or channel impedance. Also, by tuning the resistance parameters through varying the fabrication process, it might be possible to separate the prominence

of the high-frequency-resonance-peak position, which seems more sensitive. Therefore, this could be an interesting direction for future work for FET-biosensor research.

Table 3.2 Comparison of the current resonance-based Ebola-GP detection with various literature reports (FET resistance and chromatography based) and commercial product.

Technique	**Ebola type**	**Medium**	**Measurement time**	**LOD**	**Sensitivity**	**Ref.**
Chromatography (desktop, lab)	Ebola (GP)	Serum	30 min	100 ng/ml	--	[208]
Chromatography (desktop, lab)	Ebola (GP)	Serum	--	150 ng/ml	--	[209]
ReEBOV™ Antigen Kit (WHO) (desktop, lab)	(EBOV) VP40 antigen	Blood, Serum	15 min	625 ng/ml	--	[210]
FET (Resistance) (point-of-detect)	Ebola (GP)	PBS, Serum	75-100 s	1 ng/ml	3 %	[204]
Interferometric reflectance imaging sensor	Pseudotyped Ebola virus	Blood, serum	Several hours	5×10^3 pfu/ml	--	[170]
Opto-microfluidic system	Ebola virus	De-ionized Water	10 min	0.2 pfu/ml	--	[211]
FET (Resonance) (point-of -detect)	Ebola (GP)	PBS	30-40 s	1 ng/ml	17% (low freq. resonance) 36% (High freq. resonance)	This work

3.4 Summary and conclusions

Through a specific antigen−antibody biorecognition process, a high-performance, rapid, electronic-resonance-frequency-modulation-based, dielectric-gated rGO bioelectronic FET platform was demonstrated for Ebola detection. With good selectivity, the maximum calculated sensitivity was found for the inflection-resonance frequency from the phase spectrum, as compared with those from other electronic parameters. A carrier-charge-injection−trapping−release−relaxation process at channel−oxide and channel−electrode interfaces has been utilized to explain the phase shift. The measured impedance spectra were modeled through a pair of *RC* circuits, adopting the contributions from channel and contact impedance to understand the sensing mechanism for correlating resonance-shift equations. In this regard, the use of advanced microcontrollers to measure these values within a specific narrow frequency range in real-time computation was proposed. It is believed that this resonance-frequency-based strategy with a dielectric, gated GFET system can not only be used for POC diagnosis of Ebola glycoprotein, but it can also be a better alternative measurement platform for FET-biosensor and -bioelectronics research for military surveillance and biosafety issues in healthcare.

CHAPTER 4 FIELD-EFFECT TRANSISTOR BASED ON PERCOLATION NETWORK OF REDUCED GRAPHENE OXIDE FOR REAL-TIME PPB-LEVEL DETECTION OF LEAD IONS IN WATER

4.1 Introduction

Heavy metal (e.g., Pb, Hg, As, Cd and Cu,) ion contaminants have become a major concern for drinking water safety. Among them, the widespread lead ion (Pb^{2+}) is one of the most hazardous heavy metals due to its serious damage on human neurological, reproductive, and developmental systems, especially in children.[108] Therefore, it is very important to monitor the lead ion level in water. The conventional analytical techniques including atomic absorption spectrometry (AAS) and inductively coupled plasma mass spectrometry (ICP-MS) are relatively costly and time-consuming, due to the requirements of complicated sample pretreatments, advanced equipment and professional operators.[212]

Numerous efforts have been made to develop other sensing systems to understand the level of lead contamination through different detection techniques, including colorimetry,[45, 213] fluorescence,[214] surface plasmon resonance,[215] surface-enhanced Raman scattering,[216] electrochemical[212] and field-effect transistor (FET) methods[198, 217]. Among these various techniques, FET has attracted great attention because of its label-free detection, fast response, simple construction, potential miniaturization, and exemption from additional sophisticated optical or electrochemical analyzers.[46, 198, 218, 219] 2D graphene-based FETs show impressive sensing performance when used as a sensing platform because this atomic-thin 2D material is extremely sensitive to local

environmental perturbations, owing to its large detection area, superior electronic properties and low intrinsic electrical noises.[148, 220, 221] Our group has demonstrated the great potential of using single-layer or few-layer reduced graphene oxide (rGO) flakes as the sensing channel in an FET for lead ion monitoring.[143, 198] However, to accommodate the relatively small size of GO sheets, advanced photolithographic procedures involving expensive cleanroom equipment are needed for the electrode fabrication. He et al. reported the fabrication of long, thin and electrically-conducting continuous rGO film on various substrates by using a micromolding-in-capillary method, and demonstrated the sensing ability of the resulting rGO strips.[222, 223] It is a low cost and scalable approach for preparation of rGO channels because the costly photolithography can be avoided for the electrode construction. Nevertheless, the preparation is still a trial-and-error approach. Developing a percolation theory analysis will be very helpful to direct the construction of GO percolation network and even expand the approach to other 2D material continuum connections.

Here we demonstrate an rGO percolation network based FET sensor through the facile micromolding-in-capillary method. The percolation theory analysis demonstrates that a percolation threshold of GO concentration for a continuous GO film pattern converges at a predicted value (~ 0.331 mg/mL for our design). The obtained rGO sensing channel can be millimeter-long, formed by 1-4 layers of rGO flakes, and exhibits p-type semiconducting properties with an adequate on/off current ratio for sensing applications. The anchored probe of L-Glutathione reduced (GSH), which chelates with lead ions, endows the sensor with real-time, selective recognition of Pb^{2+} at the ppb level in water.

4.2 Experimental methods

4.2.1 Chemicals

Single layer graphene oxide (GO) water dispersion (5 mg/mL) with a lateral dimension of 0.6 μm and a carbon content ~ 46 wt.% was purchased from ANGSTRON MATERIALS. 3-aminopropyltrithoxysilane (APTES), L-Glutathione reduced (GSH) and metal chloride or nitrate salts used to prepare metal ion solutions with ultrapure water (pH ~ 7.0) were all purchased from Sigma-Aldrich. The inductively-coupled plasma (ICP) analysis was used to quantify the prepared metal ion solutions with an error less than 5%.

4.2.2 Sensor fabrication

Device Fabrication. As the substrate, the silicon wafer with a 285 nm SiO_2 insulation layer on the surface was first modified with APTES, in order to obtain a hydrophilic surface and enhance the adsorption of GO flakes. The continuous rGO thin film patterns were prepared by the micromolding-in-capillary (MIMC) method[222, 224] with the GO suspension, followed by a thermal reduction process.[198] First, a PDMS (Sylgard 184, Dow company) stamp was prepared with a negative silicon mask (line patterns with 15 μm width and 5 μm height). The prepared PDMS stamp was cut carefully at both ends to generate an open channel. The cut PDMS stamp was treated with O_2 plasma to obtain a hydrophilic surface before being mounted on the APTES-modified Si substrate to form a compact contact. Then, a drop of GO aqueous dispersion (1.7 mg/mL) was dropped at one end of the PDMS channel. After dried up, the PDMS stamp was peeled off carefully, and the GO pattern was formed on the substrate. After a quick thermal reduction (@ 400 ^oC for 10 min in Ar), the rGO thin film pattern can be obtained. Silver conducting paint was used to prepare

the source and drain electrodes at both ends of the rGO film pattern. A subsequent Atomic Layer Deposition (ALD, Savannah S 100) process was used to deposit 3 nm Al_2O_3 on the device surface. Uniformly and densely distributed Au nanoparticles (Au NPs) as the anchors for GSH probes were sputtered on the Al_2O_3 by using a RF (60 Hz) Emitech K550x sputtering apparatus equipped with a pure Au target. Finally, the Au NPs were functionalized with GSH probes through incubation in a GSH aqueous solution (50 mg/mL) at room temperature for 1 h, and further rinsed with ultrapure water to remove extra GSH. After drying with a stream of nitrogen gas, the sensor can be used for heavy metal ion detection. The electrical properties and sensing performance were characterized by a Keithley 4200 semiconductor characterization system. 3-4 sensors were repeated for the tests, which showed similar results, to ensure the repeatability.

4.3 Results and discussion

As the sensing channel, the continuous rGO percolation network was achieved by the micromolding-in-capillary (MIMC) method with a GO aqueous dispersion, followed with quick thermal reduction. Fig. 4.1 shows a schematic of the sensor fabrication process. Before micropatterning, the silicon substrate was first modified with 3-aminopropyltrithoxysilane (APTES) to achieve a hydrophilic, positively charged surface, which can both drive the capillary behavior and ensure the uniform deposition of negatively charged GO flakes in the channel region.[222, 223] After GO suspension being dropped on the one open end of the mounted PDMS stamp, GO suspension can fill the channel space between the stamp and the substrate, and a long continuous GO micropattern along the stamp formed after drying. Without APTES surface modification, GO flakes tend to accumulate on the two sides of the channel region, due to the hydrophilic property of PDMS stamp through O_2 plasma treatment, and thus a uniform GO

percolation network cannot form (Fig. 4.2). Fig. 4.4a shows the size distribution of the GO flakes with an average lateral size of ~ 0.6 μm. No flakes with a lateral size > 1 μm can be found, which avoids PDMS channel clogging caused by GO aggregations during the micromolding process. The highly transparent feature of the GO flakes indicates their atomic thickness. The dimensions of the GO pattern can be adjusted by the PDMS stamp. Based on the GO lateral size (~ 0.6 μm), here we used a stamp with a channel size of 15 μm width, 5 μm height and 5 mm length to facilitate the formation of continuous GO patterns.[222] First, the percolation threshold of the GO concentration (*C*) for a continuous GO film pattern was estimated based on 2D continuum models[225] with the assumptions that 1) the GO dispersion sucked into the channel region by capillarity with a volume of $L \times W \times H$ (channel region with length *L*, width *W*, and height *H*) dries on the silicon substrate to form the GO film. 2) The interactions among GO flakes can be ignored, i.e., random distribution of GO flakes. Fig. 4.3a shows the schematic of the GO percolation network in the channel region. Ideally, the number of GO flakes (*N*) needed to fully cover (i.e., equals to) the channel area in monolayer:

$$N = L \cdot W / A. \tag{4.1}$$

However, in a real 2D continuum connection within the channel region, the GO flakes do not have to fully cover the entire channel area (Fig. 4.3a) to become electrically conductive. An adjusting threshold parameter η_c (critical filling fraction) can be introduced, and thus,

$$N = \eta_c \cdot L \cdot W / A\,, \tag{4.2}$$

where, the specific value of the threshold parameter η_c depends on the shape of flakes to connect the channel region, and can be obtained from relevant literatures (e.g., Table 4.1). Because of the arbitrary shape of GO flakes, the number of GO flakes required for a percolation network is

$$N = L \cdot W \sum_i \alpha_i \frac{\eta_{c,i}}{S_i}, \tag{4.3}$$

where i, α_i, $\eta_{c,i}$ and S_i stand for the shape type of GO flakes, corresponding normalized weight of GO flakes, threshold parameter and area of individual GO flake in shape i. Thus, the required concentration (C) is

$$\mathrm{C} = \frac{\rho}{V}\sum_i N_i S_i = \frac{\rho}{L \cdot W \cdot H} L \cdot W \sum_i \alpha_i \eta_{c,i} = \frac{\rho}{H}\sum_i \alpha_i \eta_{c,i}, \tag{4.4}$$

in which ρ is the areal density of GO (ρ is a constant for a specific GO). Equation (4.4) reveals that the exact value of C requires the approximation of GO shapes (i) and its relative weight (α_i). The sheet density of GO was evaluated from the graphene molecular structure as shown in Fig. 4.3b. The C=C distance is about 0.142 nm,[226] and the mass of C atom is $1.994 * 10^{-20}$ mg. In each unit cell, there are two C atoms, and the area of unit cell is calculated to be $5.239 * 10^{-16}$ cm^{-2}. Then, areal density of graphene is

$$\rho_G = \frac{mass}{area} = \frac{2 \times 1.994 \times 10^{-20}\, mg}{5.239 \times 10^{-16}\, cm^2} = 7.612 \times 10^{-5} \frac{mg}{cm^2}. \tag{4.5}$$

The GO used here has a C content ~ 46 wt.%; thus, the areal density of GO (ρ) is about

$$\rho = \frac{\rho_G}{0.46} = 1.655 \times 10^{-4} \frac{mg}{cm^2}. \tag{4.6}$$

The coefficient $\frac{\rho}{H}$ in Equation (4.4) only depends on the height H of the channel region and is $0.331 \frac{mg}{cm^3}$ for a height of 5 μm in our experiment. Equation (4.4) further elucidates that the GO mass concentration for percolation network C is independent of the absolute size of GO flakes but depends on their shapes; in other words, shape dominates in forming the 2D continuum connection. To evaluate C, we modeled the GO flakes with regular shapes of disks, squares, ellipses and rectangles (Table 4.1), and estimated the relative weight (α_i); finally, a C distribution according to

the η_c can be obtained (Fig. 4.3c). Practically, the shape of GO flakes is irregular with random distribution. Assuming with equal weight distribution, the required mass concentration of GO (C) is ~ 0.28 mg/mL. In our experiment, the aspect ratios ($\mathcal{E}$) of GO flakes are actually dominant within 1-2 (Figure 4.4a) and $\eta_{c,i}$ approaches 1, so C is approximated as

$$\mathrm{C} = \frac{\rho}{H}\sum_i \alpha_i \, \eta_{c,i} \approx \frac{\rho}{H} = 0.331 \, \frac{mg}{cm^3} \, . \tag{4.7}$$

The percolation analysis above clarifies that for a specific GO, ρ is known, and the required mass concentration of GO flakes (C) for a percolation network depends on the height of the channel region and the shapes of GO flakes. Moreover, despite the irregular shapes and random distribution of GO flakes, C converges at a narrow range, and even can be determined for a small aspect ratios ($\mathcal{E}$) of GO. To the best of our knowledge, this is the first example of applying percolation theory analysis for a continuum network construction with 2D nanomaterials.

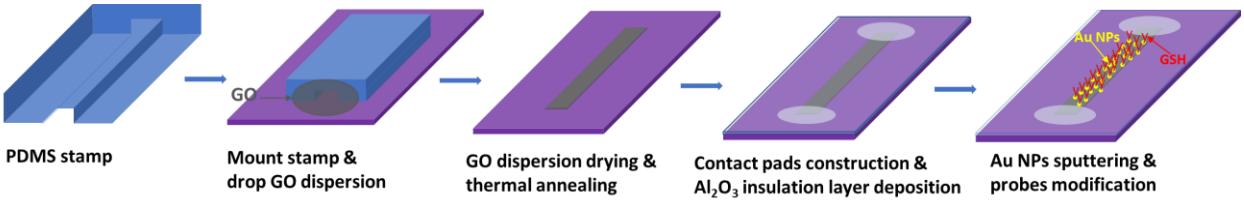

Fig. 4.1 Schematic illustration of the water sensor fabrication process using the MIMC method.

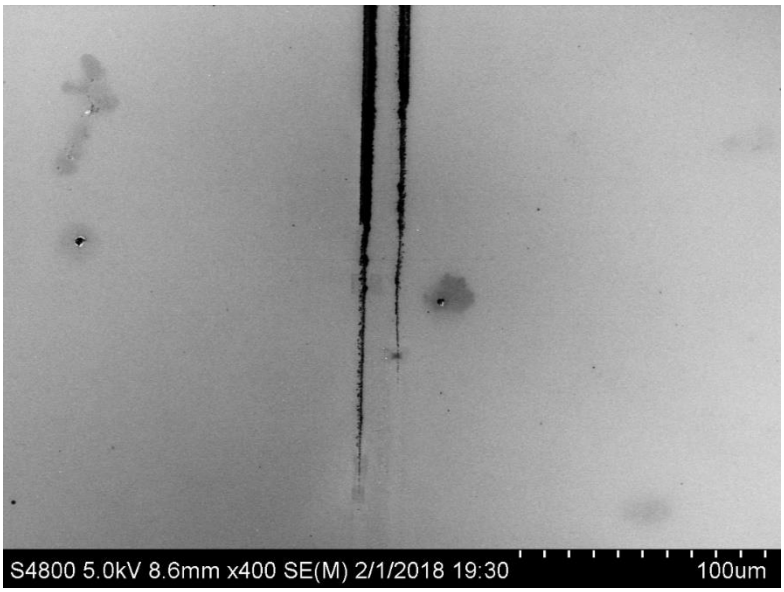

Fig. 4.2 SEM image of GO accumulation on silicon substrate without APTES modification after stamp patterning.

Table 4.1 Different modeling shapes and their corresponding critical filling fraction η_c.[225, 227, 228]

Shape	**Disks**	**Squares**	**Ellipses**	**Rectangles**
Area	$S = \frac{\pi D^2}{4}$ D= diameter	$S = l^2$ l= lateral length	$S = \pi ab/4$ a=length of major axis b=length of minor axis $\epsilon = a/b$	$S = lw$ l=length w=width $\epsilon = l/w$
$\boldsymbol{\eta_c}$	1.13	0.98	1.08@ $\epsilon = 1.5$	0.95@ $\epsilon = 1.5$
			0.99@ $\epsilon = 2$	0.89@ $\epsilon = 2$
			0.82@ $\epsilon = 3$	0.78@ $\epsilon = 3$
			0.69@ $\epsilon = 4$	0.68@ $\epsilon = 4$
			0.61@ ϵ =5	0.61@ ϵ =5

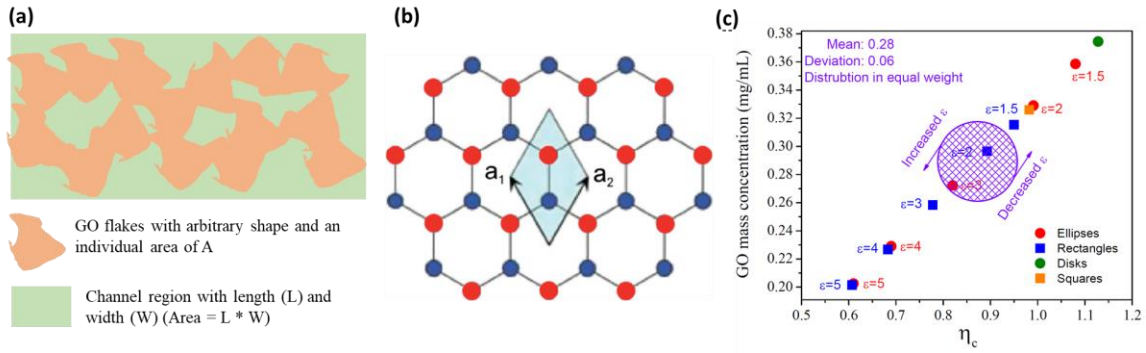

Fig. 4.3 (a) Schematic of the GO percolation network with arbitrary shapes and random distribution. (b) Molecular structure of graphene. (c) GO mass concentration (C) for percolation according to the $\eta_c$of different shapes.

The concentration of GO suspension affects the thickness of the obtained GO micropattern. Too diluted GO suspension below percolation threshold (~ 0.331 mg/mL) leads to a non-continuous network, while too high concentration causes the channel to clog (Fig. 4.5). Finally, a GO aqueous dispersion with a concentration of 1.7 mg/mL was optimized and used for micropatterning. The obtained GO pattern by using the MIMC method has a clear profile with an accurate proposed width of 15 µm (Fig. 4.4b). The GO network was constituted by the thin GO flakes connections, as shown in the inset of Fig. 4.4b. The thickness of the GO micropattern obtained by AFM measurement is ~ 1-4 nm, revealing 1-4 layers of GO flakes accumulation (Fig. 4.4c). A quick thermal annealing process was conducted to reduce the GO and improve the electrical contact among GO flakes. Because of the millimeter length of the rGO pattern, it can be observed clearly by a regular optical microscope (Fig. 4.6), and the source and drain electrodes can be easily prepared with silver paste at the two ends of the rGO pattern.

A thin Al_2O_3 insulation layer was deposited on the device by ALD to protect its electrical stability and exclude the charge transfer from analytes to the rGO sensing channel (Fig. 4.1).[198, 229] Fig. 4.4d shows the uniform isolated Au NPs in 3-5 nm which were sputtered on the Al_2O_3 layer surface as the anchors for the GSH probes. These densely deposited ultrafine Au NPs facilitate more GSH molecules modification through Au-S linkage[230, 231], which enhances the sensing performance of the device.

To investigate the conductance of the device, the drain current (I_{ds}) was measured as a function of the drain voltage (V_{ds}) ranging from -2 to 2 V. As shown in Fig. 4.4e, the obtained linear $I_{ds} - V_{ds}$ relationship presents the electrically continuous and dominated ohmic behaviors. This indicates the good electrical contacts among the accumulated rGO flakes, which is crucial to achieve comparable electrical properties with single rGO flakes.[222] The large resistance in MΩ of the device mainly results from the mm channel length (~ 5 mm) and remaining defects on the rGO sheets. The FET property of the device was characterized by measuring the drain current (I_{ds}) with the back-gate bias (applied to the back of the silicon substrate) varying from -40 to +40 V. A smooth p-type FET curve with a good on/off current ratio ~ 2 was achieved, which is similar to and comparable with our reported interdigitated single-layer rGO devices.[198, 229]

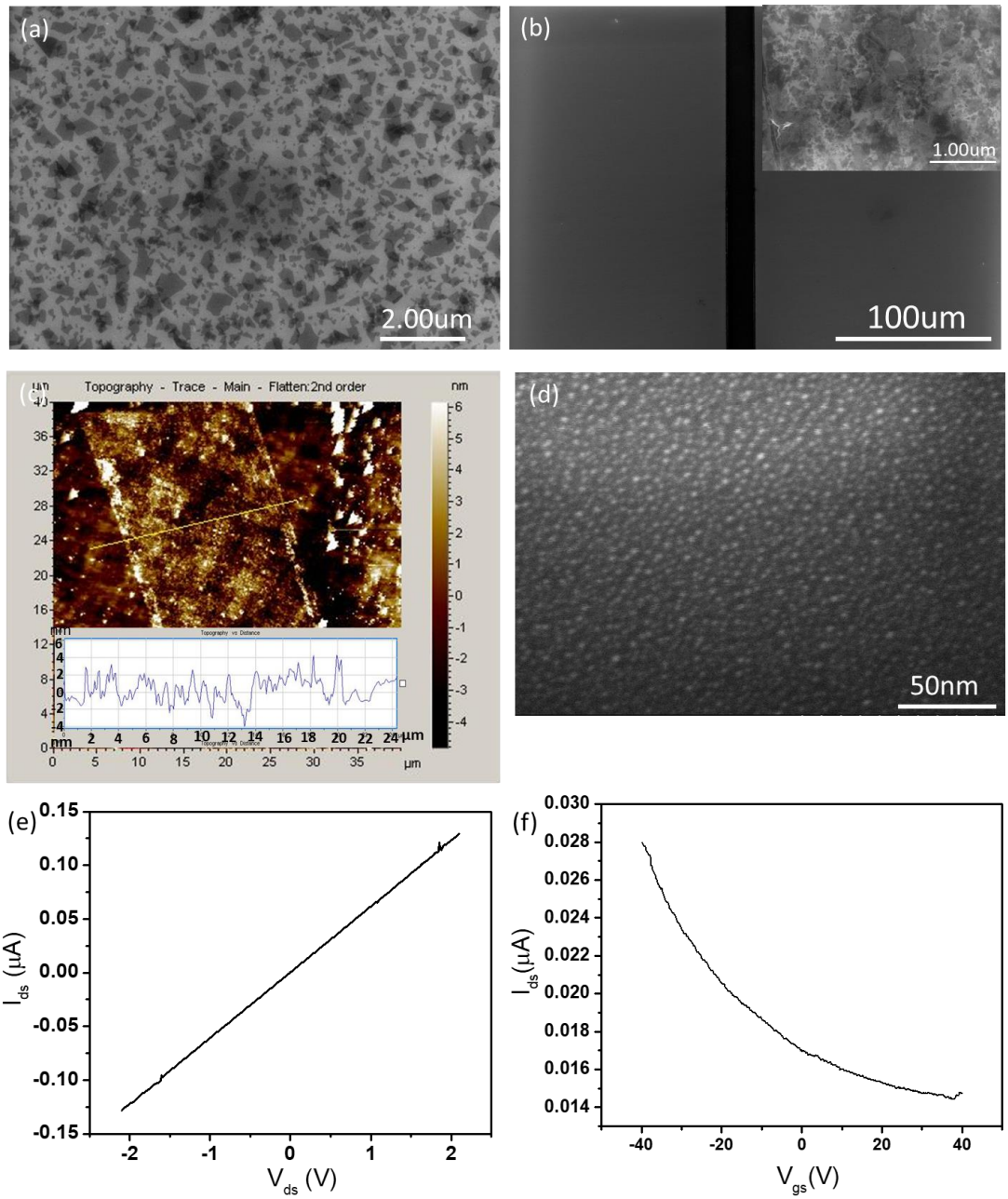

Fig. 4.4 (a) SEM image for the GO flakes size distribution. (b) SEM image of patterned GO network on the silicon substrate with a high magnification image in the inset. (c) AFM image of the GO pattern with a line scan thickness profile in the inset. (d) SEM image of the sputtered Au NPs on the Al_2O_3. (e) I_{ds}−V_{ds} characteristics of the sensor. (f) I_{ds}−V_{gs} characteristics of the sensor for V_{ds} = 0.3 V, V_{gs} = −40 to 40 V.

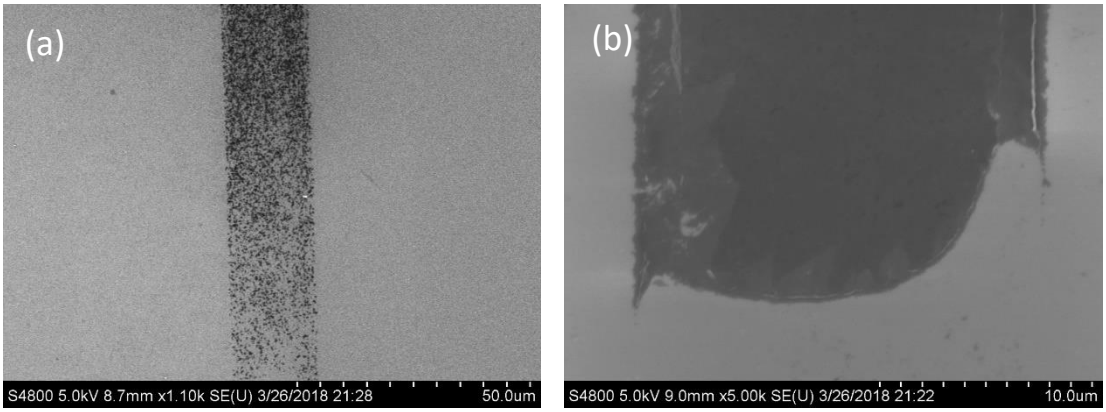

Fig. 4.5 SEM images of patterned GO with a concentration of (a) 0.2 mg/mL, and (b) 5 mg/mL.

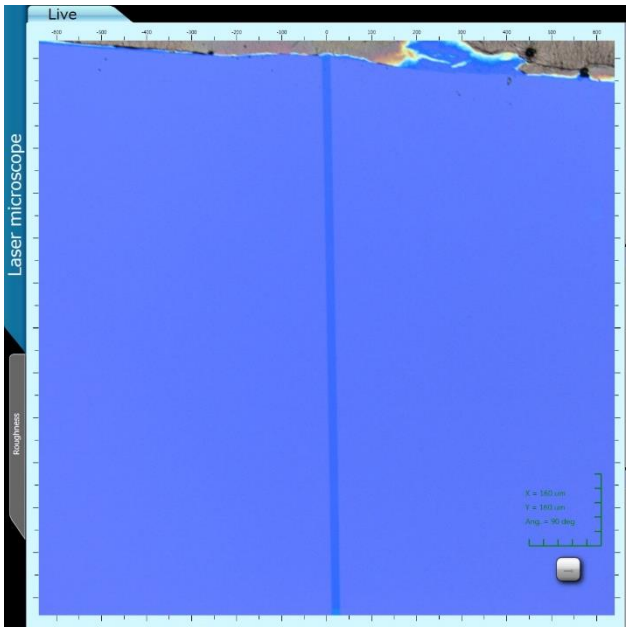

Fig. 4.6. Optical image of rGO thin film pattern on APTES modified silicon substrate.

As-fabricated sensor was applied to detect lead ions in water, in which the conductance of the sensor device (I_{ds}) was continuously monitored at a fixed V_{ds} and 0 V_{gs}, while lead ions with varying

concentrations were introduced onto the sensor surface. Fig. 4.7a shows the dynamic sensing performance to Pb^{2+} concentrations. The first drop of H_2O (constant volume of 2 µL for each dropping) was introduced onto the sensor to create a liquid test environment and to obtain a stable baseline. Our sensor shows no obvious current change to the second drop of H_2O, which helps to get rid of the volume effect in the following sensing response. Once Pb^{2+} solution was injected, the sensor responded instantly (~ 1-2 s) and stabilized in a decreasing current signal. Because of the dominated ohmic characteristic of the device (Fig. 4.4e), together with the Al_2O_3 film passivation, the Schottky barrier mechanism at the contact region and charge transfer mechanism between the analyte and rGO sensing channel can be suppressed effectively. Thus, the predominant electrostatic gating effect on the sensing channel caused by the attracted positive Pb^{2+} nearby works as the main sensing mechanism.[151, 232] This is in good agreement with the decreasing current signal I_{ds}. In this p-type depletion-mode FET device, the positive electrical field of Pb^{2+} will repulse the holes away from the gate-insulator/semiconductor interface (Al_2O_3/rGO), decreasing the charge carrier concentration within the rGO sheets, which results in a reduction of the electrical conductivity of the rGO network sensing channel. The fast response time within 2 s after adding the analyte is owing to the rapid metal ion diffusion in solution[233] and the high sensitivity of the 2D rGO sensing channel[234]. The sharp change in I_{ds} immediately after analyte injection is caused by the disturbance of adding liquid.[154] When the Pb^{2+} solutions were injected in sequence, our sensor shows a stable, step-like current decrease corresponding to the increases of Pb^{2+} concentrations, as shown in Fig. 4.7a. The Pb^{2+} concentrations as indicated in Fig. 4.7a are calculated by taking the initial two drops of H_2O into consideration to obtain the actual concentrations. The response% ($\Delta I_{ds}/I_{ds}$) shows a linear relationship with the Pb^{2+} concentrations (Fig. 4.7b). The limit of detection (LOD) calculated by using the $3\sigma/S$ approach (σ is the standard

deviation of device background signals, and S is the device sensitivity)[221] can reach 1 ppb. Since the maximum contaminant level (MCL) of lead for drinking water is 15 ppb according to the US Environmental Protection Agency, our sensor can work well around and well below this critical value.

Besides sensitivity, selectivity is another very important criterion of sensors. Several common metal ions in water were chosen to characterize the selectivity of our sensor. In the same molar concentration of 100 nM, the sensor shows much higher response to lead ions compared with other interfering ions, demonstrating its good selectivity (Fig. 4.7c). This can be attributed to the strong affinity of Pb^{2+} to GSH molecules. GSH has two free -COOH molecular arms, which can coordinate with Pb^{2+}.[45, 198, 235]

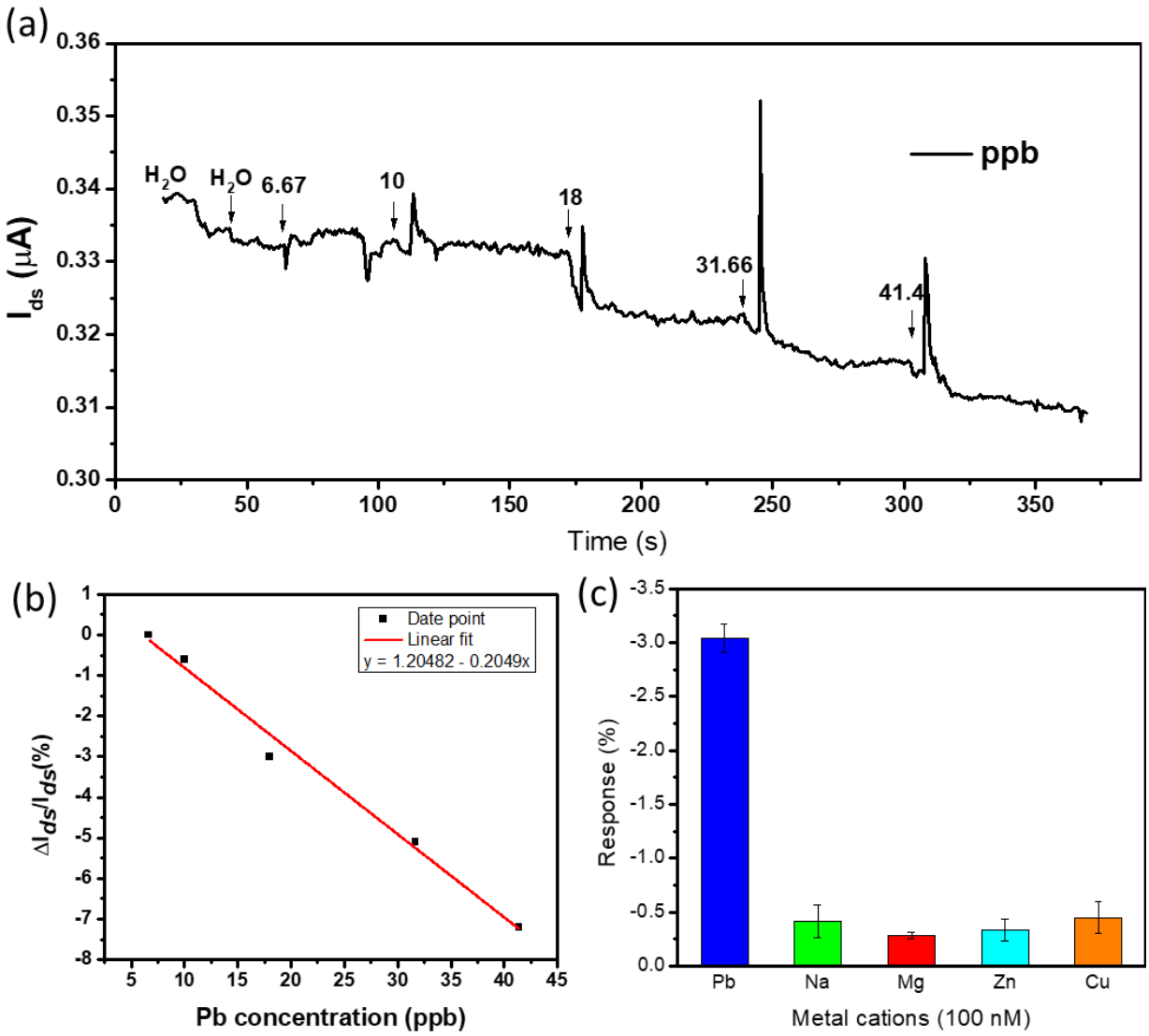

Fig. 4.7 (a) Dynamic response of the rGO FET sensor upon introduction of Pb^{2+} with varying concentrations. (b) Response% vs. Pb^{2+} concentration for calibration of the sensor. (c) Response% of the sensor to different metal ions in the same concentrations of 100 nM, corresponding to 20.7, 2.3, 2.43, 6.54 and 6.35 ppb for Pb, Na, Mg, Zn and Cu ions respectively.

4.4 Summary and conclusions

In this study, millimeter-long, ultrathin (1-4 nm), continuous rGO percolation micropatterns are prepared by using a facile, scalable micromolding-in-capillary (MIMC) method. APTES substrate modification and adequate concentration of GO dispersion are critical for quality micropattern construction. Percolation theory analysis indicates that the GO shape dominates in forming the continuum connection, and the required GO mass concentration for percolation can be estimated in spite of their arbitrary shapes. This model analysis can be expanded to construct other 2D nanomaterial percolation networks. The rGO micropattern exhibits a dominating ohmic behavior and p-type semiconducting properties with a good on/off current ratio, which is comparable with single-layer rGO devices. When the rGO micropattern was integrated into a water sensor modified with GSH probes, it shows good sensitivity (LOD ~ 1 ppb) and selectivity to Pb^{2+}. A linear relationship between the response% and the Pb^{2+} concentration can be achieved around the maximum contaminant level (MCL) of lead for drinking water (15 ppb, US EPA), which suggests the device is promising for the drinking water quality monitoring.

CHAPTER 5 FULLY INKJET-PRINTED, 2D MATERIALS-BASED FIELD-EFFECT TRANSISTOR FOR WATER SENSING (in collaboration with Northwestern University)

5.1 Introduction

2D nanomaterials attract intensive research interests in sensing applications. Their excellent electrical properties, e.g., record high conductivity of graphene and impressive semiconductor performance of transition metal dichalcogenides (TMDs), maximum sensing surface area, and mechanical robustness enable nanosensor devices with unprecedent sensitivity, robustness, and fast response. 2D material-based field-effect transistor (FET) sensors exhibit outstanding capabilities in chemical, biological, mechanical, and optical sensing.[116, 236] They have advantages in high sensitivity, simple structure, and potential for miniaturization. However, the device cost is relatively high and large-scale fabrication is still challenging due to the difficulty in accurate nanomaterial manipulation: photolithography process is usually required to pattern electrodes onto a single 2D sheet to construct the transistor device, where the ultrathin 2D flake channel are either mechanically exfoliated or grown from chemical vapor deposition (CVD).[237] Solution-processing of 2D nanosheets for printable dispersions provides an alternative for low-cost, high-throughput, and reproducible device fabrication.

Recently, electrochemical exfoliation of MoS_2 through quaternary ammonium molecules intercalation has been demonstrated to produce uniform, phase-pure, semiconducting 2H-MoS_2 at a high production volume. The fabricated thin-film transistors (TFTs) through spin-coated MoS_2 thin-film with lithographical patterning delivered a mobility of 10 $cm^2\ V^{-1}\ s^{-1}$ and a current on/off

ratio of 10^6.[238] However, printed TMD (e.g., MoS_2) TFTs usually show deteriorative charge mobility and very low on/off ratio, or can work well only under electrolytic gating conditions.[237, 239] This is mainly due to the limited gate modulation depth and difficulties to achieve ultrathin percolating networks with 2D flakes using printing techniques, such as inkjet printing, where undesired coffee-ring effect (CRE) leads to nonuniform material deposition. For example, Kim et al.[240] reported the serious on/off ratio degeneration of inkjet-printed MoS_2 TFTs compared with spin-coated ones. Researchers have adjusted the device geometry with a narrow channel length (no larger than several micrometers) close to the single-flake size to facilitate a printed flake thin film, addressing the possible film nonuniformity in a larger scale.[237, 241] However, this fabrication resolution is beyond the current capabilities of jet printing techniques including inkjet and aerosol jet printing, and undoubtedly impedes large-scale fully-printed FET device fabrication and their further practical applications.

Here, using the inkjet printing technique, robust MoS_2 semiconducting channels have been prepared with hundreds of micrometers long and a current on/off ratio up to the order of 10^3 for tested V_g ranging from -38 V to 38 V. The long channels are compatible with the inkjet printing capability for a fully printed FET device. A fully functioning water sensor has been fabricated based on the printed MoS_2 channel and graphene electrodes, and heavy metal ion sensing in water has been successfully demonstrated.

5.2 Experimental methods

5.2.1 Chemicals

Printable MoS_2 and graphene inks were prepared by Dr. Mark Hersam's group at Northwestern University. For the MoS_2 ink, a synthetic single crystal (2D Semiconductors, USA) was first electrochemically intercalated by tetraheptylammonium bromide (THAB) in acetonitrile and stabilized by polyvinylpyrrolidone (PVP; MW: 29 kDa) in isopropyl alcohol (IPA) following a protocol similar to the reported process.[238] Finally, to remove unexfoliated products, the dispersion was centrifuged in a Beckman Coulter JS-7.5 rotor at 7,500 rpm for 5 minutes. The supernatant was retained as a viable MoS_2 dispersion. To formulate an inkjet-printable ink, the MoS_2/IPA dispersion was first filtered through a 1 µm glass fiber syringe filter. The rheology of the ink was adjusted by adding 2-butanol to a final IPA : 2-butanol volume ratio of 9:1; this solvent system has been demonstrated by Hu et al.[242] to be robust for inkjet printing. The graphene ink was prepared as previously reported.[243] Metal chloride or nitrate salts used to prepare metal ion solutions with deionized (DI) water are all purchased from Sigma-Aldrich.

5.2.2 Sensor device fabrication by inkjet printing

The MoS_2-IPA/2-butanol ink was used to print an MoS_2 percolating network as the semiconducting channel, and graphene ink was used for printing conductive electrodes onto SiO_2 (300 nm)/Si wafers or polyimide substrates (#300NH from DuPont). The substrates were pre-cleaned by acetone, IPA and DI water with sonication for 10 min, respectively, prior to material deposition. Fujifilm Dimatix, DMP 2850 inkjet printer equipped with a 10 pL cartridge (Fujifilm Dimatix, DMC-11610) having a nozzle diameter of 21µm was used for the printing process. A

typical working distance between the nozzle and substrate is 1 mm. Drop spacing was optimized to be 40 μm for MoS_2 flake deposition and 30 μm for graphene flake deposition onto the substrates which are heated up to 50 ^oC. To fabricate an FET water sensor, the MoS_2 line channel was first printed followed by 4 layers of graphene electrode deposition. The MoS_2 channel length was confined to be 400 μm by the source and drain electrodes. The resulting devices were annealed at 350 ^oC for 1 h in Ar gas to remove residual additives in the inks and improve the junction contacts of the entire devices. The graphene extended gate as a sensing area was then functionalized with 1-pyrenebutyric acid through N,N-Dimethylmethanamidesolution (DMF) solution (100 mM) incubation at room temperature for 1 h to obtain the fully functioning inkjet-printed water sensor, which can be used for heavy metal ion detection. The electrical properties and sensing performance of the resulting water sensors were characterized by a Keithley 4200A-SCS semiconductor characterization system. A narrow top V_g window within ±0.5V was applied to avoid electrolysis during the sensing test.

5.3 Results and discussion

Compared with lithium intercalation and exfoliation which induces an undesired phase transition from semiconducting 2H phase to the metallic 1T phase due to massive electron injection into MoS_2 crystal,[244] quaternary ammonium molecules (i.e., THAB) exfoliation process provides a phase-pure, semiconducting 2H-MoS_2 nanosheet production in large scale.[238] The ink formulation is pivotal for inkjet printing. There are several important considerations: 1) The ink suspension should be stable without delamination during the printing period, which is necessary for a stable printing; 2) The size of suspended solid materials should be tailored within a certain size range (e.g., smaller than 1/20 of the nozzle diameter based on this study) to avoid nozzle clogging; 3)

Certain rheological properties of the ink are required to ensure stable droplet jetting under each electrical drive pulse, which is generally evaluated by the inverse Ohnesorge numbers $Z = \sqrt{\gamma\rho a}/\eta$, depending on the ink viscosity (η), surface tension (γ), and density (ρ), and the printer cartridge nozzle diameter (a). A *Z* value is expected to in the range of 1-14 for printable inks;[245] 4) A good substrate wetting of the inks, which requires the ink surface tension to be 7-10 mNm^{-1} lower than the substrate surface energy;[242] 5) Suitable fluidic properties to minimize the CRE for a uniform material deposition. To satisfy the considerations of 1) and 2), PVP-stabilized MoS_2 was processed and filtrated to ensure its stabilization and compatible size with the printer nozzle size (details in Experimental methods). To meet criteria 3), 4) and 5), the obtained PVP-stabilized MoS_2 nanosheets were formulated into printable ink using reported IPA/2-butanol (10 volume %) solvent system, which has a *Z* value of 10, and a low surface tension of ~28 mNm^{-1}, compared to that of the Si/SiO_2 ~36 mNm^{-1}.[242] More importantly, the observed Marangoni-enhanced spreading in this formulation unpins the contact line and deforms the droplet shape to efficiently suppress the CRE, supporting uniform deposition of 2D crystals.

Inside the ink, the MoS_2 nanosheets with a lateral size within 2 μm have a narrow thickness distribution, peaking at ~2 nm (3 layers), although some tiny sheets (around hundreds of nm) with 7 nm thickness can be detected (Fig. 5.1a,b). The narrow thickness distribution minimizes the variation in the energy bandgap of MoS_2 nanosheets, benefiting device performance.[246] Raman peaks of E^1_{2g} and A_{1g} at 384.9 cm^{-1} and 405.7 cm^{-1} indicate the few-layer features of exfoliated MoS_2 nanosheets (Fig. 5.1c),[247] in agreement with the AFM results.

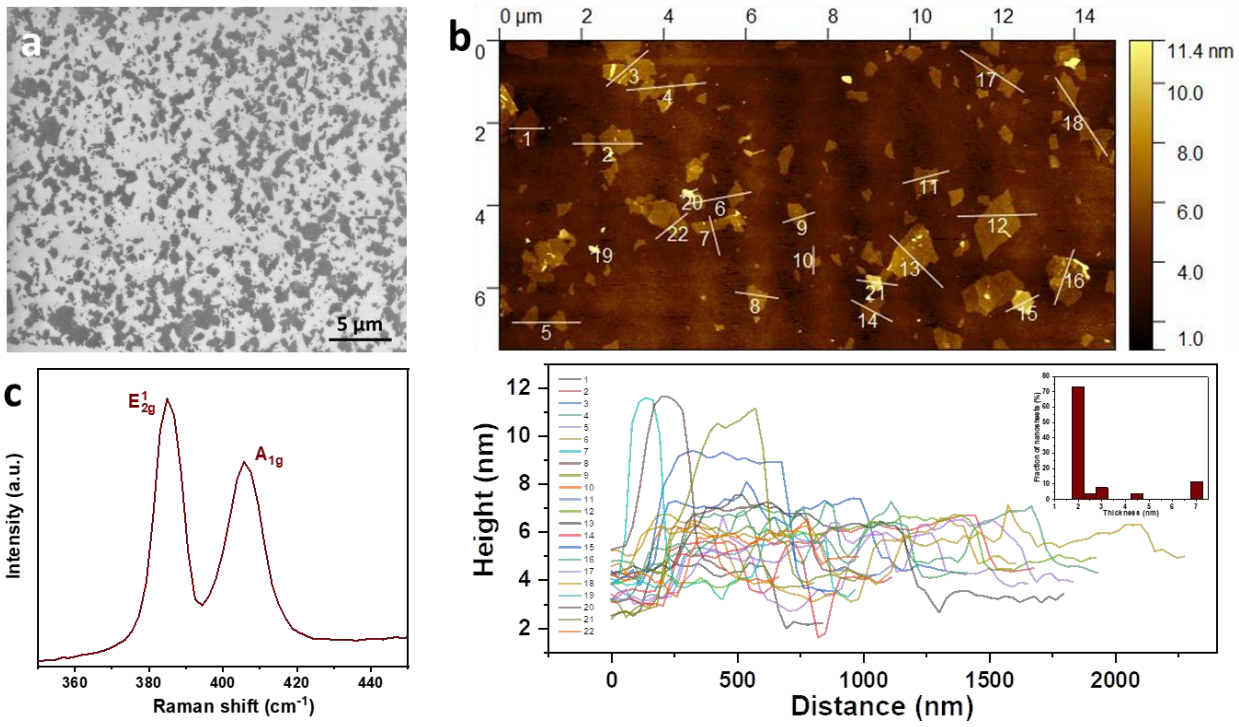

Fig. 5.1 a) SEM, b) AFM profile and c) Raman spectrum of THAB exfoliated MoS_2 nanosheets.

The diameter of individual dots deposited onto the pre-cleaned silicon wafer (with 300 nm SiO_2 on the top as the dielectric layer) using a 10 pL cartridge is about 55 µm, and a drop spacing of 40 µm was optimized to print MoS_2 lines, showing uniform edges (Fig. 5.2a,d). Channel patterns containing 5 parallel lines were first printed for electrical characterization. A percolating network can form starting with 2 printing passes (i.e., 2 layers of ink deposition) but without stable transfer curve outputs due to the very high resistance on the order of 10^{10} Ω; while a mild on/off ratio < 2 (back-gate V_g from -38 V to 38 V) was achieved with 4 printing passes. The current on/off ratio is much lower than that of the single MoS_2 nanosheet (as high as 1×10^8)[64] which could be attributed to the rapid film thickness increase during multi-line printing (i.e., overlapping deposition: the darker regions in Fig. 5.2a). Different annealing temperatures were applied for the thermal

treatment on the printed MoS_2 channels, suggesting that 350 ^oC could improve the current on/off ratio compared with lower temperatures (Fig. 5.2b). A higher annealing temperature helps reduce the unintentional impurity doping such as carbon from the residual PVP stabilization agent, which lowers the electron concentration and shifts the threshold voltage to positive direction.[238] This also coincides with the thermal decomposition of PVP starting at ~350 ^oC.[241]

In order to obtain percolating networks as thin as possible, single lines with various printing passes were then investigated. The AFM image on the edge of the single-pass printing pattern in the inset of Fig. 5.2c clearly indicates that the CRE as a major challenge in inkjet printing still could not be removed completely; therefore, a percolating nanosheet network will form on the edge of printed lines first instead of in the center. The edge thickness increases very rapidly with the printing passes, starting from ~3.8 nm for 1 printing pass to ~12 nm for 8 printing passes as shown in Fig. 5.2c. Percolating networks can be prepared from 4 printing passes with an edge thickness ~7 nm, which increases to ~10 nm for 6 printing passes (Fig. 5.2 d,e). As expected, the current on/off ratio decreases with the increase of printing passes, i.e., the percolating network thickness, from initial ~10 for 4 printing passes to ~2 for 8 printing passes (Fig. 5.2 f), because the thicker film favors a higher off current. However, thinner channels with higher on/off ratios have a larger variation, which can be understood that it approaches the percolation threshold but the network is not fully developed. The semiconducting channel printed by 6 printing passes with an on/off ratio around 6 is chosen for further FET water sensor fabrication, as a trade-off between semiconducting performance, i.e., on/off ratio, and device uniformity. A typical transfer curve of 6 passes printed channel is shown in Fig. 5.2g, exhibiting obvious n-type semiconducting output. It is also interesting to observe a much higher on/off ratio on the order of 10^3 when a larger working distance

between the nozzle and the substrate was used, which can amplify the effect of possible trajectory shifting of jetted ink droplets during multi-pass printing, i.e., a slight pattern line drifting, benefitting a thinner material deposition (Fig. 5.2h). This verifies the importance of a thin network for an adequate on/off ratio, and also implies the potential for a higher on/off ratio value if the ink and the printing conditions could be optimized further. To the best of our knowledge, this is so far the highest current on/off ratio value achieved by jet printing of MoS_2 nanosheets.

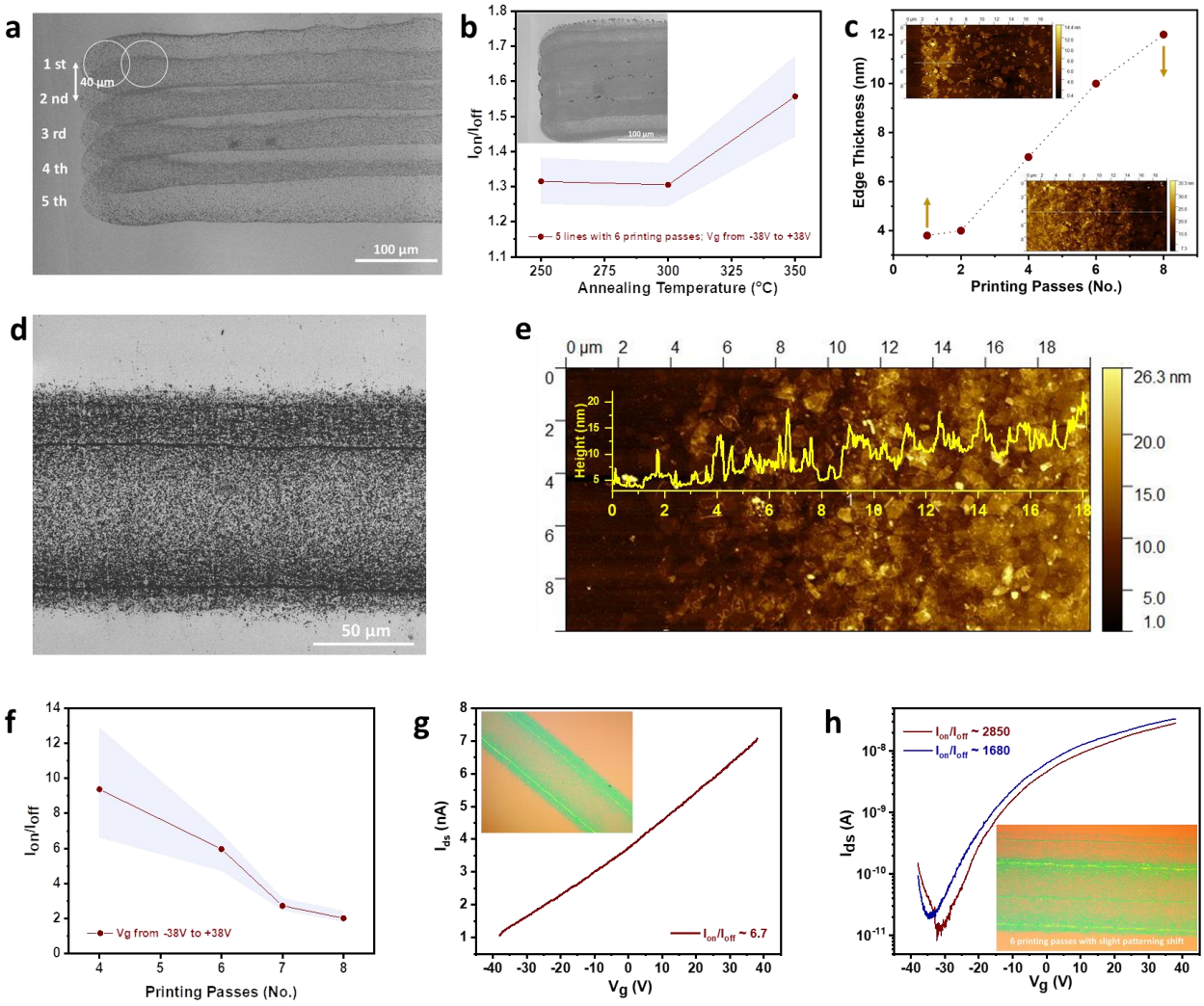

Fig. 5.2 a) SEM image of inkjet printed single-layer MoS_2 patterns containing 5 parallel lines with an optimized drop spacing of 40 µm. b) Current on/off ratio as a function of annealing temperature. c) Edge thickness vs. printing passes with AFM images of 1 printing pass and 8 printing passes in the inset. d) SEM image and e) AFM profile of printed MoS_2 single line pattern with 6 printing passes. f) Current on/off ratio of MoS_2 single line vs. printing passes. g) A typical transfer curve of MoS_2 single line pattern with 6 printing passes. h) Two transfer curves of MoS_2 single line pattern with 6 printing passes with slight patterning shift.

Upon the printed MoS_2 semiconducting channel, source/drain electrodes and an extended sensing area were further printed using graphene inks. After thermal annealing at 350 ^oC, a fully inkjet-printed FET-based water sensor device can be fabricated (Fig. 5.3a), which could be flexible when printed onto polymer substrates (Fig. 5.3b). The dimensions and good printing quality of the device are exhibited in Fig. 5.3c-e. The MoS_2 channel bridging the source/drain electrodes are designed to be 400 μm (Fig. 5.3c) to accommodate the printing resolution and possible graphene ink diffusion along the MoS_2 channel during electrode printing (Fig. 5.3d). A graphene sensing area was connected and extended several millimeters away from the MoS_2 channel to avoid the interference of the analyte onto the circuit during sensing tests. In Fig. 5.3f, the distance of two characteristic Raman peaks of the printed MoS_2 channel becomes larger compared with exfoliated single flakes, indicating their stacking together to form a percolation network, while the 2D, G and D bands from printed graphene electrodes present a multi-layer feature.[248] In combination with graphene electrodes, the semiconducting property of MoS_2 channel is maintained as shown in Fig. 5.3g, and the linear *I-V* curve shown in the inset demonstrates the good electrical contact between the MoS_2 channel and the graphene electrodes.

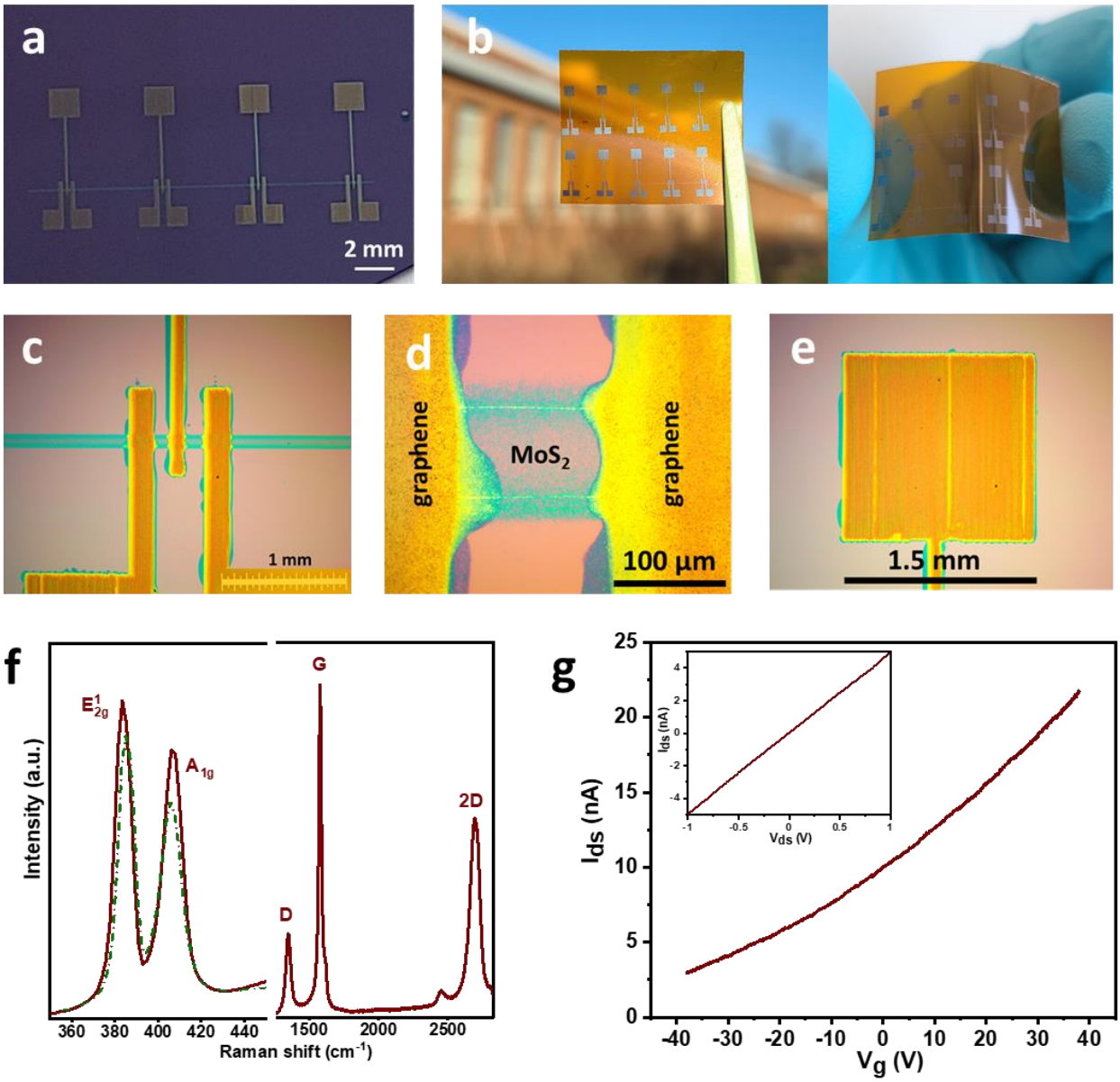

Fig. 5.3 a) Fully inkjet-printed sensor devices on Si wafer and b) polymer substrate. c-e) Optical images, f) Raman spectra of MoS_2 (left with dotted one from single flakes) and graphene (right), and g) transfer curve, with *I-V* curve in the inset, of the sensor device on Si wafer.

As a proof-of concept for device application, the extended graphene sensing area of the fabricated FET device was functionalized with 1-pyrenebutyric acid through π-π interaction for lead ion detection using aqueous solution-gated setting up (Fig. 5.4a). As shown in Fig. 5.4b, much more efficient top-gate modulation upon the FET device is observed compared with the bottom-gate modulation (i.e., bottom gate from the silicon wafer), showing an interesting inverse "p-type" transfer curve output. This implies that the printed MoS_2 channel could achieve a much higher on-off ratio if more efficient gate modulation is applied, such as using Si wafers with a thinner SiO_2 layer as substrates even for the bottom-gate measurement. The inverse output is likely due to the direct contact of the graphene sensing area with the MoS_2 channel as shown in Fig. 5.4a. When a negative V_g was applied through the analyte, the induced positive charges on the graphene surface are provided by the MoS_2 channel, leaving more unpaired electrons, which increase the channel conductance for a higher current output.

The sensor device was exposed to different Pb ion concentrations, and a top V_g scan was applied on the sensor device until a stable transfer curve output was obtained as the sensing signal to individual Pb^{2+} concentrations (within few minutes). The sensor shows a response starting from 10 nM (i.e., ~2 ppb) of Pb^{2+}, and gets saturated around 1 µM (i.e., ~200 ppb, Fig. 5.4c,d). Common cations present in water including Ca^{2+}, Mg^{2+} and Na^{+} have been used to evaluate the selectivity of the water sensor; no obvious sensing response could be measured for these interfering cations, and a test result upon Ca^{2+} exposure is shown in Fig. 5.4e as an example. It is believed that the functionalized -COOH of 1-pyrenebutyric acid on the sensing area could coordinate with Pb^{2+} at the interface between the analyte and the graphene sensing area,[45, 249] inducing a positive gate voltage, which decreased the I_{ds} according to Fig. 5.4b (top V_g configuration).

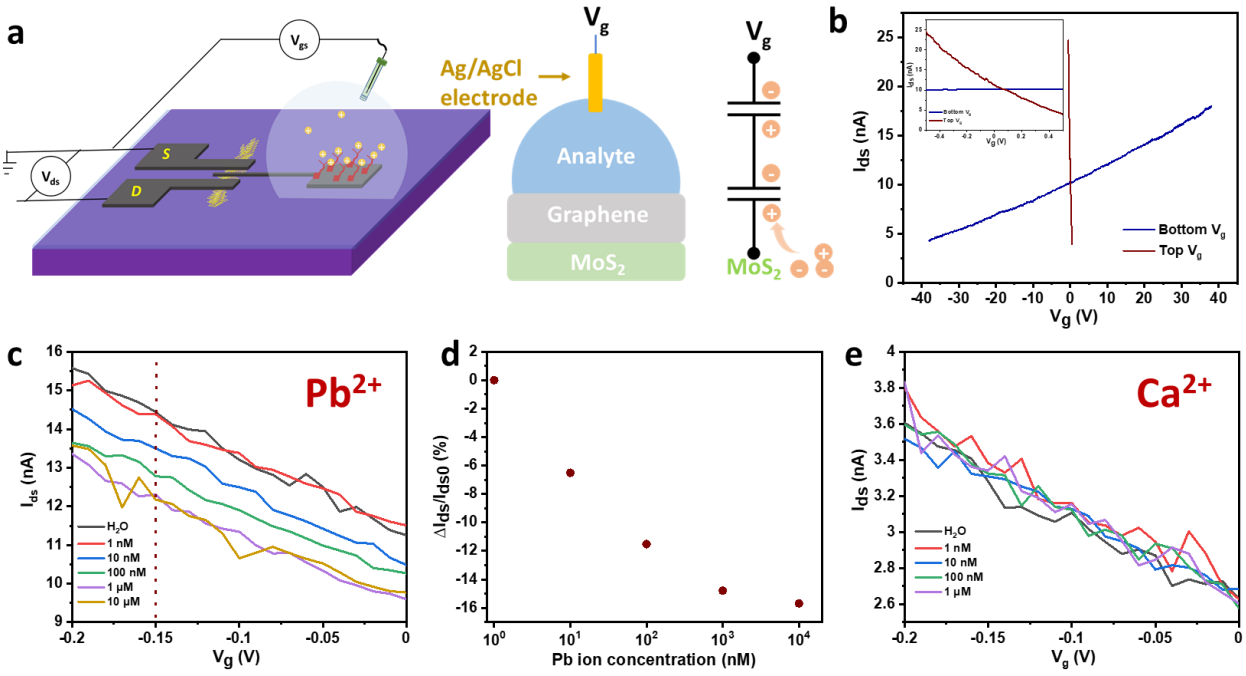

Fig. 5.4 a) Schematic of sensing test and circuit model. b) Transfer curves of the same device upon top/bottom V_g. c) Water sensor responses to Pb^{2+} in water and d) calculated sensitivity according to the I_{ds} at V_g = -0.15 V (top gate). e) Sensing response to Ca^{2+} in water.

5.4 Summary and conclusions

Using the inkjet printing technique, robust MoS_2 semiconducting channels exhibiting a current on/off ratio up to the order of 10^3 (V_g from -38 V to 38 V) have been prepared. The coffee-ring effect was minimized but it is believed to be the major barrier for further improvement. The MoS_2 channel can be hundreds of micrometers long, which is compatible with the inkjet printing resolution and facilitates a fully printed FET device. As a proof-of-concept for device application, a fully functioning FET water sensor with an extended sensing area has been fabricated based on

the printed MoS_2 sensing channel and graphene electrodes. After 1-pyrenebutyric acid functionalization, the water senor showed selective response to Pb^{2+} in water. This work has the potential to promote nanomanufacturing and application of 2D material-based sensors and other electronic devices.

CHAPTER 6 METAL-ORGANIC PRECURSOR-DERIVED TIN DIOXIDE/TIN-REDUCED GRAPHENE OXIDE SANDWICHED NANOCOMPOSITE ANODE WITH SUPERIOR LITHIUM STORAGE CAPACITY

6.1 Introduction

Commercial graphite anodes have a limited capacity (372 mAh g^{-1})[122] and thus there is a great need to explore alternative anode materials for lithium-ion batteries (LIBs) with high capacity and long life cycles to meet the requirements for electric vehicles and renewable energy storage. SnO_2 has been explored extensively as a promising anode candidate for LIBs because of its abundance, moderate lithiation potential, and high specific capacity.[250-252] The electrochemical interaction between SnO_2 and Li could involve both conversion and alloying reactions:

$$SnO_2 + 4Li^+ + 4e^- \leftrightarrow Sn + 2Li_2O \quad (6.1)$$

$$Sn + xLi^+ + xe^- \leftrightarrow Li_xSn \qquad (0 \leq x \leq 4.4) \quad (6.2)$$

The conversion reaction (Reaction 6.1) is believed to be irreversible for bulk SnO_2,[252, 253] but it could also become partially reversible for nano-sized SnO_2.[52, 254, 255] In contrast, the alloying process (Reaction 6.2) is well known to be highly reversible, exhibiting a theoretical capacity of 780 mAh g^{-1},[252] which is two times greater than that of graphite (372 mAh g^{-1}). When considering the completely reversible Reaction 6.1, the theoretical capacity can reach 1,494 mAh g^{-1};[256] however, the serious pulverization of the SnO_2-based anodes caused by the huge volume change (>300%) and the quick aggregation of tin particles during the lithium ion insertion and extraction result in rapid capacity fading.[254, 257-259] Reducing the material size down to the nanoscale and

constructing SnO_2-carbon composites have proven to be very effective in overcoming these challenges.[50, 258, 260-265]

As a good candidate for carbon matrix, highly flexible 2D graphene [referred to as reduced graphene oxide (rGO) in most reports] not only can work as a superior conductive platform for storing and transporting lithium ions and electrons, but also can effectively accommodate the large volume change of Sn-based anodes to improve capacity retention.[258, 261, 266-270] Various SnO_2-graphene structures, such as SnO_2-graphene mixture,[258] graphene-bonded SnO_2,[261, 271, 272] graphene-confined SnO_2,[269, 273] and graphene-enwrapped SnO_2,[262, 274] have been prepared and demonstrated improved lithium storage capacity. However, there are several potential issues: In some SnO_2-graphene composites, the active SnO_2 particles are just simply decorated on the surface of graphene and in direct contact with the electrolyte, resulting in side reactions and unstable interface between SnO_2 and the electrolyte; meanwhile, the SnO_2 nanostructures tend to fall off from the graphene due to the huge volume change during the cycling processes, thereby leading to a limited cycling performance.[261, 272] In some other cases, additional materials coating like carbon coating is needed to improve the cycling stability.[275-278] Compared with structures in which SnO_2 just anchors on the surface of graphene, graphene-confined SnO_2 composites stand out for the remarkable capacity retention, owning to the additional robust graphene protection around SnO_2. For example, Prabakar et al. elaborated on an SnO_2/rGO-layered composite from alternating stacks of amine-functionalized GO and Sn^{2+}-anchored GO, which retained a capacity of 872 mAh g^{-1} after 200 cycles at a current density of 100 mA g^{-1}.[269] However, reports on this kind of structures are very limited, likely due to the difficulty of synthesis and challenges in structural control. Extra surface modifications are always needed to enhance the adhesion between SnO_2 and

graphene[262, 274, 279] or among graphene layers[269] for component integration. Therefore, it is still challenging to construct such a robust graphene-confined SnO_2 composite with a simple method.

Here we demonstrate a facile metal-organic precursor coating on GO and in-situ transformation strategy to synthesize a well-ordered and densely packed SnO_2/Sn-reduced graphene oxide nanocomposite (denoted SnO_2/Sn-rGO), in which ultra-small SnO_2 nanoparticles (~ 5 nm) are uniformly anchored on the graphene sheets and perfectly confined by this self-assembled layer structure. The ultra-fine SnO_2 particles shorten the ion diffusion length, reduce the lattice strain, and enhance the reversibility of the conversion reaction (Reaction 6.1). The rGO sheets organize SnO_2 particles into a well-organized and much more stable layered structure, enhance the electrical conductivity, and buffer the SnO_2 volume expansion. In addition, the enhanced electrical conductivity of trace N doped SnO_2 and additional protective carbonaceous material around SnO_2, derived from this unique metal-organic precursor simultaneously, may further improve the electrochemical performance. Thus, the as-prepared SnO_2/Sn-rGO composite exhibits a high reversible capacity and excellent capacity retention.

6.2 Experimental methods

6.2.1 Material synthesis

Graphene oxide (GO) was synthesized from natural graphite flakes using the modified Hummers' method.[280, 281] In a typical procedure, 26.7 mg GO powder was dispersed into a deionized water/methanol mixture (2 mL/ 20 mL) under ultrasound for 0.5 h. Then, 226 mg (1 mmol) $SnCl_2 \cdot 2H_2O$ (reagent grade, Alfa Aesar) was added to the suspension and ultra-sonicated for

additional 1 h to obtain a homogenous suspension. After stirring for 5 h, followed by 0.5 h of ultrasound, 30 ml of methanol solution with 656.8 mg (8 mmol) 2-methylimidazole (Hmim) was added into the suspension under ultrasound for an additional 0.75 h. The resulting self-assembled black composite was collected by centrifugation, washed with methanol three times, and then dried overnight under vacuum at 60 °C. The obtained black precursor was then ground and annealed in a tubular furnace at 650 °C for 2 h under an Ar atmosphere with a heating rate of 2 °C min^{-1} to obtain the final product of a layered SnO_2/Sn-reduced GO nanocomposite (SnO_2/Sn-rGO). For comparison, SnO_2/Sn-C, SnO_2/Sn-rGO_1, and SnO_2/Sn-rGO_2 were synthesized by adjusting the initial GO amount to 0, 8.9, and 17.8 mg, respectively, using the same process.

6.2.2 Material characterization

The as-prepared samples were characterized using powder X-ray diffraction (XRD) on a Bruker D8 Discover X-ray diffractometer with Cu Kα radiation. Scanning electron microscopy (SEM) and energy dispersive X-ray spectroscopy (EDX) were performed by a Hitachi S-4800 equipped with a Bruker EDS detector. Transmission electron microscopy (TEM) was performed on a Hitachi H-9000-NAR at an acceleration voltage of 300 kV. Raman spectroscopy was carried out by using an XploRA PLUS Raman microscope with a 532-nm laser source. X-ray photoelectron spectroscopy (XPS) data were collected by a PerkinElmer PHI 5440 ESCA System equipped with an Mg anode. Nitrogen adsorption-desorption isotherms and the Brunauer-Emmett-Teller (BET) surface area were measured by a Micromeritics ASAP 2020, and the pore size was calculated from the Barrett-Joyner-Halenda (BJH) adsorption branch. Thermogravimetric analysis of the sample

was conducted with a SHIMADZU DTG-60 AH instrument under air flow (100 mL min^{-1}) at a heating rate of 10 °C min^{-1} from room temperature to 900 °C.

6.2.3 Coin cell assembly

The charge/discharge performance was characterized by using 2030-type coin cells assembled in an argon-filled glove box with oxygen and moisture contents below 1 ppm. Electrodes were prepared by mixing the as-prepared SnO_2/Sn-rGO composite as the active material, carboxymethyl cellulose as a binder, and carbon black as a conductor, with a weight ratio of 80:10:10 to form a slurry. The resulting slurries were coated on a Cu foil (12-μm in thickness) current collector using the doctor blade method. After drying and pressing, the Cu foil was cut into disks (1.26 cm in diameter), with typical electrode material loadings of ca. 1.5 mg cm^{-2}. Then, 1 M $LiPF_6$ dissolved in ethylene carbonate/ethyl methyl carbonate (40:60, v/v) was employed as an electrolyte, with 5 wt.% fluoroethylene carbonate and 1 wt.% vinylene carbonate as additives.

6.2.4 Electrochemistry measurements

The coin cells were tested on a LAND battery tester with a cutoff voltage range between 0.01 and 2.5 V. Cyclic voltammetry (CV) and electrochemical impedance spectroscopy (EIS) were measured on a PARSTAT 4000 electrochemical station using a three-electrode cell, with the SnO_2/Sn-rGO composite electrode as a working electrode, a lithium disk as a counter electrode, and a lithium ring as a reference electrode. CV was carried out at a scanning rate of 0.05 mV s^{-1}, while EIS was tested between 10,000-0.1 Hz with an amplitude of 10 mV.

6.3 Results and discussion

Fig. 6.1 illustrates the synthesis of the SnO_2/Sn-rGO composite. Graphene oxide (GO) powders were dispersed into an H_2O/methanol mixture under ultrasound, followed by the addition of $SnCl_2$, which formed a homogenous dispersion. A further incubation process under stirring facilitated the interaction between the tin cations and GO. Afterwards, a methanol solution of 2-methylimidazole (Hmim) was added to the dispersion under ultrasound. The resulting self-assembled black composite was annealed to obtain a layered SnO_2/Sn-reduced GO sandwich nanocomposite (SnO_2/Sn-rGO).

Fig. 6.1 Schematic illustration of the preparation of the SnO_2/Sn-rGO nanocomposite using a metal-organic precursor coating and in-situ transformation strategy.

Both the morphological structures of the self-assembled metal-organic precursor/GO composite and the final obtained SnO_2/Sn-rGO structure after pyrolysis were characterized by scanning electron microscopy (SEM) and transmission electron microscopy (TEM), as shown in Fig. 6.2. In the GO impregnation process with Sn^{2+}, Sn^{2+} could be adsorbed on the negatively charged GO surface through the electrostatic interaction. Then, organic ligand Hmim was added, and because

of its coordination with Sn^{2+},[282] a layer of metal-organic cluster from interparticle agglomeration assembled on the both sides of GO sheet, making the surface rough (Fig. 6.2a). The side view of this metal-organic precursor/GO, shown in Fig. 6.2b, illustrates the dense layer-by-layer stacks, which have an individual layer thickness of ~ 15 nm. This alignment phenomenon can be explained by the intrinsic affinity among these immature metal-organic surfaces upon departing from sonication. After pyrolysis, the metal-organic compound decomposed and had formed in-situ ultra-fine SnO_2 nanoparticles that anchored on and were sandwiched within these thermal-reduced GO sheets, which were stacked tightly through π-π interactions,[269] as shown in Fig. 6.2c,d, Fig. 6.3, and Fig. 6.4 (lower magnification). The SnO_2 nanoparticles with a size of ~ 5 nm dispersed very uniformly on the rGO sheets without agglomeration, which was confirmed by TEM images (Fig. 6.2e,f). The corresponding selected area electron diffraction (SAED) pattern (inset of Fig. 6.2e) proves the presence of tetragonal rutile-like SnO_2 (JCPDS No. 41-1445), consistent with the X-ray diffraction (XRD) analysis (Fig. 6.7a). In the high-resolution TEM (HRTEM), lattice fringes of 0.335 and 0.261 nm were assigned to the interplanar distance of (110) and (101) planes in tetragonal SnO_2 (Fig. 6.2f), respectively. Because of the dense SnO_2 nanoparticles loading and stacking feature of SnO_2/Sn-rGO, it is difficult to observe rGO directly here, which can be easily captured on samples with lower SnO_2 loading (Fig. 6.5). The homogeneity of this self-assembled nanocomposite is also demonstrated by the uniform distribution of elements in the energy-dispersive X-ray spectroscopy (EDX) (Fig. 6.4).

For comparison, composites with lower GO contents and pristine metal-organic precursor without GO were also synthesized. As shown in Fig. 6.6a-c, after pyrolysis, the metal-organic precursor itself can be transformed into aggregates of SnO_2 nanoparticles within 5 ~ 15 nm. With a lower

GO content, thicker metal-organic layers formed on the GO surface in the metal-organic precursor/GO stage, finally, thicker composite layer after pyrolysis, and SnO_2 aggregation can be observed (Fig. 6.6d-i). This highlights the pivotal role of an adequate amount of GO platforms in achieving a smaller SnO_2 and homogenous nanocomposite.

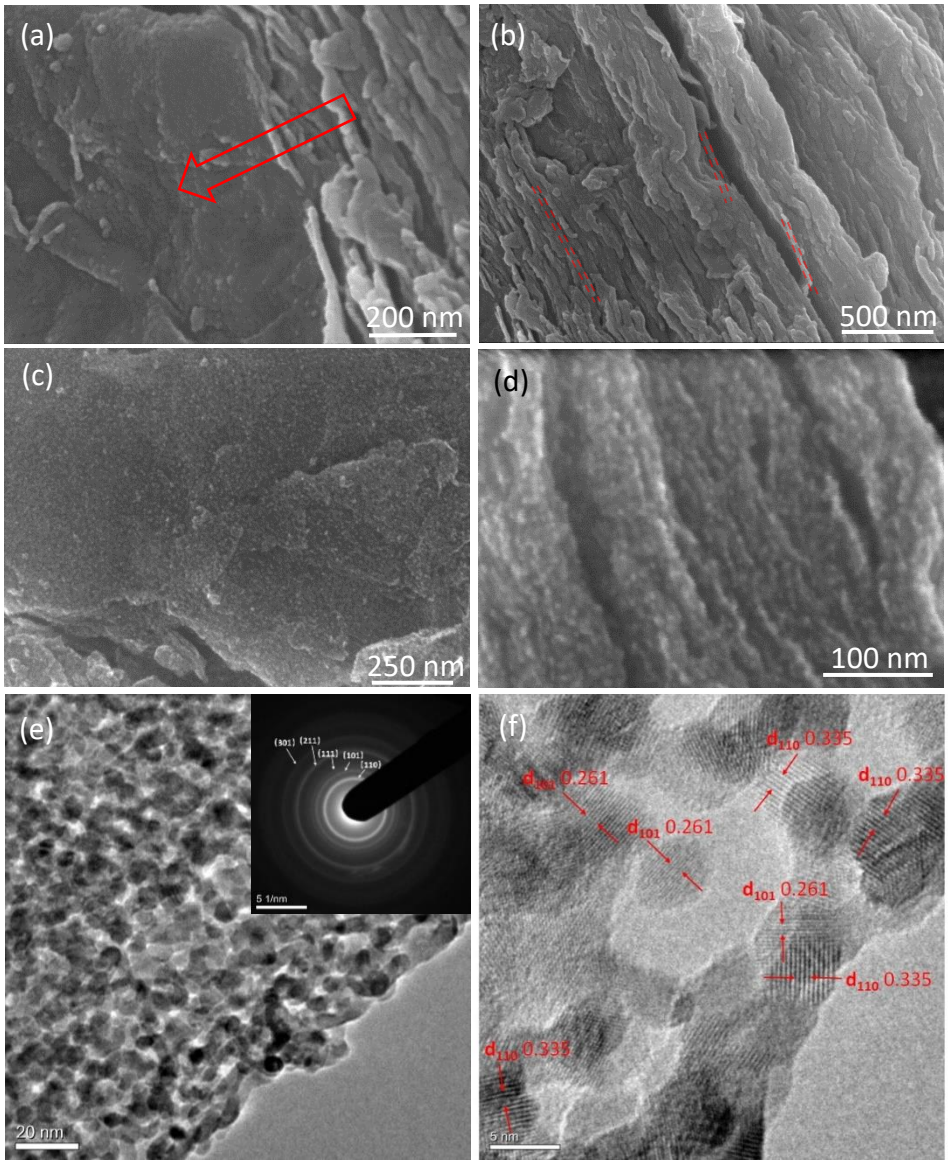

Fig. 6.2 a, b) SEM images of the metal-organic precursor/GO composites (arrow indicates the surface); c, d) SEM images; e) TEM (SAED pattern in the inset); and f) HRTEM images of SnO_2/Sn-rGO nanocomposites.

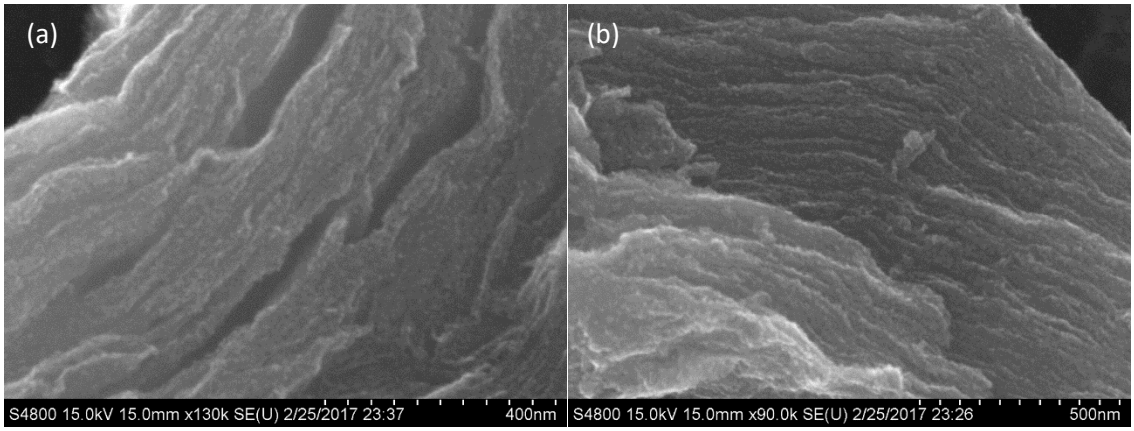

Fig. 6.3 a, b) SEM images of the SnO_2/Sn-rGO composite.

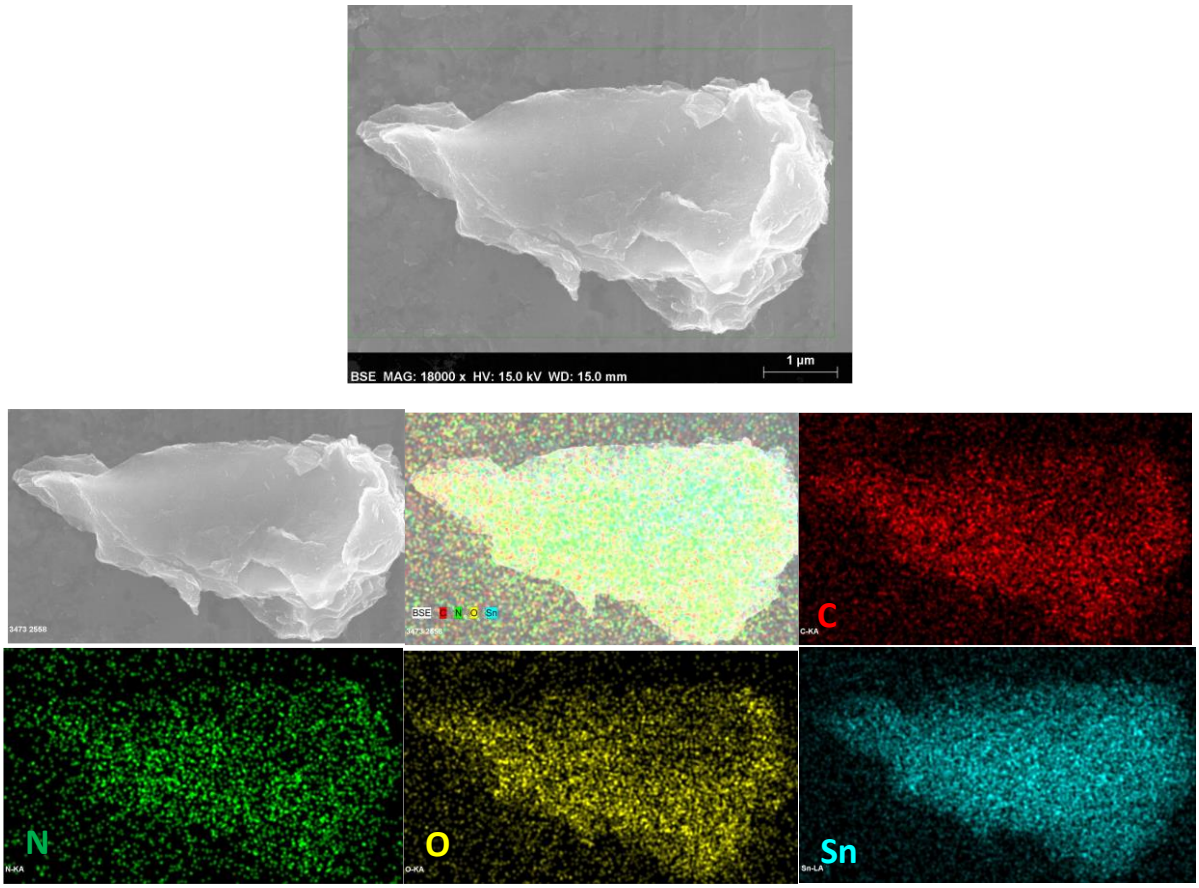

Fig. 6.4 EDX images of the SnO_2/Sn-rGO composite.

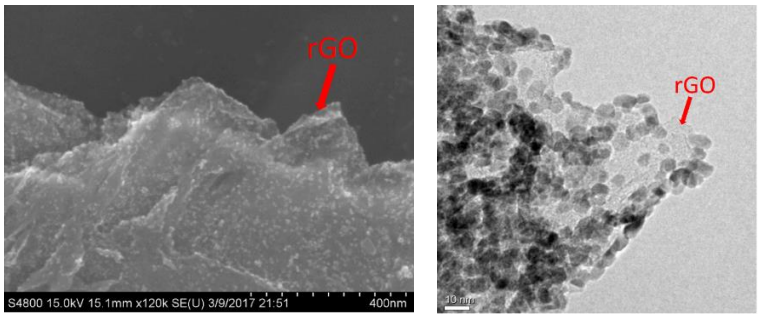

Fig. 6.5 a) SEM and b) TEM images of SnO_2/Sn-rGO composite with lower SnO_2 loading.

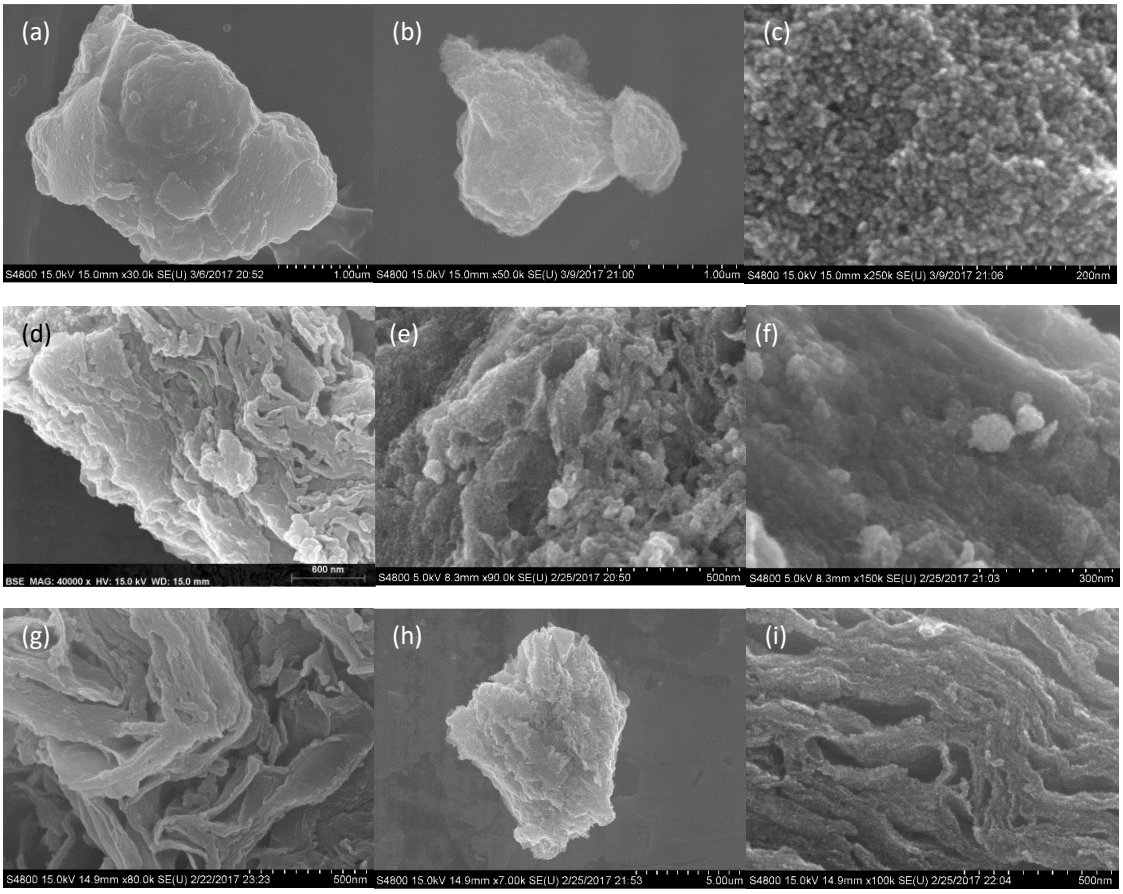

Fig. 6.6 a, d, g) SEM images of metal-organic precursor, metal-organic precursor/GO_1, and metal-organic precursor/GO_2 respectively; b & c, e & f, h & i) corresponding SEM images of SnO_2/Sn-C, SnO_2/Sn-rGO_1, and SnO_2/Sn-rGO_2 after pyrolysis, respectively.

In the XRD pattern of SnO_2/Sn-rGO (Fig. 6.7a), the major broadened diffraction peaks of SnO_2 indicate their small crystallite sizes, and much weaker Sn diffraction peaks (JCPDS No. 04-0673) also can be found, suggesting the existence of Sn with a low content. Using Relative Intensity Ratio (RIR)-based semi-quantitative phase analysis, the calculated weight fractions of SnO_2 and Sn are 87 and 13 wt.%, respectively.

The Raman spectrum shown in Fig. 6.7b confirms the SnO_2 and rGO components. The low intensity of the SnO_2 signal could be attributed to the small size of the SnO_2 and graphene/carbon coverage.[255] Besides the distinct Raman-active A_{1g} and B_{2g} modes of SnO_2, with peaks at 609 and 731 cm^{-1}, respectively, an inactive A_{2g} mode around 515 cm^{-1} in the rutile structure appears due to the small particle size (~ 5 nm), lattice distortion, and modification of bond length.[53, 283, 284] As the precursor to SnO_2 nanoparticles, tin is homogenously distributed in an N-rich metal-organic cluster (metal-organic precursor/GO), and thus it is possible that some N may substitute O under O/Sn-rich growth conditions due to its ion size, electronegativity, and energy-matching to distort the lattice of SnO_2.[283, 285] The two broad peaks at 1,323 and 1,577 cm^{-1} are the typical D-band and G-band of rGO, respectively. As-prepared SnO_2/Sn-rGO has SnO_2 as a major phase of the Sn element. The large amount of oxygen element can be introduced via the strong affinity of Sn^{2+} with water (OH^-) to form $Sn(OH)_2$ [286-288] in the Sn^{2+} and GO solution incubation process, and with the oxygen-containing groups on the GO. This is supported by the high oxygen content (~ 30 wt.%) in the metal-organic precursor/GO composite, as indicated by EDX analysis. The expected configuration of the metal-organic precursor is shown in Fig. 6.8. The formation of a small amount of Sn in SnO_2/Sn-rGO may be due to the carbothermal reduction of partial SnO_2 in the richer carbon interior of the composite during pyrolysis.[289, 290]

Thermogravimetric analysis (TGA) was carried out in air to investigate the components (Fig. 6.7c). The initial weight loss of 0.58 wt.% before reaching 150 °C corresponds with the removal of physically absorbed water in the sample; the subsequent rapid weight loss of 9.45 wt.% until reaching 500 °C was mainly attributed to the thermal oxidative degradation of rGO and carbon from the carbonization of metal-organic precursor[291] (proofs and discussion in Fig. 6.9). The final residue is SnO_2, mainly from the original ones in the composite and some oxide of Sn, and the content was calculated to be 90.5 wt.%; as a result, the Sn element content in the SnO_2/Sn-rGO was 71.3 wt.%. Together, with the aforementioned weight fraction of SnO_2 and Sn, the SnO_2 and Sn contents in the SnO_2/Sn-rGO were estimated to be ~ 76.1 and ~ 11.4 wt.%, respectively. If the metal-organic precursor-derived carbon in the SnO_2/Sn-rGO was evaluated by the pyrolysis of pristine metal-organic precursor (Fig. 6.9c), the carbon and rGO contents were ~ 0.5 and ~ 12 wt.%, respectively.

The surface chemical composition of SnO_2/Sn-rGO was revealed by X-ray photoelectron spectroscopy (XPS) analysis (Fig. 6.7d and Fig. 6.10). The three major elements are C, O, and Sn, with an atom ratio of 48.6 : 37.6 : 13.8, corresponding to 20.7 : 21.3 : 58 wt.%, respectively. Compared with the TG analysis (C < 12.5 wt.%, Sn ~ 71.3 wt.%), the higher C and lower Sn element contents suggest that more SnO_2/Sn, especially Sn particles, are sandwiched in the interior of the composite. The high-resolution Sn 3d spectrum (Fig. 6.10a) shows two symmetrical peaks, located at 487 and 495.5 eV, respectively, which are in agreement with those reported for SnO_2, thus implying that Sn exists only in the 4^+ state on the surface.[53, 260] This makes it difficult to

capture the Sn lattice in the TEM test. A trace level of N atom from the decomposing Hmim could also be detected, suggesting trace N doping in the SnO_2 lattice. Brunauer-Emmett-Teller (BET) analysis indicated the microporous structure of SnO_2/Sn-rGO with a surface area of 165.3 m^2 g^{-1} and pore size of approximately 3 nm, calculated from the Barrett-Joyner-Halenda (BJH) adsorption branch (Fig. 6.7e). Abundant pores will facilitate the diffusion of electrolyte and ion transport.

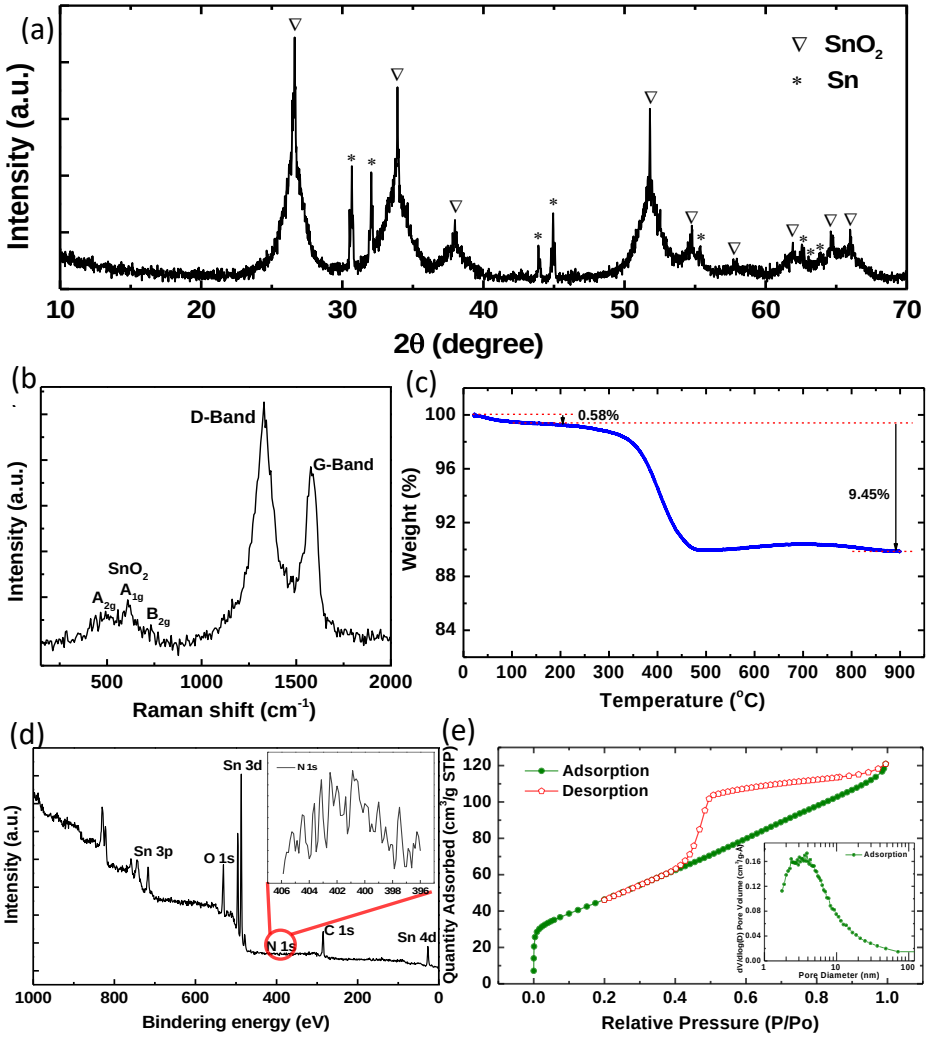

Fig. 6.7 a) XRD pattern; b) Raman spectrum; c) TG curve in air; d) XPS spectrum; and e) N_2 adsorption/desorption isotherms (pore-size distribution plot in the inset) of the SnO_2/Sn-rGO nanocomposite.

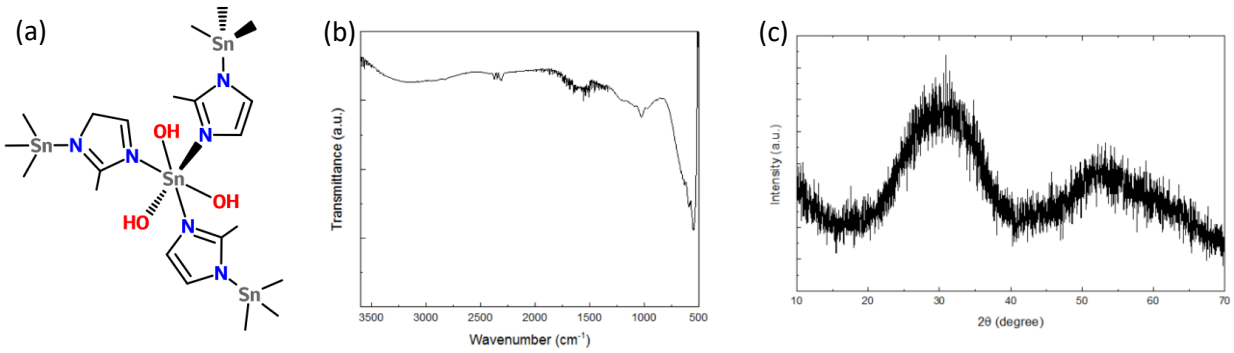

Fig. 6.8 a) Schematic for the metal-organic structure; b) FTIR spectrum; and c) XRD pattern of the metal-organic precursor/GO composite. The XRD pattern indicates the amorphous and disorder configuration of the metal-organic precursor structure. A supposed configuration is shown in Fig. 6.8a.

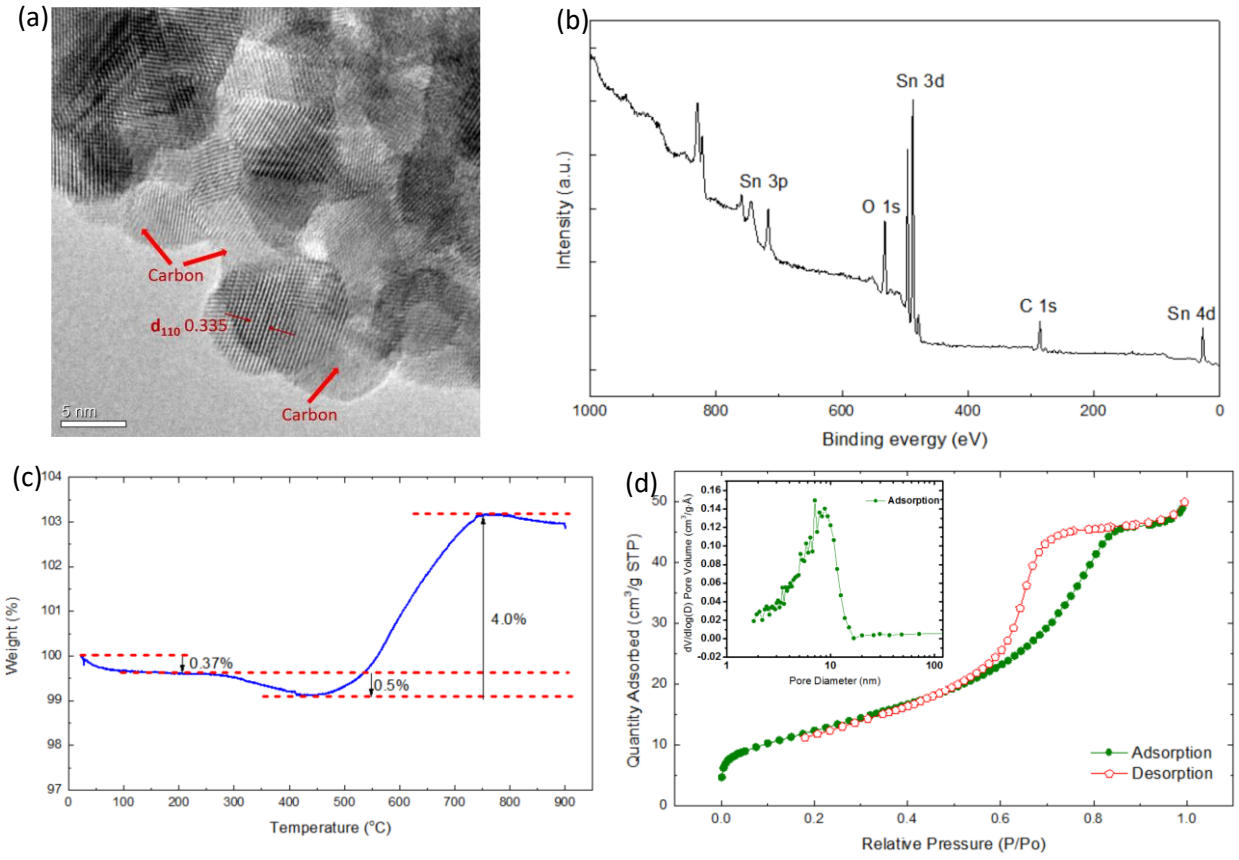

Fig. 6.9 a) TEM image; b) XPS spectrum; c) TG curve in air; and d) nitrogen adsorption/desorption isotherms (inset: pore-size distribution plot calculated from the Barrett-Joyner-Halenda adsorption branch) of the SnO_2/Sn-C. As shown in the TEM image (Fig. 6.9a), besides the crystal aggregations, some amorphous structures which partially covered the SnO_2 particles can be observed. These amorphous structures can be the carbon from the carbonization of metal-organic precursor. Also, the C peak in XPS spectrum (Fig. 6.9b), weight loss from 200 ^{o}C to 450 ^{o}C in the TGA curve (Fig. 6.9c), and microporous structure with a BET surface area of 44.5 m^2 g^{-1} (Fig. 6.9d) all indicate the existence of carbonaceous material in this decomposed product of metal-organic precursor (SnO_2/Sn-C). It is reasonable to speculate the existing of a similar thin layer of carbon surrounding the SnO_2 particles in the SnO_2/Sn-rGO composite.

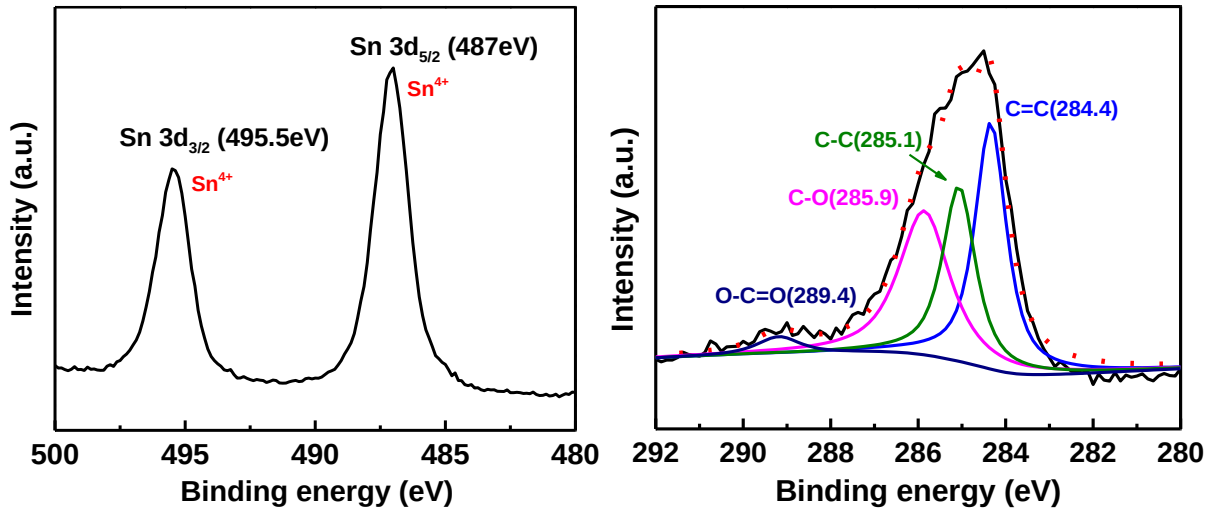

Fig. 6.10 a) XPS of Sn 3d and b) C 1s fine scan spectrum of the SnO_2/Sn-rGO composite.

Fig. 6.11 demonstrates the electrochemical performance of the as-prepared SnO_2/Sn-rGO composite. To limit the interfacial lithium-ion storage, mainly attributed to the high specific area and defects of rGO,[260, 292] and to reveal the intrinsic electrochemical reactivity of the SnO_2/Sn, we used a relative mild testing potential window of 0.01 – 2.5 V vs. Li^+/Li. The initial charge (lithiation) and discharge (delithiation) capacities at a current density of 80 mA g^{-1} are 2,142.9 and 1,307 mAh g^{-1}, respectively, corresponding with an initial Coulombic efficiency (CE) of 61.0% (Fig. 11a,b). The massive irreversibility of the initial lithiation is mainly ascribed to the relative high specific surface area, and abundant defects such as edges and/or oxygen-/hydrogen-containing groups of rGO component leading to the irreversible reduction of electrolyte to form the solid electrolyte interphase (SEI).[53, 258, 293] Impressively, the reversible capacity of 1,307 mAh g^{-1} we observed is far beyond the theoretical reversible capacity for bulk SnO_2 if only Reaction 6.2 is reversible (780 mAh g^{-1}); therefore, Reaction 6.1 must be reversible, at least partially. Considering that the contents of SnO_2, Sn, C, and rGO in our SnO_2/Sn-rGO composite are 76.1,

11.4, 0.5, and 12 wt.%, respectively, the theoretical capacity of our SnO_2/Sn-rGO composite is calculated to be 1,318.9 mAh g^{-1}, in which the specific capacity of C and rGO is assigned to be 744 mAh g^{-1}—twice that of graphite (372 mAh g^{-1})—because of the two sides of Li^+ storage.[293, 294] Notably, compared with some other reported high-capacity SnO_2-rGO composites, our SnO_2/Sn-rGO nanocomposite was able to exhibit a remarkable reversible capacity of 1,307 mAh g^{-1} at the initial testing stage without long-term cycling activation,[258, 261, 295-297] indicating its outstanding electrochemical reactivity.

In the second cycle, the charge and discharge capacities were 1,345.7and 1,288.5 mAh g^{-1}, and the CE increased to 95.7% demonstrating the high reversibility and stability of the SnO_2/Sn-rGO nanocomposite as an electrode material. This mainly benefits from the ultra-small SnO_2 particles and their intimate contact with rGO, which enhance the reversibility of the conversion reaction of SnO_2 during cycling (Reaction 6.1). [52, 254, 255, 258] After the initial two cycles of activation, the anode was cycled at 400 mA g^{-1} and showed capacities of 982.9, 931, and 821.8 mAh g^{-1} for the 4^{th}, 10^{th}, and 100^{th} cycles, respectively. After 200 cycles, the capacity remained at 767 mAh g^{-1} with 78% retention.

Figure 6.11c depicts the rate capability of the SnO_2/Sn-rGO composite. At 160, 400, 800, 1,600, 4,000, and 8,000 mA g^{-1}, the material exhibited capacities of 1,140, 935, 749, 512, 118, and 50 mAh g^{-1}, respectively. Even under such rigorous testing conditions, the capacity still reverted to 1,085 mAh g^{-1} (95.2% capacity retention) when the current returned to 160 mA g^{-1}, demonstrating that the composite remained stable during the extended rate cycling process.

The SnO_2/Sn-rGO composite anode was also tested by long-term cycling at a higher current density of 1,600 mA g^{-1} (Fig. 6.11d) after activation for the initial two cycles at 80 mA g^{-1}. The electrode delivered a highly reversible capacity of 512 mAh g^{-1} and excellent capacity retention, i.e., 87.7% after 400 cycles. Moreover, the CE remained close to 100% during the 400 cycles, indicating good reversibility. The superior cyclic performance of the composite electrode is associated with its very stable, homogeneous sandwiched structure, which is supported by the SEM, EDS and TEM analyses of the SnO_2/Sn-rGO electrode after 200 cycles (Fig. 6.12). No large cracks were observed on the electrode (Fig. 6.12a), and ultra-fine SnO_2 particles (~ 5 nm) were still anchoring on the surface of nanocomposite (Fig. 6.12b), suggesting the good integrity of the nanocomposite and strong interaction between the particles and rGO. The well-preserved morphology and uniform element distribution of the SnO_2/Sn-rGO after cycling further demonstrate its high structural stability without serious particle coarsening (Fig. 6.12c-g). TEM examination (Fig. 6.12h) clearly revealed that the microstructure of the SnO_2/Sn-rGO was also well maintained after cycling: ultra-small particles (~ 5 nm) were still evenly composited with rGO sheets without obvious aggregation, due to their strong interaction. The SAED pattern and HRTEM (Fig. 6.12i-l) confirm the preservation of SnO_2 particles even after a long-term cycling, manifesting the high electrochemical reversibility of the SnO_2 in our nanocomposite, which is responsible for the superior reversible capacity as an anode material for LIBs. It is found that crystallinity of the SnO_2 decreases during the cycling, indicated by the ambiguous lattice fringes.[298, 299]

Fig. 6.11e shows the cyclic voltammetry (CV) characteristics of the SnO_2/Sn-rGO composite. During the initial cathodic scan, the irreversible broad peak in the range of 1.2 to 1.8 V is associated with the formation of the SEI layer.[300] The subsequent two wider peaks below 1.2 V can be attributed to the reduction of SnO_2 ($Sn^{4+} \rightarrow Sn^0$) and the multi-step alloying reaction between Sn and Li.[53, 300] In the anodic sweep process, the sharp peak at 0.56 V is consistent with the dealloying process of Li_xSn back to Sn, and the two broad peaks between 1.0 and 2.2 V are attributed to the conversion from Sn to SnO_2.[52, 53, 256] After the first cycle of activation, the well-overlapped subsequent CV curves suggest excellent reversibility and structure stability.

Electrochemical impedance spectroscopy (EIS) was performed to analyze the resistances of the SnO_2/Sn-rGO composite anode. As shown in Fig. 6.11f, the Nyquist plot comprised two semi-circles and an inclined line, which corresponded with the SEI layer, charge transfer, and Li ion diffusion processes, respectively. By fitting the ESI results using a two-time constant equivalent circuit,[300-303] the Ohmic, SEI layer, charge transfer, and Li ion diffusion resistances were calculated to be 3.8, 11.6, 11.7, and 91.0 Ohm, respectively.

The outstanding lithium storage properties of the SnO_2/Sn-rGO can be attributed to its unique structural features. First, the ultra-small particle size not only mitigates the gradual aggregation of SnO_2/Sn during cycling,[54, 304] but also shortens the lithium-ion diffusion path, thereby enhancing the reversibility of the conversion reaction of SnO_2. Moreover, the remaining N element in the composite may lead to the lattice distortion of SnO_2, thereby improving the electrical conductivity and resulting in higher reversibility to reach a high specific capacity.[53, 305] Second, the SnO_2/Sn

particles are encapsulated and sandwiched by a robust interconnected graphene network, which can depress the coarsening of particles and effectively buffer the volume variation during the lithiation/delithiation processes. This improves the structural durability and thus the cycling performance. Finally, the highly electroconductive rGO/carbon network provides a highway for transporting electrons and Li ions, which contributes to an improved reversible capacity and rate capability.[258] All these advantages enabled by our metal-organic precursor coating and in-situ transformation strategy led to the outstanding reversible capacity, good rate performance, and long-term cycling stability of the SnO_2/Sn-rGO composite. We also compared the electrochemical performance of SnO_2/Sn-rGO with other reported SnO_2-rGO anodes and found that our material is top-ranking, especially with a prominent initial reversible capacity in a relative mild voltage window of 0.01 – 2.5 V for the tests (Table 6.1).

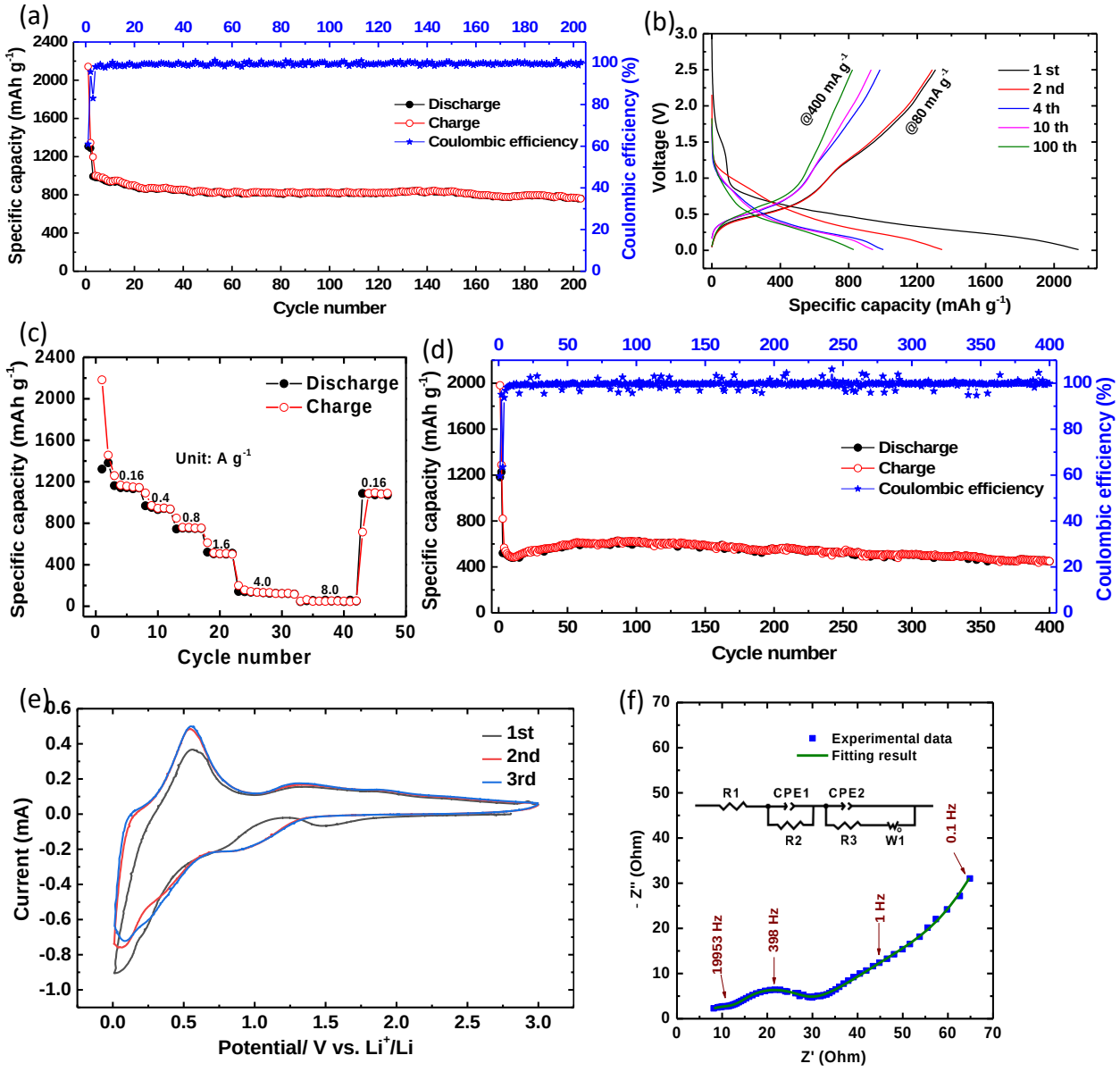

Fig. 6.11 Electrochemical performance of the SnO_2/Sn-rGO composite. a) cyclic performance at 400 mA g^{-1} after initial two cycles activation at 80 mA g^{-1}; b) charge/discharge curves; c) rate capability; d) cyclic performance at 1,600 mA g^{-1} after initial two cycles of activation at 80 mA g^{-1}; e) cyclic voltammetry; and f) Nyquist plot and corresponding equivalent circuit with two-time constant.

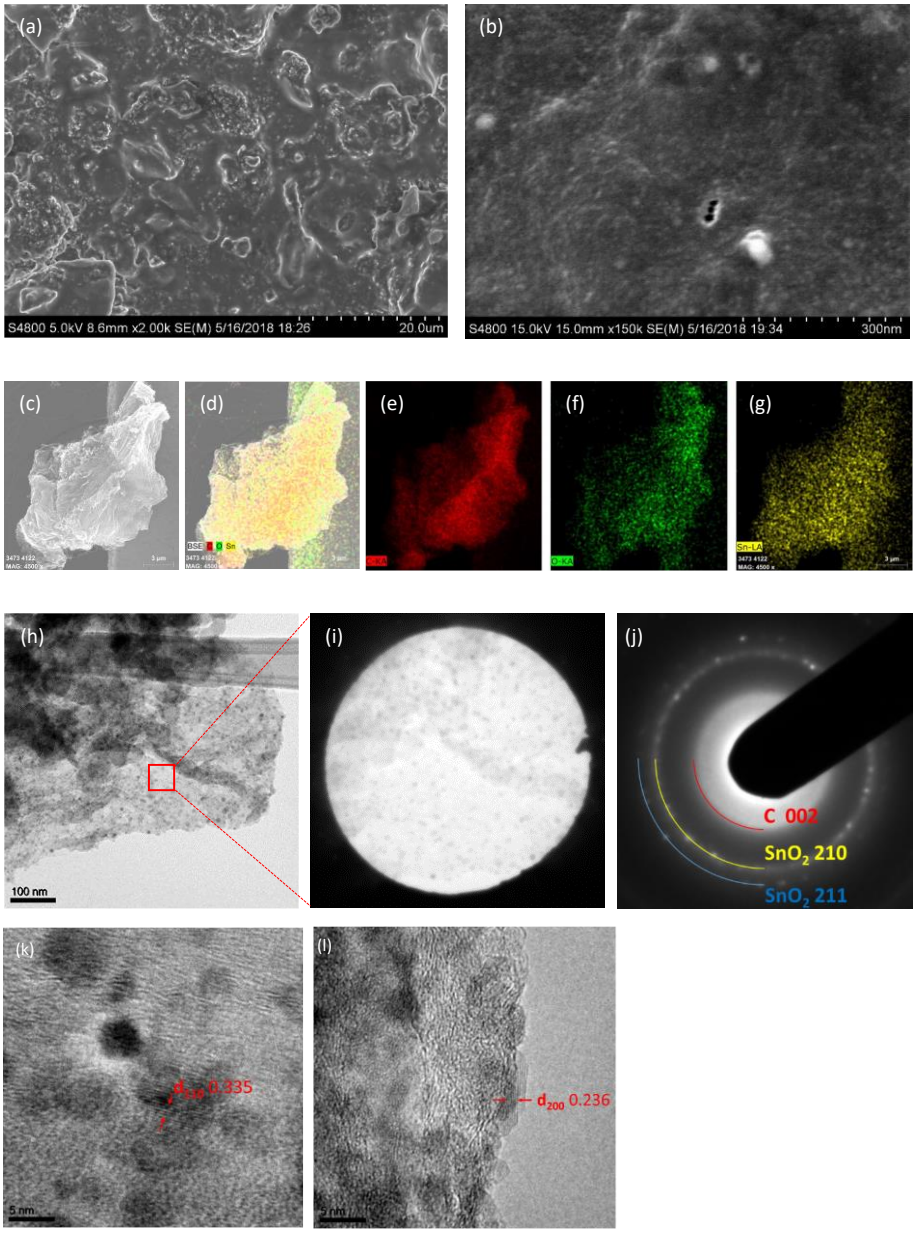

Fig. 6.12 a, b) SEM images of SnO_2/Sn-rGO electrode after 200 cycles at 1,600 mA g^{-1}; c-g) SEM image and its corresponding EDS elemental mapping; h-j) TEM image, selected area image and its corresponding SAED pattern; and k, l) HRTEM images of the SnO_2/Sn-rGO particle, which was collected from the aforementioned cycled electrode, and washed by dimethyl carbonate, 1 vol.% HCl solution, and DI water to eliminate the interference of SEI layers.

Table 6.1 Comparison of the electrochemical performance of as-prepared electrodes with previously reported SnO_2-rGO electrodes.

Samples	**Voltage range V**	**Current mA g^{-1}**	**Initial reversible capacity mAh g^{-1}**	**Cycling stability**	**Reference**
SnO_2/Sn-rGO	**0.01-2.5**	**80**	**1307**		**This work**
		400		**767 (after 200 cycles)**	
		1600		**449 (after 400 cycles)**	
1	0.01-2.5	100	1092	872 (after 200 cycles)	[269]
2	0.005-2.5	100	1032	883 (after 100 cycles)	[273]
3	0.01-2.5	100	1024	844 (after 50 cycles)	[306]
4	0.01-2.5	100	750	620 (after 100 cycles)	[288]
		400		420 (after 400 cycles)	
5	0.005-2.5	100	~800	~720 (after 200 cycyles)	[307]
6	0.01-2.5	100	1129	825 (after 50 cycles)	[308]
7	0.005-2.5	100	1273	720 (after 70 cycles)	[309]
8	0.01-3.0	200	~970	950 (after 100 cycles)	[310]
9	0.01-3.0	100	1308	1107 (after 100 cycles)	[262]
		1000		552 (after 500 cycles)	
10	0.001-3.0	100	1011	758 (after 200 cycles)	[311]
		1000		537 (after 300 cycles)	
11	0.01-3.0	100	1107	847.5 (after 50 cycles)	**[312]**

6.4 Summary and conclusions

A facile self-assembly approach using metal-organic precursor coating and in-situ transformation is demonstrated to synthesize a well-ordered, sandwich-like SnO_2/Sn-rGO nanocomposite with ultra-small SnO_2/Sn decorating on and confined uniformly in the densely packed rGO layers. The unique structure exhibits remarkable Li-storage capability with surprising reversibility and high stability. The SnO_2/Sn-rGO composite delivered a reversible capacity of 1,307 mAh g^{-1} at the current density of 80 mA g^{-1} and a stable capacity of 767 mAh g^{-1} after 200 cycles when cycling at 400 mA g^{-1}. Moreover, the SnO_2/Sn-rGO composite showed a highly stable capacity of 449 mA g^{-1} without obvious decay after 400 cycles at the higher current density of 1,600 mA g^{-1}. Its structural robustness and electrochemical reversibility were certified by the analyses on the electrode after long-term cycling. Therefore, this stable SnO_2/Sn-rGO composite can be a very promising candidate as the anode material for LIBs. The facile metal-organic precursor coating self-assembly strategy employed here could serve as a universal platform for constructing diverse and robust graphene-layered nanocomposites.

CHAPTER 7 TAILORING MOF-DERIVED POROUS CARBON NANORODS CONFINED RED PHOSPHOROUS FOR SUPERIOR POTASSIUM-ION STORAGE

7.1 Introduction

Due to lithium's limited reserves (0.0017 wt.%), uneven distribution in the Earth's crust, and increasing price, lithium-ion batteries (LIBs) would not meet the increasing demand for large-scale applications such as electric vehicles and stationary energy storage at a low cost.[123] Sodium and potassium become attractive alternatives in batteries due to their abundance and relatively low cost.[125] Compared with sodium (-2.71 V *vs.* standard hydrogen electrode, SHE), the lower redox potential of K/K^+ (-2.93 V *vs.* SHE), which is close to that of lithium (-3.04 V *vs.* SHE), endows potassium-ion batteries (PIBs) with the potential for high energy density.[124] However, K^+, which is larger in size (radius 1.38 Å) than Na^+ (1.02 Å) and Li^+ (0.76 Å), inevitably has a sluggish diffusion process and induces a greater volume change in electrode materials during K^+ insertion/extraction, which results in serious material pulverization and thus fast capacity fading.[313] Rationally designed anode materials are greatly needed to address these major challenges with PIBs.[126]

Phosphorus-based materials are promising anodes for PIBs, owing to the high theoretical capacity of phosphorus (1,154 mAh g^{-1} for K_4P_3); however, the drawbacks of their low electrical conductivity and huge volume variation of P (~290 % as K_4P_3) during K-ion insertion/extraction must be addressed in order to achieve a high capacity and a long cycling life.[126] Combining P-based active materials with various conductive carbonaceous supports, including carbon

nanotubes,[127] graphite,[314] amorphous carbon,[129, 315, 316] and porous carbon matrix,[12, 128, 317, 318] to construct nanocomposites has been proved highly effective in addressing these challenges. The carbonaceous materials not only provide a highly conductive scaffold but also buffer the volume change during cycling, thereby preserving the integrity of the electrode. Among these phosphorus/carbon nanocomposites (P/Cs), red P-impregnated porous carbon composites, prepared via the P vaporization-condensation-conversion approach, stand out for their robust capacity preservation and excellent rate capability as anodes for PIBs.[128, 317] For instance, Huang et al.[12] loaded red P into the commercial activated carbon YP50F via the vaporization-condensation-conversion approach. The as-prepared P/C composite with 45 wt.% of P exhibited a maximum capacity of 430 mAh g^{-1}, while the P/C composite with a lower P content of 32 wt.% maintained 70% capacity after 500 cycles. Liu et al.[128] infiltrated red P into carbon nanotube-backboned mesoporous carbon using the same approach. With a P content of ~40 wt.%, the as-obtained P/C nanocomposite delivered an impressive reversible capacity of ~500 mAh g^{-1} at a small current and a stable capacity of 244 mAh g^{-1} at 500 mA g^{-1} for 200 cycles. The issue with the previously reported P-infiltrated porous carbon composites is the conflict between their long-term cycling performance and high capacity. In other words, when the P loading is high, the capacity of the P/C composite is higher while the cycling is poor; in contrast, when the P loading is low, the cycling performance is good while the capacity is relatively low. The use of porous carbon with a large pore volume and suitable pore size may help to address this issue. Therefore, due to their tailorable components and permanent porous structure,[5, 105, 319] this study explores metal-organic frameworks (MOFs) as distinctive self-templated precursors to fabricate porous carbon materials using a simple morphological-preservation calcination process.

MOF-derived porous carbon recently has been demonstrated as a carbon matrix for P impregnation. For example, Li et al.[106] loaded red P into zeolitic imidazolate framework-8 (ZIF-8)-derived nanoporous carbon as an anode for sodium-ion batteries (NIBs), which showed a super cycle life over 1,000 cycles; however, the relatively low capacity of ~450 mAh g^{-1} was attributed to the limited P content (22.6 wt.%) due to the small pore size and pore volume of the ZIF-8-derived carbon. Therefore, to achieve high capacity, MOF precursors that can generate larger pore size and pore volume are desired. We identified that Zn-MOF-74 from the MOF family has abundant oxygen-containing groups and Zn element, which benefit relatively larger pore size and pore volume during the high-temperature calcination process, resulting in rich mesopores.[320] However, the Zn-MOF-74 reported in the literature typically have a micro-sized and non-uniform morphology,[320-323] which is unfavorable for homogeneously loading phosphorus and application in high-performance anodes.

In this study we report the very facile, one-step, solvothermal synthesis of uniform, well-developed Zn-MOF-74 hexagonal nano/microrods using a mixed-solvent strategy, in which the size of the rods can be accurately controlled and tuned simply by varying the H_2O content in the H_2O/*N*,*N*-dimethylformamide (DMF) mixed solvent. The rod diameter of the Zn-MOF-74 can be tuned from tens of nanometers to hundreds of nanometers and further to micron size, and the length from hundreds of nanometers to micron size. The obtained Zn-MOF-74 nanorods were transformed into nanoporous carbon nanorods through a morphological-preservation calcination process and followed by red P impregnation. While the maximum P loading was up to ~66 wt.%, showing a maximum capacity of 763 mAh g^{-1}, the optimal P loading was demonstrated to be ~50 wt.%,

leaving adequate free spaces for volume expansion upon potassiation, which delivered a robust capacity preservation and excellent rate capability when applied as an anode for PIBs.

7.2 Experimental methods

7.2.1 Material synthesis

Materials. Zinc acetate dihydrate [$Zn(CH_3COO)_2 \cdot 2H_2O \geq 99\%$], anhydrous *N*,*N*-dimethylformamide (DMF > 99.8%), and red P (≥ 97%) were purchased from Sigma-Aldrich. 2,5-dihydroxyterephtalic acid ($C_8H_6O_6$ > 98%) was obtained from TCI Chemicals. The red P was purified by boiling deionized (DI) water and stored in a glovebox before use.

Synthesis of Zn-MOF-74 Rod (ZRod). In a typical procedure to synthesize Zn-MOF-74 rods with 300-400 nm diameter and ~1 μm length, first 2,5-dihydroxyterephtalic acid ($C_8H_6O_6$, 0.6 g, 0.003 mol) was dissolved in a mixed solvent containing 0.75 mL DI H_2O and 30 mL DMF. $Zn(CH_3COO)_2 \cdot 2H_2O$ (1.008g, 0.0046 mol) was dissolved in another mixed solvent with the same components (i.e., 0.75 mL H_2O and 30 mL DMF). Then the $C_8H_6O_6$ solution was poured into the $Zn(CH_3COO)_2$ solution and stirred for 20 min at room temperature. The as-obtained yellow suspension was then heated at 100 °C for 24 h in an 80-mL Teflon-lined autoclave. After cooling down to room temperature, the resultant yellow materials were collected by centrifugation and washed with DMF two times and methanol three times, in sequence. After drying overnight under vacuum at 50 °C, the as-obtained yellow powder was ground to yield the Zn-MOF-74 rods (denoting ZRod-0.025, where 0.025 refers to volume ratio of H_2O/DMF, i.e., 0.75/30 = 0.025 here).

For the mixed solvent, the content of DMF was kept constant (30 mL) and the H_2O content was adjusted to tune the nanorod size in a wide range.

Preparation of Zn-MOF-74-Derived Carbon Nanorods (ZCRods). The as-synthesized Zn-MOF-74 Rods (ZRods) were calcinated in a tubular furnace at 1,000 °C for 4.5 h under argon gas flow (50 mL min^{-1}) with a heating rate of 3 °C min^{-1} to obtain the product of carbon nanorods (ZCRods) with a carbon yield of ~10 wt.%.

Preparation of Red P@Carbon Nanorod Composite (P@ZCRods). Red P was loaded into the synthesized carbon nanorods by a vaporization-condensation-conversion approach according to our previous reports.[12] In brief, the P and ZCRods were sealed into a Pyrex glass tube under vacuum after purging three times with Ar gas. Using a tube furnace, the sealed tube was heated at 550 °C for 2h, cooled down to 260 °C at 1 °C min^{-1}, and kept at 260 °C for 24h for the conversion of white P into red P. The resultant P@C composite was washed with carbon disulfide to remove possible white P residual and then vacuum-dried to obtain the final product, which was denoted as Px@ZCRod (x indicates the P content of x wt.% used for the loading process).

7.2.2 Material characterization

The as-prepared samples were characterized using powder X-ray diffraction (XRD) on a Bruker D8 DISCOVER X-ray diffractometer with Cu Kα radiation. Scanning electron microscopy (SEM) and energy dispersive X-ray spectroscopy (EDX) were performed by a Hitachi S-4800 equipped

with a Bruker energy-dispersive system (EDS) detector. The Raman spectroscopy was measured using an XploRA PLUS Raman microscope with a 532-nm laser source. The X-ray photoelectron spectroscopy (XPS) was carried out using a PerkinElmer PHI 5440 ESCA System equipped with an Mg anode. The nitrogen adsorption−desorption isotherms and the Brunauer−Emmett−Teller (BET) surface area were measured using Micromeritics ASAP 2020 equipment, and the pore size was calculated from the Barrett−Joyner−Halenda (BJH) adsorption branch. Thermogravimetric analysis (TGA) was conducted with a TA Instrument SDT650 under an argon flow (100 mL min^{-1}) at a heating rate of 10 °C min^{-1} from room temperature to 800 °C.

7.2.3 Coin cell assembly

The electrochemical performance was characterized by using 2030-type coin cells assembled in an argon-filled glovebox, with oxygen and moisture contents below 1 ppm. The electrodes were prepared by mixing the as-prepared materials as the active material, sodium carboxymethyl cellulose and styrene-butadiene rubber as binder, and carbon black as a conductor, with a weight ratio of 80:5:5:10 to form a slurry, which was coated onto a Cu foil current collector (12 μm-thick) using the doctor blade method. After drying and pressing, the Cu foil was punched into disks (1.1 cm in diameter), with typical electrode material loadings of ca. 1-1.1 mg cm^{-2}. A potassium foil was used as the counter electrode. Then, 2.4 M potassium bis(fluoroslufonyl)imide (KFSI) dissolved in ethylene carbonate/ethyl methyl carbonate (1:1, v/v) was employed as an electrolyte.

7.2.4 Electrochemistry measurements

The coin cells were tested on a LAND battery tester, with a cutoff voltage range between 0.01 and 3 V. The current densities and capacities were calculated based on the total mass of P@ZCRod composites loaded on the electrodes. The potassiation behavior was defined as “charge”, because the composites work as anodes. The cyclic voltammetry (CV) and electrochemical impedance spectroscopy (EIS) were measured on a PARSTAT 4000 electrochemical station using a three-electrode cell, with the P@ZCRod composite electrode as the working electrode, a potassium disk as the counter electrode, and a potassium arc as the reference electrode. CV was carried out at a scanning rate of 0.05 mV s^{-1}, while EIS was tested between 10,000 and 0.01 Hz with an amplitude of 10 mV.

7.3 Results and discussion

Fig. 7.1 illustrates the synthesis of red P-impregnated Zn-MOF-74-derived carbon nanorods with accurate morphology modulation. The previously reported Zn-MOF-74 in the literature are typically microcrystalline and have a non-uniform morphology;[320-323] in contrast, we synthesized uniform rod-shaped Zn-MOF-74 (ZRods) with controllable dimensions using a one-step solvothermal reaction between $Zn(CH_3COO)_2$ and 2,5-dihydroxyterephtalic acid ($C_8H_6O_6$), in which the size of the resulting ZRods was significantly affected by varying the H_2O content in the H_2O/*N*,*N*-dimethylformamide (DMF) mixed solvent. The ZRod diameters exhibited an inverted volcano relationship with an increased H_2O content and thus could be well tuned, from tens of nanometers to hundreds of nanometers and further to micrometers, while the length could be tuned from hundreds of nanometers to micrometers.

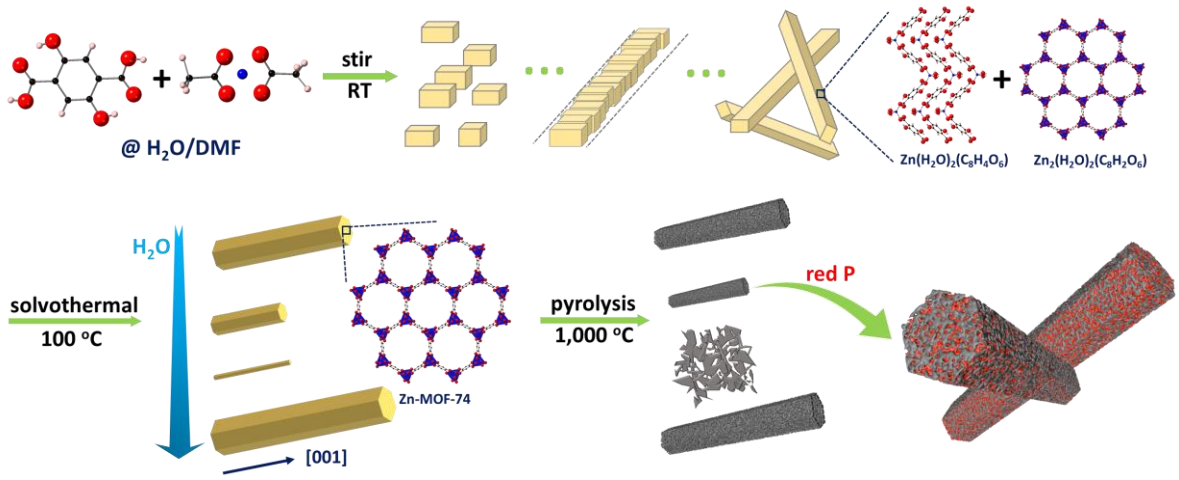

Fig. 7.1 Schematic illustration of the synthesis of ZRods, porous ZCRods, and P@ZCRods composites. The size of the ZRods can be tailored by varying the H_2O content in the mixed solvent H_2O/DMF during the solvothermal process.

The morphologies of ZRods synthesized by varying the H_2O content in the solvothermal reaction are shown in Fig. 7.2a-e and Fig. A1 (in Appendix). All the samples exhibited a clear rod shape within the H_2O/DMF volumetric ratio (v/v) from 0 to 0.167, and a hexagonal cross-section can be observed. This is significantly different from previously reported microcrystalline Zn-MOF-74 (without any specific morphology) synthesized using $Zn(NO_3)_2$ as the Zn source,[320-323] which was verified by our results (Fig. A2). The H_2O content exhibited impressive efficiency in tailoring ZRods from the nanoscale to micron size (Fig. 7.2). The inverted volcano relationship between the ZRod diameters and the H_2O content is summarized in Fig. 7.2f. At first the diameters of the ZRods decreased from ~500 nm (upon a single DMF solvent), and then increased with the increasing H_2O content in the mixed solvent. A minimum diameter of 30-40 nm can be achieved at a volume ratio

of H_2O/DMF = 0.05 (Fig. 7.2c), which consists of ~2400-4200 Zn-MOF-74 1D channels with a pore size of ~10.54 Å.[322] ZRods with diameters > ~80 nm have mild aspect ratios of ~4-7 (Fig. 7.2a,b,d,e and Fig. A1a-e, h-j), while those with diameters < 80 nm have much higher aspect ratios up to ~20 (Fig. 7.2c and Fig. A1f,g), indicating a widely tunable ZRod length ranging from hundreds of nanometers to several micrometers. Another tendency, as shown in Fig. 7.2f, is that smaller ZRod diameters present smaller diameter deviations.

During the reaction, after mixing the $Zn(CH_3COO)_2$ and 2,5-dihydroxyterephtalic acid ($C_8H_6O_6$) solutions together, the clear solution transformed into a yellow suspension within a few seconds, indicating a rapid reaction. This is attributed to the acetate-introduced deprotonation of $C_8H_6O_6$ by competitively accessing the protons in the solution.[324, 325] Upon increasing the H_2O content in the mixed solvent, a slower color transformation was observed. As a result of the increased dosage of H_2O, more protons joined in the competitive reaction and partially supplied the coordination with the carboxyl groups of both $C_8H_6O_6$ and acetate, which slowed down the combination between the $C_8H_6O_6$ and Zn nodes for nucleation. When the reactant of zinc acetate was replaced with zinc nitrate, stirring at room temperature did not lead to nucleation because of the lack of deprotonated $C_8H_6O_6$.[325]

To obtain uniform rod-shaped Zn-MOF-74, we identified CH_3COO^- to be critical to the hexagonal-pillar-shape formation, which has not been clarified before. Very recently, a rod-shaped Zn-MOF-74 was prepared using zinc acetate and 2,5-dihydroxyterephtalic acid in the presence of salicylic acid as a modulator, which was believed to stabilize the active metal sites on the MOF surface and

thus direct its growth;[326] however, the effect of CH_3COO^- was not identified. We noticed that the molecular structure of salicylic acid contains carboxyl and phenolic hydroxyl groups; however, compared with carboxyl groups, the weakly acidic phenolic hydroxyl groups have much weaker interactions with metal ions or clusters.[327, 328] Therefore, the carboxyl groups in carboxylate salts (e.g., zinc acetate) played the same role as those in salicylic acid, promoting the formation of Zn-MOF-74 rods as well. The mechanism was well validated by our synthesized, well-developed Zn-MOF-74 hexagonal nano/microrods in the absence of salicylic acid (Fig. 7.2a-e and Fig. A1). During the reaction, the CH_3COO^- groups preferred to coordinate with the metal nodes around the one-dimensional (1D) channels of Zn-MOF-74. This interaction stabilized the metal nodes, selectively capped the surface, and led to the oriented growth of the Zn-MOF-74 into pillars (Fig. A3).[329, 330] The hexagonal cross-section of MOF pillars indicates the oriented growth is along the [001] direction due to the conformal features with multichannel bundles, as shown in Fig. A3.[331]

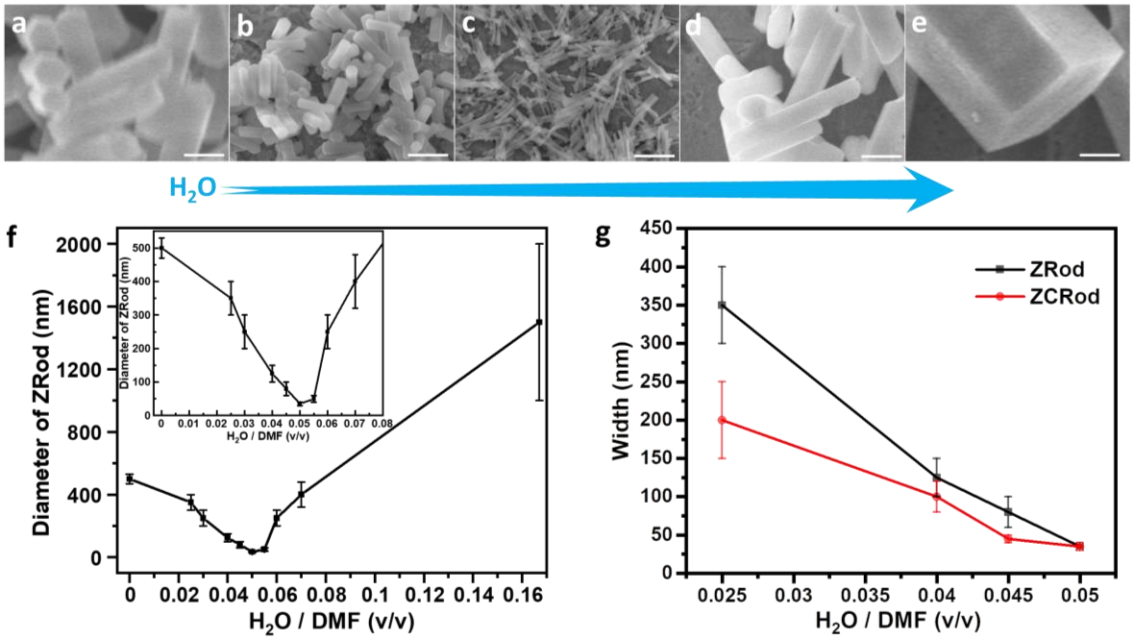

Fig. 7.2 a-e) SEM images of ZRods synthesized with an H_2O/DMF volume ratio of a) 0, b) 0.04, c) 0.05, d) 0.07, and e) 0.167. Scale bar: 500 nm. f) Relationship between the ZRod diameter and the H_2O content as the solvent. g) Comparison of the diameter between the ZRods and ZCRods, indicating the shrinkage of ZRods after carbonization.

H_2O is responsible for the ability to adjust the size of ZRods; a schematic illustration is shown in Fig. A4. Protons, dissociated from H_2O, can coordinate with the carboxyl groups of both $C_8H_6O_6$ and acetate or they can attack/cleave the newly formed coordination bonds of Zn-deprotonated $C_8H_6O_6$,[331, 332] both of which significantly affect the coordination chemistry during the dissolution-recrystallization process of the solvothermal reaction. The protons prefer to satisfy the coordination with the carboxyl groups rather than attack the Zn-deprotonated $C_8H_6O_6$ bonds for its straightforward and relative facile process in this competitive and reversible reaction system. At a low H_2O content (H_2O/DMF < 0.05, v/v), after coordination with the carboxyl groups, fewer

protons dissociated from the H_2O could attack and cleave the newly formed coordination bonds of Zn-deprotonated $C_8H_6O_6$ (dissolution effect), resulting in a relatively free growth of ZRods into larger sizes. At a higher H_2O content (H_2O/DMF > 0.05, v/v), massive protons attack the Zn-deprotonated $C_8H_6O_6$ bonds and dissolve small precipitates, which then reconstruct into larger and more thermodynamically stable ZRods via Ostwald ripening.[327] A minimum-diameter ZRod at H_2O/DMF = 0.05 (v/v) is the trade-off between these two mechanisms dominated at low and high H_2O content ranges. In this scenario, our strategy to use a mixed solvent (i.e., H_2O/DMF) could be potentially effective in morphology control and size tuning for a variety of MOFs with organic carboxylates as links.[282]

To uncover the formation process of ZRods, products in different reaction stages were collected for characterization via scanning electron microscopy (SEM) and X-ray diffraction (XRD) (Fig. A5,6 and details in the Appendix section). The results revealed that by using zinc acetate as the metal source, the crystalline phase of Zn-MOF-74 can form at room temperature through a dynamical transformation from simple, linear $Zn(H_2O)_2(C_8H_4O_6)$ structures into 3D Zn-MOF-74 structures. The carboxyl groups on $C_8H_6O_6$ first coordinate with the Zn nodes, forming a linear structure, and then the weakly acidic phenolic hydroxyl groups join the coordination with the metal nodes, finalizing the 3D MOF structure. The solvothermal condition promotes this transformation process due to the higher energy for the reaction, resulting in phase-pure, more thermodynamically stable Zn-MOF-74 crystals (Fig. 7.1).

The carbonization of ZRods at 1,000 °C in an argon environment yielded Zn-MOF-74-derived carbon nanorods (ZCRods), as shown in Fig. 7.3a-f. In the calcination process, the Zn element in the Zn-MOF-74 first transformed into ZnO, which was subsequently reduced to Zn by carbon and then finally evaporated ($ZnO + C \rightarrow Zn(g) + CO$) while organic ligands decomposed into porous carbonaceous material.[333] The energy-dispersive X-ray spectroscopy (EDX) elemental analysis manifested the derived carbon contained ~93.5 wt.% of C and ~6.5 wt.% of O (Fig. A7a). Among these representative ZCRods that were derived from ZRods with various diameters, ZCRod-0.05 displayed a distinct carbon cluster morphology (Fig. 7.3a) compared with the wire-like precursor (ZRod-0.05), which had a diameter of ~30-40 nm (Fig. 7.2c). Moreover, some wire/rod-like structures could be observed on the carbon cluster surface, indicating significant agglomeration during high-temperature carbonization due to the small size of the precursor.[334] In contrast, ZRods with larger diameters presented much better morphology preservation during calcination, resulting in well-dispersed carbon nanorods (Fig. 7.3b-f). For example, highly separated hexagonal carbon nanorods of ZCRod-0.025 (Fig. 7.3d-f) with a diameter of 150-250 nm were prepared from ZRod-0.025 with a diameter of 300-400 nm. A size shrinkage of ~40% was observed during the thermal decomposition of ZRod-0.025 into ZCRod-0.025 (Fig. 7.2g), which is consistent with the previous report.[326] The SEM images of ZCRod-0.025 at a lower magnification (Fig. 7.3d,e) demonstrate its highly uniform morphology, i.e., ~150-250 nm in diameter and ~800 nm in length. The morphology of ZRod-0.025 precursor was well preserved; a clear hexagonal cross-section can be observed on ZCRod-0.025 (Fig. 7.3e,f), which exhibits a highly porous internal structure covered with a less porous surface (Fig. 7.3f). The diameter shrinkage of ZRods after carbonization are summarized in Fig. 7.2g.

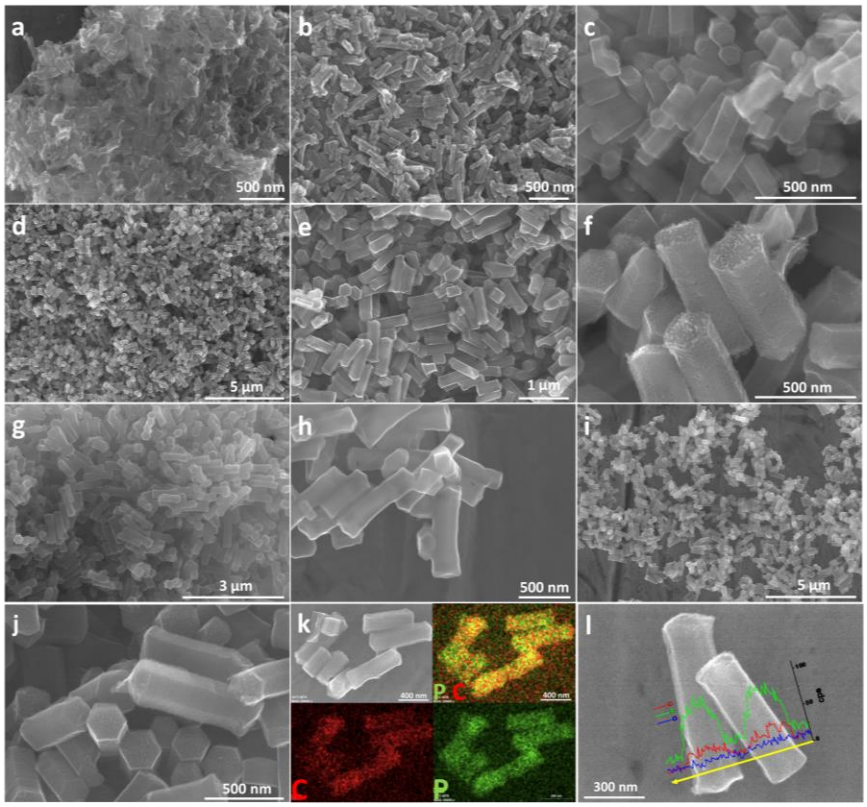

Fig. 7.3 a-f) SEM images of a) ZCRod-0.05, b) ZCRod-0.045, c) ZCRod-0.04, d-f) ZCRod-0.025, g, h) P70@ZCRod-0.025, respectively. i, j) SEM images, k) EDX elemental mapping, and l) line scan of P50@ZCRod-0.025.

As shown in Fig. 7.3, ZCRod-0.025 possesses more uniform morphology with less agglomeration, compared with other samples, which help minimize the possible P deposition between the carbon nanorods; thus, ZCRod-0.025 was used as the carbon matrix for further red P loading. To calculate the theoretical P loading in ZCRod-0.025, its porous structure was examined using N_2 adsorption/desorption (Fig. 7.4f). ZCRod-0.025 exhibited abundant mesopores and the pore volume was measured to be 1.387 $cm^3\ g^{-1}$, allowing for a maximum P loading of 2.529 g per gram of ZCRod-0.025, corresponding to 71.7 wt.% of P in the P@ZCRod-0.025 composite.

P70@ZCRod-0.025 designed with 70 wt.% of P was prepared (P70 indicates a P content of 70 wt.% used for the loading process). After P impregnation using the vaporization-condensation-conversion process, the size and shape of ZCRod-0.025 were retained; however, the surface of the nanorods became smooth and porous structures were no longer observed (Fig. 7.3g,h and Fig. A8). This indicates a successful P loading approaching the utmost loading capacity of ZCRod-0.025 (i.e., 71.7 wt.% of P). The actual P content of P70@ZCRod-0.025 was determined to be ~66 wt.% via thermogravimetric analysis (TGA) (Fig. A9). However, due to the huge volume expansion 290% of P upon potassiation to K_4P_3,[317, 335] the cyclic performance of P70@ZCRod-0.025 is expected to be poor due to the lack of free space for the P expansion.

The optimized P-loading into ZCRod-0.025 was calculated to be 50 wt.% of the P@ZCRod-0.025 composite, leaving just enough free spaces to accommodate the huge volume change of P during cycling (calculation details in the Appendix section). As shown in Fig. 7.3i,j, P50@ZCRod-0.025 presents a porous surface and no P agglomerates can be seen, implying a full impregnation of P into the porous carbon nanorods while leaving free spaces. EDX elemental mapping and line scan analysis demonstrated a homogeneous distribution of P in P50@ZCRod-0.025 (Fig. 7.3k,l). The actual P content was confirmed to be approximately 50 wt.% as designed, by TGA in Fig. A9. As expected, the Brunauer-Emmett-Teller (BET) surface area of ZCRod-0.025 (1,702 $m^2 g^{-1}$) decreased dramatically to ~61 $m^2 g^{-1}$ after P-loading; the micropore characteristic diminished while some mesopores ranging ~3-10 nm were still reserved, which can help to accommodate the P expansion during potassiation (Fig. 7.4f).

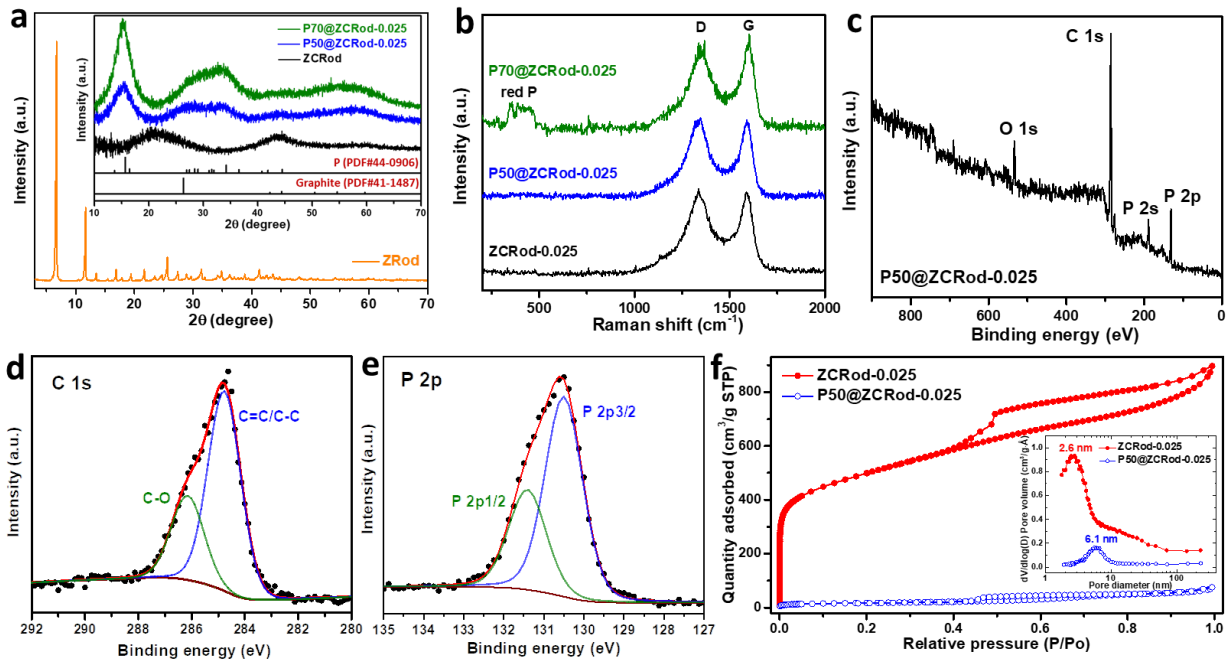

Fig. 7.4 a) XRD pattern of ZRod. Inset: XRD patterns of ZCRod, P50@ZCRod-0.025, and P70@ZCRod-0.025. b) Raman spectra of ZCRod-0.025, P50@ZCRod-0.025, and P70@ZCRod-0.025. c) Global XPS profiles, high-resolution XPS spectra of d) C 1s and e) P 2p of P50@ZCRod-0.025. f) N_2 adsorption-desorption isotherms and pore size distributions (inset) of ZCRod-0.025 and P50@ZCRod-0.025.

XRD patterns are used for phase identification on the products (Fig. 7.4a). Through high-temperature carbonization the highly crystalline Zn-MOF-74 transformed into amorphous carbon, as indicated by the broad peak around 44° corresponding to (101) facet of carbon and the lack of an obvious characteristic peak at ~26° related to a graphitic carbon (002) diffraction. Instead, a very broad peak between 15 and 34° associated with the overlapping of pore structures was observed.[12] After red P infiltration the obtained P50@ZCRod-0.025 and P70@ZCRod-0.025 showed additional peaks located at 15° and 33°, which could be indexed to the monoclinic red P,

while the broad peak associated with the pores had diminished, suggesting the successful incorporation of red P into the porous ZCRod-0.0025 matrix.

As shown in the Raman spectra (Fig. 7.4b), ZCRod-0.025 exhibited two peaks at 1,337 and 1,589 cm^{-1} belonging to the D and G band of carbon, respectively. Their relatively high intensity ratio (I_D/I_G) of ~ 1.02 from peak fitting reveals the highly defective nature of Zn-MOF-74-derived carbon. After P infiltration, the P50@ZCRod-0.025 nanocomposite with a P content of ~50 wt.% maintained a Raman spectrum similar to that of ZCRod-0.025, without any peaks of red P ranging from 300 to 500 cm^{-1}, because P was embedded in the internal pores of ZCRod-0.025, without formation of large crystallites. In contrast, the characteristic peaks of red P were detected in P70@ZCRod-0.025 because, with the maximized P content, the pores on the surface were fully infiltrated with P, forming relatively large P crystallites.

The surface chemical composition and bonding states of P50@ZCRod-0.025 were identified by X-ray photoelectron spectroscopy (Fig. 7.4c-e). C, O, and P elements were detected with an atomic ratio of 79.3:9.1:11.6, corresponding to 65.4:10.0:24.6 wt.%, respectively (Fig. 7.4c). The much lower P content on the surface, i.e., 24.6 wt.%, compared with the overall P content of ~50 wt.% in the composite, further illustrates a preferential P impregnation into the internal structures of ZCRod-0.025. The deconvoluted C 1s and P 2p spectra demonstrate that C exists in the form of C=C/C-C and C-OH/C-O-C (Fig. 7.4d), and P is in the elemental state (Fig. 7.4e). The hierarchical structure of P50@ZCRod-0.025, with red P well encapsulated in the internal pores, could provide

robust protection to the active P when applied as the anode for PIBs, benefiting long-term cycling stability.

P@ZCR-0.025 were applied as anode materials for PIBs. As expected, due to the higher red P mass-loading, P70@ZCRod-0.025 delivered a higher initial reversible capacity (depotassiation) of 763.2 mAh g^{-1} at 50 mA g^{-1}, with a remarkable initial Coulombic efficiency (CE) of 84.4%. However, the red P fully loaded P70@ZCRod-0.025 presented rapid capacity fading from the 13th cycle with CE deterioration (Fig. 7.5a). In contrast, P50@ZCRod-0.025 possessed a reversible capacity of 589.2 mAh g^{-1} and an initial CE of 78.5%; a reversible capacity of 401.8 mAh g^{-1} was maintained at 100 mA g^{-1} for the 75th cycle with a CE > 99%. This proved that P50@ZCRod-0.025 possessed enough reserved free spaces to accommodate the P expansion upon potassiation without damaging the composite nanostructure.

The galvanostatic charge/discharge profiles of P50@ZCRod-0.025 (Fig. 7.5b) revealed that after the first cycle of activation a maximum reversible capacity of 595.8 mAh g^{-1} was achieved in the second cycle, and the CE increased to 97.1% from the initial 78.5%, indicating the high electrochemical reversibility of P50@ZCRod-0.025. Subtracting the capacity contribution from the carbon matrix (Fig. A10), the P component in this composite contributed ~1,029 mAh g^{-1}, beyond the theoretical capacity of forming KP (865 mAh g^{-1}), approaching 90% of that for K_4P_3 (1,154 mAh g^{-1}). Therefore, K_4P_3 is confirmed to be the final potassiation phase. The specific energy density of the P50@ZCRod-0.025 composite at 50 mA g^{-1} was calculated to be ~1,495 Wh kg^{-1} by selecting a popular $K_xMnFe(CN)_6$ as a reference cathode, which has an average voltage of

~3.6 V;[336] in contrast, commercial graphite anode showed a specific energy density of 863 Wh kg^{-1} (Fig. A11).

The potassiation/depotassiation process was investigated using cyclic voltammetry (CV). As shown in Fig. 7.5g, during the first cathodic scan three peaks at 1.55, 0.82, and 0.12 V are observed, followed by an uncompleted peak with scanning down to 0.01 V. The broad peak at 0.82 V, which disappears in the subsequent cycles, is assigned to the solid electrolyte interphase (SEI) formation due to the decomposition of carbonate electrolyte, which usually happens at 0.5-1.0 V.[317, 335] The other peaks are ascribed to the potassiation of P to form various K_xP phases. The subsequent cathodic scans show three peaks at 1.67, 1.10, and 0.24 V, followed by the unfinished peak at a lower voltage. Recently we investigated the potassiation process of a highly crystalline red P nanorod/C composite through the *dQ*/*dV* plot upon the initial charge curve (potassiation), indicating a stepwise reaction as $P \rightarrow KP_{15} \rightarrow K_3P_{11} \rightarrow K_4P_6 \rightarrow KP \rightarrow K_4P_3$.[335] In light of the different capacity of K_xP phases, the cathodic peaks around 1.67, 1.10, and 0.24 V are assigned to the formation of KP_{15}, K_3P_{11}, and K_4P_6/KP, respectively, followed by a further transformation into K_4P_3 as the final potassiation phase. Four anodic peaks at 0.24, 0.66, 1.60, and 2.05 V revealed a stepwise depotassiation process accordingly.[335] The well-overlapped peaks after first cathodic scan demonstrated the excellent electrochemical reversibility and cycling stability of P50@ZCRod-0.025 as an anode for PIBs. In addition, the redox peaks in CV scans are very consistent with the voltage plateaus shown in Fig. 7.5b, thereby supporting a stepwise potassiation/depotassiation mechanism.

The rate capability of the P50@ZCRod-0.025 anode is shown in Fig. 7.5c,d, which indicates the reversible capacities of 579.8, 549.6, 506.7, 458.3, 384.8, 255.7, and 187.5 mAh g^{-1} at 0.05, 0.1, 0.25, 0.5, 1, 2.5, and 5 A g^{-1} , respectively. An impressive capacity retention of 32.3% was demonstrated when the discharge rate increased from 0.05 to 5 A g^{-1}. With the current density back to 0.1 A g^{-1}, the capacity recovered to 543 mAh g^{-1} again and the anode could still be sustainably cycled afterwards, with the CE close to 100%, revealing an excellent rate capability, a highly reversible reaction, and robust cycling stability. Fig. 7.5e compares the rate capability of the P50@ZCRod-0.025 anode with other P/C composite anodes for PIBs in the literature. Obviously, our P50@ZCRod-0.025 performed much better than red P@3D carbon sheets,[318] red P@mesoporous carbon,[128] red P@active carbon,[12] red P@rGO,[337] black P/carbon composites,[314, 338] and even the red P/CNT/Ketjen black composite whose specific capacity is calculated based on the mass of red P.[127] Very recently we reported a P@hollow carbon yolk/shell nanocomposite as an anode for PIBs that demonstrated a record reversible capacity and very good rate capability (Fig. 7.5e), primarily due to the high P content of 75 wt.% in the composite, but its stable cycling was limited within 40 cycles.[335] Thus, the P50@ZCRod-0.025 anode still stands out for its long cycling stability and higher capacity retention, i.e., 32.2% of P50@ZCRod-0.025 *vs.* 29% of P@hollow carbon, when the current density increased from 0.05 to 5 A g^{-1}. The superior rate capability is associated with the low impedance (Fig. A12), which was measured using a three-electrode cell after two activation cycles. The impedance decreased with the increase of the state of charge (SOC), similar to that of the P@hollow carbon composite.[335] By fitting the impedance spectra with equivalent circuits in Fig. A13, the fitting results of the impedance spectra at various SOCs for P50@ZCRod-0.025 were shown in Table A1. Take the impedance of P50@ZCRod-0.025 at the 50%-SOC as an example, showing an Ohmic resistance of 1.7 Ohm, total charge

transfer resistances for carbon and K-P alloys of 36 Ohm, and a K-ion diffusion resistance of 43.5 Ohm (Table A1). The decreased impedance with increased SOC is likely due to the conductivity enhancement of the K-P alloys with the increase of metallic K contents[339, 340] and improved contact between the expanded K-P alloys and the carbon matrix, i.e., the volume expansion of red P during potassiation provides new contact with carbon pores in the previously reserved void spaces.

The cyclic performance of the P50@ZCRod-0.025 anode was also evaluated at a high current density of 2.5 A g^{-1} (Fig. 7.5f), which showed a reversible capacity of 289.6 mAh g^{-1} and retained 150.7 mAh g^{-1} after 400 cycles with a CE of ~100%, thereby indicating high cycling stability. The outstanding cyclic performance of the composite anode is related to its stable hierarchical structure, in which red P is well encapsulated in the internal pores of the carbon nanorods and thus provides robust protection to the electrochemical active P during cycling, while the reserved free space accommodates the volume expansion of P without damaging the integrity of the composite. This is supported by the SEM analysis on the P50@ZCRod-0.025 electrode after cycling. As shown in Fig. A14, the electrode constituted with well-dispersed and uniform P50@ZCRod-0.025 remained intact without visible cracks (Fig. A14a,b); meanwhile, P50@ZCRod-0.025 perfectly maintained their integrity and morphology, i.e., hexagonal pillars (Fig. A14c,d), thus demonstrating the structural stability of our nanocomposite and the effectiveness of reserving free space in porous carbon matrix to address the huge volume variation of P during K-ion insertion/extraction.

The P50@ZCRod-0.025 nanocomposite stands out among the various phosphorus-based anodes for PIBs reported to date for its superior potassium storage performance in terms of remarkable

initial CE (78.5%), top-ranking reversible capacity (up to 595.8 mAh g^{-1}), high-efficient use of red P (contributed ~1,029 mAh g^{-1} as P in nanocomposite), superior rate capability (187.5 mAh g^{-1} at 5 A g^{-1}), and robust long-term cycling stability (retaining 150.7 mAh g^{-1} at 2.5 A g^{-1} after 400 cycles) (Table A2). Its outstanding electrochemical performance is primarily attributed to the unique structural advantages of ZCRod-0.025 as a porous carbon matrix for P impregnation. First, the carefully modulated ZCRod-0.025 with a diameter around 200 nm ensures a uniform material morphology and very good dispersity as an anode in practice (Fig. 7.3i,j, and Fig. A14), providing conductive nanoscaffolds for electrochemical-active but poor electrical-conducting red P to boost rate capability. Second, the highly mesoporous structure of ZCRod-0.025 has a high pore volume (1.387 cm^3 g^{-1}) and thus allows for high P loading along with the reserved free space to accommodate the volume expansion of the P during potassiation, benefiting a high specific capacity and cycling stability. Third, the carbon nanopores confine the red P into nanoscale, which relieves the absolute volume change and strain during the potassiation/depotassiation process and diminishes the K-ion diffusion path, thereby enhancing the electrochemical reversibility of red P. Lastly, the hierarchical structure of ZCRod-0.025 has more internal pores and thus well encapsulates the red P in P50@ZCRod-0.025, providing robust protection to the active P and resulting in high CE and long cycling stability.

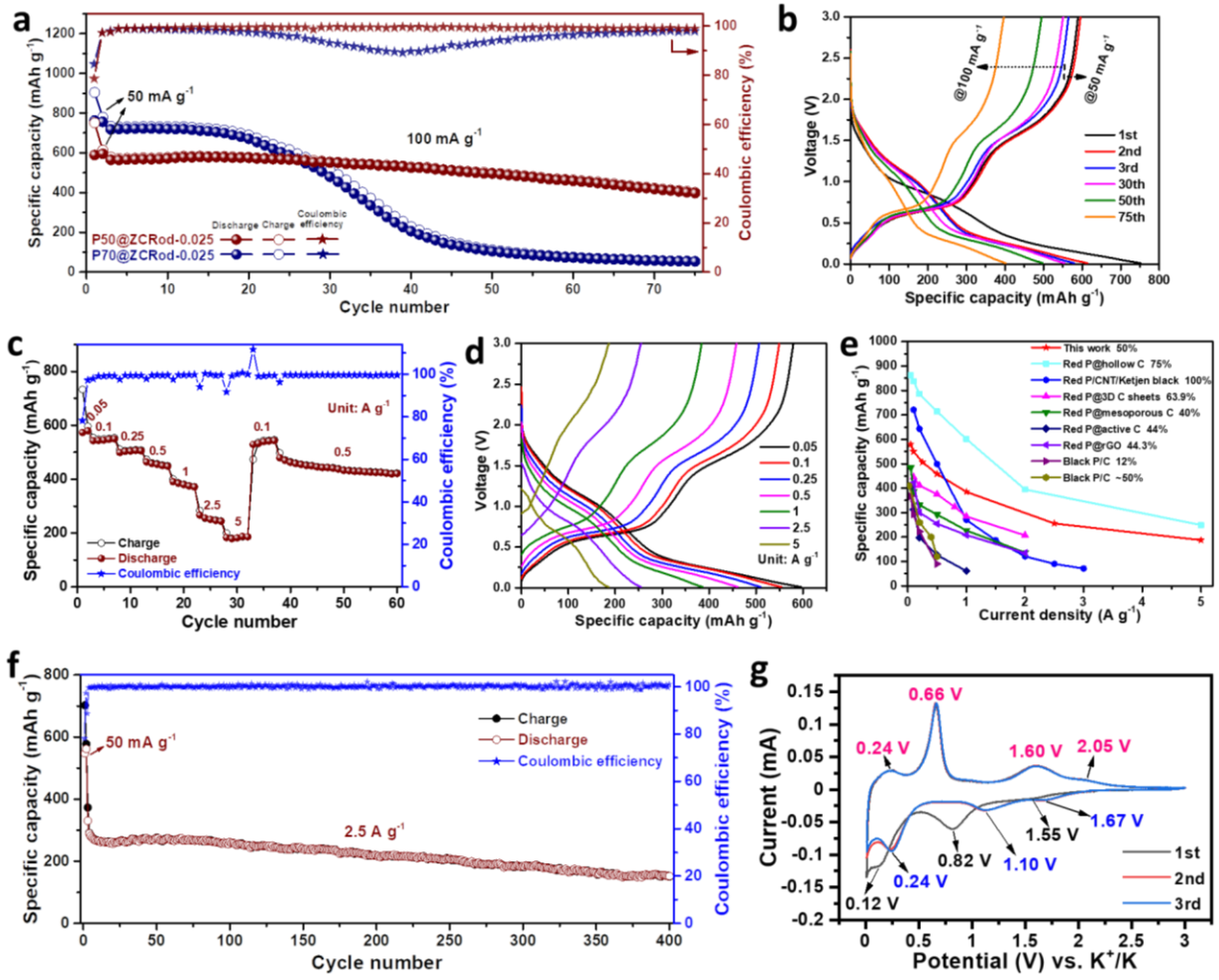

Fig. 7.5 Electrochemical Performance of the P50@ZCRod-0.025 anode. a) Cyclic performance at 100 mA g^{-1} after initial two cycles of activation at 50 mA g^{-1}, compared with P70@ZCRod-0.025, b) charge/discharge curves, c, d) rate capability, and e) comparison with other P/C anodes (specific capacities are calculated based on the mass of composites; the weight contents of P are indicated after annotations), f) cyclic performance at 2.5 A g^{-1} after the initial two cycles of activation at 50 mA g^{-1}, and g) cyclic voltammetry.

7.4 Summary and conclusions

A very facile solvothermal method has been developed for the synthesis of uniform Zn-MOF-74 hexagonal nano/microrods, whose diameter can be accurately modulated from tens of nanometers to micron size by varying the H_2O content in the mixed solvent. An inverted volcano relationship between the ZRod diameters and H_2O contents has been observed. This morphology and size modulation on Zn-MOF-74 is attributed to the orientational coordination of carboxylates with metal nodes and a competitive reaction of protons dissociated from H_2O. The tailored Zn-MOF-74 enables the hierarchically porous carbon nanorods (ZCRod-0.025) with more internal pores and very good dispersity, via calcination. When applied as a carbon matrix for red P impregnation, ZCRod-0.025 exhibited a high loading capacity and perfect encapsulation of P in P50@ZCRod-0.025, resulting in superior potassium storage performance, with a remarkable initial CE (78.5%), top-ranking reversible capacity (up to 595.8 mAh g^{-1}), superior rate capability (187.5 mAh g^{-1} at 5 A g^{-1}), and robust long-term cycling stability (retaining 150.7 mAh g^{-1} at 2.5 A g^{-1} after 400 cycles), thereby standing out among the various phosphorus-based anodes for PIBs reported to date. Therefore, this P50@ZRCod-0.025 nanocomposite can be a very promising anode material for PIBs. Furthermore, the methodology for Zn-MOF-74 not only promotes advanced applications of Zn-MOF-74 as well as its derived carbon materials, but also potentially opens a general route in MOF chemistry for the oriented evolution of various carboxylate-based MOFs.

CHAPTER 8 CONCLUSIONS AND OUTLOOK

8.1 Summary of dissertation work

In summary, owing to the distinctive and fascinating properties of nanomaterials with different dimensions, they offer potential scientific solutions to environmental and energy challenges that human beings are facing. Rational design, synthesis, and integration of different nanomaterials is an effective way to improve the performance and realize real device applications. In this dissertation research, the deposition method of graphene oxide (GO) onto electrodes is firstly improved, which enables a reliable fabrication of high-quality rGO-based FET devices. Through a combination of probe modified 0D Au nanoparticle, 2D rGO, and Al_2O_3 thin film, an effective sensing platform has been realized for water contamination monitoring. Assisted by a novel pulse-driven capacitive signal transduction mechanism, this sensing platform can achieve selective and ultrahigh sensitive detection of lead ions in water, with a LOD < 1 ppb and a sensitivity ~350% for 2.5 ppb of lead ions. When employed for the Ebola-glycoprotein (GP) detection, among those different electronic parameters driven by an AC voltage input, the maximum sensitivity was calculated from the inflection-resonance frequency on the phase spectrum: a sensitivity of ~36−160% corresponding to 0.001−3.401 mg/L of Ebola-GP can be achieved from the high inflection-resonance frequency. More importantly, the sensing platform structure and the high-efficiency signal transduction mechanism can be applied in other FET-based sensing devices for better performance. Following the percolation theory analysis on a 2D continuum model, a scalable micromolding-in-capillary method and an inkjet printing technique have also been investigated for sensor fabrication in order to minimize the fabrication cost of the rGO/MoS_2-based FET sensors.

Combining the high capacity of 0D SnO_2 nanoparticles with excellent mechanical and electrical properties of rGO, a SnO_2/Sn-rGO sandwiched nanocomposite has been prepared through facile metal-organic precursor coating on GO and an in-situ transformation strategy. When applied as an anode for LIBs, the structural robustness and electrochemical reversibility of the SnO_2/Sn-rGO nanocomposite were demonstrated by the superior Li storage capability of a reversible capacity of 1,307 mAh g^{-1} at a current density of 80 mA g^{-1} and a stable capacity of 767 mAh g^{-1} after 200 cycles when cycling at 400 mA g^{-1}. Moreover, the SnO_2/Sn-rGO composite delivered a highly stable capacity of 449 mA g^{-1} without obvious decay after 400 cycles at a higher current density of 1,600 mA g^{-1}. Because of the abundant potassium reserves, potassium-ion batteries (PIBs) have the potential to realize large-scale applications at a low cost. In order to harness the high capacity of red P as an anode for PIBs, Zn-MOF-74 derived nanoporous carbon nanorods were synthesized as an impregnation matrix via a facile morphology adjustment on Zn-MOF-74 using a mixed-solvent strategy. The prepared P@C nanocomposite displayed outstanding potassium storage performance in terms of initial Coulombic efficiency (78.5%), reversible capacity (up to 595.8 mAh g^{-1}), rate capability (187.5 mAh g^{-1} at 5 A g^{-1}), and long-term cycling stability (retaining 150.7 mAh g^{-1} at 2.5 A g^{-1} after 400 cycles). Therefore, the P@C nanocomposite can be a very promising anode material for PIBs. Furthermore, the methodology for ZnMOF-74 not only promotes advanced applications of Zn-MOF-74 as well as its derived carbon materials, but also potentially opens a general route in MOF chemistry for the oriented evolution of various carboxylate-based MOFs.

8.2 Proposed future research directions

Inkjet printing, as a typical non-contact printing technique, is very attractive in the field of printing nanoelectronic devices such as sensors because of its high compatibility with both the printed nanosized materials and types of substrates, efficient material usage, and easily tailorable printing patterns. We have successfully printed MoS_2 channels having good semiconducting properties, and further printed a fully functioning FET water sensor with an MoS_2 channel and graphene electrodes. The device demonstrated the capability of heavy metal ion detection in water. But a dilemma between the semiconducting performance (e.g., current on/off ratio) and device variation of the printed MoS_2 channels exists, i.e., devices with better semiconducting performance usually have larger sensing signal variations. Further ink formulation (e.g., through adjusting the IPA/2-butanol of the solvent system) to further suppress the CRE and printing condition optimization to improve the deposition uniformity are suggested to achieve more uniform and better semiconducting performance of the printed MoS_2 sensing channels, which leads to a higher sensitivity and better signal uniformity of the fabricated senser devices. In addition, efforts are needed to further investigate the interactions between chemical probes and heavy metal ions through in-situ characterization techniques, which could guide us to design new sensing probes with higher sensitivity and selectivity.

We have demonstrated the facile solvothermal synthesis of uniform Zn-MOF-74 hexagonal nano/microrods (ZRods) with an accurate diameter modulation, and proposed a regulation mechanism for the morphology and size modulation based on the capping effect of the carboxyl groups and a competitive reaction of protons dissociated from H_2O. This methodology for Zn-MOF-74 could be potentially effective in tuning other MOFs with organic carboxylates as links.

Efforts should be made to investigate the feasibility of this modulation method onto other carboxylate-based MOFs such as MOF-5 and MOF-177. If this methodology is proved to be universal, it could be used for the directed evolution of a vast amount of MOFs and promote their advanced applications. Once uniform MOF crystals are obtained, ordered superframeworks or arrangements could be constructed. For example, MOF-74 nanorods could be aligned by entropic force into rod bundles to take full advantage of the structural features of MOF-74, i.e., the honeycomb pattern of rods and pores are along the crystallographic *c* axis, which is excellent for liquid filtration or gas separation. Along this line of thinking, in the future, an elaborate, cascade multivariate MOF bundle would be able to process the guest molecule step by step in these functionalized microreactors until the final product.

The synthesized Zn-MOF-74 derived carbon nanorods exhibited abundant mesopores and the pore volume was measured to be 1.387 $cm^3 g^{-1}$, allowing for a maximum P loading 71.7 wt.% of P in the P@C composite. The developed P@C nanocomposite with an optimized phosphorus loading of 50 wt.% in the composite displayed impressive potassium storage performance such as a top-ranking reversible capacity (up to 595.8 mAh g^{-1}). There are still many MOF/COF-derived carbons having larger pore volumes, which could accommodate more phosphorous for a higher capacity when used as battery anodes. For example, MOF-5 derived carbon having a very high total pore volumes, up to 5.53 $cm^3 g^{-1}$,[333] promises a much higher phosphorus loading, but may be previously limited by its micro-sized and non-uniform morphology. The MOF modulation method reported here may help to realize both size and morphology regulation on MOF-5, and its derived carbon matrices are worth exploration in the preparation of P@C composites for battery anodes.

REFERENCES

1. Landrigan, P. J.; Fuller, R.; Acosta, N. J. R.; Adeyi, O.; Arnold, R.; Basu, N. N.; Balde, A. B.; Bertollini, R.; Bose-O'Reilly, S.; Boufford, J. I.; Breysse, P. N.; Chiles, T.; Mahidol, C.; Coll-Seck, A. M.; Cropper, M. L.; Fobil, J.; Fuster, V.; Greenstone, M.; Haines, A.; Hanrahan, D.; Hunter, D.; Khare, M.; Krupnick, A.; Lanphear, B.; Lohani, B.; Martin, K.; Mathiasen, K. V.; McTeer, M. A.; Murray, C. J. L.; Ndahimananjara, J. D.; Perera, F.; Potocnik, J.; Preker, A. S.; Ramesh, J.; Rockstrom, J.; Salinas, C.; Samson, L. D.; Sandilya, K.; Sly, P. D.; Smith, K. R.; Steiner, A.; Stewart, R. B.; Suk, W. A.; van Schayck, O. C. P.; Yadama, G. N.; Yumkella, K.; Zhong, M., The Lancet Commission on Pollution and Health. *Lancet* **2018,** *391* (10119), 462-512.

2. Zhang, H. B.; Nai, J. W.; Yu, L.; Lou, X. W., Metal-Organic-Framework-Based Materials as Platforms for Renewable Energy and Environmental Applications. *Joule* **2017,** *1* (1), 77-107.

3. Liu, D.; Ni, K.; Ye, J.; Xie, J.; Zhu, Y.; Song, L., Tailoring the Structure of Carbon Nanomaterials toward High-End Energy Applications. *Adv. Mater.* **2018,** *30* (48), e1802104.

4. Sun, H.; Zhang, Y.; Zhang, J.; Sun, X. M.; Peng, H. S., Energy Harvesting and Storage in 1d Devices. *Nature Reviews Materials* **2017,** *2* (6).

5. Dang, S.; Zhu, Q. L.; Xu, Q., Nanomaterials Derived from Metal-Organic Frameworks. *Nature Reviews Materials* **2018,** *3* (1).

6. Perreault, F.; Fonseca de Faria, A.; Elimelech, M., Environmental Applications of Graphene-Based Nanomaterials. *Chem. Soc. Rev.* **2015,** *44* (16), 5861-96.

7. Mao, S.; Chang, J.; Pu, H.; Lu, G.; He, Q.; Zhang, H.; Chen, J., Two-Dimensional Nanomaterial-Based Field-Effect Transistors for Chemical and Biological Sensing. *Chem. Soc. Rev.* **2017,** *46* (22), 6872-6904.

8. Zhang, H. Y.; Wang, Y.; Xiao, S.; Wang, H.; Wang, J. H.; Feng, L., Rapid Detection of Cr(vi) Ions Based on Cobalt(ii)-Doped Carbon Dots. *Biosens. Bioelectron.* **2017,** *87*, 46-52.

9. Vikesland, P. J., Nanosensors for Water Quality Monitoring. *Nat. Nanotechnol.* **2018,** *13* (8), 651-660.

10. Roser, H. R. a. M., Energy Production & Changing Energy Sources. OurWorldInData.org, 2019.

11. Panwar, N. L.; Kaushik, S. C.; Kothari, S., Role of Renewable Energy Sources in Environmental Protection: A Review. *Renew Sust Energ Rev* **2011,** *15* (3), 1513-1524.

12. Huang, X. K.; Liu, D.; Guo, X. R.; Sui, X. Y.; Qu, D. Y.; Chen, J. H., Phosphorus/Carbon Composite Anode for Potassium-Ion Batteries: Insights into High Initial Coulombic Efficiency

and Superior Cyclic Performance. *Acs Sustainable Chemistry & Engineering* **2018,** *6* (12), 16308-16314.

13. Sun, Y. M.; Liu, N. A.; Cui, Y., Promises and Challenges of Nanomaterials for Lithium-Based Rechargeable Batteries. *Nature Energy* **2016,** *1*, 16071.

14. Pokropivny, V. V.; Skorokhod, V. V., Classification of Nanostructures by Dimensionality and Concept of Surface Forms Engineering in Nanomaterial Science. *Mat Sci Eng C-Bio S* **2007,** *27* (5-8), 990-993.

15. I, G. A., Glossary of Nano Technology and Related Terms - Nanostructured Material.

16. Alivisatos, A. P., Perspectives on the Physical Chemistry of Semiconductor Nanocrystals. *J. Phys. Chem.* **1996,** *100* (31), 13226-13239.

17. Roduner, E., Size Matters: Why Nanomaterials Are Different. *Chem. Soc. Rev.* **2006,** *35* (7), 583-92.

18. Stark, W. J.; Stoessel, P. R.; Wohlleben, W.; Hafner, A., Industrial Applications of Nanoparticles. *Chem. Soc. Rev.* **2015,** *44* (16), 5793-805.

19. Hvolbaek, B.; Janssens, T. V. W.; Clausen, B. S.; Falsig, H.; Christensen, C. H.; Norskov, J. K., Catalytic Activity of Au Nanoparticles. *Nano Today* **2007,** *2* (4), 14-18.

20. Zhu, Q. L.; Xu, Q., Immobilization of Ultrafine Metal Nanoparticles to High-Surface-Area Materials and Their Catalytic Applications. *Chem* **2016,** *1* (2), 220-245.

21. Wang, C.; Ciganda, R.; Salmon, L.; Gregurec, D.; Irigoyen, J.; Moya, S.; Ruiz, J.; Astruc, D., Highly Efficient Transition Metal Nanoparticle Catalysts in Aqueous Solutions. *Angew Chem Int Ed Engl* **2016,** *55* (9), 3091-5.

22. Green, I. X.; Tang, W. J.; Neurock, M.; Yates, J. T., Spectroscopic Observation of Dual Catalytic Sites During Oxidation of Co on a Au/TiO_2 Catalyst. *Science* **2011,** *333* (6043), 736-739.

23. Shang, L.; Liang, Y. H.; Li, M. Z.; Waterhouse, G. I. N.; Tang, P.; Ma, D.; Wu, L. Z.; Tung, C. H.; Zhang, T. R., "Naked" Magnetically Recyclable Mesoporous Au-Gamma-Fe_2O_3 Nanocrystal Clusters: A Highly Integrated Catalyst System. *Adv. Funct. Mater.* **2017,** *27* (9).

24. Strickler, A. L.; Escudero-Escribano, M. A.; Jaramillo, T. F., Core-Shell Au@Metal-Oxide Nanoparticle Electrocatalysts for Enhanced Oxygen Evolution. *Nano Lett.* **2017,** *17* (10), 6040-6046.

25. Poizot, P.; Laruelle, S.; Grugeon, S.; Dupont, L.; Tarascon, J. M., Nano-Sized Transition-Metal Oxides as Negative-Electrode Materials for Lithium-Ion Batteries. *Nature* **2000,** *407* (6803), 496-9.

26. Ahn, H. J.; Choi, H. C.; Park, K. W.; Kim, S. B.; Sung, Y. E., Investigation of the Structural and Electrochemical Properties of Size-Controlled SnO_2 Nanoparticles. *J. Phys. Chem. B* **2004,** *108* (28), 9815-9820.

27. Faraday, M., X. The Bakerian Lecture. —Experimental Relations of Gold (and Other Metals) to Light. *Philosophical Transactions of the Royal Society of London* **1857,** *147*, 145-181.

28. Dreaden, E. C.; Alkilany, A. M.; Huang, X.; Murphy, C. J.; El-Sayed, M. A., The Golden Age: Gold Nanoparticles for Biomedicine. *Chem. Soc. Rev.* **2012,** *41* (7), 2740-79.

29. Wang, X.; Qian, X. M.; Beitler, J. J.; Chen, Z. G.; Khuri, F. R.; Lewis, M. M.; Shin, H. J. C.; Nie, S. M.; Shin, D. M., Detection of Circulating Tumor Cells in Human Peripheral Blood Using Surface-Enhanced Raman Scattering Nanoparticles. *Cancer Res* **2011,** *71* (5), 1526-1532.

30. Dreaden, E. C.; Mwakwari, S. C.; Sodji, Q. H.; Oyelere, A. K.; El-Sayed, M. A., Tamoxifen-Poly(Ethylene Glycol)-Thiol Gold Nanoparticle Conjugates: Enhanced Potency and Selective Delivery for Breast Cancer Treatment. *Bioconjug Chem* **2009,** *20* (12), 2247-53.

31. Tang, Z.; Ahuja, T.; Wang, S.; Wang, G., Near Infrared Luminescence of Gold Nanoclusters Affected by the Bonding of 1,4-Dithiolate Durene and Monothiolate Phenylethanethiolate. *Nanoscale* **2012,** *4* (14), 4119-24.

32. Hou, W.; Dasog, M.; Scott, R. W., Probing the Relative Stability of Thiolate- and Dithiolate-Protected Au Monolayer-Protected Clusters. *Langmuir* **2009,** *25* (22), 12954-61.

33. Yee, C. K.; Ulman, A.; Ruiz, J. D.; Parikh, A.; White, H.; Rafailovich, M., Alkyl Selenide- and Alkyl Thiolate-Functionalized Gold Nanoparticles: Chain Packing and Bond Nature. *Langmuir* **2003,** *19* (22), 9450-9458.

34. Hu, B.; Kong, F.; Gao, X.; Jiang, L.; Li, X.; Gao, W.; Xu, K.; Tang, B., Avoiding Thiol Compound Interference: A Nanoplatform Based on High-Fidelity Au-Se Bonds for Biological Applications. *Angew Chem Int Ed Engl* **2018,** *57* (19), 5306-5309.

35. Quek, S. Y.; Choi, H. J.; Louie, S. G.; Neaton, J. B., Thermopower of Amine-Gold-Linked Aromatic Molecular Junctions from First Principles. *ACS Nano* **2011,** *5* (1), 551-7.

36. Li, Z.; Kosov, D. S., Nature of Well-Defined Conductance of Amine-Anchored Molecular Junctions: Density Functional Calculations. *Phys. Rev. B* **2007,** *76* (3), 035415.

37. Aslam, M.; Fu, L.; Su, M.; Vijayamohanan, K.; Dravid, V. P., Novel One-Step Synthesis of Amine-Stabilized Aqueous Colloidal Gold Nanoparticleselectronic Supplementary Information (Esi) Available: Ftir, Tem, Uv-Vis and Xrd Results. See http://www.rsc.org/suppdata/jm/b4/b402823f. *J. Mater. Chem.* **2004,** *14* (12), 1795.

38. Wulandari, P.; Nagahiro, T.; Michioka, K.; Tamada, K.; Ishibashi, K.-i.; Kimura, Y.; Niwano, M., Coordination of Carboxylate on Metal Nanoparticles Characterized by Fourier Transform Infrared Spectroscopy. *Chem. Lett.* **2008,** *37* (8), 888-889.

39. Walter, M.; Akola, J.; Lopez-Acevedo, O.; Jadzinsky, P. D.; Calero, G.; Ackerson, C. J.; Whetten, R. L.; Gronbeck, H.; Hakkinen, H., A Unified View of Ligand-Protected Gold Clusters as Superatom Complexes. *Proc Natl Acad Sci U S A* **2008,** *105* (27), 9157-62.

40. Ligare, M. R.; Baker, E. S.; Laskin, J.; Johnson, G. E., Ligand Induced Structural Isomerism in Phosphine Coordinated Gold Clusters Revealed by Ion Mobility Mass Spectrometry. *Chem Commun (Camb)* **2017,** *53* (53), 7389-7392.

41. Wolfbeis, O. S., An Overview of Nanoparticles Commonly Used in Fluorescent Bioimaging. *Chem. Soc. Rev.* **2015,** *44* (14), 4743-4768.

42. Lv, H.; Xi, Z.; Chen, Z.; Guo, S.; Yu, Y.; Zhu, W.; Li, Q.; Zhang, X.; Pan, M.; Lu, G.; Mu, S.; Sun, S., A New Core/Shell NiAu/Au Nanoparticle Catalyst with Pt-Like Activity for Hydrogen Evolution Reaction. *J. Am. Chem. Soc.* **2015,** *137* (18), 5859-62.

43. Saha, K.; Agasti, S. S.; Kim, C.; Li, X.; Rotello, V. M., Gold Nanoparticles in Chemical and Biological Sensing. *Chem. Rev.* **2012,** *112* (5), 2739-79.

44. Ahmad, R.; Griffete, N.; Lamouri, A.; Felidj, N.; Chehimi, M. M.; Mangeney, C., Nanocomposites of Gold Nanoparticles@Molecularly Imprinted Polymers: Chemistry, Processing, and Applications in Sensors. *Chem. Mater.* **2015,** *27* (16), 5464-5478.

45. Chai, F.; Wang, C.; Wang, T.; Li, L.; Su, Z., Colorimetric Detection of Pb^{2+} Using Glutathione Functionalized Gold Nanoparticles. *ACS Appl Mater Interfaces* **2010,** *2* (5), 1466-70.

46. Thakur, B.; Zhou, G.; Chang, J.; Pu, H.; Jin, B.; Sui, X.; Yuan, X.; Yang, C. H.; Magruder, M.; Chen, J., Rapid Detection of Single E. Coli Bacteria Using a Graphene-Based Field-Effect Transistor Device. *Biosens. Bioelectron.* **2018,** *110*, 16-22.

47. Das, S.; Jayaraman, V., SnO_2: A Comprehensive Review on Structures and Gas Sensors. *Prog. Mater Sci.* **2014,** *66*, 112-255.

48. Han, X.; Jin, M.; Xie, S.; Kuang, Q.; Jiang, Z.; Jiang, Y.; Xie, Z.; Zheng, L., Synthesis of Tin Dioxide Octahedral Nanoparticles with Exposed High-Energy {221} Facets and Enhanced Gas-Sensing Properties. *Angew Chem Int Ed Engl* **2009,** *48* (48), 9180-3.

49. Zhang, J.; Guo, J.; Xu, H.; Cao, B., Reactive-Template Fabrication of Porous SnO_2 Nanotubes and Their Remarkable Gas-Sensing Performance. *ACS Appl Mater Interfaces* **2013,** *5* (16), 7893-8.

50. Deng, Y. F.; Fang, C. C.; Chen, G. H., The Developments of SnO_2/Graphene Nanocomposites as Anode Materials for High Performance Lithium Ion Batteries: A Review. *J. Power Sources* **2016,** *304*, 81-101.

51. Kim, H.; Park, G. O.; Kim, Y.; Muhammad, S.; Yoo, J.; Balasubramanian, M.; Cho, Y. H.; Kim, M. G.; Lee, B.; Kang, K.; Kim, H.; Kim, J. M.; Yoon, W. S., New Insight into the Reaction Mechanism for Exceptional Capacity of Ordered Mesoporous SnO_2 Electrodes via Synchrotron-Based X-Ray Analysis. *Chem. Mater.* **2014,** *26* (22), 6361-6370.

52. Bohme, S.; Philippe, B.; Edstrom, K.; Nyholm, L., Photoelectron Spectroscopic Evidence for Overlapping Redox Reactions for SnO_2 Electrodes in Lithium-Ion Batteries. *J. Phys. Chem. C* **2017,** *121* (9), 4924-4936.

53. Wang, L. P.; Leconte, Y.; Feng, Z.; Wei, C.; Zhao, Y.; Ma, Q.; Xu, W.; Bourrioux, S.; Azais, P.; Srinivasan, M.; Xu, Z. J., Novel Preparation of N-Doped SnO_2 Nanoparticles Via Laser-Assisted Pyrolysis: Demonstration of Exceptional Lithium Storage Properties. *Adv. Mater.* **2017,** *29* (6), 1603286.

54. Kim, C.; Noh, M.; Choi, M.; Cho, J.; Park, B., Critical Size of a Nano SnO_2 Electrode for Li-Secondary Battery. *Chem. Mater.* **2005,** *17* (12), 3297-3301.

55. Liu, X. H.; Zhong, L.; Huang, S.; Mao, S. X.; Zhu, T.; Huang, J. Y., Size-Dependent Fracture of Silicon Nanoparticles During Lithiation. *ACS Nano* **2012,** *6* (2), 1522-31.

56. Shao, M.; Peles, A.; Shoemaker, K., Electrocatalysis on Platinum Nanoparticles: Particle Size Effect on Oxygen Reduction Reaction Activity. *Nano Lett.* **2011,** *11* (9), 3714-9.

57. Wang, S.; Shi, L.; Chen, G.; Ba, C.; Wang, Z.; Zhu, J.; Zhao, Y.; Zhang, M.; Yuan, S., In Situ Synthesis of Tungsten-Doped SnO_2 and Graphene Nanocomposites for High-Performance Anode Materials of Lithium-Ion Batteries. *ACS Appl. Mat. Interfaces* **2017,** *9* (20), 17164-17172.

58. Liu, X.; Astruc, D., From Galvanic to Anti-Galvanic Synthesis of Bimetallic Nanoparticles and Applications in Catalysis, Sensing, and Materials Science. *Adv. Mater.* **2017,** *29* (16), 1605305.

59. Gawande, M. B.; Goswami, A.; Asefa, T.; Guo, H.; Biradar, A. V.; Peng, D. L.; Zboril, R.; Varma, R. S., Core-Shell Nanoparticles: Synthesis and Applications in Catalysis and Electrocatalysis. *Chem. Soc. Rev.* **2015,** *44* (21), 7540-90.

60. Yao, Y.; Huang, Z.; Xie, P.; Lacey, S. D.; Jacob, R. J.; Xie, H.; Chen, F.; Nie, A.; Pu, T.; Rehwoldt, M.; Yu, D.; Zachariah, M. R.; Wang, C.; Shahbazian-Yassar, R.; Li, J.; Hu, L., Carbothermal Shock Synthesis of High-Entropy-Alloy Nanoparticles. *Science* **2018,** *359* (6383), 1489-1494.

61. Novoselov, K. S.; Geim, A. K.; Morozov, S. V.; Jiang, D.; Zhang, Y.; Dubonos, S. V.; Grigorieva, I. V.; Firsov, A. A., Electric Field Effect in Atomically Thin Carbon Films. *Science* **2004,** *306* (5696), 666-9.

62. Geim, A. K.; Novoselov, K. S., The Rise of Graphene. *Nat. Mater.* **2007,** *6* (3), 183-91.

63. Xu, M.; Liang, T.; Shi, M.; Chen, H., Graphene-Like Two-Dimensional Materials. *Chemical Reviews* **2013,** *113* (5), 3766-98.

64. Radisavljevic, B.; Radenovic, A.; Brivio, J.; Giacometti, V.; Kis, A., Single-Layer MoS_2 Transistors. *Nat. Nanotechnol.* **2011,** *6* (3), 147-50.

65. R. F. Frindt, A. D. Y., Physical Properties of Layer Structures : Optical Properties and Photoconductivity of Thin Crystals of Molybdenum Disulphide. *Proceedings of the Royal Society of London. Series A. Mathematical and Physical Sciences* **1963,** *273* (1352), 69-83.

66. Joensen, P.; Frindt, R. F.; Morrison, S. R., Single-Layer MoS_2. *Mater. Res. Bull.* **1986,** *21* (4), 457-461.

67. Li, L.; Yu, Y.; Ye, G. J.; Ge, Q.; Ou, X.; Wu, H.; Feng, D.; Chen, X. H.; Zhang, Y., Black Phosphorus Field-Effect Transistors. *Nat. Nanotechnol.* **2014,** *9* (5), 372-7.

68. Mao, S.; Chang, J. B.; Pu, H. H.; Lu, G. H.; He, Q. Y.; Zhang, H.; Chen, J. H., Two-Dimensional Nanomaterial-Based Field-Effect Transistors for Chemical and Biological Sensing. *Chemical Society Reviews* **2017,** *46* (22), 6872-6904.

69. Tan, C.; Cao, X.; Wu, X. J.; He, Q.; Yang, J.; Zhang, X.; Chen, J.; Zhao, W.; Han, S.; Nam, G. H.; Sindoro, M.; Zhang, H., Recent Advances in Ultrathin Two-Dimensional Nanomaterials. *Chem. Rev.* **2017,** *117* (9), 6225-6331.

70. Chen, C.; Xie, X.; Anasori, B.; Sarycheva, A.; Makaryan, T.; Zhao, M.; Urbankowski, P.; Miao, L.; Jiang, J.; Gogotsi, Y., MoS_2-on-Mxene Heterostructures as Highly Reversible Anode Materials for Lithium-Ion Batteries. *Angew Chem Int Ed Engl* **2018,** *57* (7), 1846-1850.

71. Zhang, C.; Wang, A.; Zhang, J.; Guan, X.; Tang, W.; Luo, J., 2d Materials for Lithium/Sodium Metal Anodes. *Adv. Energy Mater.* **2018,** *8* (34), 1802833.

72. Mannix, A. J.; Kiraly, B.; Hersam, M. C.; Guisinger, N. P., Synthesis and Chemistry of Elemental 2d Materials. *Nature Reviews Chemistry* **2017,** *1* (2), 0014.

73. Peigney, A.; Laurent, C.; Flahaut, E.; Bacsa, R. R.; Rousset, A., Specific Surface Area of Carbon Nanotubes and Bundles of Carbon Nanotubes. *Carbon* **2001,** *39* (4), 507-514.

74. Zhang, T.; Cheng, Z.; Wang, Y.; Li, Z.; Wang, C.; Li, Y.; Fang, Y., Self-Assembled 1-Octadecanethiol Monolayers on Graphene for Mercury Detection. *Nano Letters* **2010,** *10* (11), 4738-41.

75. Müller, T.; Flynn, G. W.; Mathauser, A. T.; Teplyakov, A. V., Temperature-Programmed Desorption Studies of N-Alkane Derivatives on Graphite: Desorption Energetics and the Influence of Functional Groups on Adsorbate Self-Assembly. *Langmuir* **2003,** *19* (7), 2812-2821.

76. Zhang, Z.; Huang, H.; Yang, X.; Zang, L., Tailoring Electronic Properties of Graphene by Π–Π Stacking with Aromatic Molecules. *J. Phys. Chem. Lett.* **2011,** *2* (22), 2897-2905.

77. Li, Y.; Wang, C.; Zhu, Y.; Zhou, X.; Xiang, Y.; He, M.; Zeng, S., Fully Integrated Graphene Electronic Biosensor for Label-Free Detection of Lead (ii) Ion Based on G-Quadruplex Structure-Switching. *Biosens. Bioelectron.* **2017,** *89* (Pt 2), 758-763.

78. Wen, Y.; Li, F. Y.; Dong, X.; Zhang, J.; Xiong, Q.; Chen, P., The Electrical Detection of Lead Ions Using Gold-Nanoparticle- and Dnazyme-Functionalized Graphene Device. *Advanced healthcare materials* **2013,** *2* (2), 271-4.

79. Splendiani, A.; Sun, L.; Zhang, Y.; Li, T.; Kim, J.; Chim, C. Y.; Galli, G.; Wang, F., Emerging Photoluminescence in Monolayer MoS_2. *Nano Lett.* **2010,** *10* (4), 1271-5.

80. Stankovich, S.; Dikin, D. A.; Piner, R. D.; Kohlhaas, K. A.; Kleinhammes, A.; Jia, Y.; Wu, Y.; Nguyen, S. T.; Ruoff, R. S., Synthesis of Graphene-Based Nanosheets via Chemical Reduction of Exfoliated Graphite Oxide. *Carbon* **2007,** *45* (7), 1558-1565.

81. Mao, S.; Pu, H. H.; Chen, J. H., Graphene Oxide and Its Reduction: Modeling and Experimental Progress. *RSC Adv.* **2012,** *2* (7), 2643-2662.

82. Xu, J.; Wang, M.; Wickramaratne, N. P.; Jaroniec, M.; Dou, S.; Dai, L., High-Performance Sodium Ion Batteries Based on a 3d Anode from Nitrogen-Doped Graphene Foams. *Adv. Mater.* **2015,** *27* (12), 2042-8.

83. Share, K.; Cohn, A. P.; Carter, R.; Rogers, B.; Pint, C. L., Role of Nitrogen-Doped Graphene for Improved High-Capacity Potassium Ion Battery Anodes. *ACS Nano* **2016,** *10* (10), 9738-9744.

84. Ma, C. C.; Shao, X. H.; Cao, D. P., Nitrogen-Doped Graphene Nanosheets as Anode Materials for Lithium Ion Batteries: A First-Principles Study. *J. Mater. Chem.* **2012,** *22* (18), 8911-8915.

85. Hamalainen, J.; Ritala, M.; Leskela, M., Atomic Layer Deposition of Noble Metals and Their Oxides. *Chem. Mater.* **2014,** *26* (1), 786-801.

86. Kazyak, E.; Wood, K. N.; Dasgupta, N. P., Improved Cycle Life and Stability of Lithium Metal Anodes through Ultrathin Atomic Layer Deposition Surface Treatments. *Chem. Mater.* **2015,** *27* (18), 6457-6462.

87. Zhao, Y.; Goncharova, L. V.; Lushington, A.; Sun, Q.; Yadegari, H.; Wang, B.; Xiao, W.; Li, R.; Sun, X., Superior Stable and Long Life Sodium Metal Anodes Achieved by Atomic Layer Deposition. *Adv. Mater.* **2017,** *29* (18), 1606663.

88. Ahmed, B.; Anjum, D. H.; Gogotsi, Y.; Alshareef, H. N., Atomic Layer Deposition of SnO_2 on Mxene for Li-Ion Battery Anodes. *Nano Energy* **2017,** *34*, 249-256.

89. Li, H.; Gao, Y.; Shao, Y.; Su, Y.; Wang, X., Vapor-Phase Atomic Layer Deposition of Co_9S_8 and Its Application for Supercapacitors. *Nano Lett.* **2015,** *15* (10), 6689-95.

90. Hamalainen, J.; Mattinen, M.; Mizohata, K.; Meinander, K.; Vehkamaki, M.; Raisanen, J.; Ritala, M.; Leskela, M., Atomic Layer Deposition of Rhenium Disulfide. *Adv. Mater.* **2018,** *30* (24), e1703622.

91. Kim, H., Atomic Layer Deposition of Metal and Nitride Thin Films: Current Research Efforts and Applications for Semiconductor Device Processing. *J Vac Sci Technol B* **2003,** *21* (6), 2231-2261.

92. Johnson, R. W.; Hultqvist, A.; Bent, S. F., A Brief Review of Atomic Layer Deposition: From Fundamentals to Applications. *Mater. Today* **2014,** *17* (5), 236-246.

93. Meng, X.; Wang, X.; Geng, D.; Ozgit-Akgun, C.; Schneider, N.; Elam, J. W., Atomic Layer Deposition for Nanomaterial Synthesis and Functionalization in Energy Technology. *Materials Horizons* **2017,** *4* (2), 133-154.

94. Marichy, C.; Bechelany, M.; Pinna, N., Atomic Layer Deposition of Nanostructured Materials for Energy and Environmental Applications. *Adv. Mater.* **2012,** *24* (8), 1017-32.

95. Grillo, F.; Moulijn, J. A.; Kreutzer, M. T.; van Ommen, J. R., Nanoparticle Sintering in Atomic Layer Deposition of Supported Catalysts: Kinetic Modeling of the Size Distribution. *Catal. Today* **2018,** *316*, 51-61.

96. Zhao, Y.; Li, X. F.; Yan, B.; Xiong, D. B.; Li, D. J.; Lawes, S.; Sun, X. L., Recent Developments and Understanding of Novel Mixed Transition-Metal Oxides as Anodes in Lithium Ion Batteries. *Adv. Energy Mater.* **2016,** *6* (8), 1502175.

97. Wang, H.; Zhu, Q.-L.; Zou, R.; Xu, Q., Metal-Organic Frameworks for Energy Applications. *Chem* **2017,** *2* (1), 52-80.

98. Li, B.; Wen, H. M.; Cui, Y.; Zhou, W.; Qian, G.; Chen, B., Emerging Multifunctional Metal-Organic Framework Materials. *Adv. Mater.* **2016,** *28* (40), 8819-8860.

99. Lustig, W. P.; Mukherjee, S.; Rudd, N. D.; Desai, A. V.; Li, J.; Ghosh, S. K., Metal-Organic Frameworks: Functional Luminescent and Photonic Materials for Sensing Applications. *Chem. Soc. Rev.* **2017,** *46* (11), 3242-3285.

100. Liu, J.; Chen, L.; Cui, H.; Zhang, J.; Zhang, L.; Su, C. Y., Applications of Metal-Organic Frameworks in Heterogeneous Supramolecular Catalysis. *Chem. Soc. Rev.* **2014,** *43* (16), 6011-61.

101. Bradshaw, D.; Garai, A.; Huo, J., Metal-Organic Framework Growth at Functional Interfaces: Thin Films and Composites for Diverse Applications. *Chem. Soc. Rev.* **2012,** *41* (6), 2344-81.

102. Lian, X.; Fang, Y.; Joseph, E.; Wang, Q.; Li, J.; Banerjee, S.; Lollar, C.; Wang, X.; Zhou, H. C., Enzyme-MOF (Metal-Organic Framework) Composites. *Chem. Soc. Rev.* **2017,** *46* (11), 3386-3401.

103. Liang, Z. B.; Qu, C.; Guo, W. H.; Zou, R. Q.; Xu, Q., Pristine Metal-Organic Frameworks and Their Composites for Energy Storage and Conversion. *Adv. Mater.* **2018,** *30* (37).

104. Chaikittisilp, W.; Ariga, K.; Yamauchi, Y., A New Family of Carbon Materials: Synthesis of MOF-Derived Nanoporous Carbons and Their Promising Applications. *J. Mater. Chem. A* **2013,** *1* (1), 14-19.

105. Shen, K.; Chen, X. D.; Chen, J. Y.; Li, Y. W., Development of MOF-Derived Carbon-Based Nanomaterials for Efficient Catalysis. *Acs Catalysis* **2016,** *6* (9), 5887-5903.

106. Li, W.; Hu, S.; Luo, X.; Li, Z.; Sun, X.; Li, M.; Liu, F.; Yu, Y., Confined Amorphous Red Phosphorus in MOF-Derived N-Doped Microporous Carbon as a Superior Anode for Sodium-Ion Battery. *Adv. Mater.* **2017,** *29* (16).

107. UNICEF, W. a. *Progress on Drinking Water, Sanitation and Hygiene: 2017 Update and Sdg Baselines*; 2017.

108. Jaishankar, M.; Tseten, T.; Anbalagan, N.; Mathew, B. B.; Beeregowda, K. N., Toxicity, Mechanism and Health Effects of Some Heavy Metals. *Interdiscip Toxicol* **2014,** *7* (2), 60-72.

109. Li, M.; Gou, H. L.; Al-Ogaidi, I.; Wu, N. Q., Nanostructured Sensors for Detection of Heavy Metals: A Review. *Acs Sustainable Chemistry & Engineering* **2013,** *1* (7), 713-723.

110. Broadhurst, M. J.; Brooks, T. J.; Pollock, N. R., Diagnosis of Ebola Virus Disease: Past, Present, and Future. *Clin Microbiol Rev* **2016,** *29* (4), 773-93.

111. Chang, J.; Pu, H.; Wells, S. A.; Shi, K.; Guo, X.; Zhou, G.; Sui, X.; Ren, R.; Mao, S.; Chen, Y.; Hersam, M. C.; Chen, J., Semi-Quantitative Design of Black Phosphorous Field-Effect Transistor Sensors for Heavy Metal Ion Detection in Aqueous Media. *Molecular Systems Design & Engineering* **2019**.

112. Chen, K.; Lu, G.; Chang, J.; Mao, S.; Yu, K.; Cui, S.; Chen, J., Hg(ii) Ion Detection Using Thermally Reduced Graphene Oxide Decorated with Functionalized Gold Nanoparticles. *Anal. Chem.* **2012,** *84* (9), 4057-62.

113. Zhou, G. H.; Chang, J. B.; Pu, H. H.; Shi, K. Y.; Mao, S.; Sui, X. Y.; Ren, R.; Cui, S. M.; Chen, J. H., Ultrasensitive Mercury Ion Detection Using DNA-Functionalized Molybdenum Disulfide Nanosheet/Gold Nanoparticle Hybrid Field Effect Transistor Device. *Acs Sensors* **2016,** *1* (3), 295-302.

114. Chen, K.; Gao, W.; Emaminejad, S.; Kiriya, D.; Ota, H.; Nyein, H. Y.; Takei, K.; Javey, A., Printed Carbon Nanotube Electronics and Sensor Systems. *Adv. Mater.* **2016,** *28* (22), 4397-414.

115. Rim, Y. S.; Bae, S. H.; Chen, H.; De Marco, N.; Yang, Y., Recent Progress in Materials and Devices toward Printable and Flexible Sensors. *Adv. Mater.* **2016,** *28* (22), 4415-40.

116. Sui, X.; Downing, J. R.; Hersam, M. C.; Chen, J., Additive Manufacturing and Applications of Nanomaterial-Based Sensors. *Mater. Today* **2021**.

117. Nayak, P. K.; Yang, L.; Brehm, W.; Adelhelm, P., From Lithium-Ion to Sodium-Ion Batteries: Advantages, Challenges, and Surprises. *Angew Chem Int Ed Engl* **2018,** *57* (1), 102-120.

118. Etacheri, V.; Marom, R.; Elazari, R.; Salitra, G.; Aurbach, D., Challenges in the Development of Advanced Li-Ion Batteries: A Review. *Energy Environ. Sci.* **2011,** *4* (9), 3243.

119. Persson, K.; Sethuraman, V. A.; Hardwick, L. J.; Hinuma, Y.; Meng, Y. S.; van der Ven, A.; Srinivasan, V.; Kostecki, R.; Ceder, G., Lithium Diffusion in Graphitic Carbon. *J. Phys. Chem. Lett.* **2010,** *1* (8), 1176-1180.

120. Sethuraman, V. A.; Hardwick, L. J.; Srinivasan, V.; Kostecki, R., Surface Structural Disordering in Graphite Upon Lithium Intercalation/Deintercalation. *J. Power Sources* **2010,** *195* (11), 3655-3660.

121. Ramireddy, T.; Xing, T.; Rahman, M. M.; Chen, Y.; Dutercq, Q.; Gunzelmann, D.; Glushenkov, A. M., Phosphorus–Carbon Nanocomposite Anodes for Lithium-Ion and Sodium-Ion Batteries. *J. Mater. Chem. A* **2015,** *3* (10), 5572-5584.

122. Nitta, N.; Wu, F. X.; Lee, J. T.; Yushin, G., Li-Ion Battery Materials: Present and Future. *Mater. Today* **2015,** *18* (5), 252-264.

123. Zhang, W.; Liu, Y.; Guo, Z., Approaching High-Performance Potassium-Ion Batteries via Advanced Design Strategies and Engineering. *Science Advances* **2019,** *5* (5), eaav7412.

124. Liu, Y.; Tai, Z.; Zhang, J.; Pang, W. K.; Zhang, Q.; Feng, H.; Konstantinov, K.; Guo, Z.; Liu, H. K., Boosting Potassium-Ion Batteries by Few-Layered Composite Anodes Prepared via Solution-Triggered One-Step Shear Exfoliation. *Nat. Commun.* **2018,** *9* (1), 3645.

125. Kubota, K.; Dahbi, M.; Hosaka, T.; Kumakura, S.; Komaba, S., Towards K-Ion and Na-Ion Batteries as "Beyond Li-Ion". *Chem Rec* **2018,** *18* (4), 459-479.

126. Hwang, J. Y.; Myung, S. T.; Sun, Y. K., Recent Progress in Rechargeable Potassium Batteries. *Adv. Funct. Mater.* **2018,** *28* (43), 1802938.

127. Chang, W. C.; Wu, J. H.; Chen, K. T.; Tuan, H. Y., Red Phosphorus Potassium-Ion Battery Anodes. *Adv Sci (Weinh)* **2019,** *6* (9), 1801354.

128. Liu, D.; Huang, X. K.; Qu, D. Y.; Zheng, D.; Wang, G. W.; Harris, J.; Si, J. Y.; Ding, T. Y.; Chen, J. H.; Qu, D. Y., Confined Phosphorus in Carbon Nanotube-Backboned Mesoporous Carbon as Superior Anode Material for Sodium/Potassium-Ion Batteries. *Nano Energy* **2018,** *52*, 1-10.

129. Zhang, W.; Pang, W. K.; Sencadas, V.; Guo, Z., Understanding High-Energy-Density Sn_4P_3 Anodes for Potassium-Ion Batteries. *Joule* **2018,** *2* (8), 1534-1547.

130. Zheng, J.; Yang, Y.; Fan, X.; Ji, G.; Ji, X.; Wang, H.; Hou, S.; Zachariah, M.; Wang, C., Super Stable Antimony-Carbon Composite Anodes for Potassium-Ion Batteries. *Energy Environ. Sci.* **2019**.

131. Zhao, Y.; Zhu, J.; Ong, S. J. H.; Yao, Q.; Shi, X.; Hou, K.; Xu, Z. J.; Guan, L., High-Rate and Ultralong Cycle-Life Potassium Ion Batteries Enabled by in Situ Engineering of Yolk–Shell FeS_2@C Structure on Graphene Matrix. *Adv. Energy Mater.* **2018,** *0* (0), 1802565.

132. Mason, L. H.; Harp, J. P.; Han, D. Y., Pb Neurotoxicity: Neuropsychological Effects of Lead Toxicity. *Biomed Res Int* **2014,** *2014*, 840547.

133. Flint Water Crisis Fast Facts. https://www.cnn.com/2016/03/04/us/flint-water-crisis-fast-facts/index.html (accessed 02272017).

134. Masten, S. J.; Davies, S. H.; McElmurry, S. P., Flint Water Crisis: What Happened and Why? *J Am Water Works Assoc* **2016,** *108* (12), 22-34.

135. Heard-Garris, N. J.; Roche, J.; Carter, P.; Abir, M.; Walton, M.; Zimmerman, M.; Cunningham, R., Voices from Flint: Community Perceptions of the Flint Water Crisis. *J Urban Health* **2017,** *94* (6), 776-779.

136. Olson, T. M.; Wax, M.; Yonts, J.; Heidecorn, K.; Haig, S. J.; Yeoman, D.; Hayes, Z.; Raskin, L.; Ellis, B. R., Forensic Estimates of Lead Release from Lead Service Lines During the Water Crisis in Flint, Michigan. *Environ Sci Tech Let* **2017,** *4* (9), 356-361.

137. Wang, J.; Lu, J.; Hocevar, S. B.; Farias, P. A.; Ogorevc, B., Bismuth-Coated Carbon Electrodes for Anodic Stripping Voltammetry. *Anal. Chem.* **2000,** *72* (14), 3218-22.

138. Bruland, K. W.; Coale, K. H.; Mart, L., Analysis of Seawater for Dissolved Cadmium, Copper and Lead: An Intercomparison of Voltammetric and Atomic Absorption Methods. *Mar. Chem.* **1985,** *17* (4), 285-300.

139. Demetriades, D.; Economou, A.; Voulgaropoulos, A., A Study of Pencil-Lead Bismuth-Film Electrodes for the Determination of Trace Metals by Anodic Stripping Voltammetry. *Anal. Chim. Acta* **2004,** *519* (2), 167-172.

140. Mas-Balleste, R.; Gomez-Navarro, C.; Gomez-Herrero, J.; Zamora, F., 2d Materials: To Graphene and Beyond. *Nanoscale* **2011,** *3* (1), 20-30.

141. Huang, X.; Yin, Z.; Wu, S.; Qi, X.; He, Q.; Zhang, Q.; Yan, Q.; Boey, F.; Zhang, H., Graphene-Based Materials: Synthesis, Characterization, Properties, and Applications. *Small* **2011,** *7* (14), 1876-902.

142. Trung, T. Q.; Tien, N. T.; Kim, D.; Jung, J. H.; Yoon, O. J.; Lee, N. E., High Thermal Responsiveness of a Reduced Graphene Oxide Field-Effect Transistor. *Adv. Mater.* **2012,** *24* (38), 5254-60.

143. Zhou, G.; Chang, J.; Cui, S.; Pu, H.; Wen, Z.; Chen, J., Real-Time, Selective Detection of Pb^{2+} in Water Using a Reduced Graphene Oxide/Gold Nanoparticle Field-Effect Transistor Device. *ACS Appl Mater Interfaces* **2014,** *6* (21), 19235-41.

144. Hasegawa, M.; Hirayama, Y.; Ohno, Y.; Maehashi, K.; Matsumoto, K., Characterization of Reduced Graphene Oxide Field-Effect Transistor and Its Application to Biosensor. *Japanese Journal of Applied Physics* **2014,** *53* (5).

145. Kwak, Y. H.; Choi, D. S.; Kim, Y. N.; Kim, H.; Yoon, D. H.; Ahn, S. S.; Yang, J. W.; Yang, W. S.; Seo, S., Flexible Glucose Sensor Using CVD-Grown Graphene-Based Field Effect Transistor. *Biosens. Bioelectron.* **2012,** *37* (1), 82-7.

146. Fu, W.; Nef, C.; Tarasov, A.; Wipf, M.; Stoop, R.; Knopfmacher, O.; Weiss, M.; Calame, M.; Schonenberger, C., High Mobility Graphene Ion-Sensitive Field-Effect Transistors by Noncovalent Functionalization. *Nanoscale* **2013,** *5* (24), 12104-10.

147. Zhang, X.; Zhang, Y.; Liao, Q.; Song, Y.; Ma, S., Reduced Graphene Oxide-Functionalized High Electron Mobility Transistors for Novel Recognition Pattern Label-Free DNA Sensors. *Small* **2013,** *9* (23), 4045-50.

148. Cai, B.; Wang, S.; Huang, L.; Ning, Y.; Zhang, Z.; Zhang, G. J., Ultrasensitive Label-Free Detection of PNA-DNA Hybridization by Reduced Graphene Oxide Field-Effect Transistor Biosensor. *ACS Nano* **2014,** *8* (3), 2632-8.

149. Yin, Z.; He, Q.; Huang, X.; Zhang, J.; Wu, S.; Chen, P.; Lu, G.; Chen, P.; Zhang, Q.; Yan, Q.; Zhang, H., Real-Time DNA Detection Using Pt Nanoparticle-Decorated Reduced Graphene Oxide Field-Effect Transistors. *Nanoscale* **2012,** *4* (1), 293-7.

150. Galstyan, V.; Comini, E.; Kholmanov, I.; Faglia, G.; Sberveglieri, G., Reduced Graphene Oxide/ZnO Nanocomposite for Application in Chemical Gas Sensors. *RSC Adv.* **2016,** *6* (41), 34225-34232.

151. Sudibya, H. G.; He, Q.; Zhang, H.; Chen, P., Electrical Detection of Metal Ions Using Field-Effect Transistors Based on Micropatterned Reduced Graphene Oxide Films. *ACS Nano* **2011,** *5* (3), 1990-4.

152. Xu, B.; Zhu, M.; Zhang, W.; Zhen, X.; Pei, Z.; Xue, Q.; Zhi, C.; Shi, P., Ultrathin Mxene-Micropattern-Based Field-Effect Transistor for Probing Neural Activity. *Adv. Mater.* **2016,** *28* (17), 3333-9.

153. Park, S. J.; Kwon, O. S.; Lee, S. H.; Song, H. S.; Park, T. H.; Jang, J., Ultrasensitive Flexible Graphene Based Field-Effect Transistor (FET)-Type Bioelectronic Nose. *Nano Lett.* **2012,** *12* (10), 5082-90.

154. Knopfmacher, O.; Hammock, M. L.; Appleton, A. L.; Schwartz, G.; Mei, J.; Lei, T.; Pei, J.; Bao, Z., Highly Stable Organic Polymer Field-Effect Transistor Sensor for Selective Detection in the Marine Environment. *Nat. Commun.* **2014,** *5*, 2954.

155. Park, J. W.; Park, S. J.; Kwon, O. S.; Lee, C.; Jang, J., Polypyrrole Nanotube Embedded Reduced Graphene Oxide Transducer for Field-Effect Transistor-Type H_2O_2 Biosensor. *Anal. Chem.* **2014,** *86* (3), 1822-8.

156. Tung, V. C.; Allen, M. J.; Yang, Y.; Kaner, R. B., High-Throughput Solution Processing of Large-Scale Graphene. *Nat. Nanotechnol.* **2009,** *4* (1), 25-9.

157. Rc Charging Circuit. https://www.electronics-tutorials.ws/rc/rc_1.html.

158. Ryder, C. R.; Wood, J. D.; Wells, S. A.; Hersam, M. C., Chemically Tailoring Semiconducting Two-Dimensional Transition Metal Dichalcogenides and Black Phosphorus. *ACS Nano* **2016,** *10* (4), 3900-17.

159. Agency, U. S. E. P. Drinking Water Requirements for States and Public Water Systems-Lead and Copper Rule. https://www.epa.gov/dwreginfo/lead-and-copper-rule.

160. Mao, S.; Pu, H. H.; Chang, J. B.; Sui, X. Y.; Zhou, G. H.; Ren, R.; Chen, Y. T.; Chen, J. H., Ultrasensitive Detection of Orthophosphate Ions with Reduced Graphene Oxide/Ferritin Field-Effect Transistor Sensors. *Env. Sci. -Nano* **2017,** *4* (4), 856-863.

161. Bittle, E. G.; Basham, J. I.; Jackson, T. N.; Jurchescu, O. D.; Gundlach, D. J., Mobility Overestimation Due to Gated Contacts in Organic Field-Effect Transistors. *Nat. Commun.* **2016,** *7*, 10908.

162. Ki Min, B.; Kim, S. K.; Jun Kim, S.; Ho Kim, S.; Kang, M. A.; Park, C. Y.; Song, W.; Myung, S.; Lim, J.; An, K. S., Electrical Double Layer Capacitance in a Graphene-Embedded Al_2O_3 Gate Dielectric. *Sci Rep* **2015,** *5*, 16001.

163. Organization, W. H. Ebola Virus Disease. https://www.who.int/en/news-room/fact-sheets/detail/ebola-virus-disease (accessed 07/23).

164. Stamm, L. V., Ebola Virus Disease: Rapid Diagnosis and Timely Case Reporting are Critical to the Early Response for Outbreak Control. *Am J Trop Med Hyg* **2015,** *93* (3), 438-40.

165. Sullivan, N. J.; Geisbert, T. W.; Geisbert, J. B.; Xu, L.; Yang, Z. Y.; Roederer, M.; Koup, R. A.; Jahrling, P. B.; Nabel, G. J., Accelerated Vaccination for Ebola Virus Haemorrhagic Fever in Non-Human Primates. *Nature* **2003,** *424* (6949), 681-4.

166. Tseng, D.; Mudanyali, O.; Oztoprak, C.; Isikman, S. O.; Sencan, I.; Yaglidere, O.; Ozcan, A., Lensfree Microscopy on a Cellphone. *Lab Chip* **2010,** *10* (14), 1787-92.

167. Henkel, J. H.; Aberle, S. W.; Kundi, M.; Popow-Kraupp, T., Improved Detection of Respiratory Syncytial Virus in Nasal Aspirates by Seminested RT-PCR. *J Med Virol* **1997,** *53* (4), 366-71.

168. Li, Y.; Cu, Y. T.; Luo, D., Multiplexed Detection of Pathogen DNA with DNA-Based Fluorescence Nanobarcodes. *Nat. Biotechnol.* **2005,** *23* (7), 885-9.

169. Yanik, A. A.; Huang, M.; Kamohara, O.; Artar, A.; Geisbert, T. W.; Connor, J. H.; Altug, H., An Optofluidic Nanoplasmonic Biosensor for Direct Detection of Live Viruses from Biological Media. *Nano Lett.* **2010,** *10* (12), 4962-9.

170. Daaboul, G. G.; Lopez, C. A.; Chinnala, J.; Goldberg, B. B.; Connor, J. H.; Unlu, M. S., Digital Sensing and Sizing of Vesicular Stomatitis Virus Pseudotypes in Complex Media: A Model for Ebola and Marburg Detection. *ACS Nano* **2014,** *8* (6), 6047-6055.

171. Jares-Erijman, E. A.; Jovin, T. M., FRET Imaging. *Nat. Biotechnol.* **2003,** *21* (11), 1387-95.

172. Lal, S.; Link, S.; Halas, N. J., Nano-Optics from Sensing to Waveguiding. *Nat. Photonics* **2007,** *1* (11), 641-648.

173. Bishnoi, S. W.; Rozell, C. J.; Levin, C. S.; Gheith, M. K.; Johnson, B. R.; Johnson, D. H.; Halas, N. J., All-Optical Nanoscale pH Meter. *Nano Lett.* **2006,** *6* (8), 1687-92.

174. Anker, J. N.; Hall, W. P.; Lyandres, O.; Shah, N. C.; Zhao, J.; Van Duyne, R. P., Biosensing with Plasmonic Nanosensors. *Nat. Mater.* **2008,** *7* (6), 442-53.

175. Homola, J., Present and Future of Surface Plasmon Resonance Biosensors. *Anal Bioanal Chem* **2003,** *377* (3), 528-39.

176. Arnold, S.; Khoshsima, M.; Teraoka, I.; Holler, S.; Vollmer, F., Shift of Whispering-Gallery Modes in Microspheres by Protein Adsorption. *Opt. Lett.* **2003,** *28* (4), 272-4.

177. Fan, X.; White, I. M.; Shopova, S. I.; Zhu, H.; Suter, J. D.; Sun, Y., Sensitive Optical Biosensors for Unlabeled Targets: A Review. *Anal. Chim. Acta* **2008,** *620* (1-2), 8-26.

178. Burg, T. P.; Godin, M.; Knudsen, S. M.; Shen, W.; Carlson, G.; Foster, J. S.; Babcock, K.; Manalis, S. R., Weighing of Biomolecules, Single Cells and Single Nanoparticles in Fluid. *Nature* **2007,** *446* (7139), 1066-9.

179. Marx, K. A., Quartz Crystal Microbalance: A Useful Tool for Studying Thin Polymer Films and Complex Biomolecular Systems at the Solution-Surface Interface. *Biomacromolecules* **2003,** *4* (5), 1099-120.

180. Lange, K.; Rapp, B. E.; Rapp, M., Surface Acoustic Wave Biosensors: A Review. *Anal Bioanal Chem* **2008,** *391* (5), 1509-19.

181. Pineda, M. F.; Chan, L. L. Y.; Kuhlenschmidt, T.; Choi, C. J.; Kuhlenschmidt, M.; Cunningham, B. T., Rapid Specific and Label-Free Detection of Porcine Rotavirus Using Photonic Crystal Biosensors. *Ieee Sensors Journal* **2009,** *9* (4), 470-477.

182. Zhan, B.; Li, C.; Yang, J.; Jenkins, G.; Huang, W.; Dong, X., Graphene Field-Effect Transistor and Its Application for Electronic Sensing. *Small* **2014,** *10* (20), 4042-65.

183. Mao, S.; Chang, J.; Zhou, G.; Chen, J., Nanomaterial-Enabled Rapid Detection of Water Contaminants. *Small* **2015,** *11* (40), 5336-59.

184. Makowski, M. S.; Ivanisevic, A., Molecular Analysis of Blood with Micro-/Nanoscale Field-Effect-Transistor Biosensors. *Small* **2011,** *7* (14), 1863-75.

185. Terrel, M.; Digonnet, M. J.; Fan, S., Ring-Coupled Mach-Zehnder Interferometer Optimized for Sensing. *Appl. Opt.* **2009,** *48* (26), 4874-9.

186. Rosman, C.; Prasad, J.; Neiser, A.; Henkel, A.; Edgar, J.; Sonnichsen, C., Multiplexed Plasmon Sensor for Rapid Label-Free Analyte Detection. *Nano Lett.* **2013,** *13* (7), 3243-7.

187. Datar, R.; Kim, S.; Jeon, S.; Hesketh, P.; Manalis, S.; Boisen, A.; Thundat, T., Cantilever Sensors: Nanomechanical Tools for Diagnostics. *MRS Bull.* **2011,** *34* (6), 449-454.

188. Ahn, J. H.; Choi, S. J.; Han, J. W.; Park, T. J.; Lee, S. Y.; Choi, Y. K., Double-Gate Nanowire Field Effect Transistor for a Biosensor. *Nano Lett.* **2010,** *10* (8), 2934-8.

189. Ohno, Y.; Maehashi, K.; Yamashiro, Y.; Matsumoto, K., Electrolyte-Gated Graphene Field-Effect Transistors for Detecting pH and Protein Adsorption. *Nano Lett.* **2009,** *9* (9), 3318-22.

190. Chang, J.; Zhou, G.; Gao, X.; Mao, S.; Cui, S.; Ocola, L. E.; Yuan, C.; Chen, J., Real-Time Detection of Mercury Ions in Water Using a Reduced Graphene Oxide/DNA Field-Effect Transistor with Assistance of a Passivation Layer. *Sensing and Bio-Sensing Research* **2015,** *5*, 97-104.

191. Ahrberg, C. D.; Manz, A.; Neuzil, P., Palm-Sized Device for Point-of-Care Ebola Detection. *Anal. Chem.* **2016,** *88* (9), 4803-7.

192. Cordoba-Torres, P.; Mesquita, T. J.; Nogueira, R. P., Relationship between the Origin of Constant-Phase Element Behavior in Electrochemical Impedance Spectroscopy and Electrode Surface Structure. *J. Phys. Chem. C* **2015,** *119* (8), 4136-4147.

193. Goldmann, C.; Krellner, C.; Pernstich, K. P.; Haas, S.; Gundlach, D. J.; Batlogg, B., Determination of the Interface Trap Density of Rubrene Single-Crystal Field-Effect Transistors and Comparison to the Bulk Trap Density. *J. Appl. Phys.* **2006,** *99* (3), 034507.

194. Chua, L. L.; Zaumseil, J.; Chang, J. F.; Ou, E. C.; Ho, P. K.; Sirringhaus, H.; Friend, R. H., General Observation of N-Type Field-Effect Behaviour in Organic Semiconductors. *Nature* **2005,** *434* (7030), 194-9.

195. Joshi, P.; Romero, H. E.; Neal, A. T.; Toutam, V. K.; Tadigadapa, S. A., Intrinsic Doping and Gate Hysteresis in Graphene Field Effect Devices Fabricated on SiO_2 Substrates. *J Phys Condens Matter* **2010,** *22* (33), 334214.

196. Wang, H.; Wu, Y.; Cong, C.; Shang, J.; Yu, T., Hysteresis of Electronic Transport in Graphene Transistors. *ACS Nano* **2010,** *4* (12), 7221-8.

197. Lee, Y. G.; Kang, C. G.; Jung, U. J.; Kim, J. J.; Hwang, H. J.; Chung, H. J.; Seo, S.; Choi, R.; Lee, B. H., Fast Transient Charging at the Graphene/SiO_2 Interface Causing Hysteretic Device Characteristics. *Appl. Phys. Lett.* **2011,** *98* (18), 183508.

198. Maity, A.; Sui, X.; Tarman, C. R.; Pu, H.; Chang, J.; Zhou, G.; Ren, R.; Mao, S.; Chen, J., Pulse-Driven Capacitive Lead Ion Detection with Reduced Graphene Oxide Field-Effect Transistor Integrated with an Analyzing Device for Rapid Water Quality Monitoring. *ACS Sens* **2017,** *2* (11), 1653-1661.

199. Staii, C.; Johnson, A. T., Jr.; Shao, R.; Bonnell, D. A., High Frequency Scanning Gate Microscopy and Local Memory Effect of Carbon Nanotube Transistors. *Nano Lett.* **2005,** *5* (5), 893-6.

200. Lee, J. E.; Fusco, M. L.; Hessell, A. J.; Oswald, W. B.; Burton, D. R.; Saphire, E. O., Structure of the Ebola Virus Glycoprotein Bound to an Antibody from a Human Survivor. *Nature* **2008,** *454* (7201), 177-82.

201. Rodgers, R. S. The Constant Phase Element (CPE). https://electrochemistryresources.com/the-constant-phase-element-cpe/ (accessed 07/23).

202. Bonanni, A.; Pumera, M., Graphene Platform for Hairpin-DNA-Based Impedimetric Genosensing. *ACS Nano* **2011,** *5* (3), 2356-61.

203. Pumera, M.; Ambrosi, A.; Bonanni, A.; Chng, E. L. K.; Poh, H. L., Graphene for Electrochemical Sensing and Biosensing. *TrAC, Trends Anal. Chem.* **2010,** *29* (9), 954-965.

204. Chen, Y.; Ren, R.; Pu, H.; Guo, X.; Chang, J.; Zhou, G.; Mao, S.; Kron, M.; Chen, J., Field-Effect Transistor Biosensor for Rapid Detection of Ebola Antigen. *Sci Rep* **2017,** *7* (1), 10974.

205. Conway, B. E., *Electrochemical Supercapacitors: Scientific Fundamentals and Technological Applications*. Springer, Boston, MA: 1999.

206. Xia, J. L.; Chen, F.; Wiktor, P.; Ferry, D. K.; Tao, N. J., Effect of Top Dielectric Medium on Gate Capacitance of Graphene Field Effect Transistors: Implications in Mobility Measurements and Sensor Applications. *Nano Lett.* **2010,** *10* (12), 5060-4.

207. Uniprot. http://www.uniprot.org (accessed Oct 2017).

208. Duan, D.; Fan, K.; Zhang, D.; Tan, S.; Liang, M.; Liu, Y.; Zhang, J.; Zhang, P.; Liu, W.; Qiu, X.; Kobinger, G. P.; Gao, G. F.; Yan, X., Nanozyme-Strip for Rapid Local Diagnosis of Ebola. *Biosens. Bioelectron.* **2015,** *74*, 134-41.

209. Yen, C. W.; de Puig, H.; Tam, J. O.; Gomez-Marquez, J.; Bosch, I.; Hamad-Schifferli, K.; Gehrke, L., Multicolored Silver Nanoparticles for Multiplexed Disease Diagnostics: Distinguishing Dengue, Yellow Fever, and Ebola Viruses. *Lab Chip* **2015,** *15* (7), 1638-41.

210. Organization, W. H. First Antigen Rapid Test for Ebola through Emergency Assessment and Eligible for Procurement. https://www.who.int/medicines/ebola-treatment/1st_antigen_RT_Ebola/en/ (accessed 07/24).

211. Cai, H.; Parks, J. W.; Wall, T. A.; Stott, M. A.; Stambaugh, A.; Alfson, K.; Griffiths, A.; Mathies, R. A.; Carrion, R.; Patterson, J. L.; Hawkins, A. R.; Schmidt, H., Optofluidic Analysis System for Amplification-Free, Direct Detection of Ebola Infection. *Sci Rep* **2015,** *5*, 14494.

212. Wang, L.; Wen, Y.; Li, L.; Yang, X.; Jia, N.; Li, W.; Meng, J.; Duan, M.; Sun, X.; Liu, G., Sensitive and Label-Free Electrochemical Lead Ion Biosensor Based on a DNAzyme Triggered G-Quadruplex/Hemin Conformation. *Biosens. Bioelectron.* **2018,** *115*, 91-96.

213. Yun, W.; Cai, D.; Jiang, J.; Zhao, P.; Huang, Y.; Sang, G., Enzyme-Free and Label-Free Ultra-Sensitive Colorimetric Detection of Pb^{2+} Using Molecular Beacon and Dnazyme Based Amplification Strategy. *Biosens. Bioelectron.* **2016,** *80*, 187-193.

214. Liang, L.; Lan, F.; Ge, S.; Yu, J.; Ren, N.; Yan, M., Metal-Enhanced Ratiometric Fluorescence/Naked Eye Bimodal Biosensor for Lead Ions Analysis with Bifunctional Nanocomposite Probes. *Anal. Chem.* **2017,** *89* (6), 3597-3605.

215. Li, N. T.; Zhang, D. M.; Zhang, Q.; Lu, Y. L.; Jiang, J.; Liu, G. L.; Liu, Q. J., Combining Localized Surface Plasmon Resonance with Anodic Stripping Voltammetry for Heavy Metal Ion Detection. *Sensors and Actuators B-Chemical* **2016,** *231*, 349-356.

216. Shi, Y.; Wang, H.; Jiang, X.; Sun, B.; Song, B.; Su, Y.; He, Y., Ultrasensitive, Specific, Recyclable, and Reproducible Detection of Lead Ions in Real Systems through a Polyadenine-Assisted, Surface-Enhanced Raman Scattering Silicon Chip. *Anal. Chem.* **2016,** *88* (7), 3723-9.

217. Venkatesh, S.; Li, T.; Wang, X. S.; Yeung, C. C.; Pei, K.; Sun, Q. J.; Wu, W.; Li, R. K. Y.; Lam, M. H. W.; Chan, P. K. L.; Wylie, J. J.; Roy, V. A. L., Dual-Gated Transistor Platform for on-Site Detection of Lead Ions at Trace Levels. *Anal. Chem.* **2018,** *90* (12), 7399-7405.

218. Kaisti, M., Detection Principles of Biological and Chemical FET Sensors. *Biosens. Bioelectron.* **2017,** *98*, 437-448.

219. Kumar, P.; Kim, K. H.; Bansal, V.; Lazarides, T.; Kumar, N., Progress in the Sensing Techniques for Heavy Metal Ions Using Nanomaterials. *J. Ind. Eng. Chem.* **2017,** *54*, 30-43.

220. Zhu, Y.; Murali, S.; Cai, W.; Li, X.; Suk, J. W.; Potts, J. R.; Ruoff, R. S., Graphene and Graphene Oxide: Synthesis, Properties, and Applications. *Adv. Mater.* **2010,** *22* (35), 3906-24.

221. Chen, H.; Chen, P.; Huang, J.; Selegard, R.; Platt, M.; Palaniappan, A.; Aili, D.; Tok, A. I.; Liedberg, B., Detection of Matrilysin Activity Using Polypeptide Functionalized Reduced Graphene Oxide Field-Effect Transistor Sensor. *Anal. Chem.* **2016,** *88* (6), 2994-8.

222. He, Q.; Sudibya, H. G.; Yin, Z.; Wu, S.; Li, H.; Boey, F.; Huang, W.; Chen, P.; Zhang, H., Centimeter-Long and Large-Scale Micropatterns of Reduced Graphene Oxide Films: Fabrication and Sensing Applications. *ACS Nano* **2010,** *4* (6), 3201-8.

223. He, Q.; Wu, S.; Gao, S.; Cao, X.; Yin, Z.; Li, H.; Chen, P.; Zhang, H., Transparent, Flexible, All-Reduced Graphene Oxide Thin Film Transistors. *ACS Nano* **2011,** *5* (6), 5038-44.

224. Kim, E.; Xia, Y.; Whitesides, G. M., Micromolding in Capillaries: Applications in Materials Science. *Journal of the American Chemical Society* **1996,** *118* (24), 5722-5731.

225. Mertens, S.; Moore, C., Continuum Percolation Thresholds in Two Dimensions. *Phys Rev E Stat Nonlin Soft Matter Phys* **2012,** *86* (6 Pt 1), 061109.

226. Cooper, D. R.; D'Anjou, B.; Ghattamaneni, N.; Harack, B.; Hilke, M.; Horth, A.; Majlis, N.; Massicotte, M.; Vandsburger, L.; Whiteway, E.; Yu, V., Experimental Review of Graphene. *ISRN Condensed Matter Physics* **2012,** *2012*, 1-56.

227. Li, J. T.; Ostling, M., Precise Percolation Thresholds of Two-Dimensional Random Systems Comprising Overlapping Ellipses. *Physica a-Statistical Mechanics and Its Applications* **2016,** *462*, 940-950.

228. Li, J.; Ostling, M., Percolation Thresholds of Two-Dimensional Continuum Systems of Rectangles. *Phys Rev E Stat Nonlin Soft Matter Phys* **2013,** *88* (1), 012101.

229. Maity, A.; Sui, X.; Jin, B.; Pu, H.; Bottum, K. J.; Huang, X.; Chang, J.; Zhou, G.; Lu, G.; Chen, J., Resonance-Frequency Modulation for Rapid, Point-of-Care Ebola-Glycoprotein Diagnosis with a Graphene-Based Field-Effect Biotransistor. *Anal. Chem.* **2018,** *90* (24), 14230-14238.

230. Li, H.; Zhang, J.; Zhou, X.; Lu, G.; Yin, Z.; Li, G.; Wu, T.; Boey, F.; Venkatraman, S. S.; Zhang, H., Aminosilane Micropatterns on Hydroxyl-Terminated Substrates: Fabrication and Applications. *Langmuir* **2010,** *26* (8), 5603-9.

231. Ghosh, P. S.; Kim, C. K.; Han, G.; Forbes, N. S.; Rotello, V. M., Efficient Gene Delivery Vectors by Tuning the Surface Charge Density of Amino Acid-Functionalized Gold Nanoparticles. *ACS Nano* **2008,** *2* (11), 2213-8.

232. Heller, I.; Janssens, A. M.; Mannik, J.; Minot, E. D.; Lemay, S. G.; Dekker, C., Identifying the Mechanism of Biosensing with Carbon Nanotube Transistors. *Nano Lett.* **2008,** *8* (2), 591-5.

233. Kariuki, S.; Dewald, H. D., Evaluation of Diffusion Coefficients of Metallic Ions in Aqueous Solutions. *Electroanalysis* **1996,** *8* (4), 307-313.

234. Robinson, J. T.; Perkins, F. K.; Snow, E. S.; Wei, Z.; Sheehan, P. E., Reduced Graphene Oxide Molecular Sensors. *Nano Lett.* **2008,** *8* (10), 3137-40.

235. Ali, E. M.; Zheng, Y.; Yu, H. H.; Ying, J. Y., Ultrasensitive Pb^{2+} Detection by Glutathione-Capped Quantum Dots. *Anal. Chem.* **2007,** *79* (24), 9452-8.

236. Chen, J.; Pu, H.; Hersam, M. C.; Westerhoff, P., Molecular Engineering of 2d Nanomaterial Field-Effect Transistor Sensors: Fundamentals and Translation across the Innovation Spectrum. *Adv. Mater.* **2021,** *n/a* (n/a), e2106975.

237. Mondal, S. K.; Biswas, A.; Pradhan, J. R.; Dasgupta, S., Inkjet-Printed MoS_2 Transistors with Predominantly Intraflake Transport. *Small Methods* **2021,** *5* (12), e2100634.

238. Lin, Z.; Liu, Y.; Halim, U.; Ding, M.; Liu, Y.; Wang, Y.; Jia, C.; Chen, P.; Duan, X.; Wang, C.; Song, F.; Li, M.; Wan, C.; Huang, Y.; Duan, X., Solution-Processable 2d Semiconductors for High-Performance Large-Area Electronics. *Nature* **2018,** *562* (7726), 254-258.

239. Kelly, A. G.; Hallam, T.; Backes, C.; Harvey, A.; Esmaeily, A. S.; Godwin, I.; Coelho, J.; Nicolosi, V.; Lauth, J.; Kulkarni, A.; Kinge, S.; Siebbeles, L. D.; Duesberg, G. S.; Coleman, J. N., All-Printed Thin-Film Transistors from Networks of Liquid-Exfoliated Nanosheets. *Science* **2017,** *356* (6333), 69-73.

240. Kim, J.; Rhee, D.; Song, O.; Kim, M.; Kwon, Y. H.; Lim, D. U.; Kim, I. S.; Mazanek, V.; Valdman, L.; Sofer, Z.; Cho, J. H.; Kang, J., All Solution-Processed Van Der Waals Heterostructures for Wafer-Scale Electronics. *Adv. Mater.* **2021,** *n/a* (n/a), e2106110.

241. Carey, T.; Arbab, A.; Anzi, L.; Bristow, H.; Hui, F.; Bohm, S.; Wyatt-Moon, G.; Flewitt, A.; Wadsworth, A.; Gasparini, N.; Kim, J. M.; Lanza, M. R.; McCulloch, I.; Sordan, R.; Torrisi, F., Inkjet Printed Circuits with 2d Semiconductor Inks for High-Performance Electronics. *Adv. Electron. Mater.* **2021,** *7* (7).

242. Hu, G.; Yang, L.; Yang, Z.; Wang, Y.; Jin, X.; Dai, J.; Wu, Q.; Liu, S.; Zhu, X.; Wang, X.; Wu, T. C.; Howe, R. C. T.; Albrow-Owen, T.; Ng, L. W. T.; Yang, Q.; Occhipinti, L. G.; Woodward, R. I.; Kelleher, E. J. R.; Sun, Z.; Huang, X.; Zhang, M.; Bain, C. D.; Hasan, T., A General Ink Formulation of 2d Crystals for Wafer-Scale Inkjet Printing. *Sci Adv* **2020,** *6* (33), eaba5029.

243. Seo, J. T.; Zhu, J.; Sangwan, V. K.; Secor, E. B.; Wallace, S. G.; Hersam, M. C., Fully Inkjet-Printed, Mechanically Flexible MoS_2 Nanosheet Photodetectors. *ACS Appl Mater Interfaces* **2019,** *11* (6), 5675-5681.

244. Kappera, R.; Voiry, D.; Yalcin, S. E.; Branch, B.; Gupta, G.; Mohite, A. D.; Chhowalla, M., Phase-Engineered Low-Resistance Contacts for Ultrathin MoS_2 Transistors. *Nat. Mater.* **2014,** *13* (12), 1128-34.

245. Torrisi, F.; Hasan, T.; Wu, W.; Sun, Z.; Lombardo, A.; Kulmala, T. S.; Hsieh, G. W.; Jung, S.; Bonaccorso, F.; Paul, P. J.; Chu, D.; Ferrari, A. C., Inkjet-Printed Graphene Electronics. *ACS Nano* **2012,** *6* (4), 2992-3006.

246. Mak, K. F.; Lee, C.; Hone, J.; Shan, J.; Heinz, T. F., Atomically Thin MoS_2: A New Direct-Gap Semiconductor. *Phys. Rev. Lett.* **2010,** *105* (13), 136805.

247. Liu, K. K.; Zhang, W.; Lee, Y. H.; Lin, Y. C.; Chang, M. T.; Su, C. Y.; Chang, C. S.; Li, H.; Shi, Y.; Zhang, H.; Lai, C. S.; Li, L. J., Growth of Large-Area and Highly Crystalline MoS_2 Thin Layers on Insulating Substrates. *Nano Lett.* **2012,** *12* (3), 1538-44.

248. Hao, Y.; Wang, Y.; Wang, L.; Ni, Z.; Wang, Z.; Wang, R.; Koo, C. K.; Shen, Z.; Thong, J. T., Probing Layer Number and Stacking Order of Few-Layer Graphene by Raman Spectroscopy. *Small* **2010,** *6* (2), 195-200.

249. Sui, X.; Pu, H.; Maity, A.; Chang, J.; Jin, B.; Lu, G.; Wang, Y.; Ren, R.; Mao, S.; Chen, J., Field-Effect Transistor Based on Percolation Network of Reduced Graphene Oxide for

Real-Time ppb-Level Detection of Lead Ions in Water. *ECS Journal of Solid State Science and Technology* **2020,** *9* (11), 115012.

250. Idota, Y.; Kubota, T.; Matsufuji, A.; Maekawa, Y.; Miyasaka, T., Tin-Based Amorphous Oxide: A High-Capacity Lithium-Ion-Storage Material. *Science* **1997,** *276* (5317), 1395-1397.

251. Park, M. S.; Wang, G. X.; Kang, Y. M.; Wexler, D.; Dou, S. X.; Liu, H. K., Preparation and Electrochemical Properties of SnO_2 Nanowires for Application in Lithium-Ion Batteries. *Angew Chem Int Ed Engl* **2007,** *46* (5), 750-3.

252. Chen, J. S.; Lou, X. W., SnO_2-Based Nanomaterials: Synthesis and Application in Lithium-Ion Batteries. *Small* **2013,** *9* (11), 1877-93.

253. Courtney, I. A.; Dahn, J. R., Electrochemical and in Situ X-Ray Diffraction Studies of the Reaction of Lithium with Tin Oxide Composites. *J. Electrochem. Soc.* **1997,** *144* (6), 2045-2052.

254. Huang, J. Y.; Zhong, L.; Wang, C. M.; Sullivan, J. P.; Xu, W.; Zhang, L. Q.; Mao, S. X.; Hudak, N. S.; Liu, X. H.; Subramanian, A.; Fan, H. Y.; Qi, L. A.; Kushima, A.; Li, J., In Situ Observation of the Electrochemical Lithiation of a Single SnO_2 Nanowire Electrode. *Science* **2010,** *330* (6010), 1515-1520.

255. Hu, R.; Ouyang, Y.; Liang, T.; Wang, H.; Liu, J.; Chen, J.; Yang, C.; Yang, L.; Zhu, M., Stabilizing the Nanostructure of SnO_2 Anodes by Transition Metals: A Route to Achieve High Initial Coulombic Efficiency and Stable Capacities for Lithium Storage. *Adv. Mater.* **2017,** *29* (13), 1605006.

256. Jiang, B.; He, Y.; Li, B.; Zhao, S.; Wang, S.; He, Y. B.; Lin, Z., Polymer-Templated Formation of Polydopamine-Coated SnO_2 Nanocrystals: Anodes for Cyclable Lithium-Ion Batteries. *Angew Chem Int Ed Engl* **2017,** *56* (7), 1869-1872.

257. Beaulieu, L. Y.; Eberman, K. W.; Turner, R. L.; Krause, L. J.; Dahn, J. R., Colossal Reversible Volume Changes in Lithium Alloys. *Electrochem Solid St* **2001,** *4* (9), A137-A140.

258. Zhou, X.; Wan, L. J.; Guo, Y. G., Binding SnO_2 Nanocrystals in Nitrogen-Doped Graphene Sheets as Anode Materials for Lithium-Ion Batteries. *Adv. Mater.* **2013,** *25* (15), 2152-7.

259. Cheng, Y. C.; Nie, A. M.; Gan, L. Y.; Zhang, Q. Y.; Schwingenschlogl, U., A Global View of the Phase Transitions of SnO_2 in Rechargeable Batteries Based on Results of High Throughput Calculations. *J. Mater. Chem. A* **2015,** *3* (38), 19483-19489.

260. Li, Y.; Zhang, H.; Chen, Y.; Shi, Z.; Cao, X.; Guo, Z.; Shen, P. K., Nitrogen-Doped Carbon-Encapsulated SnO_2@Sn Nanoparticles Uniformly Grafted on Three-Dimensional Graphene-Like Networks as Anode for High-Performance Lithium-Ion Batteries. *ACS Appl Mater Interfaces* **2016,** *8* (1), 197-207.

261. Sun, J. H.; Xiao, L. H.; Jiang, S. D.; Li, G. X.; Huang, Y.; Geng, J. X., Fluorine-Doped SnO_2@Graphene Porous Composite for High Capacity Lithium-Ion Batteries. *Chem. Mater.* **2015,** *27* (13), 4594-4603.

262. Hu, X.; Zeng, G.; Chen, J. X.; Lu, C. Z.; Wen, Z. H., 3d Graphene Network Encapsulating SnO_2 Hollow Spheres as a High-Performance Anode Material for Lithium-Ion Batteries. *J. Mater. Chem. A* **2017,** *5* (9), 4535-4542.

263. Wan, Y. X.; Xu, X. Q.; Liu, J. W.; Sha, Y.; Chen, Y. J.; Li, L. L.; Xue, G.; Wang, X. L.; Zhou, D. S., A Cold-Flow Process for Fabricating a High-Volumetric-Energy-Density Anode for Lithium-Ion Batteries. *Advanced Materials Technologies* **2017,** *2* (1), 1600156.

264. Yang, L. Y.; Li, S. T.; Liu, J.; Zhu, K. J.; Liu, S. L.; Lei, M., Hollow Bean-Pod-Like SiO_2-Supported-SnO_2/C Nanocomposites for Durable Lithium and Sodium Storage. *J. Mater. Chem. A* **2017,** *5* (4), 1629-1636.

265. Lian, P. C.; Wang, J. Y.; Cai, D. D.; Ding, L. X.; Jia, Q. M.; Wang, H. H., Porous SnO_2@C/Graphene Nanocomposite with 3d Carbon Conductive Network as a Superior Anode Material for Lithium-Ion Batteries. *Electrochim. Acta* **2014,** *116*, 103-110.

266. Zhao, Y.; Li, X. F.; Yan, B.; Li, D. J.; Lawes, S.; Sun, X. L., Significant Impact of 2d Graphene Nanosheets on Large Volume Change Tin-Based Anodes in Lithium-Ion Batteries: A Review. *J. Power Sources* **2015,** *274*, 869-884.

267. Liu, L. J.; Huang, X. K.; Guo, X. R.; Mao, S.; Chen, J. H., Decorating in Situ Ultrasmall Tin Particles on Crumpled N-Doped Graphene for Lithium-Ion Batteries with a Long Life Cycle. *J. Power Sources* **2016,** *328*, 482-491.

268. Paek, S. M.; Yoo, E.; Honma, I., Enhanced Cyclic Performance and Lithium Storage Capacity of SnO_2/Graphene Nanoporous Electrodes with Three-Dimensionally Delaminated Flexible Structure. *Nano Lett.* **2009,** *9* (1), 72-5.

269. Prabakar, S. J.; Hwang, Y. H.; Bae, E. G.; Shim, S.; Kim, D.; Lah, M. S.; Sohn, K. S.; Pyo, M., SnO_2/Graphene Composites with Self-Assembled Alternating Oxide and Amine Layers for High Li-Storage and Excellent Stability. *Adv. Mater.* **2013,** *25* (24), 3307-12.

270. Wang, P.; Zhang, Y.; Yin, Y.; Fan, L.; Zhang, N.; Sun, K., In Situ Synthesis of $CuCo_2S_4$@N/S-Doped Graphene Composites with Pseudocapacitive Properties for High-Performance Lithium-Ion Batteries. *ACS Appl Mater Interfaces* **2018,** *10* (14), 11708-11714.

271. Zhang, L.; Zhao, K.; Yu, R.; Yan, M.; Xu, W.; Dong, Y.; Ren, W.; Xu, X.; Tang, C.; Mai, L., Phosphorus Enhanced Intermolecular Interactions of SnO_2 and Graphene as an Ultrastable Lithium Battery Anode. *Small* **2017,** *13* (20), 1603973.

272. Chen, W. H.; Song, K. M.; Mi, L. W.; Feng, X. M.; Zhang, J. M.; Cui, S. Z.; Liu, C. T., Synergistic Effect Induced Ultrafine SnO_2/Graphene Nanocomposite as an Advanced Lithium/Sodium-Ion Batteries Anode. *J. Mater. Chem. A* **2017,** *5* (20), 10027-10038.

273. Shao, Q.; Tang, J.; Sun, Y.; Li, J.; Zhang, K.; Yuan, J.; Zhu, D. M.; Qin, L. C., Unique Interconnected Graphene/SnO_2 Nanoparticle Spherical Multilayers for Lithium-Ion Battery Applications. *Nanoscale* **2017,** *9* (13), 4439-4444.

274. Ji, G.; Ding, B.; Sha, Z.; Wu, J.; Ma, Y.; Lee, J. Y., Conformal Graphene Encapsulation of Tin Oxide Nanoparticle Aggregates for Improved Performance in Reversible Li^+ Storage. *Nanoscale* **2013,** *5* (13), 5965-72.

275. Zhang, C. F.; Peng, X.; Guo, Z. P.; Cai, C. B.; Chen, Z. X.; Wexler, D.; Li, S.; Liu, H. K., Carbon-Coated SnO_2/Graphene Nanosheets as Highly Reversible Anode Materials for Lithium Ion Batteries. *Carbon* **2012,** *50* (5), 1897-1903.

276. Shahid, M.; Yesibolati, N.; Reuter, M. C.; Ross, F. M.; Alshareef, H. N., Layer-by-Layer Assembled Graphene-Coated Mesoporous SnO_2 Spheres as Anodes for Advanced Li-Ion Batteries. *J. Power Sources* **2014,** *263*, 239-245.

277. Cheng, J. L.; Xin, H. L.; Zheng, H. M.; Wang, B., One-Pot Synthesis of Carbon Coated-SnO_2/Graphene-Sheet Nanocomposite with Highly Reversible Lithium Storage Capability. *J. Power Sources* **2013,** *232*, 152-158.

278. Ye, F.; Zhao, B. T.; Ran, R.; Shao, Z. P., A Polyaniline-Coated Mechanochemically Synthesized Tin Oxide/Graphene Nanocomposite for High-Power and High-Energy Lithium-Ion Batteries. *J. Power Sources* **2015,** *290*, 61-70.

279. Wang, X.; Cao, X. Q.; Bourgeois, L.; Guan, H.; Chen, S. M.; Zhong, Y. T.; Tang, D. M.; Li, H. Q.; Zhai, T. Y.; Li, L.; Bando, Y.; Golberg, D., N-Doped Graphene-SnO_2 Sandwich Paper for High-Performance Lithium-Ion Batteries. *Adv. Funct. Mater.* **2012,** *22* (13), 2682-2690.

280. Hummers, W. S.; Offeman, R. E., Preparation of Graphitic Oxide. *Journal of the American Chemical Society* **1958,** *80* (6), 1339-1339.

281. Liang, Y.; Li, Y.; Wang, H.; Zhou, J.; Wang, J.; Regier, T.; Dai, H., Co_3O_4 Nanocrystals on Graphene as a Synergistic Catalyst for Oxygen Reduction Reaction. *Nat. Mater.* **2011,** *10* (10), 780-6.

282. Furukawa, H.; Cordova, K. E.; O'Keeffe, M.; Yaghi, O. M., The Chemistry and Applications of Metal-Organic Frameworks. *Science* **2013,** *341* (6149), 1230444.

283. Sun, X. Q.; Long, R.; Cheng, X. F.; Zhao, X.; Dai, Y.; Huang, B. B., Structural, Electronic, and Optical Properties of N-Doped SnO_2. *J. Phys. Chem. C* **2008,** *112* (26), 9861-9864.

284. Livraghi, S.; Barbero, N.; Agnoli, S.; Barolo, C.; Granozzi, G.; Sauvage, F.; Giamello, E., A Multi-Technique Comparison of the Electronic Properties of Pristine and Nitrogen-Doped Polycrystalline SnO_2. *Phys. Chem. Chem. Phys.* **2016,** *18* (32), 22617-27.

285. Yan, Y.; Zhang, S. B.; Pantelides, S. T., Control of Doping by Impurity Chemical Potentials: Predictions for P-Type ZnO. *Phys. Rev. Lett.* **2001,** *86* (25), 5723-6.

286. Pettine, M.; Millero, F. J.; Macchi, G., Hydrolysis of Tin(ii) in Aqueous Solutions. *Anal. Chem.* **2002,** *53* (7), 1039-1043.

287. Francis, M. D.; Tofe, A. J.; Hiles, R. A.; Birch, C. G.; Bevan, J. A.; Grabenstetter, R. J., Inorganic Tin: Chemistry, Disposition and Role in Nuclear Medicine Diagnostic Skeletal Imaging Agents. *Int J Nucl Med Biol* **1981,** *8* (2-3), 145-52.

288. Li, S.; Wang, Y. Z.; Lai, C.; Qiu, J. X.; Ling, M.; Martens, W.; Zhao, H. J.; Zhang, S. Q., Directional Synthesis of Tin Oxide@Graphene Nanocomposites via a One-Step up-Scalable Wet-Mechanochemical Route for Lithium Ion Batteries. *J. Mater. Chem. A* **2014,** *2* (26), 10211-10217.

289. Youn, D. H.; Heller, A.; Mullins, C. B., Simple Synthesis of Nanostructured Sn/Nitrogen-Doped Carbon Composite Using Nitrilotriacetic Acid as Lithium Ion Battery Anode. *Chem. Mater.* **2016,** *28* (5), 1343-1347.

290. Wen, Z. H.; Cui, S. M.; Kim, H. J.; Mao, S.; Yu, K. H.; Lu, G. H.; Pu, H. H.; Mao, O.; Chen, J. H., Binding Sn-Based Nanoparticles on Graphene as the Anode of Rechargeable Lithium-Ion Batteries. *J. Mater. Chem.* **2012,** *22* (8), 3300-3306.

291. Chen, L. F.; Xu, Q., Converting MOFs into Amination Catalysts. *Science* **2017,** *358* (6361), 304-305.

292. Kaskhedikar, N. A.; Maier, J., Lithium Storage in Carbon Nanostructures. *Adv. Mater.* **2009,** *21* (25-26), 2664-2680.

293. Raccichini, R.; Varzi, A.; Passerini, S.; Scrosati, B., The Role of Graphene for Electrochemical Energy Storage. *Nat. Mater.* **2015,** *14* (3), 271-9.

294. Dahn, J. R.; Zheng, T.; Liu, Y. H.; Xue, J. S., Mechanisms for Lithium Insertion in Carbonaceous Materials. *Science* **1995,** *270* (5236), 590-593.

295. Lian, P. C.; Zhu, X. F.; Liang, S. Z.; Li, Z.; Yang, W. S.; Wang, H. H., High Reversible Capacity of SnO_2/Graphene Nanocomposite as an Anode Material for Lithium-Ion Batteries. *Electrochim. Acta* **2011,** *56* (12), 4532-4539.

296. Chen, Y.; Song, B. H.; Chen, R. M.; Lu, L.; Xue, J. M., A Study of the Superior Electrochemical Performance of 3 nm SnO_2 Nanoparticles Supported by Graphene. *J. Mater. Chem. A* **2014,** *2* (16), 5688-5695.

297. Wang, D. N.; Yang, J. L.; Li, X. F.; Geng, D. S.; Li, R. Y.; Cai, M.; Sham, T. K.; Sun, X. L., Layer by Layer Assembly of Sandwiched Graphene/SnO_2 Nanorod/Carbon Nanostructures with Ultrahigh Lithium Ion Storage Properties. *Energy Environ. Sci.* **2013,** *6* (10), 2900-2906.

298. Wang, R.; Xu, C.; Sun, J.; Gao, L.; Yao, H., Solvothermal-Induced 3d Macroscopic SnO_2/Nitrogen-Doped Graphene Aerogels for High Capacity and Long-Life Lithium Storage. *ACS Appl Mater Interfaces* **2014,** *6* (5), 3427-36.

299. Zhou, X.; Chen, S.; Yang, J.; Bai, T.; Ren, Y.; Tian, H., Metal-Organic Frameworks Derived Okra-Like SnO_2 Encapsulated in Nitrogen-Doped Graphene for Lithium Ion Battery. *ACS Appl Mater Interfaces* **2017,** *9* (16), 14309-14318.

300. Huang, X.; Cui, S.; Chang, J.; Hallac, P. B.; Fell, C. R.; Luo, Y.; Metz, B.; Jiang, J.; Hurley, P. T.; Chen, J., A Hierarchical Tin/Carbon Composite as an Anode for Lithium-Ion Batteries with a Long Cycle Life. *Angew Chem Int Ed Engl* **2015,** *54* (5), 1490-3.

301. Huang, X. K.; Shi, K. Y.; Yang, J.; Mao, G.; Chen, J. H., MnO_2-GO Double-Shelled Sulfur (S@MnO_2@GO) as a Cathode for Li-S Batteries with Improved Rate Capability and Cyclic Performance. *J. Power Sources* **2017,** *356* (Supplement C), 72-79.

302. Huang, X. K.; Mao, S.; Chang, J. B.; Hallac, P. B.; Fell, C. R.; Luo, Y. T.; Metz, B.; Jiang, J. W.; Chen, J. H., Improving Cyclic Performance of Si Anode for Lithium-Ion Batteries by Forming an Intermetallic Skin. *RSC Adv.* **2015,** *5* (48), 38660-38664.

303. Huang, X. K.; Sui, X. Y.; Yang, H. N.; Ren, R.; Wu, Y. P.; Guo, X. R.; Chen, J. H., Hf-Free Synthesis of Si/C Yolk/Shell Anodes for Lithium-Ion Batteries. *J. Mater. Chem. A* **2018,** *6* (6), 2593-2599.

304. Courtney, I. A.; Dahn, J. R., Key Factors Controlling the Reversibility of the Reaction of Lithium with SnO_2 and Sn_2BPO_6 Glass. *J. Electrochem. Soc.* **1997,** *144* (9), 2943-2948.

305. Pelliccione, C. J.; Timofeeva, E. V.; Segre, C. U., Potential-Resolved in Situ X-Ray Absorption Spectroscopy Study of Sn and SnO_2 Nanomaterial Anodes for Lithium-Ion Batteries. *J. Phys. Chem. C* **2016,** *120* (10), 5331-5339.

306. Cai, D. P.; Yang, T.; Liu, B.; Wang, D. D.; Liu, Y.; Wang, L. L.; Li, Q. H.; Wang, T. H., A Nanocomposite of Tin Dioxide Octahedral Nanocrystals Exposed to High-Energy Facets Anchored onto Graphene Sheets for High Performance Lithium-Ion Batteries. *J. Mater. Chem. A* **2014,** *2* (34), 13990-13995.

307. Song, H. W.; Li, N.; Cui, H.; Wang, C. X., Enhanced Capability and Cyclability of SnO_2-Graphene Oxide Hybrid Anode by Firmly Anchored SnO_2 Quantum Dots. *J. Mater. Chem. A* **2013,** *1* (26), 7558-7562.

308. Lin, J.; Peng, Z.; Xiang, C.; Ruan, G.; Yan, Z.; Natelson, D.; Tour, J. M., Graphene Nanoribbon and Nanostructured SnO_2 Composite Anodes for Lithium Ion Batteries. *ACS Nano* **2013,** *7* (7), 6001-6.

309. Li, Z. T.; Wu, G. L.; Liu, D.; Wu, W. T.; Jiang, B.; Zheng, J. T.; Li, Y. P.; Li, J. H.; Wu, M. B., Graphene Enhanced Carbon-Coated Tin Dioxide Nanoparticles for Lithium-Ion Secondary Batteries. *J. Mater. Chem. A* **2014,** *2* (20), 7471-7477.

310. Dong, W.; Xu, J.; Wang, C.; Lu, Y.; Liu, X.; Wang, X.; Yuan, X.; Wang, Z.; Lin, T.; Sui, M.; Chen, I. W.; Huang, F., A Robust and Conductive Black Tin Oxide Nanostructure Makes Efficient Lithium-Ion Batteries Possible. *Adv. Mater.* **2017,** *29* (24), 1700136.

311. Wang, J.; Fang, F.; Yuan, T.; Yang, J.; Chen, L.; Yao, C.; Zheng, S.; Sun, D., Three-Dimensional Graphene/Single-Walled Carbon Nanotube Aerogel Anchored with SnO_2 Nanoparticles for High Performance Lithium Storage. *ACS Appl Mater Interfaces* **2017,** *9* (4), 3544-3553.

312. Yang, S.; Yue, W. B.; Zhu, J.; Ren, Y.; Yang, X. J., Graphene-Based Mesoporous SnO_2 with Enhanced Electrochemical Performance for Lithium-Ion Batteries. *Adv. Funct. Mater.* **2013,** *23* (28), 3570-3576.

313. Xu, Y.-S.; Duan, S.-Y.; Sun, Y.-G.; Bin, D.; Tao, X.-S.; Zhang, D.; Liu, Y.; Cao, A.-M.; Wan, L.-j., Recent Developments in Electrode Materials for Potassium-Ion Batteries. *J. Mater. Chem. A* **2019**.

314. Wu, X.; Zhao, W.; Wang, H.; Qi, X. J.; Xing, Z.; Zhuang, Q. C.; Ju, Z. C., Enhanced Capacity of Chemically Bonded Phosphorus/Carbon Composite as an Anode Material for Potassium-Ion Batteries. *J. Power Sources* **2018,** *378*, 460-467.

315. Zhang, W.; Mao, J.; Li, S.; Chen, Z.; Guo, Z., Phosphorus-Based Alloy Materials for Advanced Potassium-Ion Battery Anode. *J. Am. Chem. Soc.* **2017,** *139* (9), 3316-3319.

316. Yang, F.; Gao, H.; Hao, J.; Zhang, S.; Li, P.; Liu, Y.; Chen, J.; Guo, Z., Yolk–Shell Structured FeP@C Nanoboxes as Advanced Anode Materials for Rechargeable Lithium-/Potassium-Ion Batteries. *Adv. Funct. Mater.* **2019,** *29* (16), 1808291.

317. Wu, Y.; Hu, S.; Xu, R.; Wang, J.; Peng, Z.; Zhang, Q.; Yu, Y., Boosting Potassium-Ion Battery Performance by Encapsulating Red Phosphorus in Free-Standing Nitrogen-Doped Porous Hollow Carbon Nanofibers. *Nano Lett.* **2019,** *19* (2), 1351-1358.

318. Xiong, P.; Bai, P.; Tu, S.; Cheng, M.; Zhang, J.; Sun, J.; Xu, Y., Red Phosphorus Nanoparticle@3d Interconnected Carbon Nanosheet Framework Composite for Potassium-Ion Battery Anodes. *Small* **2018**, e1802140.

319. Tang, J.; Yamauchi, Y., Carbon Materials: MOF Morphologies in Control. *Nat Chem* **2016,** *8* (7), 638-9.

320. Ye, L.; Chai, G. L.; Wen, Z. H., Zn-MOF-74 Derived N-Doped Mesoporous Carbon as pH-Universal Electrocatalyst for Oxygen Reduction Reaction. *Adv. Funct. Mater.* **2017,** *27* (14), 1606190.

321. Adhikari, A. K.; Lin, K. S., Synthesis, Fine Structural Characterization, and CO_2 Adsorption Capacity of Metal Organic Frameworks-74. *J Nanosci Nanotechnol* **2014,** *14* (4), 2709-17.

322. Diaz-Garcia, M.; Mayoral, A.; Diaz, I.; Sanchez-Sanchez, M., Nanoscaled M-MOF-74 Materials Prepared at Room Temperature. *Crystal Growth & Design* **2014,** *14* (5), 2479-2487.

323. Wang, L. J.; Deng, H.; Furukawa, H.; Gandara, F.; Cordova, K. E.; Peri, D.; Yaghi, O. M., Synthesis and Characterization of Metal-Organic Framework-74 Containing 2, 4, 6, 8, and 10 Different Metals. *Inorg. Chem.* **2014,** *53* (12), 5881-3.

324. McGuire, C. V.; Forgan, R. S., The Surface Chemistry of Metal-Organic Frameworks. *Chem Commun (Camb)* **2015,** *51* (25), 5199-217.

325. Yue, Y.; Qiao, Z. A.; Fulvio, P. F.; Binder, A. J.; Tian, C.; Chen, J.; Nelson, K. M.; Zhu, X.; Dai, S., Template-Free Synthesis of Hierarchical Porous Metal-Organic Frameworks. *J. Am. Chem. Soc.* **2013,** *135* (26), 9572-5.

326. Pachfule, P.; Shinde, D.; Majumder, M.; Xu, Q., Fabrication of Carbon Nanorods and Graphene Nanoribbons from a Metal-Organic Framework. *Nat Chem* **2016,** *8* (7), 718-24.

327. Feng, L.; Li, J.-L.; Day, G. S.; Lv, X.-L.; Zhou, H.-C., Temperature-Controlled Evolution of Nanoporous MOF Crystallites into Hierarchically Porous Superstructures. *Chem* **2019**.

328. Julien, P. A.; Uzarevic, K.; Katsenis, A. D.; Kimber, S. A.; Wang, T.; Farha, O. K.; Zhang, Y.; Casaban, J.; Germann, L. S.; Etter, M.; Dinnebier, R. E.; James, S. L.; Halasz, I.; Friscic, T., In Situ Monitoring and Mechanism of the Mechanochemical Formation of a Microporous MOF-74 Framework. *J. Am. Chem. Soc.* **2016,** *138* (9), 2929-32.

329. Pham, M. H.; Vuong, G. T.; Fontaine, F. G.; Do, T. O., Rational Synthesis of Metal-Organic Framework Nanocubes and Nanosheets Using Selective Modulators and Their Morphology-Dependent Gas-Sorption Properties. *Crystal Growth & Design* **2012,** *12* (6), 3091-3095.

330. Tsuruoka, T.; Furukawa, S.; Takashima, Y.; Yoshida, K.; Isoda, S.; Kitagawa, S., Nanoporous Nanorods Fabricated by Coordination Modulation and Oriented Attachment Growth. *Angew Chem Int Ed Engl* **2009,** *48* (26), 4739-43.

331. Zou, L.; Hou, C.-C.; Liu, Z.; Pang, H.; Xu, Q., Super-Long Single-Crystal Metal-Organic Framework Nanotubes. *Journal of the American Chemical Society* **2018**.

332. Zou, L.; Kitta, M.; Hong, J.; Suenaga, K.; Tsumori, N.; Liu, Z.; Xu, Q., Fabrication of a Spherical Superstructure of Carbon Nanorods. *Adv. Mater.* **2019,** *0* (0), 1900440.

333. Srinivas, G.; Krungleviciute, V.; Guo, Z. X.; Yildirim, T., Exceptional CO_2 Capture in a Hierarchically Porous Carbon with Simultaneous High Surface Area and Pore Volume. *Energy Environ. Sci.* **2014,** *7* (1), 335-342.

334. Zhang, H. G.; Hwang, S.; Wang, M. Y.; Feng, Z. X.; Karakalos, S.; Luo, L. L.; Qiao, Z.; Xie, X. H.; Wang, C. M.; Su, D.; Shao, Y. Y.; Wu, G., Single Atomic Iron Catalysts for Oxygen Reduction in Acidic Media: Particle Size Control and Thermal Activation. *Journal of the American Chemical Society* **2017,** *139* (40), 14143-14149.

335. Huang, X.; Sui, X.; Ji, W.; Wang, Y.; Qu, D.; Chen, J., From Phosphorus Nanorods/C to York-Shell P@Hollow C for Potassium-Ion Batteries: High Capacity with Stable Cyclic Performance. *J. Mater. Chem. A* **2020**.

336. Xue, L.; Li, Y.; Gao, H.; Zhou, W.; Lu, X.; Kaveevivitchai, W.; Manthiram, A.; Goodenough, J. B., Low-Cost High-Energy Potassium Cathode. *J. Am. Chem. Soc.* **2017,** *139* (6), 2164-2167.

337. Wang, H.; Wang, L.; Wang, L.; Xing, Z.; Wu, X.; Zhao, W.; Qi, X.; Ju, Z.; Zhuang, Q., Phosphorus Particles Embedded in Reduced Graphene Oxide Matrix to Enhance Capacity and Rate Capability for Capacitive Potassium-Ion Storage. *Chemistry* **2018,** *24* (52), 13897-13902.

338. Sultana, I.; Rahman, M. M.; Ramireddy, T.; Chen, Y.; Glushenkov, A. M., High Capacity Potassium-Ion Battery Anodes Based on Black Phosphorus. *J. Mater. Chem. A* **2017,** *5* (45), 23506-23512.

339. Schachter, R.; Michel, C. G.; Kuck, M. A.; Baumann, J. A.; Olego, D. J.; Polgar, L. G.; Raccah, P. M.; Spicer, W. E., Semiconductor Properties of Polyphosphides. *Appl. Phys. Lett.* **1984,** *45* (3), 277-279.

340. Vonschnering, H. G.; Honle, W., Bridging Chasms with Polyphosphides. *Chem. Rev.* **1988,** *88* (1), 243-273.

APPENDIX

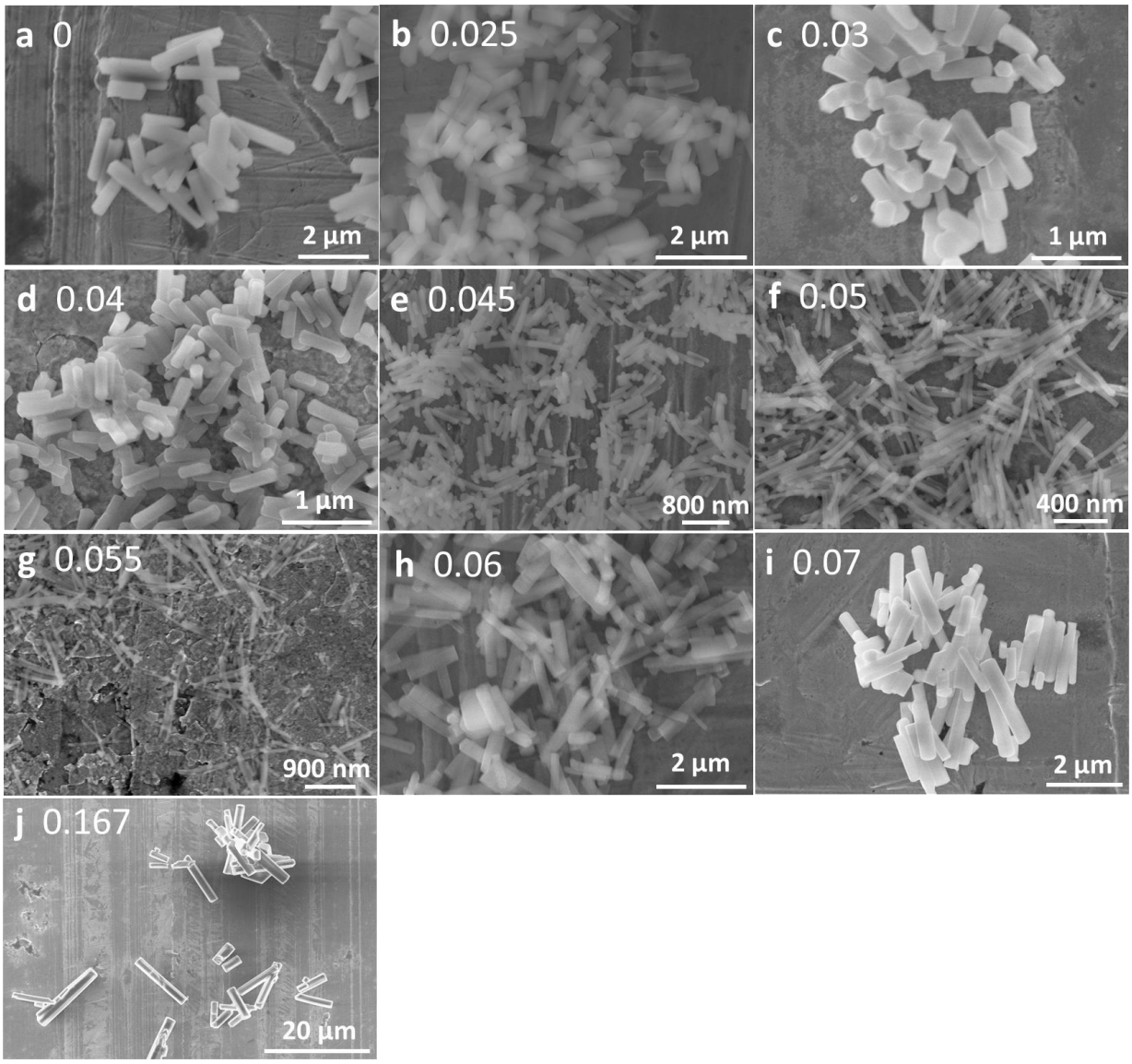

Fig. A1 a-j) SEM images of ZRods synthesized with an H_2O/DMF volume ratio of a) 0, b) 0.025, c) 0.03, d) 0.04, e) 0.045, f) 0.05, g) 0.055, h) 0.06, i) 0.07, and j) 0.167, respectively.

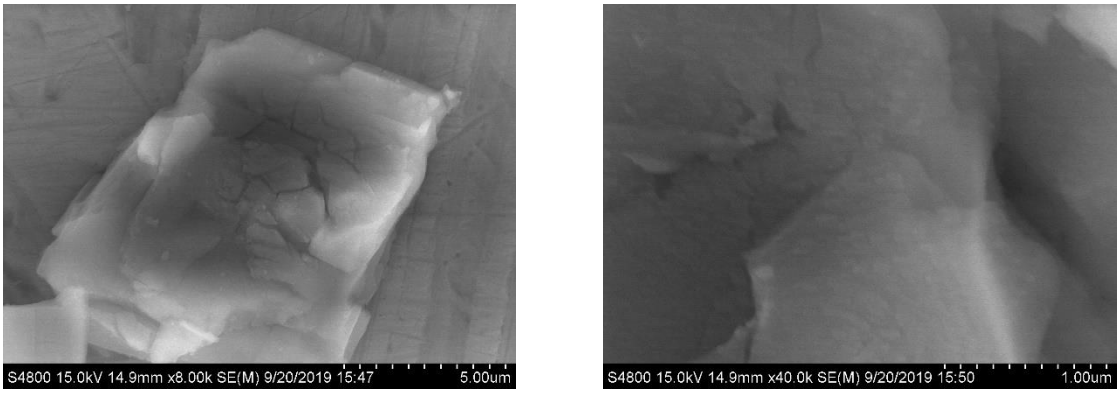

Fig. A2 SEM images of Zn-MOF-74 synthesized using $Zn(NO)_3 \cdot 6H_2O$ as the Zn source with the same Zn element content, and a volume ratio of H_2O/DMF = 0.05 (v/v) as the solvent in the same synthesis condition for ZRod-0.05.

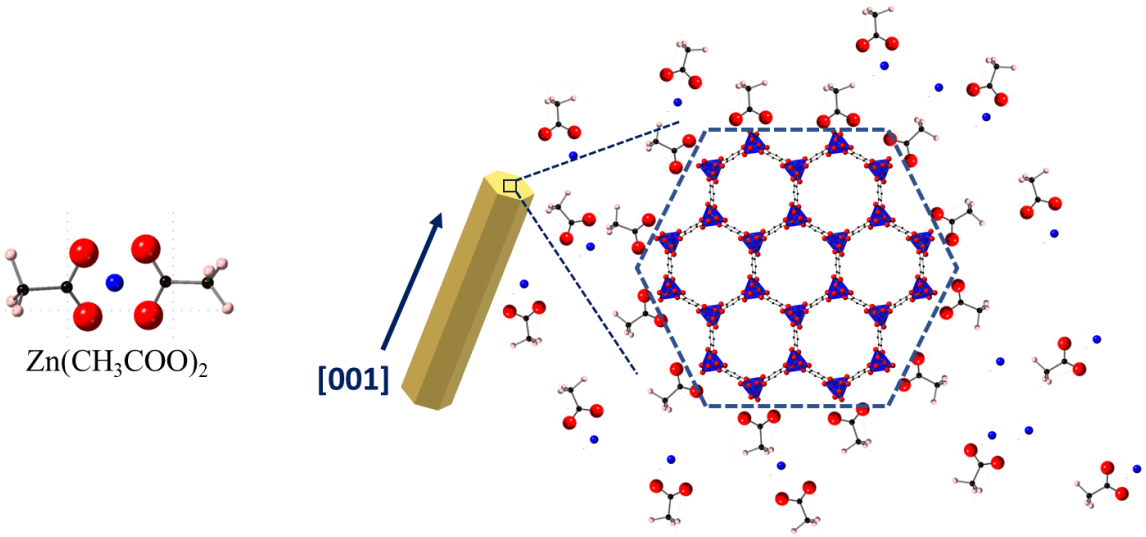

Fig. A3 CH_3COO^- groups prefer to coordinate with metal nodes around the one-dimensional (1D) channels of Zn-MOF-74 during the reaction, promoting an oriented growth along [001] direction.

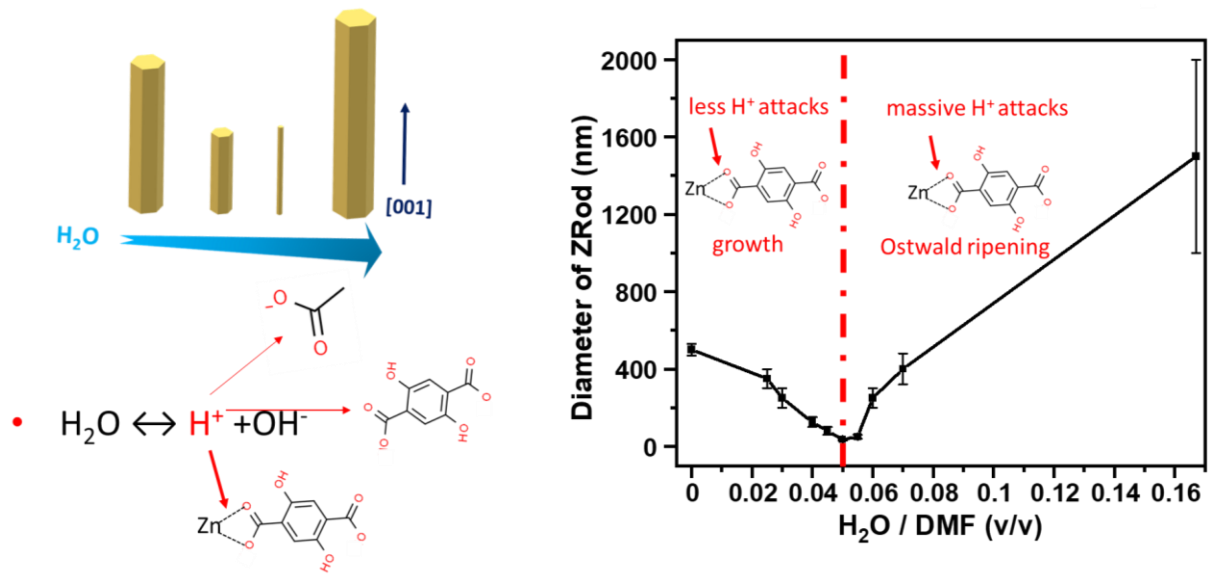

Fig. A4 Schematic illustration for the size adjustment of ZRods with H_2O content.

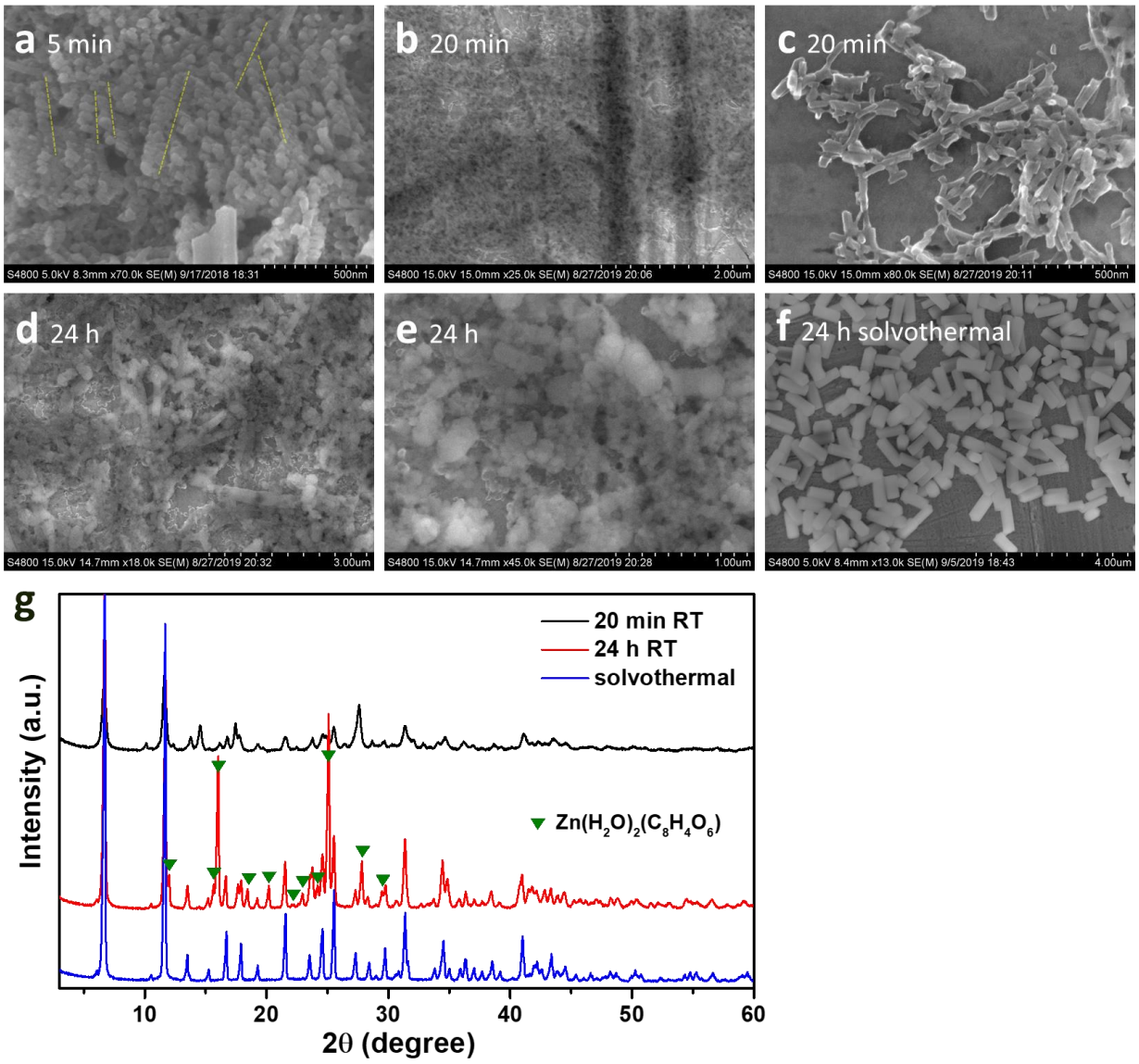

Fig. A5 SEM images of products with H_2O/DMF = 0.025 (v/v) in the mixed solvent after stirring for a) 5 min (dotted lines indicate particle alignment), b,c) 20 min, d,e) 24 h, at room temperature, and f) solvothermal reaction at 100°C for 24 h (ZRod-0.025). g) XRD patterns of products above. Peaks indexed to the $Zn(H_2O)_2(C_8H_4O_6)$ are in accordance with reference [1]. All the samples were collected by centrifugation and washed with DMF and methanol.

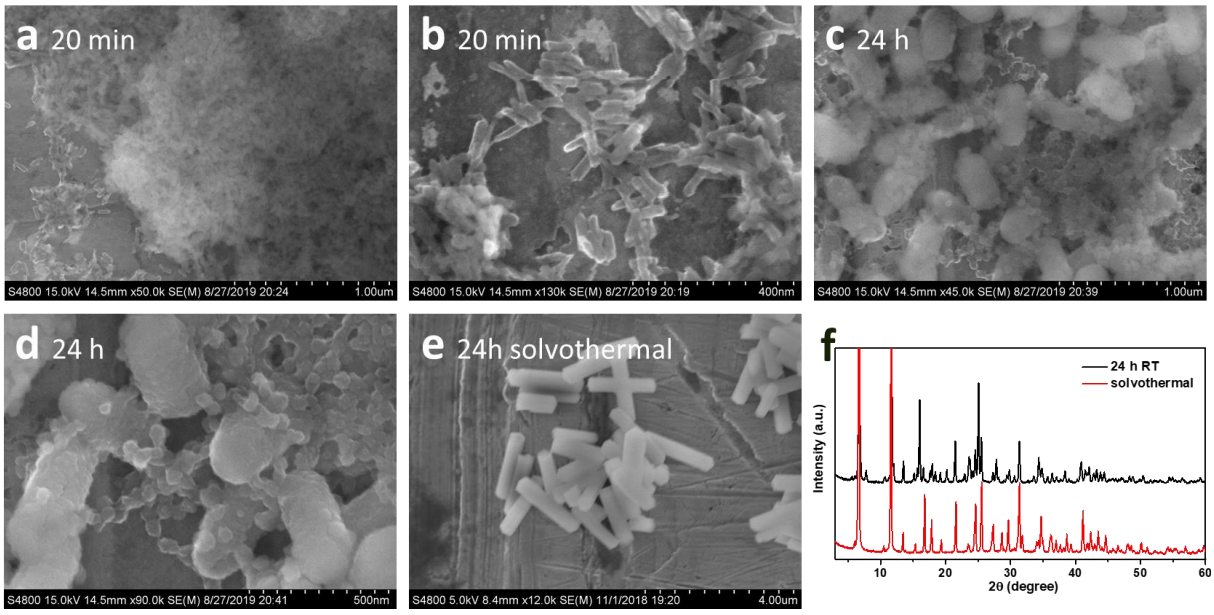

Fig. A6 SEM images of products using DMF solvent after stirring for a,b) 20 min, c,d) 24 h, at room temperature, and e) solvothermal reaction at 100℃ for 24 h (ZRod-0). f) XRD patterns of products above.

The formation process of ZRods

To gain insight into the formation process of Zn-MOF-74 rods (ZRods), after mixing $Zn(CH_3COO)_2$ and $C_8H_6O_6$ solutions with H_2O/DMF = 0.025 (v/v) and stirring for 5 min, 20 min, and 24 h at room temperature, the products were collected for scanning electron microscopy (SEM) imaging (Fig. A5a-e). At the initial stage (5 min, Fig. A5a), small particles around 40 nm formed, and tended to a linear alignment, implying a possible oriented attachment [2]. After 20 min, rough nanorod structures with a diameter of ~40 nm and a length of 60~100 nm were obtained (Fig. A5b,c), possibly due to the fusion of the initial aligned particles. In contrast to the well-developed hexagonal pillars from the solvothermal reaction (i.e., ZRod-0.025 in Fig. A1b and Fig. A5f),

prolonging the stir for 24 h still could not produce pillared crystals, but resulted in particles ~50 nm and their aggregates (Fig. A5d,e).

The crystal structures of these products were examined by X-ray diffraction (XRD), as shown in Fig. A5g. The solvothermal reaction led to the crystalline Zn-MOF-74 (Fig. A5g and Fig. 7.4a), whose pattern matched well with simulated XRD pattern [3]. In contrast, the sample collected after 20 min reaction at room temperature possessed the characteristic peaks of the linear structure of $Zn(H_2O)_2(C_8H_4O_6)$ [4] and Zn-MOF-74 ($Zn_2(H_2O)_2(C_8H_2O_6)$), with other peaks belonging to unidentified intermediate phases. Continuing the reaction at room temperature for 24 h enhanced the peak intensity due to the crystal growth and maturation, and all the peaks could be indexed to the $Zn(H_2O)_2(C_8H_4O_6)$ and Zn-MOF-74. These results reveal that, by using zinc acetate as metal source, the crystalline phase of Zn-MOF-74 can form at room temperature [5] through a dynamical transformation from a simple, linear $Zn(H_2O)_2(C_8H_4O_6)$ structure into 3D Zn-MOF-74 structure. The carboxyl groups on $C_8H_6O_6$ first coordinate with the Zn nodes, forming a linear structure, and then weakly acidic phenolic hydroxyl groups join in the coordination with metal nodes, finalizing 3D MOF structure. A similar stepwise structure transformation process from a linear to 3D structure was also observed in mechanochemical Zn-MOF-74 synthesis [1]. The solvothermal condition promotes this transformation process due to the higher energy for reaction, resulting in phase-pure, more thermodynamically stable Zn-MOF-74 crystals. Similar morphology and crystalline structure transformations have also been clarified during the ZRod-0 formation in a single DMF solvent (Fig. A6), suggesting a universal formation mechanism of Zn-MOF-74 regardless of the H_2O content in the solvent.

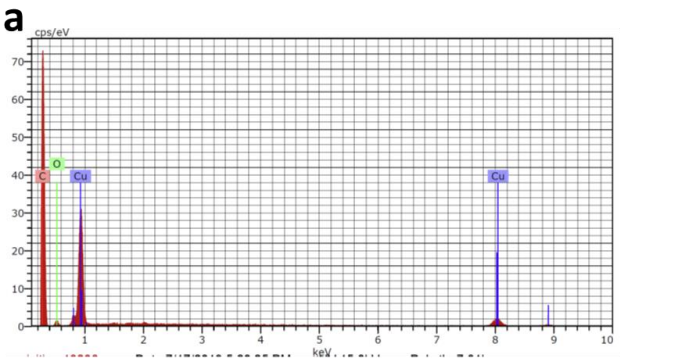

Acquisition 13208 Date:7/17/2019 5:20:25 PM HV:15.0kV

El	AN	Series	unn. C [wt.%]	norm. C [wt.%]	Atom. C [at.%]	Error [%]
C	6	K-series	62.26	60.64	86.08	7.2
O	8	K-series	4.32	4.21	4.49	1.1
Cu	29	K-series	36.09	35.15	9.43	1.3
		Total:	102.67	100.00	100.00	

Mass concentration

C	O
93.5%	6.5%

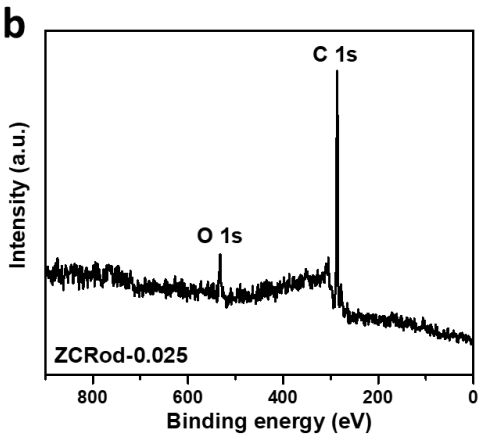

Atomic concentration

C	O
85.3%	14.7%

Corresponding mass concentration

C	O
81.4%	18.6%

Fig. A7 a) EDX elemental analysis and b) XPS spectrum of ZCRod-0.025. The Cu element in Fig. A7a is from the copper tape as the substrate in the measurement.

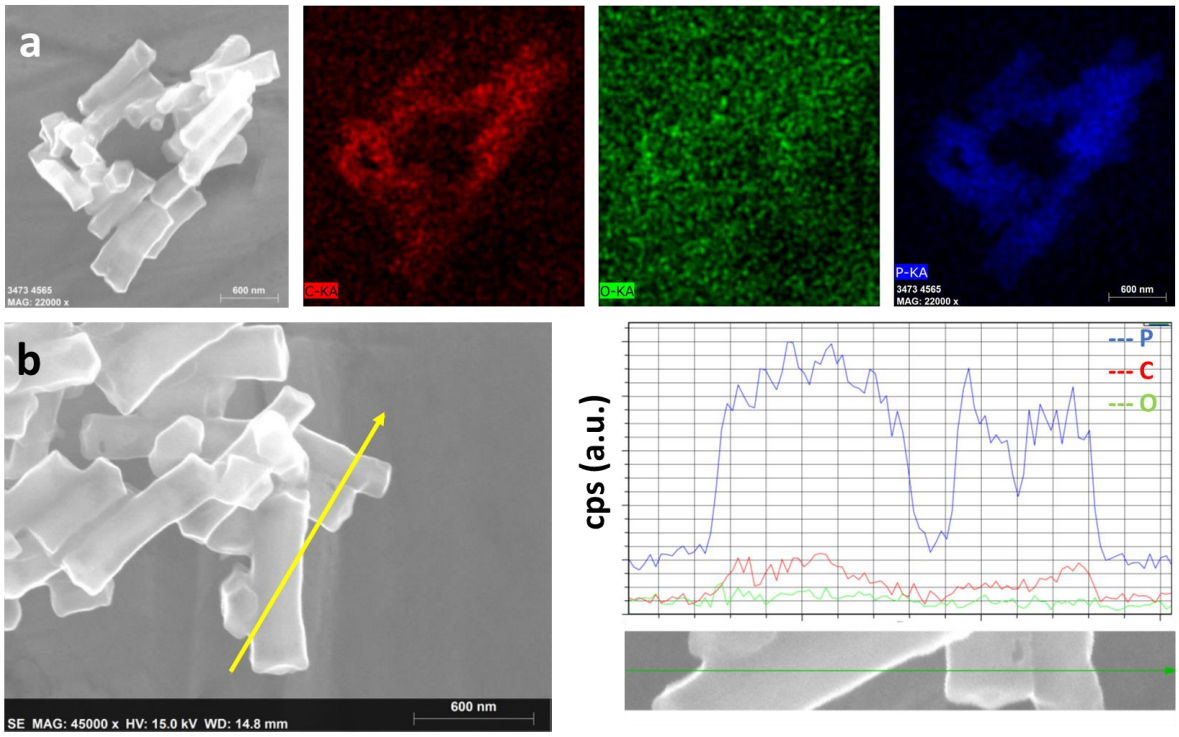

Fig. A8 a) EDX mapping analysis and b) EDX line scan on P70@ZCRod-0.025.

EDX mapping images manifest the uniform distribution of P in the carbon matrix (Fig. A8a), which is also supported by EDS line scan (Fig. A8b). In addition, no P particles can be observed on the nanorod surface. These features confirm the successful P loading into ZCRcod-0.025, which does have the capability to accommodate a P loading of ~70 wt.%.

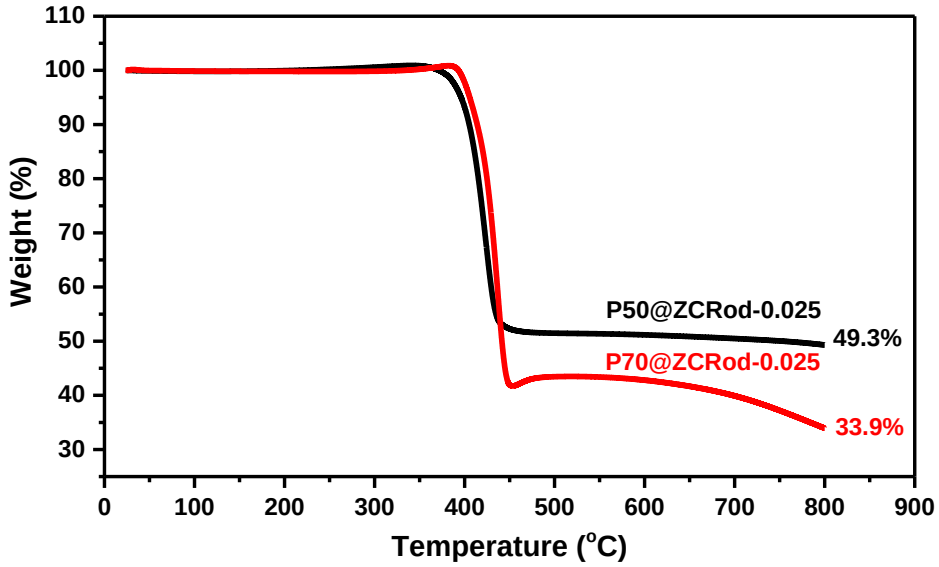

Fig. A9 TGA plots of P50@ZCRod-0.025 and P70@ZCRod-0.025.

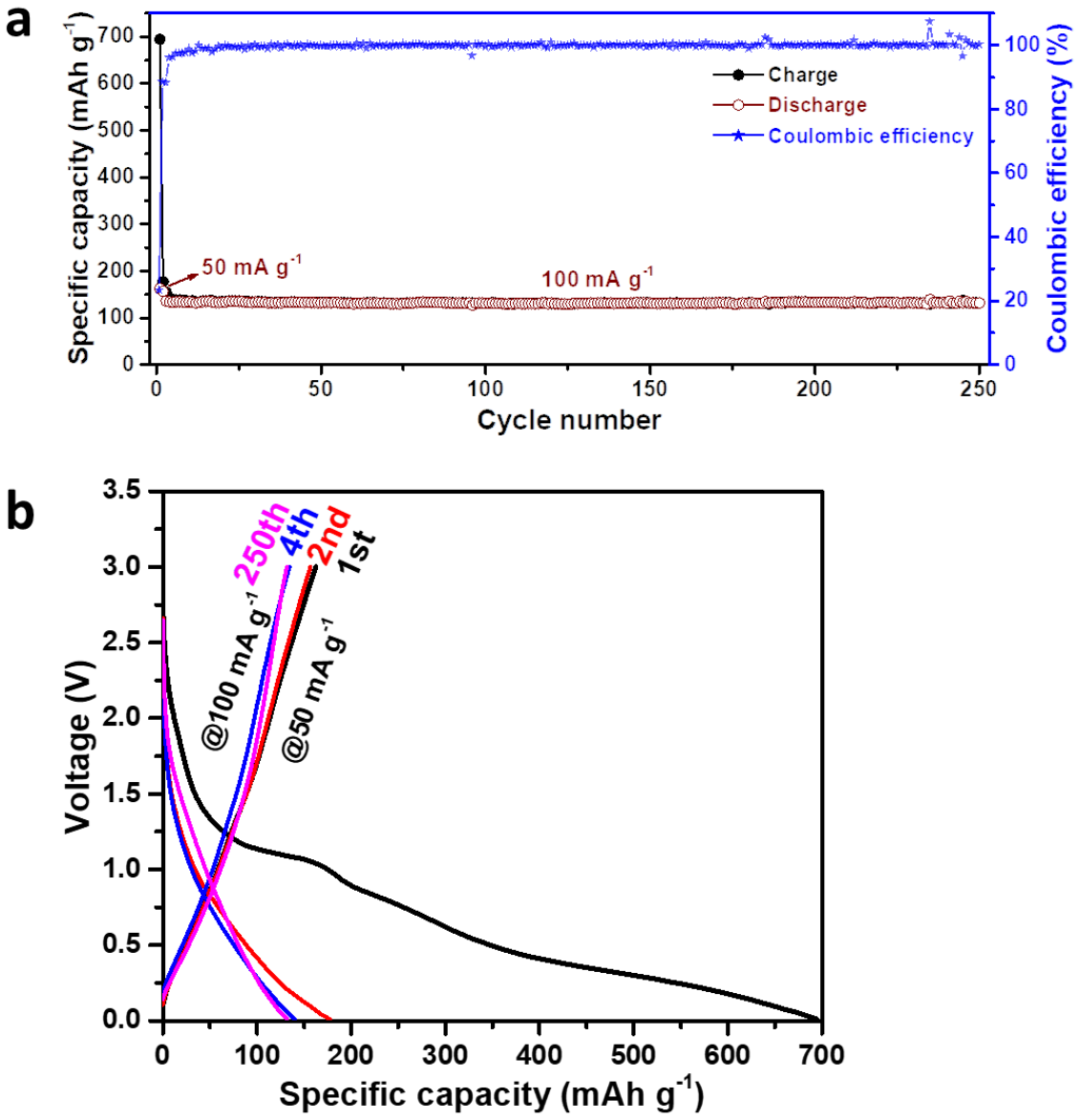

Fig. A10 a) Cyclic performance at 100 mA g^{-1} after initial two cycles of activation at 50 mA g^{-1} of ZCRod-0.025, and b) relevant charge/discharge curves.

ZCRod-0.025 has reversible capacities of 162.5 and 136 mAh g^{-1} at 50 and 100 mA g^{-1}, respectively.

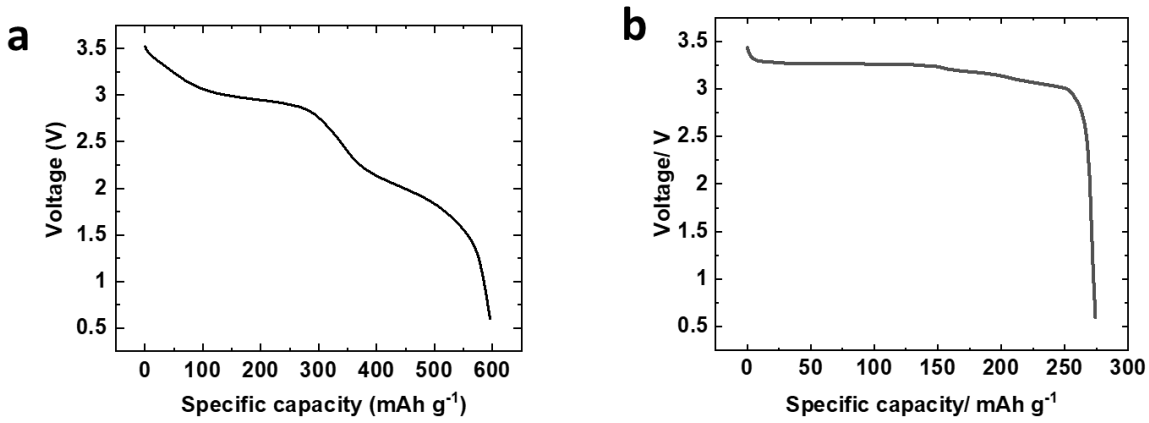

Fig. A11 Gravimetric energy density estimation of a) the P50@ZCRod-0.025 composite (~1,495 Wh kg^{-1}) and b) commercial graphite anode (~863 Wh kg^{-1}) by selecting $K_xMnFe(CN)_6$ as a reference cathode which has an average voltage of ~3.6 V.

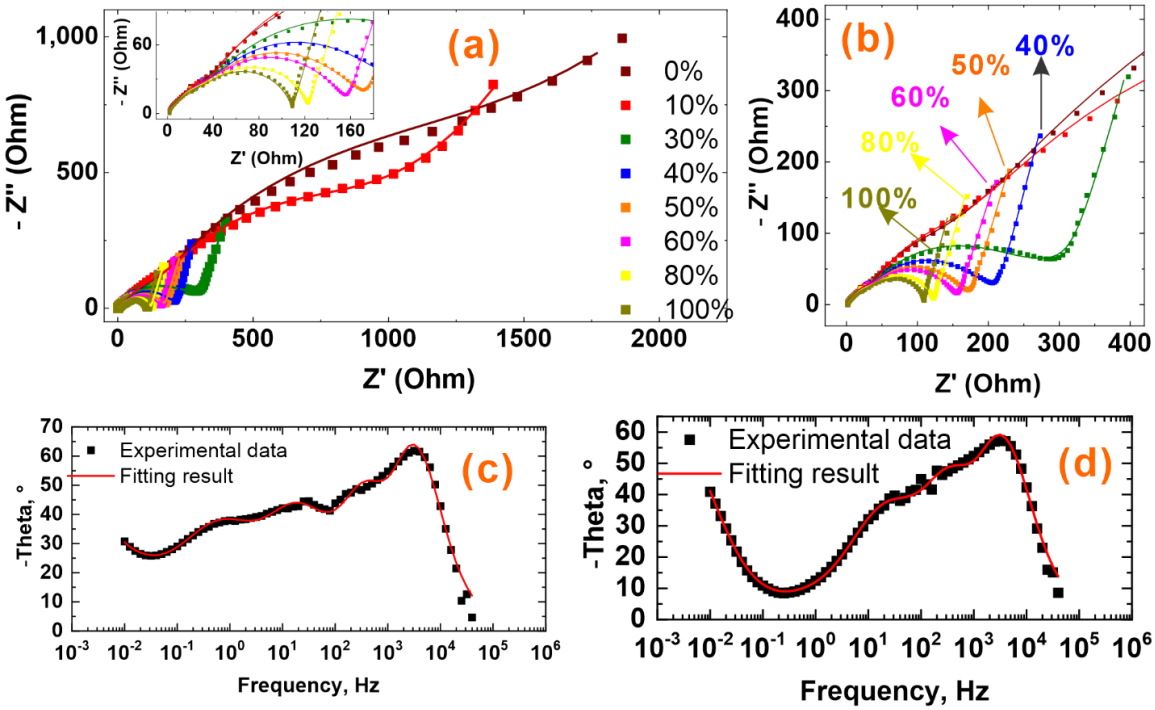

Fig. A12 EIS of P50@ZCRod-0.025 at different states of charge (SOCs): a, b) Nyquist plots, c) Bode plot at SOC of 10%, and d) Bode plot at SOC of 40%.

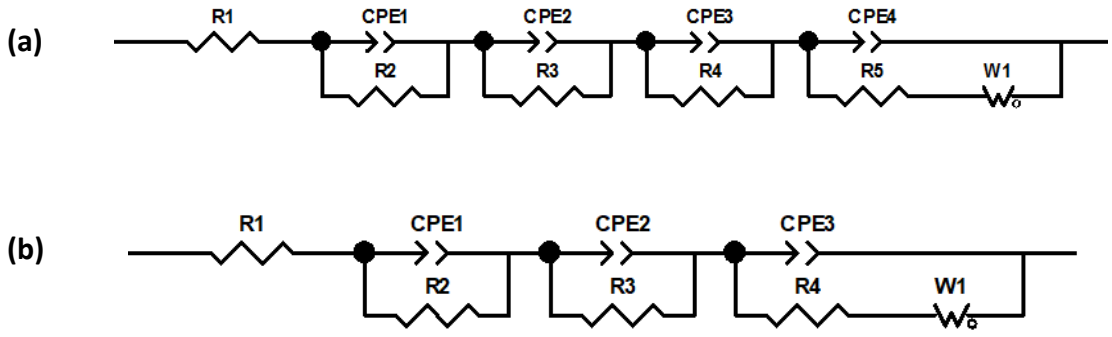

Fig. A13 a) Four-time constant and b) three-time constant equivalent circuits for fitting the impedance results.

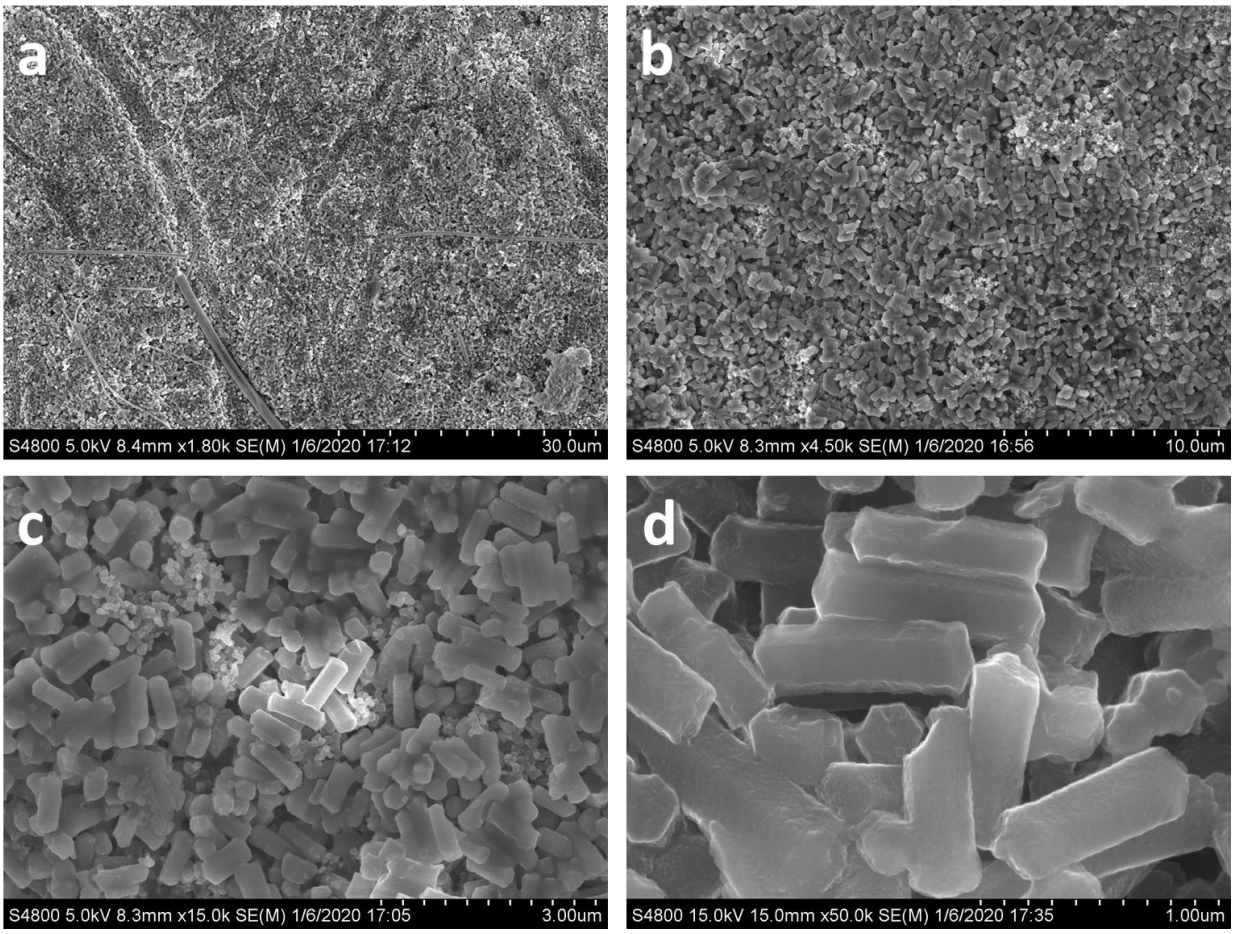

Fig. A14 SEM images of the P50@ZCRod-0.025 electrode after 300 cycles at 2.5 A g^{-1} and washed with DMC.

Table A1 Fitting results of the electrochemical impedance spectra at various states of charge (SOCs).

SOC, %	R1(+)	R1(Err%)	R2(+)	R2(Err%)	R3(+)	R3(Err%)	R4(+)	R4(Err%)	R5(X)	R5(Err%)	W1-R(+)	W1-R(Err%)
0	1.6	1.9	4.9	25.6	20.0	27.6	104.0	21.0	1200.0	N/A	880.0	N/A
10	1.7	1.4	5.9	20.9	24.3	22.9	115.4	20.5	1000.0	N/A	4065.0	59.1
30	1.5	2.6	4.2	27.8	20.2	25.1	10.4	4.7	N/A	N/A	205.4	13.6
40	1.7	1.4	5.4	25.7	24.0	27.7	9.6	6.3	N/A	N/A	84.6	20.9
50	1.7	1.4	4.9	26.8	22.7	26.7	8.4	6.5	N/A	N/A	43.5	31.5
60	1.8	1.5	5.3	33.7	24.1	38.4	12.3	10.7	N/A	N/A	31.4	56.2
70	1.7	1.3	5.6	31.7	26.7	37.5	14.9	15.3	N/A	N/A	13.5	155.2
80	1.7	1.5	5.4	42.6	28.4	70.0	46.1	54.1	N/A	N/A	4.9	1683.2
90	1.8	2.2	5.0	47.2	32.1	62.9	59.8	79.8	N/A	N/A	3.0	4054.1
100	1.8	1.4	5.0	43.3	24.1	61.3	36.1	46.8	N/A	N/A	2.6	2544.8

Note: At SOCs of 0% and 10%, the EIS were fitted by a four-time-constant equivalent circuit (Fig. A13a) while at other SOCs, the EIS were fitted by a three-time-constant equivalent circuit (Fig. A13b), which was mostly judged based on their Bode plots. At the 0%-SOC, the R4 and the R5 have to be fixed to estimated values; otherwise, the fitted results do not match the experimental data well. Similarly, at the 10%-SOC, the R4 has to be fixed to the estimated value. At the SOCs between 30% and 50%, the fitting error for each parameter is relatively small, suggesting good fitting results. Take SOC of 50% as an example, the Ohmic resistance (R1) is 1.7 Ohm while R2, R3, and R4 are charge transfer resistances for carbon and K-P alloys with a sum of 36 Ohm; in contrast, W1-R represents the K-ion diffusion resistance (43.5 Ohm). The relatively low resistances explain the good rate capability of P50@ZCRod-0.025.

In some cases, the fitting errors at high SOCs such at SOCs of 80-100% are far greater than 100%, which lead those fitting results unreliable.

Table A2 Comparison of the electrochemical performance of the P50@ZCRod-0.025 composite with other phosphorus-based anodes for PIBs. (The specific capacities are calculated based on the mass of composites.)

Materials	**Current density ($mA\ g^{-1}$)**	**Initial reversible capacity ($mAh\ g^{-1}$) and initial CE**	**Cycling stability ($mAh\ g^{-1}$)**	**Reference**
P50@ZCRod-0.025	**50** **100** **2,500** **5,000**	**589.2 78.5%** **289.6** **187.5**	**401.8 after 75 cycles** **150.7 after 400 cycles**	**This work**
Red P@hollow C	50 250 5,000	841 67% 249	724 after 40 cycles	[6]
Red P/CNT/Ketjen black	25 1,000 2,000	624.5 68.26% 270 121	750 after 7 cycles ~220 after 60 cycles	[7]
Red P@3D C sheets	100 2,000	457 59% 323.7	273.1 after 40 cycles	[8]

Table A2 Comparison of the electrochemical performance of the P50@ZCRod-0.025 composite with other phosphorus-based anodes for PIBs (continued).

Red P@mesoporous C	50 500 2,000	490.9 136	63.5%	396 after 75 cycles 244 after 200 cycles	[9]
Red P@active C	50	170	53%	142 after 100 cycles	[10]
Red P@active C@PPy	20 50 500	416 132	58.9%	 220 after 200 cycles	[11]
Red P@rGO	100 500 2,000	556.1 134.4	52.6%	~359 after 50 cycles ~248 after 500 cycles	[12]
Black P/graphite	250 750	~917 ~560 ~560	~70% ~92%	~420 after 50 cycles ~238 after 100 cycles	[13]
Black P/C	50 500	443 120	60%	270 after 50 cycles	[14]

Table A2 Comparison of the electrochemical performance of the P50@ZCRod-0.025 composite with other phosphorus-based anodes for PIBs (continued).

SnP@C	50 100 1,000	478.1	70.3%	 355 after 100 cycles 234.9 after 200 cycles	[15]
SnP_3/C	50 500 1,200	410 212	58.8%	408 after 50 cycles 225 after 80 cycles	[16]
Sn_4P_3/C	50	~350	59.4%	~307.2 after 50 cycles	[17]
Sn_4P_3@C fibers	50 500 2,000	514.7 169.6	64.2%	403.1 after 200 cycles 160.7 after 1,000 cycles	[18]
MoP@ C fibers	100 2,000	~350 223	~42%	~280 after 100 cycles	[19]
FeP@C nanobox	100 2,000	264 37	47%	205 after 300 cycles	[20]

Table A2 Comparison of the electrochemical performance of the P50@ZCRod-0.025 composite with other phosphorus-based anodes for PIBs (continued).

CoP@porous C sheets	100 500	182	19.6%	127 after 1,000 cycles 114 after 1,000 cycles	[21]
GeP_5	50 500 1,000	750 284.2	58.6%	495.1 after 50 cycles 213.7 after 2,000 cycles	[22]

Calculation for the optimal red P loading into ZCRod-0.025

Pore volume of ZCRod-0.025 = 1.387 cm^3 g^{-1}

Red P density ≈ 2.2 g cm^{-3}

Volume expansion of P into K_4P_3 ≈ 293% from reference[6]

Optimal red P loading amount per gram of ZCRod-0.025 = 1.387 / 2.93 * 2.2 = 1.04 g

Optimal red P loading percentage = 1.04 / (1+1.04) = 51%

Appendix References

[1] Julien PA, Uzarevic K, Katsenis AD, Kimber SA, Wang T, Farha OK, et al. In Situ Monitoring and Mechanism of the Mechanochemical Formation of a Microporous MOF-74 Framework. *J Am Chem Soc* **2016**;138:2929-32.

[2] De Yoreo JJ, Gilbert PU, Sommerdijk NA, Penn RL, Whitelam S, Joester D, et al. CRYSTAL GROWTH. Crystallization by Particle Attachment in Synthetic, Biogenic, and Geologic Environments. *Science*. **2015**;349:aaa6760.

[3] Rowsell JL, Yaghi OM. Effects of Functionalization, Catenation, and Variation of the Metal Oxide and Organic Linking Units on the Low-Pressure Hydrogen Adsorption Properties of Metal-Organic Frameworks. *J Am Chem Soc* **2006**;128:1304-15.

[4] Ghermani NE, Morgant G, d'Angelo J, Desmaële D, Fraisse B, Bonhomme F, et al. Covalently Bonded Infinite Zigzag Chain Structure in a Novel Zn(II) Complex of 2,5-dihydroxy-1,6-benzenedicarboxylic Acid. *Polyhedron*. **2007**;26:2880-4.

[5] Tranchemontagne DJ, Hunt JR, Yaghi OM. Room Temperature Synthesis of Metal-Organic Frameworks: MOF-5, MOF-74, MOF-177, MOF-199, and IRMOF-0. *Tetrahedron*. **2008**;64:8553-7.

[6] Huang X, Sui X, Ji W, Wang Y, Qu D, Chen J. From Phosphorus Nanorods/C to York-Shell P@Hollow C for Potassium-Ion Batteries: High Capacity with Stable Cyclic Performance. *J Mater Chem A*. **2020**.

[7] Chang WC, Wu JH, Chen KT, Tuan HY. Red Phosphorus Potassium-Ion Battery Anodes. *Adv Sci* (Weinh). **2019**;6:1801354.

[8] Xiong P, Bai P, Tu S, Cheng M, Zhang J, Sun J, et al. Red Phosphorus Nanoparticle@3D Interconnected Carbon Nanosheet Framework Composite for Potassium-Ion Battery Anodes. *Small*. **2018**:e1802140.

[9] Liu D, Huang XK, Qu DY, Zheng D, Wang GW, Harris J, et al. Confined Phosphorus in Carbon Nanotube-Backboned Mesoporous Carbon as Superior Anode Material for Sodium/Potassium-Ion Batteries. *Nano Energy*. **2018**;52:1-10.

[10] Huang XK, Liu D, Guo XR, Sui XY, Qu DY, Chen JH. Phosphorus/Carbon Composite Anode for Potassium-Ion Batteries: Insights into High Initial Coulombic Efficiency and Superior Cyclic Performance. *Acs Sustainable Chemistry & Engineering*. **2018**;6:16308-14.

[11] Fang K, Liu D, Xiang XY, Zhu XX, Tang HL, Qu DY, et al. Air-Stable Red Phosphorus Anode for Potassium/Sodium-Ion Batteries Enabled through Dual-Protection Design. *Nano Energy*. **2020**;69.

[12] Wang H, Wang L, Wang L, Xing Z, Wu X, Zhao W, et al. Phosphorus Particles Embedded in Reduced Graphene Oxide Matrix to Enhance Capacity and Rate Capability for Capacitive Potassium-Ion Storage. *Chemistry*. **2018**;24:13897-902.

[13] Jin H, Wang H, Qi Z, Bin DS, Zhang T, Wan Y, et al. A Black Phosphorus-Graphite Composite Anode for Li-/Na-/K-Ion Batteries. *Angew Chem Int Ed Engl*. **2020**;59:2318-22.

[14] Sultana I, Rahman MM, Ramireddy T, Chen Y, Glushenkov AM. High Capacity Potassium-Ion Battery Anodes Based on Black Phosphorus. *J Mater Chem A*. **2017**;5:23506-12.

[15] Li B, Shang S, Zhao J, Itkis DM, Jiao X, Zhang C, et al. Metastable Trigonal SnP: A Promising Anode Material for potassium-ion battery. *Carbon*. **2020**.

[16] Verma R, Didwal PN, Ki HS, Cao G, Park CJ. SnP3/Carbon Nanocomposite as an Anode Material for Potassium-Ion Batteries. *ACS Appl Mater Interfaces*. **2019**;11:26976-84.

[17] Zhang W, Mao J, Li S, Chen Z, Guo Z. Phosphorus-Based Alloy Materials for Advanced Potassium-Ion Battery Anode. *J Am Chem Soc* **2017**;139:3316-9.

[18] Zhang W, Pang WK, Sencadas V, Guo Z. Understanding High-Energy-Density Sn_4P_3 Anodes for Potassium-Ion Batteries. *Joule*. **2018**;2:1534-47.

[19] Yi Z, Liu Y, Li Y, Zhou L, Wang Z, Zhang J, et al. Flexible Membrane Consisting of MoP Ultrafine Nanoparticles Highly Distributed Inside N and P Codoped Carbon Nanofibers as High-Performance Anode for Potassium-Ion Batteries. *Small*. **2020**;16:e1905301.

[20] Yang F, Gao H, Hao J, Zhang S, Li P, Liu Y, et al. Yolk–Shell Structured FeP@C Nanoboxes as Advanced Anode Materials for Rechargeable Lithium‐/Potassium‐Ion Batteries. *Adv Funct Mater* **2019**;29:1808291.

[21] Bai J, Xi B, Mao H, Lin Y, Ma X, Feng J, et al. One-Step Construction of N,P-Codoped Porous Carbon Sheets/CoP Hybrids with Enhanced Lithium and Potassium Storage. *Adv Mater* **2018**;30:e1802310.

[22] Zhang WC, Wu ZB, Zhang J, Liu GP, Yang NH, Liu RS, et al. Unraveling the Effect of Salt Chemistry on Long-Durability High-Phosphorus-Concentration Anode for Potassium Ion Batteries. *Nano Energy*. **2018**;53:967-74.